NONEQUILIBRIUM GREEN FUNCTION APPROACH TO ELASTIC AND INELASTIC SPIN-CHARGE TRANSPORT IN TOPOLOGICAL INSULATOR-BASED HETEROSTRUCTURES AND MAGNETIC TUNNEL JUNCTIONS

by

Farzad Mahfouzi

A dissertation submitted to the Faculty of the University of Delaware in partial fulfillment of the requirements for the degree of Doctor of Philosophy in Physics

Summer 2014

ProQuest LLC.
789 East Eisenhower Parkway
P.O. Box 1346
Ann Arbor, MI 48106 - 1346

NONEQUILIBRIUM GREEN FUNCTION APPROACH TO ELASTIC AND INELASTIC SPIN-CHARGE TRANSPORT IN TOPOLOGICAL INSULATOR-BASED HETEROSTRUCTURES AND MAGNETIC TUNNEL JUNCTIONS

by

Farzad Mahfouzi

Approved: _____

Edmund R. Nowak, Ph.D.
Chair of the Department of Physics

Approved: _____

George H. Watson , Ph.D.
Dean of the College of Art and Science

Approved: _____

James G. Richards, Ph.D.
Vice Provost for Graduate and Professional Education

I certify that I have read this dissertation and that in my opinion it meets the academic and professional standard required by the University as a dissertation for the degree of Doctor of Philosophy.

Signed: _____

Branislav K. Nikolic, Ph.D.
Professor in charge of dissertation

I certify that I have read this dissertation and that in my opinion it meets the academic and professional standard required by the University as a dissertation for the degree of Doctor of Philosophy.

Signed: _____

Stephen Barr, Ph.D.
Member of dissertation committee

I certify that I have read this dissertation and that in my opinion it meets the academic and professional standard required by the University as a dissertation for the degree of Doctor of Philosophy.

Signed: _____

James MacDonald, Ph.D.
Member of dissertation committee

I certify that I have read this dissertation and that in my opinion it meets the academic and professional standard required by the University as a dissertation for the degree of Doctor of Philosophy.

Signed: _____

Matthew F. Doty, Ph.D.
Member of dissertation committee

ACKNOWLEDGEMENTS

I would like to express my special appreciation and thanks to my advisor Prof. Branislav. K. Nikolić, for all of his invaluable advices on both research as well as on my career. I would also like to thank my committee members, Prof. James MacDonald, Prof. Stephen Barr, Prof. Matthew Doty for serving as my committee members.

I would also like to thank all of my friends in UD for their supports and helps. In particular I would like to thank, Dr. Hector Mera for invaluable discussions we had specially at coffee time. Also I am grateful to Kamal Saha, Taha Salavati-fard, Po-Hao Chang, Laura Rose Vanderhauf, Tarique Aziz, Son-Hsien Chen, Derya Vural, Curtis Walkons, Prachanda Subedi, Seth Meiselman, Ryan Stearrett, Prayash Sharma Pyakurel, Nasrin Afzal, Parker Anderson and many others for their helps and friendship. I would also like to thank the secretaries in Department of Physics and Astronomy specially Mrs. Maura Perkins and Mrs. Debra Morris, for coping with all of my botherings.

A special thanks to my family. Words can not express how grateful I am to my mother, father and sisters for all of the sacrifices that you have made on my behalf. Your prayer for me was what sustained me thus far. Thank you for supporting me for everything, and especially I can not thank you enough for encouraging me throughout this experience.

TABLE OF CONTENTS

LIST OF FIGURES

ABSTRACT

Current and future technological needs increasingly motivate the intensive scientific research of the properties of materials at the nano-scale. One of the most important domains in this respect at present concerns nano-electronics and its diverse applications. The great interest in this domain arises from the potential reduction of the size of the circuit components, maintaining their quality and functionality, and aiming at greater efficiency, economy, and storage characteristics for the corresponding physical devices. The aim of this thesis is to present a contribution to the analysis of the electronic charge and spin transport phenomena that occur at the quantum level in nano-structures.

This thesis spans the areas of quantum transport theory through time-dependent systems, electron-boson interacting systems and systems of interest to spintronics. A common thread in the thesis is to develop the theoretical foundations and computational algorithms to numerically simulate such systems. In order to optimize the numerical calculations I resort to different techniques (such as graph theory in finding inverse of a sparse matrix, adaptive grids for integrations and programming languages (*e.g.,* MATLAB and C++) and distributed computing tools (MPI, CUDA).

Outline of the Thesis

After giving an introduction to the topics covered in this thesis in Chapter. 1, I present the theoretical foundations to the field of non-equilibrium quantum statistics in Chapter. 2. The applications of this formalism and the results are covered in the subsequent chapters as follows:

1. **Spin and charge quantum pumping in time-dependent systems:**

   Covered in Chapters. 3, . 4 and . 5, this topics was initially motivated by experiments on measuring voltage signal from a magnetic tunnel junction (MTJ) exposed to a microwave radiation in ferromagnetic resonance (FMR) condition.

In Chapter. 3 we found a possible explanation for the finite voltage signal measured from a tunnel junction consisting of only a single ferromagnet (FM). I show that this could be due to the existence of Rashba spin-orbit coupling (SOC) at the interface of the FM and insulator. Assuming that the measured signals are quantum mechanical effect where a solution to the time dependent Schrödinger equation is required, I use Keldysh Green function formalism to introduce a "multi-photon" approach which takes into account the effects of time-dependent term exactly up to scatterings from a finite number of photons. We then proceed to find the corresponding Green function numerically using a recursive method which allows us to increase the size of the system significantly. We also implement other approximations such as adiabatic and rotating frame approaches and compared them with our approach. In Chapter. 4, I investigate the spin and charge pumping from a precessing magnetization attached to the edge of a 2-dimensional topological insulator (2DTI). We show that, in this system a huge spin current (or voltage signal if the FM covers only one edge) can be pumped for very small cone angles of the precessing FM (proportional to the intensity of the applied microwave). In Chapter. 5 I present the third project in this field of research, where, I investigated the pumping from FM attached to a 3-dimensional TI.

2. **Spin-transfer torque:**

   Presented in Chapter. 6, in this work I investigate the torque induced by a flow of spin-polarized current into a FM and check the condition in which it can cause the magnetization to flip. Motivated by recent experimental developments in the field, here I consider systems with strong SOC such as TIs within a magnetic tunnel junction (MTJ) heterostructure. In the theoretical part I show the correct way (as opposed to the conventional approach used in some theoretical works which suffers from violation of the gauge invariance) to calculate linear-response torque to the external applied voltage and for the numerical calculation I adopted a parallelized adaptive integration algorithm in order to take care of very sharp changes that appear in momentum and energy dependence of the spin-transfer torques.

3. **Transport through many-body interacting systems:**

   As demonstrated in Chapter. 7, in this research I use Keldysh Green function formalism resummation of the corresponding Feynman diagrams, including the self-consistent second Born approximation with and without bubble diagrams (*i.e.,* GW-like), to find the effect of coupling on I-V characteristics and STT in MTJs. Particularly, I investigated if the electron-magnon coupling can explain the zero-bias anomaly observed experimentally in MTJs which is considered to be a signature of inelastic tunneling spectrum.

LIST OF ABBREVIATIONS

2DEG	two-dimensional electron gas.
ARPES	angle resolved photoemission spectroscopy.
DFT	density functional theory.
FI	ferromagnetic insulator.
FM	ferromagnetic metal.
FMR	ferromagnetic resonance.
GMR	giant magnetoresistance.
Gr	graphene.
IVC	current-voltage characteristics.
MRAM	magnetic random access memory.
MTJ	magnetic tunnel junction.
NEGF	non-equilibrium Green function.
QL	quintuple layer.
SHE	spin Hall effect.
SOC	spin-orbit coupling.
STT	spin transfer torque.
TAMR	tunneling anisotropic magnetoresistance.
TI	topological insulator.
TME	topological magnetoelectric effect.
TMR	tunneling magnetoresistance.
VCMA	voltage controlled magnetic anisotropy.
YIG	yttrium iron garnet.
$\mathrm{Tr}(A)$	trace of matrix A
$\mathcal{T}$	time ordering operator.
$\mathbf{A}$	operator (matrix) defined in a single particle Hilbert space.
$\hat{a}$	operator defined in Fock space.
$\check{a}$	operator defined in Fock+Keldysh space.
$\check{\mathbf{A}}$	operator defined in Hilbert+Keldysh space. A simiar notation has been used in multi-photon approach.

$\breve{\mathbf{A}}$	operator defined in Hilbert+Keldysh+Exciton space.
G^r	retarded Green function.
G^a	advanced Green function.
$G^<$	lesser Green function.
$G^>$	greater Green function.
$\Re(A)$	real part of A.
$\Im(A)$	imaginary part of A.
α_R	Rashba spin-orbit coupling strength.

Chapter 1

INTRODUCTION

Spintronics explores phenomena intertwining electronic charge and spin [5]. The ability of spintronics to re-energize itself in directions that germinate new subfields has made it one of the most fertile grounds for basic research aimed at future applications. It has also crucially relied on the discovery of *new materials* (such as diluted magnetic semiconductors and oxides [6, 7]) and *heterostructures* (such as spin valves, magnetic tunnel junctions, and multilayers for electrical manipulation of magnetism [6, 8]) where control over spin-dependent properties of interfaces is essential. The first-generation spintronics [9], which is primarily focused on giant magnetoresistance (GMR) in FM/N/FM (FM-ferromagnetic metal; N-normal metal) spin valves and tunneling magnetoresistance (TMR) in FM/I/FM (I-insulator) magnetic tunnel junctions (MTJs), operates with *independent* spin-$\uparrow$ and spin-$\downarrow$ transport channels and spin-polarized charge currents. On the other hand, the so-called *second-generation* spintronics [10] aims to harness spin coherence, in which a persistent component of the spin can be maintained transverse to an applied magnetic field or magnetization, as well as low-dissipation *pure* (i.e., not accompanied by any net charge flux) spin currents [11].

The May 2012 special Insight issue of Nature Materials has highlighted five emerging subfields of the second-generation spintronics: (*i*) spin-transfer torque (STT), where spin current drives magnetization dynamics [12]; (*ii*) spin Hall effect (SHE), where longitudinal charge current $I = I^{\uparrow} + I^{\downarrow}$ generates transverse pure spin current $I^{S_z} = I^{\uparrow} - I^{\downarrow}$ in systems with intrinsic or extrinsic spin-orbit coupling (SOC) [13]; (*iii*) spin caloritronics, where temperature gradients drive spin currents carried by electrons

or magnons [14]; (*iv*) silicon spintronics, exploring injection, propagation over large distances [15] and detection of spins in silicon [16]; and (*v*) spintronic aspects of graphene (Gr) and TI as newly discovered "Dirac materials" [17]. These are nonmagnetic materials which possess a usual band gap in the bulk, while hosting conducting surfaces (or edges in 2D) whose massless Dirac electrons have spins locked to their momenta due to the strong Rashba-type SOC. The spin-momentum locking prevents backscattering off weak time-reversal invariant perturbations which do not close the bulk band gap, such as lattice distortions and non-magnetic impurities. It is worth mentioning that the first principle calculation [18, 19] has ignited the fabrication of Bi_2Se_3, Bi_2Te_3 and Sb_2Te_3 in the form of thin films [20] and nanowires [21] (made possible by their layered structure). Spin-momentum locked Dirac cone of the surface states has been confirmed using angle-resolved photoemission spectroscopy (ARPES) [22]. Furthermore, DFT-based calculations has predicted [23] that doping Gr with heavy adatoms could yield a robust 2D TI—its bulk band gap can reach room temperature, while Gr sheets are much easier to probe and integrate into devices than HgTe/CdTe quantum wells [24, 25, 26] as the only presently available realization of 2D TIs.

In the first part of my thesis concerning noninteracting systems, I focus on STT [12, 27], and its reciprocal effect termed spin pumping [28, 29, 30]. However, unlike conventional versions of these effects, where SOC is either neglected or enters indirectly through the finite spin-diffusion length, here we propose novel heterostructures which crucially involve strong SOC at the interface between FM or ferromagnetic insulator (FI) layer and a normal layer made of metals, graphene, TIs or band insulators. In the second part I investigate the effect of electron-magnon coupling on trasport properties of MTJs. In the following we present a short introduction to the topics covered in this thesis.

1.1 Spin and Charge Pumping in MTJs

Pumping is a phenomenon that converts ac variations of the parameters of an open quantum system into a dc flow of particles in the absence of an applied bias

voltage. In the adiabatic regime, when the time variation of the parameters is slow comparing to the natural frequencies of the system, the pumped charge depends only on the trajectory defined in the parameter space. In this case, in his seminal paper [31] Thouless showed that the particle transport during the time cycle can be expressed as a Berry phase and it is proportional to the frequency of the oscillation. For noninteracting electrons, the formulation of the pumping current in terms of the variations of the scattering matrix was developed by Brouwer [32] for adiabatic pumping and followed a work by Büttiker, Pretre, and Thomas [33]. Similarly, the effect can also be used to generate and manipulate spin current in spintronic devices.

The spin pumping by precessing magnetization is a phenomenon where the moving magnetization of a single ferromagnetic layer, driven by microwave radiation under the ferromagnetic resonance conditions (FMR), emits spin current into adjacent normal metal layers [28]. The emitted spin current is *pure* [11] in the sense that it is not accompanied by any net charge flux. This effect is termed "pumping" because it happens in the absence of any dc bias voltage, and together with closely related adiabatic quantum pumping of charge [34] or spin [35] observed in quantum dots, falls in the category of problems where an open quantum system (i.e., a finite many-particle system in contact with particle reservoirs) is exposed to time-dependent periodic externals fields. Unlike closely related adiabatic quantum pumping of charge [34] or spin [35] currents in quantum dots, which requires low temperatures and has been difficult to confirm unambiguously [36], spin pumping by moving magnetization is a ubiquitous phenomenon in magnetic multilayers at room temperature.

Since angular momentum loss carried by emitted pure spin current adds extrinsic contribution to Gilbert damping, spin pumping has initially been observed [28, 29, 37] as an increased broadening of FMR spectra upon switching from a single FM layer to FM/N multilayers (N-normal metal). Therefore, it is also an essential ingredient to understand [38] the dynamical behaviour in experiments [39] on the magnetization switching mechanisms.

1.2 Spin-Transfer Torque

The STT is a phenomenon in which a spin current of large enough density injected into a FM layer either switches its free magnetization from one static configuration to another or generates a dynamical situation with steady-state precessing magnetization [12, 27]. The origin of STT is absorption of itinerant flow of spin angular momentum components normal to the magnetization direction [40]. The reduction of current densities (currently of the order 10^6-10^8 A/cm^2) required for STT-based magnetization switching is expected to bring commercially viable magnetic random access memory (MRAM) [41]. The rich nonequilibrium physics [42] arising in the interplay of spin currents carried by fast conduction electrons and collective magnetization dynamics, viewed as a slow classical degree of freedom [43], is also of great fundamental interest.

The conventional STT is typically measured [42], or exploited for MRAM devices [41], using MgO-based MTJs [44] with noncollinear magnetizations of the two FM layers. The STT has been studied extensively in FM/N [45], FM/I [46] and FI/N multilayers [47]. In contrast, the exploration of heterostructures, where SOC brings novel physics and new avenues for applications of STT and spin pumping, is in its infancy. For example, since 2010 several experiments [48, 49, 50, 51] have detected switching of magnetization of a *single* FM layer in lateral N/FM or N/FM/I heterostructures with in-plane injected unpolarized charge current. Because Pt/Co/AlO_x or Ta/CoFeB/MgO heterostructures lack the second FM layer with fixed magnetization (acting as spin-polarizer in conventional FM/I/FM vertical MTJs), SOC must be involved in this process. Since these heterostructures are *inversion asymmetric*, one explanation assumes that there is a strong Rashba-type SOC [52] at the Pt/Co (and/or Co/AlO_x [48, 49] or CoFeB/MgO [53]) interface, so that longitudinal current-induces nonequilibrium transverse spin accumulation—the so-called Edelstein effect [54, 55]—which then generates SO torque [56] with large field-like component. The second mechanism, where SH current generated within the bulk of the N layer flows perpendicularly through the Pt/Co or Ta/CoFeB interface to induce STT on the magnetization of the

FM layer [50, 51], can operate concurrently and independently. Unlike the SO torques, which transfer orbital momentum from the lattice to the spin system, the mechanism in the second explanation is equivalent to conventional STT arising from a polarizing layer that would be located below the Co layer with its in-plane magnetization perpendicular to the transport direction. However, various experiments have reported conflicting results for the size and direction of the torque, whose sensitivity on the thickness of Co layer is difficult to reconcile with predictions based on simplistic model Hamiltonians of experimental devices [57, 58, 59]. In what follows and the rest of the thesis, unless mentioned otherwise, we choose the z-axis to be perpendicular to the existing planes in the system and should the transport be in-plane we choose x-axis to be along the transport direction.

While experiments have suggested presence of giant magnitude of Rashba SOC, $\alpha(\vec{\sigma}\times\hat{\mathbf{k}})\cdot\mathbf{e}_z$, at the Pt/Co [48, 49] or Ta/CoFeB interfaces [53], whose strength α is two to three orders of magnitudes larger than in traditional [52] two-dimensional electron gases (2DEGs) within semiconductor heterostructures (see Table 1 in Ref. [56]), no direct measurement of α has been reported and only one very recent DFT study [60] has addressed this problem quantitatively.

Another type of SOC-driven STT has been predicted in *vertical* N/I/FM [61, 62] and N/TI/FM [62] heterostructures, where current flows *perpendicularly* to the plane with the strong Rashba SOC. These effects are far less transparent than the SO torques since they are a second order ($\propto \alpha_R^2$) quantum-mechanical process, closely related to the tunneling anisotropic magnetoresistance [30, 63, 64, 65] (TAMR) in the case of N/I/FM junctions [62, 61], or a combination of TAMR-based effect and spin-polarizing action of the TI slab where charge current becomes spin-polarized in the direction perpendicular to the transport and normal to the quintuple layers (QLs) of the TI in the case of N/TI/FM junctions [62].

The two types of *unconventional* SOC-driven torques could have important roles in optimizing devices for ST-based MRAM [41] and nano-oscillator [66] applications. For example, their usage could drastically simplify complex stacking structures of

presently used MTJs, typically involving more than 10 different layers, due to the need to: optimize spin polarization across the junction; stabilize the fixed layer magnetization; and minimize stray fields [42, 67]. The absolute current (< 1 mA) applied in-plane through a thin lateral surface of recently fabricated [48, 49] $Pt/Co/AlO_x$ heterostructures provides significant gains in terms of integration and power consumption. Another key issue is that conventional STT-MRAM devices [41] operate with collinearly magnetized MTJs, so that initial STT is zero and one has to rely on thermal fluctuations or small misalignments of the layer magnetizations to initiate the switching. This leads to undesirable long mean switching times [68] and broad switching time distributions [69]. To overcome these impediments, in Chapter. 6 of this thesis we propose a greatly simplified version of orthogonal STT-MRAM [67], where the TI layer caps FM/I/FM′ MTJ to form TI/FM/I/FM′ stack. Should the injected current have in-plane component in QLs, the TI layer polarizes the current in the direction perpendicular to the transport [62], thereby initiating STT on the free magnetization of the FM layer (pointing along the z-axis) whose switching is detected by the FM′ layer.

Another interesting effect is when heterostructures of FI (or FM) attached to the surface state of 3D TI opens an energy gap at the Dirac cone at the interface due to the proximity-induced [70] exchange coupling Δ_{surf}. The corresponding *massive* Dirac fermions lead to chiral 1D edge states along FM domain walls where the mass changes sign. They also exhibit half-quantized QH conductivity $\sigma_H = \pm e^2/2h$ [71], even in the limit of vanishingly small $\Delta_{\text{surf}} \to 0$, which is closely related to parity anomaly in high energy physics [71]. Finally, the heterostructures with $\Delta_{\text{surf}} \neq 0$ would exhibit topological magnetoelectric effect (TME) where magnetization is generated by electric field, and vice versa, with a quantized coefficient [71].

The TI surfaces are also intensely explored as a new resource for spintronics [17]. For example, magnetization of FI overlayer could be switched by the interfacial quantum Hall current [72, 73, 74] in the lateral geometry. In this thesis we show that in *vertical* FM/TI heterostructures [62, 75] precessing magnetization of FM (or FI) layer

would pump charge current perpendicularly through the FM/TI interface with its magnitude and angular dependence being highly sensitive to massive Dirac fermions at the interface [75]. A related prediction was made by Ref. [76] where lateral precessing FM on the surface of 3D TI heterostructure would generate topological (i.e., insensitive to impurities) charge pumping with jumps in the time dependence of charge current signifying parity anomaly. Another challenge is to find FI overlayers that can be deposited onto Gr-based 2D TIs, which would generate a giant spin battery effect [77] or *quantized charge pumping as the most direct probe of topological invariants* (as predicted by Ref. [78] and Ref. [77]).

1.3 Electron-Magnon Interaction Effect on Electronic Transport

One of the most important topics in the field of spintronics is to understand interactions between collective spin dynamics (*i.e.*, magnons) and electronic transport in ferromagnetic materials. In particular, the effect of electron-magnon scattering on spin dephasing or the effects based on the conversion of electronic spin current into spin dynamics and vice versa, are two of many phenomena that have challenged condensed matter physicists for many years. While in quantum spin pumping and STT effects we consider the ferromagnet as a whole and ignore the internal collective dynamics of the local spin moments, in reality these internal degrees of freedom are believed to alter the results significantly. In fact, when passing hot electrons through a magnetic material, excitations of the collective modes can be created in the material through inelastic scattering accompanied by a spin flip and transfer of angular momentum as well as energy to the magnetic system. The spin flip of the electron due to the inelastic scattering from the magnetic material creates a Stoner excitation or a collective excitation in form of a magnon. This phenomenon can also be used to convert electronic spin current into magnetic spin current, which unlike electronic spin current, can propagate for a long distance in magnetic dielectrics (*e.g.*, yttrium iron garnet, YIG) without significant dissipation as a result of very small magnetic damping. In this case the efficiency of such an effect is mainly limited by the efficiency of the electronic spin current

to magnonic spin current conversion. The fact that this effect is in principle similar to the energy conversion mechanisms in other branches of physics such as exitonic solar cells, similar techniques that are used to improve the efficiency of the conversion can be used here as well. Two of such techniques include, multiple magnonic excitation [79] and renormalizing the effective coupling through quantum many-body vortex corrections. While different experimental groups are currently working on this topic, on the theoretical front due to its intrinsic nonlinearity and time dependent nature of the effects, the quantum simulation of the problem has become very difficult. To cite Ashcroft and Mermin [80] : "The development of a tractable model of a magnetic metal, capable of describing both the characteristic electron spin correlations as well as the electronic transport properties predicted by simple band theory, remains one of the major unsolved problems of modern solid state theory."

In order to model collective modes in a ferromagnet correctly, one should consider different types of interactions in the system. Few of such interactions include: the exchange interaction; the spin-orbit interaction; the Zeeman interaction, and the magnetic dipole-dipole interactions. While the exchange interaction causes the alignment of the spins, it can arise from either direct (*i.e.* overlap of the wavefunctions), indirect (*i.e.* mediated by nonmagnetic atoms or conduction electrons) or itinerant exchange (*i.e.* exchange between itinerant electrons) interactions. The spin-orbit interaction couples the magnetism to the crystal configuration of the lattice which leads to the magnetocrystalline anisotropy in ferromagnetic materials. Furthermore, the Zeeman interaction describes the coupling of angular momentum to an external magnetic field. And finally, the dipole-dipole interaction leads to the existence of domain-walls. It is worth mentioning that a rigorous quantum consideration of the effect of lattice structure and magnetic dipole interaction is still in order [79]. In this thesis we address the effect of such collective modes in current-voltage characteristics (IVC) in MTJs. To do this we consider phenomenological modeling of the ferromagnet taking into account the exchange coupling, anisotropic magnetic field and the Zeeman interaction. The formulation and the results are covered in Chapter 7.

Chapter 2

QUANTUM MECHANICAL FORMULATION OF SYSTEMS OUT OF EQUILIBRIUM

2.1 Introduction

Physics of nano-scale electronic systems is an area of both theoretical and experimental research activities that has been growing explosively worldwide during the past two decades. The necessity to miniaturize the electronic devices, which has already made the dimensions of current transistors used in computer chips to be in the range of nano-meters, has made the effects of low dimensionality (*e.g.*, surface effects) and quantum wave function of the electrons more significant. Further progress on this path requires the electronic devices to use full advantages of quantum-mechanical behavior of electrons in such scales rather than classical or semi-classical approximations that has been sufficient to theoretically explain most of the effects observed in the conventional electronic devices. Additionally, due to their very sensitive and nontrivial nature, fabrication and investigating the possible applications of nano-electronic devices experimentally are very expensive and time consuming such that in this field theoretical modelings and predictions have more important place than ever in the history of science. Fortunately, in this field the sizes of the building blocks of the devices are small enough that make it possible to start performing controlled modeling simulations to guide the experiments in building proper devices for the practical purposes. Furthermore, in nano-structured materials due to their very high specific surface area, the surfaces and interfaces play important role in the dynamics of the electrons. This in turn necessitates the real space modeling of the devices. The usage of intrinsic quantum properties of the electrons (*e.g.*, spin, pseudo-spin) is also another possible advantage of the nano-scale devices that has opened the whole new field of spintronics.

Unlike charge, the spin of the electrons is in general a nonconservative quantity that idealistically can be manipulated in a controlled fashion that can be used as another mean to; alter the charge current flow, transport the information (*i.e.*, spin current) or perform quantum computations. Such applications has made the field of spintronics as one of the most promising areas of condensed matter physics, materials science, and nanotechnology that can have a great impact on the functionality of the future devices.

The outline of this chapter is as follows. In Sec .2.2 we present the Schrödinger equation in atomic orbital representation with the aim of discretization of the Hamiltonian. In Sec .2.3 after giving an introduction to the Green function (GF) approach of solving the single particle Schrödinger equation, we proceed with a generalization of the technique to many-particle systems in equilibrium. Furthermore, we present some technical details regarding the different approaches to reduce the size of the Hamiltonian and regard the effect of the rest of the system as a self-energy term. In Sec .2.4 we generalize the GF approach to the nonequilibrium case using the, so called, Keldysh technique and present the expressions for the observables in this formalism in the subsequent subsections. In Sec .2.5 we present a generalization of the GF approach to interacting cases and obtain the expressions for the observables in the presence of the interactions. Although the effort has been made to write this chapter comprehensively, we assume that the reader is already familiar with the basics of the topics.

2.2 Tight-Binding Hamiltonian

A general trend in theoretical physics to simulate a system is to start from a minimal model that contains only the relevant features of the system and ignore the effects that are believed to be insignificant in the regime of interest. In the phenomenological modeling of a system we introduce a set of initially unknown parameters that are only found after comparing the results of calculations with the experimentally measured results. In this thesis in order to model the nano-structured systems we use tight binding approach which is a phenomenological method to construct the Hamiltonian suitable for numerical simulations of quantum systems. In following we present an

introduction to the tight binding approach using the atomic orbitals as the localized Wannier functions [81].

The dynamics of an electron inside a crystal of atoms obeys the Schrödinger equation

$$i\frac{\partial}{\partial t}\Psi(\mathbf{x},t)=\left[-\frac{\hbar^2}{2m}\nabla^2+\sum_i U(\mathbf{R}_i+\mathbf{x},t)\right]\Psi(\mathbf{x},t), \tag{2.1}$$

where $\mathbf{R}_i$ and $U(\mathbf{x},t)$ correspond to the location and potential profile of each atom, respectively. Assuming that the localized states corresponding to the atoms form a complete set that covers the whole or the physically relevant portion of the Hilbert space of a single electron, one can expand the wave function in terms of the local states, $\Psi(\mathbf{x},t)=\sum_{i,\alpha}a_{i\alpha}(t)\psi_\alpha(\mathbf{R}_i+\mathbf{x})$, where $\psi_\alpha(\mathbf{x})$, corresponds to the localized eigenstates of a single atom satisfying the atomistic Schrödinger equation, $[-\hbar^2\nabla^2/2m+U(\mathbf{x})]\psi_\alpha(\mathbf{x})=\varepsilon_\alpha\psi_\alpha(\mathbf{x})$. Substituting this expansion into the Schrödinger equation, we get

$$i\frac{\partial}{\partial t}c_{i\alpha}(t)=\varepsilon_\alpha c_{i\alpha}(t)+\sum_{j\beta}T_{i\alpha,j\beta}c_{j\beta}(t), \tag{2.2}$$

where $c(t)=\mathbf{A}^{\frac{1}{2}}a(t)$, and $\mathbf{T}$ is called the hopping matrix which is defined as $\mathbf{T}=\mathbf{A}^{-\frac{1}{2}}\mathbf{V}\mathbf{A}^{-\frac{1}{2}}$, with

$$\mathbf{A}_{i\alpha,j\beta}=\int d\mathbf{x}\psi^*_\beta(\mathbf{R}_j+\mathbf{x})\psi_\alpha(\mathbf{R}_i+\mathbf{x}), \tag{2.3}$$

as the overlap matrix and,

$$\mathbf{V}_{i\alpha,j\beta}=\sum_{k\neq i}\int d\mathbf{x}\psi^*_\beta(\mathbf{R}_j+\mathbf{x})U(\mathbf{R}_k+\mathbf{x})\psi_\alpha(\mathbf{R}_i+\mathbf{x}). \tag{2.4}$$

Note that the overlap matrix commutes with the diagonal matrix formed by the atomic eigenenergies ε_α, and additionally, for a normalized set of local states we have $\mathbf{A}_{i\alpha,i\beta}=\delta_{\alpha\beta}$. Unlike the original Schrödinger equation, Eq. (2.2) is a discrete equation that can be solved numerically. It is in fact straightforward to find the eigenenergies and eigenstates of the Schrödinger equation in the new representation, by diagonalizing the Hamiltonian matrix

$$\mathbf{H}_{i\alpha,j\beta}=\varepsilon_{i\alpha}\delta_{\alpha\beta}\delta_{ij}+\mathbf{T}_{i\alpha,j\beta}. \tag{2.5}$$

Another approach to find the observables of this system is to use GF approach which is the subject of the next section.

2.3 GF Formalism

In general, GF approach is introduced when the solution to a system of linear integro-differential equations is required. In fact the GF is nothing more than the propagator of the system which is defined as

$$c_{i\alpha}(t) = \sum_{j\beta} \mathcal{T}(e^{-i\int_0^t dt' \mathbf{H}(t')})_{i\alpha,j\beta} c_{j\beta}(t_0) = -i \sum_{j\beta} \mathbf{G}_{i\alpha,j\beta}(t,t_0) c_{j\beta}(t_0), \tag{2.6}$$

which says, if the quantum state of the system is known at time t_0, the GF can be used to obtain the quantum state at another time t. Here $\mathcal{T}$ is the time ordering operator which orders operators (*i.e.*, time dependent Hamiltonians) such that $\mathcal{T}[\mathbf{H}(t_1)\mathbf{H}(t_2)] = \theta(t_1-t_2)\mathbf{H}(t_1)\mathbf{H}(t_2) + \theta(t_2-t_1)\mathbf{H}(t_2)\mathbf{H}(t_1)$, where, $\theta(x)$ is the Heaviside step function ($\theta_x = 1$ for $x \geq 0$ and $\theta_x = 0$ for $x < 0$). Eq. (2.2) requires the GF matrix to obey the following equation of motion called Dyson equation,

$$\left(i\frac{\partial}{\partial t} - \mathbf{H}\right) \mathbf{G}(t,t_0) = \delta(t-t_0)\mathbf{1}. \tag{2.7}$$

Here, $\mathbf{1}$ is the identity matrix. The conventional solution of this equation which has the form of Feynman propagators reads,

$$\mathbf{G}(t,t_0) = \theta(t-t_0)\mathbf{G}^r(t,t_0) - \theta(t_0-t)\mathbf{G}^a(t,t_0), \tag{2.8}$$

where, $\mathbf{G}^r$ ($\mathbf{G}^a$) is called retarded (advanced) GF and read

$$\mathbf{G}^r(E) = \frac{1}{(E-i\eta)\mathbf{1} - \mathbf{H}}, \quad \mathbf{G}^a(E) = [\mathbf{G}^r(E)]^\dagger. \tag{2.9}$$

2.3.1 GF Approach for Open Quantum System

The GF approach proves to be advantageous comparing to the diagonalization method when we have an open systems (the size of the system is infinite). In this case we can define a region of interest called the central region where the observables are being measured and consider the rest of the system as the reservoirs which can be

modeled as a self-energy term in the Hamiltonian. We can demonstrate this in details considering an infinite size of 1D chain of atoms with a nearest neighbored hopping such that $\mathbf{T}_{i\alpha,i+1\beta} = \mathbf{T}^{\dagger}_{i+1\alpha,i\beta} = \mathbf{t}_{\alpha\beta}$. In this case Eq. (2.2) after Fourier transformation in time reads

$$(E - i\eta - \varepsilon_{\alpha})c_{i\alpha}(E) - \sum_{\beta} \mathbf{t}_{\alpha\beta} c_{i+1\beta}(E) - \sum_{\beta} \mathbf{t}^{\dagger}_{\alpha\beta} c_{i-1\beta}(E) = 0, \tag{2.10}$$

Assuming a finite size for the chain, we can try to solve this system of equations starting from either end of the chain inside one of the reservoirs. In this case for the "last" atom ($i = N$, where $N \to \infty$) we have

$$c_{N\alpha} = \sum_{\beta} \left[\frac{1}{(E - i\eta)\mathbf{1} - \varepsilon} \mathbf{t}^{\dagger} \right]_{\alpha\beta} c_{N-1\beta}. \tag{2.11}$$

We can then plug in this solution into the equation for $i = N - 1$ and obtain

$$c_{N-1\alpha} = \sum_{\beta} \left[\frac{1}{(E - i\eta)\mathbf{1} - \varepsilon - \mathbf{\Sigma}_N(E)} \mathbf{t}^{\dagger} \right]_{\alpha\beta} c_{N-2\beta}. \tag{2.12}$$

where $\mathbf{\Sigma}^{r}_{N}(E) = \mathbf{t}\left[(E - i\eta)\mathbf{1} - \varepsilon\right]^{-1}\mathbf{t}^{\dagger}$ is the self-energy due to removal of the Nth atom. We can continue this for the rest of the atoms in the reservoir and remove them one by one and obtain the following recursive relation for the self-energy

$$\mathbf{\Sigma}^{r}_{n-1} = \mathbf{t} \frac{1}{(E - i\eta)\mathbf{1} - \varepsilon - \mathbf{\Sigma}_n} \mathbf{t}^{\dagger}. \tag{2.13}$$

For an infinite iteration which corresponds to infinite number of atoms in the reservoir the self-energy converges to a finite value. This approach is in essence nothing more than Gauss-Gordan elimination method to find solution to a linear system of equations.

Another numerical approach which converges much faster than the above iteration scheme is to eliminate half of the atoms in each iteration instead of a single atom. In this case we assume that the number of atoms is 2^N and in first iteration we remove the atoms with even labels, $(2, 4, 6, ...)$. The Schrödinger equation in this case reads

$$(\mathbf{g}_0^{-1} - \mathbf{t}\mathbf{g}_0\mathbf{t}^{\dagger})c_1 - \mathbf{t}\mathbf{g}_0\mathbf{t}c_3 - \mathbf{t}^{\dagger}c_0 = 0, \tag{2.14}$$

$$(\mathbf{g}_0^{-1} - \mathbf{t}\mathbf{g}_0\mathbf{t}^{\dagger} - \mathbf{t}^{\dagger}\mathbf{g}_0\mathbf{t})c_{2i+1} - \mathbf{t}^{\dagger}\mathbf{g}_0\mathbf{t}^{\dagger}c_{2i-1} - \mathbf{t}\mathbf{g}_0\mathbf{t}c_{2i+3} = 0. \tag{2.15}$$

where $\mathbf{g}_0^{-1} = (E - i\eta)\mathbf{1} - \varepsilon$. In the second step, we repeat the same procedure and remove the atoms with labels $(3, 7, 11, ...)$ to obtain a Schrödinger equation for the atoms with labels $4i + 1$. Performing this elimination n times gives

$$(\mathbf{g}_0^{-1} - \sum_{m=0}^{n-1} \mathbf{u}_m \mathbf{g}_m \mathbf{v}_m) c_1 - \mathbf{u}_n c_{2^n+1} - \mathbf{v}_0 c_0 = 0, \tag{2.16}$$

$$\mathbf{g}_n^{-1} c_{2^n i+1} - \mathbf{v}_n c_{2^n(i-1)+1} - \mathbf{u}_n c_{2^n(i+1)+1} = 0, \tag{2.17}$$

where $\mathbf{u}_0 = \mathbf{t}$, $\mathbf{v}_0 = \mathbf{t}^\dagger$ and the recursive relations are given by

$$\mathbf{g}_n^{-1} = \mathbf{g}_{n-1}^{-1} - \mathbf{u}_{n-1}\mathbf{g}_{n-1}\mathbf{v}_{n-1} - \mathbf{v}_{n-1}\mathbf{g}_{n-1}\mathbf{u}_{n-1}, \tag{2.18}$$

$$\mathbf{u}_n = \mathbf{u}_{n-1}\mathbf{g}_{n-1}\mathbf{u}_{n-1}, \tag{2.19}$$

$$\mathbf{v}_n = \mathbf{v}_{n-1}\mathbf{g}_{n-1}\mathbf{v}_{n-1}. \tag{2.20}$$

The advantage of this numerical approach comparing to the previous approach is that, here the convergence is quadratic instead of linear. The disadvantage is that at some energies the iteration might not converge. Third approach to find the self-energy of the reservoirs which does not suffer from convergence is to use analytic solution to the self-consistent equation. (2.13). Should $\mathbf{t}$ and ε be diagonal matrices (in general, one could try to perform a unitary transformation to diagonalize them if possible), we can solve Eq. (2.13) and obtain

$$\mathbf{\Sigma}^r(E) = \begin{cases} \frac{1}{2}(E\mathbf{1} - \varepsilon) - i\sqrt{\mathbf{t}^\dagger\mathbf{t} - \frac{1}{4}(E\mathbf{1} - \varepsilon)^2}, & \text{if } |E\mathbf{1} - \varepsilon| \leq |\mathbf{t}| \\ \frac{1}{2}(E\mathbf{1} - \varepsilon) - sign(E\mathbf{1} - \varepsilon)\sqrt{\frac{1}{4}(E\mathbf{1} - \varepsilon)^2 - \mathbf{t}^\dagger\mathbf{t}}, & \text{otherwise} \end{cases}. \tag{2.21}$$

Once the self-energies of the leads are obtained from either of above approaches, the GF for the central region can be obtained from

$$\mathbf{G}_c^r(E) = \frac{1}{E\mathbf{1} - \mathbf{H} - \mathbf{\Sigma}^r(E)}. \tag{2.22}$$

When constructing the above matrix numerically, it is important to know that only the matrix elements of the self-energy that are connected to the reservoirs are nonzero and the rest are zero.

2.3.2 GF Approach for Many-Particle Systems

A generalization of this formalism to many-particle quantum system can be achieved by the introduction of the particle annihilation and creation operators, $\hat{c}_{i\alpha}$ (annihilates a particle at site i in orbital α) and $\hat{c}^{\dagger}_{i\alpha}$(creates a particle at site i in orbital α). These operators act in the Fock space and depending on the bosonic or fermionic nature of the particles, they commute or anticommute respectively as following,

$$[\hat{c}^{\dagger}_{i\alpha}(t), \hat{c}_{j\beta}(t)]_{\pm} = \delta_{ij}\delta_{\alpha\beta}\hat{1}, \quad [\hat{c}^{\dagger}_{i\alpha}(t), \hat{c}^{\dagger}_{j\beta}(t)]_{\pm} = 0, \quad [\hat{c}_{i\alpha}(t), \hat{c}_{j\beta}(t)]_{\pm} = 0, \tag{2.23}$$

where, $\hat{1}$ is an identity operator in Fock space. In this case the number operator can be defined as $\hat{N}_{i\alpha}(t) = \hat{c}^{\dagger}_{i\alpha}(t)\hat{c}_{i\alpha}(t)$. For a diagonal Hamiltonian, the total energy in Fock space can be defined in terms of the number operator, $\hat{H}(t) = \sum_{i\alpha} E_{i\alpha}\hat{N}_{i\alpha}(t)$, which (using the unitary transformation matrices that diagonalize the Hamiltonian and redefining the particle operators) can as well be generalized to a non-diagonal Hamiltonian, $\hat{H}(t) = \sum_{i\alpha,j\beta} \mathbf{H}_{i\alpha,j\beta}\hat{c}^{\dagger}_{i\alpha}(t)\hat{c}_{j\beta}(t)$. Using this Hamiltonian together with the (anti)commutation relations, we can find the dynamical equation of motion for the creation/annihilation operators using the Heisenberg equation which leads to Eq. (2.2). This means, all of the above arguments can be applied directly to the many-particle systems as well. In particular, the GF and Eq. (2.6) introduced above can be used to find the propagation of creation/annihilation operators in time.

As an example, the (anti)commutation relation for different times can be written as

$$i[\hat{c}^{\dagger}_{i\alpha}(t'), \hat{c}_{j\beta}(t)]_{\pm} = \sum_{k\alpha'} \mathbf{G}_{i\alpha,k\alpha'}(t',t)[\hat{c}^{\dagger}_{k\alpha'}(t), \hat{c}_{j\beta}(t)]_{\pm} = \hat{1}\mathbf{G}_{i\alpha,j\beta}(t',t). \tag{2.24}$$

Taking expectation value of both sides in Fock space leads to

$$\mathbf{G}^{<}(t',t) - \mathbf{G}^{>}(t,t') = \mathbf{G}(t',t), \tag{2.25}$$

where, we define the lesser ($\mathbf{G}^{<}$) and greater ($\mathbf{G}^{>}$) GFs as follows

$$\begin{aligned} \mathbf{G}^{<}_{i\alpha,j\beta}(t,t') &= i\langle \hat{c}^{\dagger}_{i\alpha}(t)\hat{c}_{j\beta}(t')\rangle, \\ \mathbf{G}^{>}_{i\alpha,j\beta}(t,t') &= \mp i\langle \hat{c}_{j\beta}(t')\hat{c}^{\dagger}_{i\alpha}(t)\rangle. \end{aligned} \tag{2.26}$$

After a Fourier transformation, the above expression reads

$$\mathbf{G}^{<}(E) - \mathbf{G}^{>}(E) = \mathbf{G}^{r}(E) - \mathbf{G}^{a}(E) = 2\pi\delta(E - \mathbf{H}). \tag{2.27}$$

In order to find the expressions for the lesser and greater GFs, we start from the definition of the expectation value for a system at statistical equilibrium,

$$\langle ... \rangle = \mathrm{Tr}_F(e^{(\mu\hat{N}-\hat{H})/kT}...)/\mathrm{Tr}_F(e^{(\mu\hat{N}-\hat{H})/kT}), \tag{2.28}$$

where, Tr_F means trace in the Fock space. Using the (anti)commutation relations for the particle operators and the Hamiltonian we get

$$\mathbf{G}^{<}_{i\alpha,j\beta}(t,t') = \mp \sum_{k\alpha'} (e^{(\mu\mathbf{1}-\mathbf{H})/kT})_{i\alpha,k\alpha'} \mathbf{G}^{>}_{k\alpha',j\beta}(t,t'), \tag{2.29}$$

This can be checked readily by going to a representation that the Hamiltonian is diagonal, and using $e^{x\hat{c}^\dagger\hat{c}}\hat{c}^\dagger = e^{x}\hat{c}^\dagger e^{x\hat{c}^\dagger\hat{c}}$, and then back to the original representation. Using Eq. (2.27) leads to

$$\begin{aligned} \mathbf{G}^{<}(E) &= 2\pi f_{\pm}(E)\delta(E - \mathbf{H}) = f_{\pm}(E)(\mathbf{G}^{r}(E) - \mathbf{G}^{a}(E)), \\ \mathbf{G}^{>}(E) &= (f_{\pm}(E) \mp 1)(\mathbf{G}^{r}(E) - \mathbf{G}^{a}(E)), \end{aligned} \tag{2.30}$$

where, $f_{\pm}(E) = 1/(e^{(E-\mu)/kT} \pm 1)$ is the distribution function. It is straightforward to check that the above expressions can be rewritten as,

$$\begin{aligned} \mathbf{G}^{<}(E) &= \mathbf{G}^{r}(E) 2i f_{\pm}(E) \eta \mathbf{G}^{a}(E) = f_{\pm}(E)\mathbf{G}^{r}_{c}(E)(\mathbf{\Sigma}^{r}(E) - \mathbf{\Sigma}^{a}(E))\mathbf{G}^{a}_{c}(E), \\ \mathbf{G}^{>}(E) &= \mathbf{G}^{r}(E) 2i (f_{\pm}(E) \mp 1) \eta \mathbf{G}^{a}(E) = (f_{\pm}(E) \mp 1)\mathbf{G}^{r}_{c}(E)(\mathbf{\Sigma}^{r}(E) - \mathbf{\Sigma}^{a}(E))\mathbf{G}^{a}_{c}(E). \end{aligned} \tag{2.31}$$

It is worth mentioning that even though η is an infinitesimal quantity, it gets multiplied by the singularities in the total GF which leads to a finite value for the lesser and greater GFs.

2.4 Keldysh GF Approach: Non-Interacting Case

The formulation presented Sec 2.3 can be generalized to a non-equilibrium situation using the Keldysh technique in which the basic idea can be seen as an attempt

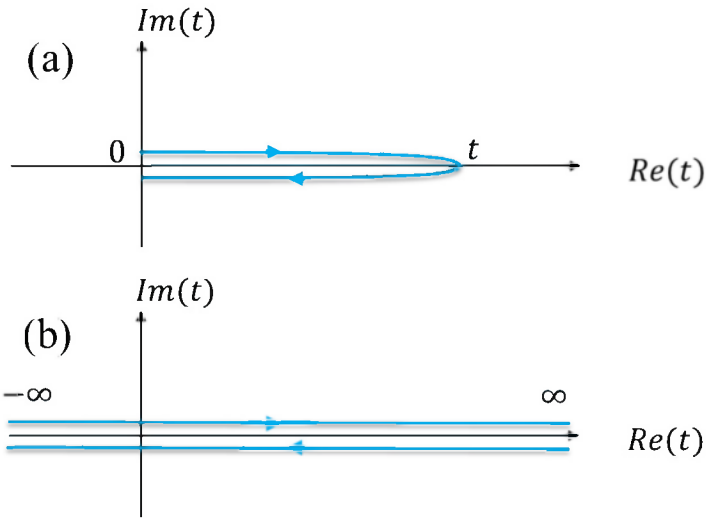

Figure 2.1: The Keldysh contour for the time integration that maps the Heisenberg equation of motion for the evolution of an operator to a Schrödinger-type evolution.

to write the Heisenberg equation for the particle creation/annihilation operator in the form of a Schrödinger equation:

$$\begin{aligned}\hat{c}_i^\dagger(t) &= \mathcal{T}(e^{-i\int_0^t dt'\hat{H}(t')})\hat{c}_i^\dagger(0)\mathcal{T}'(e^{i\int_0^t dt'\hat{H}(t')}),\\ &= \mathcal{T}_K e^{-i\int_K d\tau\hat{H}(\tau)}\hat{c}_i^\dagger(0).\end{aligned} \tag{2.32}$$

Here we dropped the atomic state indices α for convenience, $\mathcal{T}'$ is the reverse time ordering and $\mathcal{T}_K$ is time ordering on the Keldysh contour illustrated in Fig. 2.1(a). GF in this case reads

$$\begin{aligned}\langle\hat{c}_i^\dagger(t)\hat{c}_j(0)\rangle &= \langle\mathcal{T}_K e^{-i\int_K d\tau\hat{H}(\tau)}\hat{c}_i^\dagger(t)\hat{c}_j(0)\rangle_0,\\ &= \sum_{n=0}^{\infty}\frac{(-i)^n}{n!}\langle\mathcal{T}_K\left(\sum_{kl}\int_K d\tau\mathbf{H}_{kl}\hat{c}_k^\dagger(\tau)\hat{c}_l(\tau)\right)^n\hat{c}_i^\dagger(t)\hat{c}_j(0)\rangle_0, \qquad (2.33)\\ &= \sum_{n=0}^{\infty}\frac{(-i)^n}{n!}\mathbf{G}_{ij}^n(t,0), \qquad (2.34)\end{aligned}$$

where, if the whole Hamiltonian is considered as the perturbation, the particle operators in $\langle\ldots\rangle_0$ do not depend on time and the only reason to keep time dependence in the expression would be for the time ordering operation.

We notice that outside the interval $(0,t)$, we can extend the Keldysh contour to infinity as in Fig. 2.1(b) and have the results intact. We use Wick's theorem to find the following recursive relation

$$\mathbf{G}^n_{ij}(t,0) = n\sum_{k_1 l_1} H_{k_1 l_1}\int_K d\tau_1 \langle \mathcal{T}_K \hat{c}^\dagger_i(t)\hat{c}_{l_1}(\tau_1)\rangle_0 \mathbf{G}^{n-1}_{k_1 j}(\tau_1,0). \tag{2.35}$$

The prefactor n comes from the fact that number of equivalent contractions that $\hat{c}^\dagger_i$ can make with the rest of the particle operators is n. We use this expression to obtain

$$\langle \hat{c}^\dagger_i(t)\hat{c}_j(0)\rangle = \langle \hat{c}^\dagger_i(t)\hat{c}_j(0)\rangle_0 - i\sum_{k_1 l_1} H_{k_1 l_1}\int_K d\tau_1 \langle \mathcal{T}_K \hat{c}_{l_1}(\tau_1)\hat{c}^\dagger_i(t)\rangle_0 \langle \mathcal{T}_K \hat{c}^\dagger_{k_1}(\tau_1)\hat{c}_j(0)\rangle. \tag{2.36}$$

This expression can be rewritten as a recursive relation if we put the times on a Keldysh contour as (τ',τ) instead of real times $(0,t)$:

$$\mathbf{G}_{ij}(\tau,\tau') = \langle \mathcal{T}_K \hat{c}^\dagger_i(\tau)\hat{c}_j(\tau')\rangle_0 - i\sum_{k_1 l_1} H_{k_1 l_1}\int_K d\tau_1 \langle \mathcal{T}_K \hat{c}_{l_1}(\tau_1)\hat{c}^\dagger_i(\tau)\rangle_0 \mathbf{G}_{ij}(\tau,\tau'), \tag{2.37}$$

where we define $\mathbf{G}_{ij}(\tau,\tau') = i\langle \mathcal{T}_K \hat{c}^\dagger_i(\tau)\hat{c}_j(\tau')\rangle = \theta(\tau,\tau')\mathbf{G}^<_{ij} + \theta(\tau',\tau)\mathbf{G}^>_{ij}$, as the GF on the Keldysh contour. Conventional representation of the GF on the Keldysh contour is to define it in a 2×2 matrix representation such that the first (second) index corresponds to time on the forward (backward) branch of the Keldysh contour.

$$\check{\mathbf{G}}(t,t') = \begin{pmatrix} \theta(t,t')\mathbf{G}^< + \theta(t',t)\mathbf{G}^> & \mathbf{G}^> \\ \mathbf{G}^> & \theta(t,t')\mathbf{G}^> + \theta(t',t)\mathbf{G}^< \end{pmatrix} \tag{2.38}$$

$$= \begin{pmatrix} \mathbf{G}^< + \mathbf{G}^r & \mathbf{G}^> \\ \mathbf{G}^> & \mathbf{G}^> - \mathbf{G}^r \end{pmatrix}. \tag{2.39}$$

This way we can Fourier transform with respect to the real time and find the GF in energy. In this case the equation of motion can be written as

$$\check{\mathbf{G}}(E) = \check{\mathbf{g}}(E) + \check{\mathbf{g}}(E)\begin{pmatrix} \mathbf{H} & 0 \\ 0 & -\mathbf{H} \end{pmatrix}\check{\mathbf{G}}(E). \tag{2.40}$$

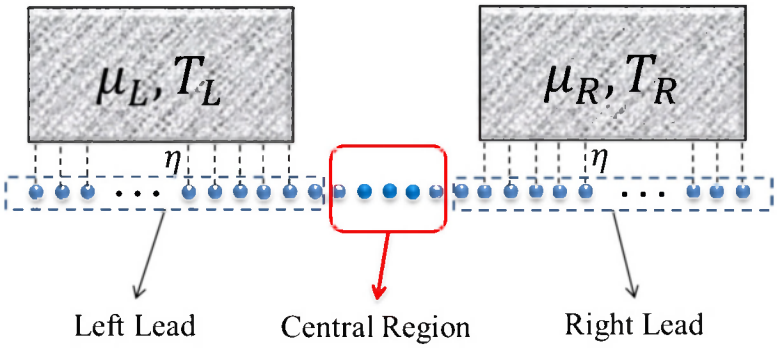

Figure 2.2: Schematic of two-terminal open quantum system attached to macroscopic reservoirs in equilibrium held at different chemical potentials and/or temperatures.

Since, $\check{\mathbf{g}}$ is the GF in the absence of the Hamiltonian, attaching each orbital of the atom weekly to a reservoir at equilibrium as shown in Fig. 2.2, we can use the expression for the equilibrium GF in the previous section to write

$$\begin{aligned}\check{\mathbf{g}}_{ij}^{-1}(E) &= \begin{pmatrix} E\delta_{ij} & 0 \\ 0 & -E\delta_{ij} \end{pmatrix} - \begin{pmatrix} \mathbf{\Sigma}_{ij}^{<} + \mathbf{\Sigma}_{ij}^{r} & \mathbf{\Sigma}_{ij}^{>} \\ \mathbf{\Sigma}_{ij}^{<} & \mathbf{\Sigma}_{ij}^{>} - \mathbf{\Sigma}_{ij}^{r} \end{pmatrix} \\ &= \begin{pmatrix} E\delta_{ij} & 0 \\ 0 & -E\delta_{ij} \end{pmatrix} - i\delta_{ij}\eta \begin{pmatrix} 1 \mp 2f_i(E) & 2(1 \mp f_i(E)) \\ 2 \mp f_i(E) & -(1 \mp 2f_i(E)) \end{pmatrix}, \end{aligned} \tag{2.41}$$

To get the second expression we used $\Sigma_{ij}^{r} = i\eta\delta_{ij}$ and Eqs. (2.30), where, $f_i(E) = 1/(e^{(E-\mu_i)/kT_i} \pm 1)$ is the position dependent equilibrium particle distribution function and η is chosen to be infinitesimally small. The equation of motion for the GF reads

$$\check{\mathbf{G}}_{ij}^{-1}(E) = \begin{pmatrix} E\delta_{ij} - \mathbf{H} & 0 \\ 0 & -E\delta_{ij} + \mathbf{H} \end{pmatrix} - \begin{pmatrix} \mathbf{\Sigma}_{ij}^{<} + \mathbf{\Sigma}_{ij}^{r} & \mathbf{\Sigma}_{ij}^{>} \\ \mathbf{\Sigma}_{ij}^{<} & \mathbf{\Sigma}_{ij}^{>} - \mathbf{\Sigma}_{ij}^{r} \end{pmatrix} \tag{2.42}$$

Finding the inverse of the above matrix, we can obtain the expression for the elements

of the GF in the Keldysh space as follows,

$$\begin{aligned}\mathbf{G}^r(E) &= \frac{1}{E\mathbf{1} - \mathbf{H} - \mathbf{\Sigma}^r(E)}, \\ \mathbf{G}^<(E) &= \mathbf{G}^r(E)\mathbf{\Sigma}^<(E)\mathbf{G}^r(E), \\ \mathbf{G}^>(E) &= \mathbf{G}^r(E)\mathbf{\Sigma}^>(E)\mathbf{G}^r(E).\end{aligned} \tag{2.43}$$

Similar to the approach that led to Eq. (2.13), we can write down the same recursive relation for the self-energy of the leads and have the equation of motion of the GF for the central region only. The self-energy for lead α reads

$$\check{\mathbf{\Sigma}}^{\alpha}_{n-1} = \mathbf{t}\frac{1}{(E-\varepsilon)\boldsymbol{\tau}_z - \check{\mathbf{\Sigma}}^{\alpha}_{n}}\mathbf{t}^{\dagger} \tag{2.44}$$

with $\check{\mathbf{\Sigma}}^{\alpha}_{N} = i\delta_{ij}\eta \begin{pmatrix} 1 \mp 2f_\alpha(E) & 2(1 \mp f_\alpha(E)) \\ 2 \mp f_\alpha(E) & -(1 \mp 2f_\alpha(E)) \end{pmatrix}$. Here and in the rest of the thesis, we use $\boldsymbol{\tau}^{x,y,z}$ to denote the Pauli matrices acting in the Keldysh space. It is worth mentioning that the conventional way of writing this expression is to write down the recursive relation for the lesser and retarded components of the GFs separately

$$\mathbf{\Sigma}^{r,\alpha}_{n-1} = \mathbf{t}\frac{1}{E\mathbf{1} - \varepsilon - \mathbf{\Sigma}^{r,\alpha}_{n}}\mathbf{t}^{\dagger} \tag{2.45}$$

$$\mathbf{\Sigma}^{<,\alpha}_{n-1} = \mathbf{\Sigma}^{r,\alpha}_{n}\mathbf{\Sigma}^{<,\alpha}_{n}\mathbf{\Sigma}^{a,\alpha}_{n} = f_\alpha(\mathbf{\Sigma}^{r,\alpha}_{n} - \mathbf{\Sigma}^{a,\alpha}_{n}), \tag{2.46}$$

with $\mathbf{\Sigma}^{r,\alpha}_{N} = i\eta\mathbf{1}$ and $\mathbf{\Sigma}^{<,\alpha}_{N} = 2i\eta f_\alpha \mathbf{1}$.

Due to the fact that the elements of a matrix defined in the Keldysh space are not independent, the Keldysh matrices obey few relationships that are worth knowing. We notice that under the unitary transformation, $\check{U} = \frac{1}{\sqrt{2}}\begin{pmatrix} 1 & -1 \\ 1 & 1 \end{pmatrix}$, matrix $\check{\mathbf{A}}$ defined in Keldysh space is transformed into:

$$\check{U}\check{\mathbf{A}}\check{U}^{\dagger} = \check{U}\begin{pmatrix} A^< + A^r & A^> \\ A^< & A^> - A^r \end{pmatrix}\check{U}^{\dagger} = \begin{pmatrix} A^r & 0 \\ A^< + A^> & A^a \end{pmatrix}. \tag{2.47}$$

Furthermore, the Keldysh-space matrices satisfy,

$$\check{\mathbf{A}}^{\dagger} = -\boldsymbol{\tau}^x\check{\mathbf{A}}\boldsymbol{\tau}^x, \tag{2.48}$$

At the beginning of this section we emphasized that the aim of the Keldysh approach is to write down the Heisenberg equation of motion for the particle operators in the form of a single particle Schrödinger equation which contains the information about the statistics of the particles. We see that this was achieved by doubling the number of GFs required to explain the system (*i.e.*, lesser and greater GFs). While the lesser GF demonstrates the propagation of the particles, the greater GF has the information about the holes which exists only in many-body systems. Besides having a clear physical meaning, these four GFs make it possible to obtain nonequilibrium expectation values of any one-particle observable, such as charge and spin currents that are the focus of the subsequent sections.

2.4.1 Observables: DC Current in Time-Independent Case

Let us start by writing down the expression for the charge and spin current operator for the flow of electrons into the lead. The Heisenberg equation for the charge $\hat{Q} = e\sum_{\mathbf{i},ss'} \hat{c}^{\dagger}_{\mathbf{i}s}\hat{c}_{\mathbf{i}s'}$ or spin density $\hat{S}_i = e\sum_{\mathbf{i},ss'} \hat{c}^{\dagger}_{\mathbf{i}s}[\sigma^i]_{ss'}\hat{c}_{\mathbf{i}s'}$ operators of electrons in lead α then yields expressions for time-dependent total current operator [82]

$$\begin{aligned}\hat{I}^i_{\alpha} &= ie\left(\hat{c}^{\dagger}(t_+)\sigma^i\hat{d}^{\alpha}(t_-) - \hat{d}^{\alpha\dagger}(t_+)\sigma^i\hat{c}(t_-)\right) \\ &= i\frac{e}{\hbar}\int dE\left(\check{c}^{\dagger}(E)\sigma^i\boldsymbol{\tau}_K\check{d}^{\alpha}(E) - \check{d}^{\alpha\dagger}(E)\sigma^i\boldsymbol{\tau}_K\check{c}(E)\right),\end{aligned} \tag{2.49}$$

Here $\sigma^{i=0}$ corresponds to a 2×2 unit matrix and $\sigma^{i=1,2,3}$ represents the x, y, z components of the Pauli matrices, respectively. Here $t_{\pm}$ corresponds to upper and lower branch of Keldysh contour and $\hat{d}^{\alpha}_j(t)$ and $\hat{c}_j(t)$ are for electrons in the lead α and central region, respectively. In the first line of Eq. (2.49) the trace is over real space (orbitals) and in the second line by doubling the size of the Hilbert space to include the Keldysh space we write down the expression in real time and then Fourier transform to energy. For $\boldsymbol{\tau}_K$ matrix defined in Keldysh space we use

$$\boldsymbol{\tau}_K = \begin{pmatrix} 1 & 0 \\ 0 & 0 \end{pmatrix}. \tag{2.50}$$

Since the leads are noninteracting for the leads particle operators in terms of the central region particle operators can be expressed as

$$\check{d}^{\alpha\dagger}(E) = \check{\mathbf{\Sigma}}^{\alpha}(E)\boldsymbol{\tau}_z\check{c}^{\dagger}(E). \tag{2.51}$$

After some straightforward algebra we get

$$\hat{I}^i_{\alpha} = i\frac{e}{\hbar}\int dE \mathrm{Tr}_{K,\sigma}\left[\check{c}^{\dagger}(E)\boldsymbol{\tau}_z\check{\mathbb{S}}^{\alpha}_i(E)\boldsymbol{\tau}_z\check{c}(E)\right], \tag{2.52}$$

with

$$\check{\mathbb{S}}^{\alpha}_i = \boldsymbol{\tau}_z\boldsymbol{\tau}_K\check{\mathbf{\Sigma}}_{\alpha}\sigma_i - \sigma_i\check{\mathbf{\Sigma}}_{\alpha}\boldsymbol{\tau}_K\boldsymbol{\tau}_z = \begin{pmatrix} [\mathbf{\Sigma}^{<}_{\alpha} + \mathbf{\Sigma}^{r}_{\alpha}, \sigma_i] & \mathbf{\Sigma}^{>}_{\alpha}\sigma_i \\ -\sigma_i\mathbf{\Sigma}^{<}_{\alpha} & 0 \end{pmatrix}. \tag{2.53}$$

Finally for the expectation value of the charge or spin current we obtain

$$I^i_{\alpha} = \frac{e}{\hbar}\int dE \mathrm{Tr}_{K,\sigma}\left[\check{\mathbf{G}}(E)\boldsymbol{\tau}_z\check{\mathbb{S}}^{\alpha}_i(E)\boldsymbol{\tau}_z\right], \tag{2.54}$$

It is worth mentioning that this expression is invariant under the following transformation,

$$\check{\mathbb{S}}^{\alpha}_i \rightarrow \check{\mathbb{S}}^{\alpha}_i + \begin{pmatrix} \mathbf{A} & \mathbf{A} \\ \mathbf{A} & \mathbf{A} \end{pmatrix}, \tag{2.55}$$

where $\mathbf{A}$ is an arbitrary matrix. A diagrammatic representation of this expression can be seen in Fig. 2.3, where the solid line (dashed line) represents GF (self-energy of the lead).

By inserting the expressions for the lesser and greater GF and obtain,

$$I^i_{\alpha} = \frac{e}{\hbar}\sum_{\beta}\int dE(f_{\alpha}(E) - f_{\beta}(E))\mathrm{Tr}\left[\sigma_i\mathbf{\Gamma}_{\alpha}\mathbf{G}^{r}\mathbf{\Gamma}_{\beta}\mathbf{G}^{a}\right], \tag{2.56}$$

In this expression the retarded and advanced GFs appear as to quantify the rate of propagation of the particles from one reservoir to another and $\mathbf{\Gamma}_{\alpha}$ takes into account the rate at which the particles jump from the reservoir to the central region. We can imagine the above expression describing particles being injected from β reservoirs

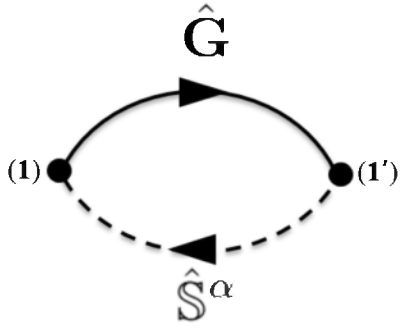

Figure 2.3: Diagrammatic representation of expression for current in Keldysh space.

and after propagating through the central region, the charge-spin components of the particle flow in α reservoir are measured.

Furthermore, since there is no spin matrix accompanied with the $\mathbf{\Gamma}_\beta$ term we can think of the injected current as being unpolarized. Should the injected spin current be polarized due to some other effects that are not taken into account in the model, we can generalize the above expression to calculate the current flow. The generalized expression for charge-spin current reads,

$$I^i_\alpha(\overrightarrow{P}^{\text{in}}) = \frac{e}{\hbar}\sum_\beta \int dE\,[f_\alpha(E) - f_\beta(E)]\,\text{Tr}\left[\sigma_i \mathbf{\Gamma}_\alpha \mathbf{G}^r \left(\mathbf{1} + \overrightarrow{P}^{\text{in}}_\beta \cdot \vec{\sigma}\right) \mathbf{\Gamma}_\beta \mathbf{G}^a\right], \quad (2.57)$$

with, $\overrightarrow{P}^{\text{in}}_\beta$ being the spin polarization vector of the injected particles.

2.4.2 Observables: GF in Time Dependent Case

Let us consider a periodically time dependent component to the Hamiltonian, where the frequency of the oscillation is much smaller than the bandwidth of the electrons. After performing a Fourier transform, the equation of motion for the GF is given by

$$\check{\mathbf{g}}^{-1}(E + n\omega)\check{\mathbf{G}}_n(E) = \delta_{n0}\check{\mathbf{1}} + \sum_{m=-N}^{N} \check{\mathbf{m}}_m \check{\mathbf{G}}_{n+m}(E), \quad (2.58)$$

where we define

$$\check{\mathbf{m}}(t) = \sum_{m=-N}^{N} \check{\mathbf{m}}_m e^{im\omega t}. \quad (2.59)$$

One could use two different approaches to solve this equation, namely: the adiabatic approach and the perturbative approach. In adiabatic approach, we first ignore the $n\omega$ term in the equation which allows us to solve the equation exactly.

$$\check{\mathbf{G}}^{ad}(E,t) = \frac{\check{\mathbf{1}}}{\check{\mathbf{g}}^{-1}(E) - \check{\mathbf{m}}(t)}, \tag{2.60}$$

where,

$$\check{\mathbf{G}}^{ad}(E,t) = \sum_{m=-\infty}^{\infty} \check{\mathbf{G}}^{ad}_{m}(E) e^{im\omega t}, \tag{2.61}$$

Then we consider the existence of $n\omega$ and solve the equation perturbatively. The recursive relation in this case reads

$$\check{\mathbf{G}}_{n}(E) = \check{\mathbf{G}}^{ad}_{n}(E) + \sum_{m} \check{\mathbf{G}}^{ad}_{n-m}(E) \left[\check{\mathbf{g}}^{-1}(E) - \check{\mathbf{g}}^{-1}(E+m\omega)\right] \check{\mathbf{G}}_{m}(E), \tag{2.62}$$

To the lowest order in ω we have

$$\check{\mathbf{G}}(E,t) = \check{\mathbf{G}}^{ad}(E,t) + i\check{\mathbf{G}}^{ad}(E,t)\frac{\partial \check{\mathbf{g}}^{-1}(E)}{\partial E}\frac{\partial}{\partial t}\check{\mathbf{G}}(E,t), \tag{2.63}$$

In non-adiabatic cases, when the frequency of the oscillation is in the order of the energy characteristics of the system such as energy gap or the energy bandwidth of the electrons (*e.g.*, photo-voltaic effect), a more general approach should be used. We assume that the amplitude of the external time-dependent field is small enough such that only scattering processes up to a finite number of photons would be sufficient to describe the system. For simplicity we assume that the time dependent term contains only a single frequency, so that the equation of motion for the GF is

$$\check{\mathbf{g}}^{-1}(E+n\omega)\check{\mathbf{G}}_{n}(E) = \delta_{n0}\check{\mathbf{1}} + \check{\mathbf{m}}\check{\mathbf{G}}_{n+1}(E) + \check{\mathbf{m}}^{\dagger}\check{\mathbf{G}}_{n-1}(E). \tag{2.64}$$

This equation presents a system of linear equations which have a block diagonal form and can be solved recursively. However, n in Eq. (2.64) runs from $-\infty$ to ∞ and, therefore, in order to solve this system of equations a cutoff in n is required. This can be achieved outside the energy bandwidth where the density of states is zero and the real part of the equilibrium GF gets smaller. Therefore let us consider that at

$E + n_0\omega = \pm N\omega$ the equilibrium GF $\check{\mathbf{g}}_{n_0}(E) = \check{\mathbf{g}}(E + n_0\omega)$ is small enough and can be considered it to be zero. In this case, the above recursive relation for the last nonzero GF in upper end (we consider to be $n_0 = N - 1$) is

$$\check{\mathbf{G}}_{N-1}(E) = \check{\mathbf{G}}_{N-2}(E)\check{\mathbf{m}}\check{\mathbf{g}}_{N-1}(E). \tag{2.65}$$

We can use this relation to remove $\mathbf{G}^r_{N-1}(E)$ from second relation for GF (for $n = N - 2$),

$$\check{\mathbf{G}}_{N-2}(E) = [\check{\mathbf{G}}_{N-3}(E)\check{\mathbf{m}} + \check{\mathbf{G}}_{n-1}(E)\check{\mathbf{m}}^\dagger]\check{\mathbf{g}}_{N-2}(E), \tag{2.66}$$

and get

$$\check{\mathbf{G}}_{N-2}(E) = [\check{\mathbf{G}}_{n-3}(E)\check{\mathbf{m}} + \check{\mathbf{G}}_{N-2}(E)\check{\mathbf{m}}\check{\mathbf{g}}_{N-1}(E)(E)\check{\mathbf{m}}^\dagger]\check{\mathbf{g}}_{N-1}(E), \tag{2.67}$$

or

$$\check{\mathbf{G}}_{N-2}(E) = \check{\mathbf{G}}_{n-3}(E)\check{\mathbf{m}}\check{\mathbf{g}}_{N-2}(E)\check{\alpha}_{N-2}, \tag{2.68}$$

where, $\check{\alpha}_{N-2} = [1 + \check{\mathbf{m}}\check{\mathbf{g}}_{N-1}(E)\check{\mathbf{m}}^\dagger\check{\mathbf{g}}_{N-2}(E)]^{-1}$. Repeating the same procedure for the next term which is equation for $n = N - 3$, we get

$$\check{\mathbf{G}}_{N-3}(E) = \check{\mathbf{G}}_{N-4}(E)\check{\mathbf{m}}\check{\mathbf{g}}_{N-3}(E)\check{\alpha}_{N-3}, \tag{2.69}$$

where, $\check{\alpha}_{N-3} = [1 + \check{\mathbf{m}}\check{\mathbf{g}}_{N-2}(E)\check{\alpha}_{N-2}\check{\mathbf{m}}^\dagger\check{\mathbf{g}}_{N-3}(E)]^{-1}$. One can write a recursive relation for $\check{\alpha}_i$ as follows

$$\check{\alpha}_i = \frac{1}{1 + \check{\mathbf{m}}\check{\mathbf{g}}_{i+1}(E)\check{\alpha}_{i+1}\check{\mathbf{m}}^\dagger\check{\mathbf{g}}_i(E)}. \tag{2.70}$$

By iterating we can eventually find $\check{\alpha}_1$ and get the following relation

$$\check{\mathbf{G}}_1(E) = \check{\mathbf{G}}_0(E)\check{\mathbf{m}}\check{\mathbf{g}}_1(E)\check{\alpha}_1. \tag{2.71}$$

The same procedure from lower end of energy band leads to,

$$\check{\beta}_{-N+2} = \frac{1}{1 + \check{\mathbf{m}}^\dagger\check{\mathbf{g}}_{-N+1}(E)\check{\mathbf{m}}\check{\mathbf{g}}_{-N+2}(E)}, \tag{2.72}$$

$$\check{\beta}_{-N+3} = \frac{1}{1 + \check{\mathbf{m}}^{\dagger}\check{\mathbf{g}}_{-N+2}(E)\check{\beta}_{-N+2}\check{\mathbf{m}}\check{\mathbf{g}}_{-N+3}(E)}, \tag{2.73}$$

and eventually we get

$$\check{\beta}_{-1} = \frac{1}{1 + \check{\mathbf{m}}^{\dagger}\check{\mathbf{g}}_{-2}(E)\check{\beta}_{-2}\check{\mathbf{m}}\check{\mathbf{g}}_{-1}(E)}. \tag{2.74}$$

Therefore,

$$\check{\mathbf{G}}_{-1}(E) = \check{\mathbf{G}}_{0}(E)\check{\mathbf{m}}^{\dagger}\check{\mathbf{g}}_{-1}(E)\check{\beta}_{-1}. \tag{2.75}$$

Now we can consider the GF equation for $n = 0$ and obtain

$$\check{\mathbf{G}}_{0}(E) = \check{\mathbf{g}}_{0}(E)\frac{1}{1 - \check{\mathbf{m}}\check{\mathbf{g}}_{1}(E)\check{\alpha}_{1}\check{\mathbf{m}}^{\dagger} - \check{\mathbf{m}}^{\dagger}\check{\mathbf{g}}_{-1}(E)\check{\beta}_{-1}\check{\mathbf{m}}}. \tag{2.76}$$

Since we know the Green' function at one point ($n = 0$) we can use $\check{\alpha}_n$ and $\check{\beta}_n$ parameters (matrices in general) and calculate the GFs at other points n. For positive n we have

$$\check{\mathbf{G}}_{n}(E) = \check{\mathbf{G}}_{0}(E)(\check{\mathbf{m}}\check{\mathbf{g}}_{1}\check{\alpha}_{1})(\check{\mathbf{m}}\check{\mathbf{g}}_{2}\check{\alpha}_{2})...(\check{\mathbf{m}}\check{\mathbf{g}}_{n}\check{\alpha}_{n}), \tag{2.77}$$

and for negative n we have

$$\check{\mathbf{G}}_{n}(E) = \check{\mathbf{G}}_{0}(E)(\check{\mathbf{m}}^{\dagger}\check{\mathbf{g}}_{-1}\check{\beta}_{-1})(\check{\mathbf{m}}^{\dagger}\check{\mathbf{g}}_{-2}\check{\beta}_{-2})...(\check{\mathbf{m}}^{\dagger}\check{\mathbf{g}}_{n}\check{\beta}_{n}). \tag{2.78}$$

Although this formalism treats the effect of external time dependent term exactly, in practice it ends up being numerically too expensive because one has to limit the calculation to scatterings from a few photons which then leads to violation of the charge conservation. In this case, should the time dependent term be small, in order to preserve the charge conservation one can obtain the GFs perturbatively to the lowest order. To do this we introduce a time-independent coupling strength λ such that the time dependent perturbation would be $\lambda\check{\mathbf{m}}(t)$ and Taylor expand the GF in time representation to the second order as follows

$$\begin{aligned}\check{\mathbf{G}}(t,t') \simeq & \check{\mathbf{g}}(t-t') + \lambda \int dt_1 \check{\mathbf{g}}(t-t_1)\check{\mathbf{m}}(t_1)\check{\mathbf{g}}(t_1-t') \\ & + \lambda^2 \int dt_1 dt_2 \check{\mathbf{g}}(t-t_1)\check{\mathbf{m}}(t_1)\check{\mathbf{g}}(t_1-t_2)\check{\mathbf{m}}(t_2)\check{\mathbf{g}}(t_2-t') + O(\lambda^3).\end{aligned} \tag{2.79}$$

In the following we introduce another approach to find the GF used in finding the observables which we call "multi-photon" approach that conserves the charge with the cost of taking into account only scatterings from a finite number of photons with a fixed frequency. In this approach we consider the total Hilbert space consisting of electrons and photons such that $\mathcal{H}_{total} = \mathcal{H}_{electrons} \otimes \mathcal{H}_{photons}$. The GF in this case can be obtained from

$$\check{\mathbf{G}}_{N_{ph}}(E) = \begin{pmatrix} \check{\mathbf{g}}^{-1}(E - N\omega) & \check{\mathbf{m}} & 0 & \dots & 0 \\ \check{\mathbf{m}}^{\dagger} & \check{\mathbf{g}}^{-1}(E - (N-1)\omega) & \check{\mathbf{m}} & \dots & 0 \\ 0 & \check{\mathbf{m}}^{\dagger} & \ddots & \vdots & \vdots \\ \vdots & \vdots & \dots & \ddots & \check{\mathbf{m}} \\ 0 & 0 & \dots & \check{\mathbf{m}}^{\dagger} & \check{\mathbf{g}}^{-1}(E + N\omega) \end{pmatrix}. \quad (2.80)$$

The goal of this chapter was to make the reader familiar with the different approximations of finding the GFs that can be applied to a system with time dependent perturbation. In the presented formalism we tried to stay in the framework of Keldysh formalism. The conventional method is to work with the lesser and retarded components of the Keldysh GF in order to find the expressions for the observables in terms of occupation number and retarded GF. In Chapter 3 we go through this approach more extensively and compare the results using all three approaches introduced above.

2.4.3 Observables: Current Noise of Non-Interacting Case

In Sec. 2.4.1 we showed that once we find the GF, current can be obtained from (2.54) with the corresponding diagrammatic representation shown in Fig. 2.3. In the following we try to obtain an expression for the current-current correlation (*i.e.*, noise power) in terms of the Keldysh GF. Since both the thermal and shot noise power do not depend on frequency over a very wide interval we consider only $\omega \to 0$ limit. The noise can be separated into two components: thermal noise ($V = 0, T \neq 0$) which is related to the conductance by the fluctuation-dissipation theorem and nonequilibrium shot noise ($V \neq 0, T = 0$) which is due to the discreteness of charge.

In macroscopic metals the shot noise is zero which is believed to be due to inelastic electron-phonon scattering that averages out the current fluctuations. In the following we ignore the inelastic scattering and formulate the noise power in the case of phase-coherence transport. The current-current correlation is defined as

$$S_{\alpha\beta}(t,t') = \langle \hat{I}_\alpha(t)\hat{I}_\beta(t')\rangle + \langle \hat{I}_\beta(t')\hat{I}_\alpha(t)\rangle - 2I_\alpha(t)I_\beta(t'). \tag{2.81}$$

Its spectral density at zero frequency is given by

$$S_{\alpha\beta}(\omega=0) = 2\int_{-\infty}^{\infty} dt \Re\left[\langle \hat{I}_\alpha(t)\hat{I}_\beta(0)\rangle - I_\alpha(t)I_\beta(0)\right]. \tag{2.82}$$

From the conservation of charge current we know that the noise power must satisfy $\sum_\alpha S_{\alpha\beta} = 0$ which could be used to find the values of $S_{\alpha\alpha}$. Therefore for simplicity we consider the cross-correlation cases where $\alpha \neq \beta$. In noninteracting case, one can use the expression for current operator and using Wick's theorem obtain the noise power in terms of the GF,

$$\begin{aligned} S_{\alpha\neq\beta}(\omega=0) = -2\frac{e^2}{h}\Re\int dE \mathrm{Tr}[&\mathbf{G}^<(\check{\mathbf{\Sigma}}^\beta\boldsymbol{\tau}_z\check{\mathbf{G}}\boldsymbol{\tau}_z\check{\mathbf{\Sigma}}^\alpha)^> + (\check{\mathbf{\Sigma}}^\alpha\boldsymbol{\tau}_z\check{\mathbf{G}}\boldsymbol{\tau}_z\check{\mathbf{\Sigma}}^\beta)^<\mathbf{G}^> \\ &- (\check{\mathbf{G}}\boldsymbol{\tau}_z\check{\mathbf{\Sigma}}^\beta)^<(\check{\mathbf{G}}\boldsymbol{\tau}_z\check{\mathbf{\Sigma}}^\alpha)^> - (\check{\mathbf{\Sigma}}^\alpha\boldsymbol{\tau}_z\check{\mathbf{G}})^<(\check{\mathbf{\Sigma}}^\beta\boldsymbol{\tau}_z\check{\mathbf{G}})^>] \\ = 2\frac{e^2}{h}\Re\int dE \mathrm{Tr}[&\boldsymbol{\tau}_z\check{\mathbf{G}}\boldsymbol{\tau}_z\check{\mathbb{S}}^\alpha\boldsymbol{\tau}_z\check{\mathbf{G}}\boldsymbol{\tau}_z\check{\mathbb{S}}^\beta] = \frac{2e^2}{h}\int dE \mathrm{Tr}[\check{\mathbf{T}}^\alpha\check{\mathbf{T}}^\beta]. \end{aligned} \tag{2.83}$$

One could also consider a general case and obtain,

$$S_{\alpha\beta}(\omega=0) = \frac{2e^2}{h}\int dE \mathrm{Tr}[\check{\mathbf{T}}^\alpha\check{\mathbf{T}}^\beta + \delta_{\alpha\beta}\boldsymbol{\tau}_z\check{\mathbf{T}}^\alpha]. \tag{2.84}$$

A diagrammatic representation of this expression is shown in Fig. 2.4. This expression can also be obtained directly using the technique used commonly in full counting statistics (FCS). In this technique, a virtual term is added to the Hamiltonian

$$\hat{H}(t) \to \hat{H}(t) + \sum_\alpha \lambda_\alpha \hat{I}^0_\alpha, \tag{2.85}$$

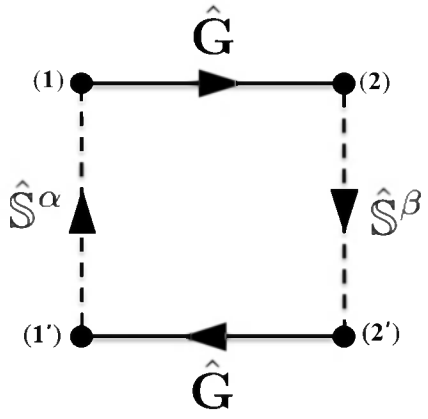

Figure 2.4: Diagrammatic representation of expression for noise power in Keldysh space.

which can be interpreted as a modification of the lead self-energy

$$\check{\mathbf{\Sigma}}_{\alpha} \to \check{\mathbf{\Sigma}}_{\alpha} + \lambda_{\alpha}\boldsymbol{\tau}_z\check{\mathbb{S}}_0^{\alpha}\boldsymbol{\tau}_z. \tag{2.86}$$

In this case the modified charge current going through each lead reads

$$I_{\alpha}^{0}(\{\lambda_{\beta}\}) = \frac{e}{\hbar}\int dE \mathrm{Tr}\left[(\check{\mathbf{1}} + \lambda_{\alpha}\boldsymbol{\tau}_z)\check{\mathbf{G}}(E,\{\lambda_{\beta}\})\boldsymbol{\tau}_z\check{\mathbb{S}}_0^{\alpha}(E)\boldsymbol{\tau}_z\right]. \tag{2.87}$$

Finally, the expression for noise power is

$$\begin{aligned} S_{\alpha\beta} &= \frac{\partial}{\partial\lambda_{\beta}} I_{\alpha}^{0}(\{\lambda_{\beta}\})|_{\{\lambda_{\beta}\}\to 0} \\ &= \frac{e}{\hbar}\int dE \mathrm{Tr}\left[\delta_{\alpha\beta}\check{\mathbf{G}}\boldsymbol{\tau}_z\check{\mathbb{S}}_0^{\alpha} + \boldsymbol{\tau}_z\check{\mathbf{G}}\boldsymbol{\tau}_z\check{\mathbb{S}}_0^{\alpha}\boldsymbol{\tau}_z\check{\mathbf{G}}\boldsymbol{\tau}_z\check{\mathbb{S}}_0^{\beta}\right]. \end{aligned} \tag{2.88}$$

Considering a two-terminal system, we can use the expression for the lesser and greater GF to obtain

$$S = \frac{2e^2}{\hbar}\int \frac{dE}{2\pi}\left\{[f_L(1-f_L) + f_R(1-f_R)]\,\mathrm{Tr}[\mathbf{T}] + (f_L - f_R)^2\mathrm{Tr}[\mathbf{T}(\mathbf{1}-\mathbf{T})]\right\}, \tag{2.89}$$

where, $\mathbf{T} = \mathbf{G}^r\mathbf{\Gamma}_R\mathbf{G}^a\mathbf{\Gamma}_L$ is called the transmission matrix. In this expression the first term is called thermal noise which goes to zero with temperature and the second term is the shot noise which is due to the fact that electrons are point like particles and goes to zero when voltage bias goes to zero.

2.5 Keldysh GF Approach: Interacting Case

In this section we generalize the formulation developed in Sec. 2.4 to the interacting case where electrons are coupled to bosonic particles in the system. In particular, let us consider the Hamiltonian to be of the form

$$\hat{H}(t) = \sum_{ij} \mathbf{H}^f_{ij} \hat{c}^\dagger_i \hat{c}_j + \sum_{ij} \mathbf{H}^b_{ij} \hat{b}^\dagger_i \hat{b}_j + \sum_{ij} (\mathbf{V}_{ij} \hat{b}_i \hat{c}^\dagger_i \hat{c}_j + \mathbf{V}^\dagger_{ij} \hat{b}^\dagger_i \hat{c}^\dagger_j \hat{c}_i). \tag{2.90}$$

In the absence of the interaction, one can find the solution to the equation of motion of the system exactly for fermions and bosons separately using the approach introduced in Sec. 2.4. Below we consider the interaction perturbatively and try to find the equation of motion for the GF in non-equilibrium situation. Similar to Sec. 2.4, we start from Heisenberg equation for the particle operators

$$i\frac{\partial}{\partial t}\hat{c}^\dagger_k(t) = [\hat{H}(t), \hat{c}^\dagger_k(t)]. \tag{2.91}$$

By going into the interaction representation

$$\hat{c}^\dagger_i(t) \to T(e^{-i\int_0^t dt' \hat{H}^f(t')}) \hat{c}^\dagger_i(t) T'(e^{i\int_0^t dt' \hat{H}^f(t')}), \tag{2.92}$$

we get

$$i\frac{\partial}{\partial t}\hat{c}^\dagger_k(t) = \sum_{ij} (\mathbf{V}_{ij} \hat{b}_i + \mathbf{V}^\dagger_{ji} \hat{b}^\dagger_j)[\hat{c}^\dagger_i \hat{c}_j, \hat{c}^\dagger_k(t)]. \tag{2.93}$$

A formal solution to this equation is given in terms of the Keldysh contour time-ordered evolution operator on the Keldysh contour, in which the GF on the Keldysh contour is given by

$$\begin{aligned}
\mathbf{G}_{ij}(\tau, \tau') &= i\langle \mathcal{T}_K \hat{c}^\dagger_i(\tau) \hat{c}_j(\tau') \rangle = i\langle \mathcal{T}_K e^{-i\int_K d\tau \hat{H}(\tau)} \hat{c}^\dagger_i(\tau) \hat{c}_j(\tau') \rangle_0 = i\langle \mathcal{T}_K \rho \hat{c}^\dagger_i(\tau) \hat{c}_j(\tau') \rangle_0 \\
&= i\sum_{n=0}^{\infty} \frac{(-i)^n}{n!} \langle \mathcal{T}_K \left(\sum_{kl} \int_K d\tau_1 \hat{h}_{lk}(\tau_1) \hat{c}^\dagger_k(\tau_1) \hat{c}_l(\tau_1) \right)^n \hat{c}^\dagger_i(\tau) \hat{c}_j(\tau') \rangle_0 \\
&= i\sum_{n=0}^{\infty} \frac{(-i)^n}{n!} \langle \mathcal{T}_K \hat{c}^\dagger_i(\tau) \hat{c}_j(\tau') \rangle_n,
\end{aligned} \tag{2.94}$$

where, $\hat{h}_{ij}(\tau) = [\mathbf{V}_{ji}\hat{b}_j(\tau) + \mathbf{V}^\dagger_{ij}\hat{b}^\dagger_i(\tau)]$. By ealuating contractions of $\hat{c}^\dagger_i(\tau)$ with the other particle operators we find

$$\begin{aligned}\mathbf{G}_{ij}(\tau,\tau') &= \mathbf{G}_{ij}(\tau,\tau') \\ &+ i\sum_{nkl}\int d\tau_1 \frac{(-i)^n}{n!}\mathbf{G}_{il}(\tau,\tau_1)\langle \mathcal{T}_K \hat{h}_{lk}(\tau_1)\hat{c}^\dagger_k(\tau_1)\hat{c}_j(\tau')\rangle_n.\end{aligned} \tag{2.95}$$

Here we can either contract the bosonic operators so that we are left with only fermionic operators or vice versa. We present both approaches where the former one leads to an effective fermion-fermion interacting model generally suitable to inevstigate transient behaviors, while the later one leads to Feynman diagrams that make it possible to find equilibrium or long time steady state solutions. Contraction of the bosonic operator gives

$$\begin{aligned}\mathbf{G}_{ij}(\tau,\tau') &= \mathbf{G}_{ij}(\tau,\tau') \\ &+ i\sum_{nk_1k_1'l_1l_1'}\int d\tau_1 d\tau_1' \frac{(-i)^n}{n!}\mathbf{G}_{il_1}(\tau,\tau_1)\mathbf{D}^{l_1k_1}_{l_1'k_1'}(\tau_1',\tau_1)\langle \mathcal{T}_K \hat{c}^\dagger_{k_1'}(\tau_1')\hat{c}_{l_1'}(\tau_1')\hat{c}^\dagger_{k_1}(\tau_1)\hat{c}_j(\tau')\rangle_n,\end{aligned} \tag{2.96}$$

where

$$\begin{aligned}\mathbf{D}^{kl}_{ij}(\tau,\tau') &= -i\langle \hat{h}_{ij}(\tau)\hat{h}_{kl}(\tau')\rangle_0 \\ &= -i\mathbf{V}^\dagger_{ij}\mathbf{V}_{lk}\langle \hat{b}^\dagger_i(\tau)\hat{b}_l(\tau')\rangle_0 - i\mathbf{V}_{ji}\mathbf{V}^\dagger_{kl}\langle \hat{b}_j(\tau)\hat{b}^\dagger_k(\tau')\rangle_0 \\ &= \mathbf{V}^\dagger_{ij}\mathbf{V}_{lk}\mathbf{B}_{il}(\tau,\tau') + \mathbf{V}_{ji}\mathbf{V}^\dagger_{kl}\mathbf{B}^T_{kj}(\tau',\tau).\end{aligned} \tag{2.97}$$

Further contraction of the bosonic operators in the density matrix ρ leads to the following expression for the expectation value of an observables $\mathcal{O}$,

$$\langle \mathcal{T}_K \mathcal{O}\rangle_n = \langle \mathcal{T}_K \left(\frac{1}{2}\sum_{kk'll'}\int_K d\tau d\tau' \mathbf{D}^{lk}_{l'k'}(\tau',\tau)\hat{c}^\dagger_{k'}(\tau')\hat{c}_{l'}(\tau')\hat{c}^\dagger_k(\tau)\hat{c}_l(\tau)\right)^n \mathcal{O}\rangle_0. \tag{2.98}$$

In this case the interacting GF can be obtained from

$$\begin{aligned}\mathbf{G}_{ij}(\tau,\tau') &= \mathbf{G}_{ij}(\tau,\tau') \\ &+ i\sum_{n\{k_ik_i'l_il_i'\}}\int d\tau_1 ... \tau_n d\tau_1' ... \tau_n' \frac{1}{n!}\mathcal{K}_n\left(\{k_il_i\tau_i, k_i'l_i'\tau_i'\}, i\tau, j\tau'\right),\end{aligned} \tag{2.99}$$

$$\tag{2.100}$$

where

$$\mathcal{K}_n = \frac{(-i)^n}{2^n}\mathbf{G}_{il_1}(\tau,\tau_1)\mathbf{D}^{l_1k_1}_{l'_1k'_1}(\tau'_1,\tau_1)...\mathbf{D}^{l_nk_n}_{l'_nk'_n}(\tau'_n,\tau_n)\det(\mathcal{A}_n), \tag{2.101}$$

with the matrix $\mathcal{A}_n$ defined as

$$\mathcal{A}_n = \begin{pmatrix} \mathbf{G}_{k_1j}(\tau_1,\tau') & \mathbf{G}_{k'_1j}(\tau'_1,\tau') & \dots & \mathbf{G}_{k_nj}(\tau_n,\tau') & \mathbf{G}_{k'_nj}(\tau'_n,\tau') \\ \mathbf{G}_{k_1l'_1}(\tau_1,\tau'_1) & \mathbf{G}_{k'_1l'_1}(\tau'_1,\tau'_1) & \dots & \mathbf{G}_{k_nl'_1}(\tau_n,\tau'_1) & \mathbf{G}_{k'_nl'_1}(\tau'_n,\tau'_1) \\ \vdots & \vdots & \ddots & \vdots & \vdots \\ \mathbf{G}_{k_1l_n}(\tau_1,\tau_n) & \mathbf{G}_{k'_1l_n}(\tau'_1,\tau_n) & \dots & \mathbf{G}_{k_nl_n}(\tau_n,\tau_n) & \mathbf{G}_{k'_nl_n}(\tau'_n,\tau_n) \\ \mathbf{G}_{k_1l'_n}(\tau_1,\tau'_n) & \mathbf{G}_{k'_1l'_n}(\tau'_1,\tau'_n) & \dots & \mathbf{G}_{k_nl'_n}(\tau_n,\tau'_n) & \mathbf{G}_{k'_nl'_n}(\tau'_n,\tau'_n) \end{pmatrix}. \tag{2.102}$$

This approach is advantageous if one is interested in the transient behavior of the system. For the long time behavior it is numerically more efficient to perform a Fourier transform of the time and then integrate over energy. However, this turns out to be in general impossible unless we expand the determinant and perform the Fourier transform on each term. Another approach which leads to the same result is to start from Eq. (2.95) and perform the contraction on the fermionic operators instead which leads to

$$\mathbf{G}_{ij}(\tau,\tau') = \sum_{n=0}^{\infty}\sum_{n_1=0}^{n-1}\frac{(-i)^{n_1}}{n_1!}\langle\mathcal{T}_K\hat{A}^{n-n1}_{ij}(\tau,\tau')\rangle_{n_1} \tag{2.103}$$

$$= \sum_{n=0}^{\infty}\sum_{n_1=0}^{\infty}\frac{(-i)^{n_1}}{n_1!}\langle\mathcal{T}_K\hat{A}^{n}_{ij}(\tau,\tau')\rangle_{n_1} \tag{2.104}$$

$$= \sum_{n=0}^{\infty}\langle\mathcal{T}_K\hat{A}^{n}_{ij}(\tau,\tau')\rangle, \tag{2.105}$$

where,

$$A^n_{ij}(\tau,\tau') = \sum_{\substack{k_0\dots k_n \\ k'_0\dots k'_n}}\int d\tau_0...\tau_n\mathbf{G}_{ik'_0}(\tau,\tau_0)\hat{h}_{k'_0k_0}(\tau_0)\mathbf{G}_{k_0k'_1}(\tau_0,\tau_1)...\hat{h}_{k'_nk_n}(\tau_n)\mathbf{G}_{k_nj}(\tau_n,\tau'). \tag{2.106}$$

One could further contract the fermionic operators in the density matrix expansion (*i.e.*, expansion with index n_1) for the purpose of having the expression in terms

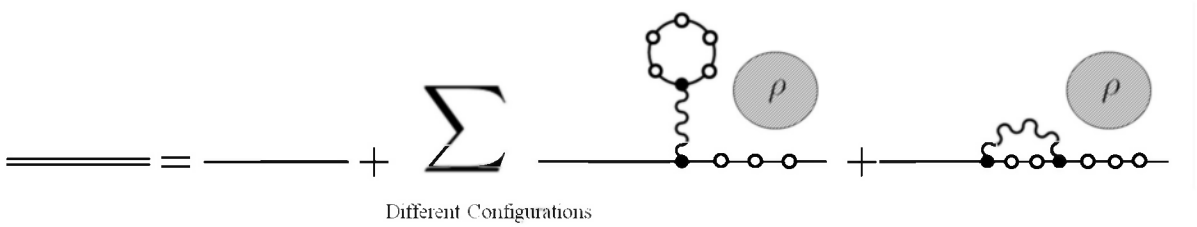

Figure 2.5: Diagrammatic representation of Eq. (2.108) where the solid lines represent electronic GF and summation is over the different configurations that the empty circles are being connected via bosonic wiggly lines interacting with the ρ medium (*i.e.*, vacuum) is performed.

of the bosonic operators only. In that case contractions of the bosonic operators would be equivalent to the expansion using Feynman diagrams. Straightforward calculation yields

$$\mathbf{G}_{ij}(\tau,\tau') = \sum_{n=0}^{\infty}\sum_{n_1=0}^{n-1}\sum_{n_2=0}^{n_1-1}\cdots\int\langle\mathcal{T}_K\hat{A}_{ij}^{n-n_1}(\tau,\tau')\frac{1}{n_1}\hat{A}_{\circ}^{n_1-n_2}\frac{1}{n_2}\hat{A}_{\circ}^{n_2-n_3}\ldots\rangle_0, \tag{2.107}$$

with $\hat{A}_{\circ}^{n} = \delta_{n0} - \delta_{n\neq 0} i\int d\tau \sum_{ij}\hat{h}_{ij}(\tau)A_{ji}^{n-1}(\tau,\tau)$ corresponding to an electronic loop in the language of Feynman diagrams, and from Keldysh contour integration we have $\langle\hat{A}_{\circ}^{n}\rangle = \delta_{n0}$. This expansion seem to have no other advantage than obtaining the perturbation series expansion from Feynman diagrams. Therefore, in the following, we try to use another approach with the goal of finding a self-consistent expressions for a subset of Feynman diagrams that are numerically tractable To do this, we use Eq. (2.103) and contract the first bosonic operator with the other bosonic operators in the expression. We see that the second bosonic operator in the contraction can be either one of the $n-1$ operators in $\hat{A}^n$ or one of the n_1 equivalent operators in the density

matrix expansion. Therefore, we get,

$$\mathbf{G}_{ij}(\tau,\tau') = \mathbf{G}_{ij}(\tau,\tau') \tag{2.108}$$
$$+ \sum_{\{k_i,k_i'\}} \int d\tau_1 d\tau_2 \mathbf{G}_{ik_1}(\tau,\tau_1) \sum_{n=1}^{\infty}\sum_{m=0}^{n-1} \mathbf{D}^{k_1k_1'}_{k_2k_2'}(\tau_1,\tau_2) \langle \mathcal{T}_K \hat{A}^{n-m}_{k_1'k_2}(\tau_1,\tau_2) \hat{A}^{m}_{k_2'j}(\tau_2,\tau')\rangle$$
$$- \sum_{\{k_i,k_i'\}} \int d\tau_1 d\tau_2 \mathbf{G}_{ik_1}(\tau,\tau_1) \sum_{n=1}^{\infty}\sum_{m=0}^{n-1} \mathbf{D}^{k_1k_1'}_{k_2k_2'}(\tau_1,\tau_2) \langle \mathcal{T}_K \hat{A}^{n-m}_{k_2'k_2}(\tau_2,\tau_2) \hat{A}^{m}_{k_1'j}(\tau_1,\tau')\rangle.$$

A diagrammatic representation of this expression is presented in Fig. 2.5. One can continue this procedure to contract the first operator in $\hat{A}^m_{k_1'j}(\tau_1,\tau')$ with the rest of the bosonic operators. In this case we can have three different terms corresponding to the contractions within $\hat{A}^m$, contractions with $\hat{A}^{n-m}$ and contractions with the vacuum. This technique can be continued to obtain all of the perturbation terms with the aim of using lower order terms to reduce calculation of higher order perturbation terms. In the rest of the thesis, we consider only the contractions within $\hat{A}^m$ and with the vacuum (*i.e.*, non-crossing diagrams) while ignoring the rest. From Eq. (2.108), it is straightforward to show that

$$\mathbf{G}_{ij}(\tau,\tau') = \mathbf{G}_{ij}(\tau,\tau') \tag{2.109}$$
$$+ \sum_{\{k_i,k_i'\}} \int d\tau_1 d\tau_2 \mathbf{G}_{ik_1}(\tau,\tau_1) \mathbf{D}^{k_1k_1'}_{k_2k_2'}(\tau_1,\tau_2) \mathbf{G}_{k_1'k_2}(\tau_1,\tau_2) \mathbf{G}_{k_2'j}(\tau_1,\tau')$$
$$- \sum_{\{k_i,k_i'\}} \int d\tau_1 d\tau_2 \mathbf{G}_{ik_1}(\tau,\tau_1) \mathbf{D}^{k_1k_1'}_{k_2k_2'}(\tau_1,\tau_2) \mathbf{G}_{k_2'k_2}(\tau_2,\tau_2) \mathbf{G}_{k_1'j}(\tau_1,\tau'),$$

where we use the following approximation

$$\langle \hat{A}\hat{B}\hat{\rho}\rangle_0 \simeq \langle \hat{A}\hat{\rho}\rangle_0 \langle \hat{B}\hat{\rho}\rangle_0. \tag{2.110}$$

Equation. (2.109) is called the self consistent Hartree-Fock approximation and its diagrammatic representation of this equation is shown in Fig. 2.6(a). By introducing

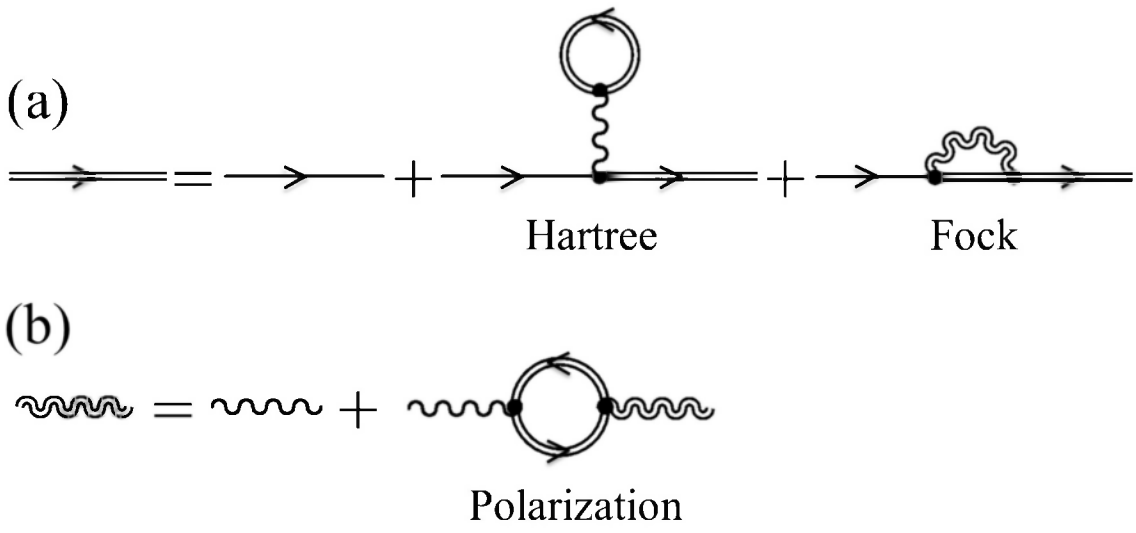

Figure 2.6: (a) Diagrammatic representation of Eq. (2.109); and (b) Diagrammatic representation of Eq. (2.113). In Chapter. 7 give a more detailed description of the diagrams and the corresponding interpretations for the specific case of electrons interacting with magnons in MTJs.

the interaction self-energy as the following

$$\begin{aligned}\boldsymbol{\Sigma}(\tau_1,\tau_2) = &\sum_{k_1' k_2}(\mathbf{V}^{\dagger}_{k_2 k_2'}\mathbf{V}_{k_1' k_1}\mathbf{B}_{k_2 k_1'}(\tau_1,\tau_2) + \mathbf{V}_{k_2' k_2}\mathbf{V}^{\dagger}_{k_1 k_1'}\mathbf{B}^{T}_{k_1 k_2'}(\tau_2,\tau_1))\mathbf{G}_{k_1' k_2}(\tau_1,\tau_2) \\ &- \delta(\tau_1-\tau_2)\int d\tau'(\mathbf{V}^{\dagger}_{k_2 k_2'}\mathbf{V}_{k_1' k_1}\mathbf{B}_{k_2 k_1'}(\tau_1,\tau') + \mathbf{V}_{k_2' k_2}\mathbf{V}^{\dagger}_{k_1 k_1'}\mathbf{B}^{T}_{k_1 k_2'}(\tau',\tau_1))\mathbf{G}_{k_2' k_2}(\tau',\tau'),\end{aligned} \tag{2.111}$$

Eq. (2.109) can be rewritten as

$$\mathbf{G}_{ij}(\tau,\tau') = \mathbf{G}_{ij}(\tau,\tau') + \sum_{k_1,k_2}\int d\tau_1 d\tau_2 \mathbf{G}_{ik_1}(\tau,\tau_1)\boldsymbol{\Sigma}_{k_1 k_2}(\tau_1,\tau_2)\mathbf{G}_{k_2 j}(\tau_2,\tau'). \tag{2.112}$$

By considering interactive bosonic GF $\mathbf{B}_{ij}(\tau,\tau') = \langle \hat{b}^{\dagger}_i(\tau)\hat{b}_j(\tau')\rangle$ we can improve the approximation further by taking into account the so called bubble (electron-hole polarization) diagrams in the calculation. Contracting $\hat{b}^{\dagger}_i(\tau)$ with the rest of the operators

leads to

$$\mathbf{B}_{ij}(\tau,\tau') = \mathbf{B}_{ij}(\tau,\tau') - \sum_{k_1}\int d\tau_1 \mathbf{B}_{ik_1}(\tau,\tau_1)\langle \hat{c}^\dagger_{k_1}(\tau_1)\hat{c}_{k_1}(\tau_1)\hat{b}_j(\tau')\rangle \tag{2.113}$$

$$\simeq \mathbf{B}_{ij}(\tau,\tau') - \sum_{k_1 k_2}\int d\tau_1 d\tau_2 \mathbf{B}_{ik_1}(\tau,\tau_1)\langle \hat{c}^\dagger_{k_1}(\tau_1)\hat{c}_{k_1}(\tau_1)\hat{c}^\dagger_{k_2}(\tau_2)\hat{c}_{k_2}(\tau_2)\rangle \mathbf{B}_{k_2 j}(\tau_2,\tau')$$

$$\simeq \mathbf{B}_{ij}(\tau,\tau') + \sum_{k_1 k_2}\int d\tau_1 d\tau_2 \mathbf{B}_{ik_1}(\tau,\tau_1)\mathbf{G}_{k_1 k_1}(\tau_1,\tau_1)\mathbf{G}_{k_2 k_2}(\tau_2,\tau_2)\mathbf{B}_{k_2 j}(\tau_2,\tau')$$

$$+ \sum_{k_1 k_2}\int d\tau_1 d\tau_2 \mathbf{B}_{ik_1}(\tau,\tau_1)\mathbf{G}_{k_1 k_2}(\tau_1,\tau_2)\mathbf{G}_{k_2 k_1}(\tau_2,\tau_1)\mathbf{B}_{k_2 j}(\tau_2,\tau')$$

In Fig. 2.5(b) we show the Feynman diagram representation of this equation. Using Eq. (2.113) the self-energy of the bosons due to the electron-boson interaction is given by

$$\mathbf{\Omega}_{ij}(\tau,\tau') = \mathbf{G}_{k'_1 k_2}(\tau,\tau')\mathbf{G}_{k'_2 k_1}(\tau',\tau), \tag{2.114}$$

where we ignored the Hartree term in order to avoid double counting.

2.5.1 Observables: Time-Dependent Case

In the presence of an external time dependent perturbation, the effect of many-body interactions could be significant due to the vertex corrections which effectively change the strength of the time-dependent perturbation. In order to obtain the terms corresponding to the vertex corrections, one can either use the Feynman diagram approach and obtain a self-consistent equation describing the renormalization of the vertices called Bethe-Salpeter equation (BSE) or use the following technique which we Taylor expand the interacting GF in terms of external time-dependent perturbation. The Dyson equation in the presence of many-body interactions and time dependent perturbation is

$$\left(i\frac{\partial}{\partial t} - \check{\mathbf{H}} - \lambda\check{\mathbf{m}}(t) - \check{\mathbf{\Sigma}}_{leads} - \check{\mathbf{\Sigma}}(\{\check{\mathbf{G}}\})\right)\check{\mathbf{G}}(t,t') = \delta(t-t')\check{\mathbf{1}}. \tag{2.115}$$

The first derivative of the GF in terms of λ is

$$\frac{\partial}{\partial\lambda}\check{\mathbf{G}}_\lambda(t,t') = \int dt_1 dt_2 \check{\mathbf{G}}_\lambda(t,t_1)\left[\check{\mathbf{m}}(t_1)\delta(t_1-t_2) + \frac{\partial}{\partial\lambda}\check{\mathbf{\Sigma}}(\{\check{\mathbf{G}}_\lambda\})(t_1,t_2)\right]\check{\mathbf{G}}_\lambda(t_2,t'). \tag{2.116}$$

Since in this thesis we are interested in the Hartree-Fock approximation only, in which the interaction self-energy is proportional to the GF, we can write

$$\frac{\partial}{\partial\lambda}\check{\mathbf{G}}_\lambda(t,t') = \int dt_1 dt_2 \check{\mathbf{G}}_\lambda(t,t_1)\left[\check{\mathbf{m}}(t_1)\delta(t_1-t_2) + \check{\mathbf{\Sigma}}\left(\{\frac{\partial\check{\mathbf{G}}_\lambda}{\partial\lambda}\}\right)(t_1,t_2)\right]\check{\mathbf{G}}_\lambda(t_2,t'). \tag{2.117}$$

For $\lambda \to 0$ this equation is called Bethe-Salpeter equation which describes the excitonic states in the system. We notice that by increasing the size of the Hilbert space to include the excitonic degree of freedom the GF in terms of energy is defined as the following

$$\check{\mathbf{G}}_n(E) = \begin{pmatrix} \check{\mathbf{G}}_n(E) & 0 \\ \check{\mathbf{G}}'_n(E) & \check{\mathbf{G}}_0(E) \end{pmatrix}, \tag{2.118}$$

where $\check{\mathbf{G}}'_n(E) = \frac{\partial\check{\mathbf{G}}_{\lambda,n}(E)}{\partial\lambda}|_{\lambda\to 0}$. One can write down a single self-consistent equation for the whole system

$$\begin{pmatrix} \check{\mathbf{g}}^{-1}(E+n\omega) & 0 \\ -\check{\mathbf{m}}_n & \check{\mathbf{g}}^{-1}(E) \end{pmatrix}\check{\mathbf{G}}_n(E) - \check{\mathbf{\Sigma}}(\{\check{\mathbf{G}}_n\})\check{\mathbf{G}}_n(E) = \check{\mathbf{1}}, \tag{2.119}$$

This equation is very similar to the Dyson equation in Keldysh space which suggests that the above equation does not have a unique solution and a general solution exists even for $\check{\mathbf{m}}_n = 0$

$$\check{\mathbf{G}}'_n(E) = a_n\check{\mathbf{G}}_n(E)\left[n\omega - \check{\mathbf{\Sigma}}(E+n\omega) + \check{\mathbf{\Sigma}}(E)\right]\check{\mathbf{G}}_0(E), \tag{2.120}$$

where a_n is an arbitrary number suggesting the occupation of the excitonic states. To our best knowledge this term has never been discussed preiously in the literature and at the time of writing this thesis the implications of this term is yet to be investigated. Therefore we ignore the general solution and concentrate on the special solutions which are linear response to the external perturbation. Once the self-consistent equation. (2.119) is solved, one can use the GFs to find observables in linear response to external time dependent perturbations which would be time dependent as well. However, since in this thesis we are interested in the dc response to time-dependent

perturbations, we need to take into account at least the second-order perturbation term. The second-order contribution to the observable reads,

$$O_n^{(2)} = \int dE \mathrm{Tr}\left[\check{\mathbf{O}}_n(E)\check{\mathbf{G}}_n''(E)\right] = \int dE \mathrm{Tr}\left[\check{\mathbf{O}}_n(E)\frac{\partial^2 \check{\mathbf{G}}_{n,\lambda}(E)}{\partial\lambda^2}|_{\lambda\to 0}\right] \tag{2.121}$$
$$= \sum_p \int dE \mathrm{Tr}\left[\check{\mathbf{O}}_n'(E)\check{\mathbf{G}}_n(E)\check{\mathbf{m}}_{n-p}'(E)\check{\mathbf{G}}_p(E)\check{\mathbf{m}}_p'(E)\check{\mathbf{G}}_0(E)\right],$$

where we have

$$\check{\mathbf{O}}_n'(E) = \check{\mathbf{O}}_n(E) + \check{\mathbf{\Sigma}}(\{\check{\mathbf{G}}_n\check{\mathbf{O}}_n'\check{\mathbf{G}}_0\}), \tag{2.122}$$
$$\check{\mathbf{m}}_n'(E) = \check{\mathbf{m}}_n + \check{\mathbf{\Sigma}}(\{\check{\mathbf{G}}_n\check{\mathbf{m}}_n'\check{\mathbf{G}}_0\}). \tag{2.123}$$

This formula can be used to investigate the energy conversion in interacting systems under a time dependent perturbation and we relegate the numerical calculations using this formulation to future works. A similar argument can be used to find the effect of interaction on the equation of motion for the GF in the adiabatic regime (see Eq. (2.63)),

$$\check{\mathbf{G}}(E,t) = \check{\mathbf{G}}^{ad}(E,t) + i\check{\mathbf{G}}^{ad}(E,t)\check{\mathbf{g}}'(E)\frac{\partial}{\partial t}\check{\mathbf{G}}(E,t), \tag{2.124}$$

where

$$\check{\mathbf{g}}'(E) = \frac{\partial \check{\mathbf{g}}_0^{-1}(E)}{\partial E} + \check{\mathbf{\Sigma}}(\{\check{\mathbf{g}}\check{\mathbf{g}}'\check{\mathbf{g}}\}), \tag{2.125}$$

and $\check{\mathbf{g}}_0$ ($\check{\mathbf{g}}$) corresponds to the noninteracting (interacting) GFs without the time-dependent term.

2.5.2 Observables: Current Noise

In the non-interacting case we showed that the noise can be calculated by adding the current operator multiplied by an auxiliary parameter to the Hamiltonian such that the expectation value of the modified density matrix would be the generating function

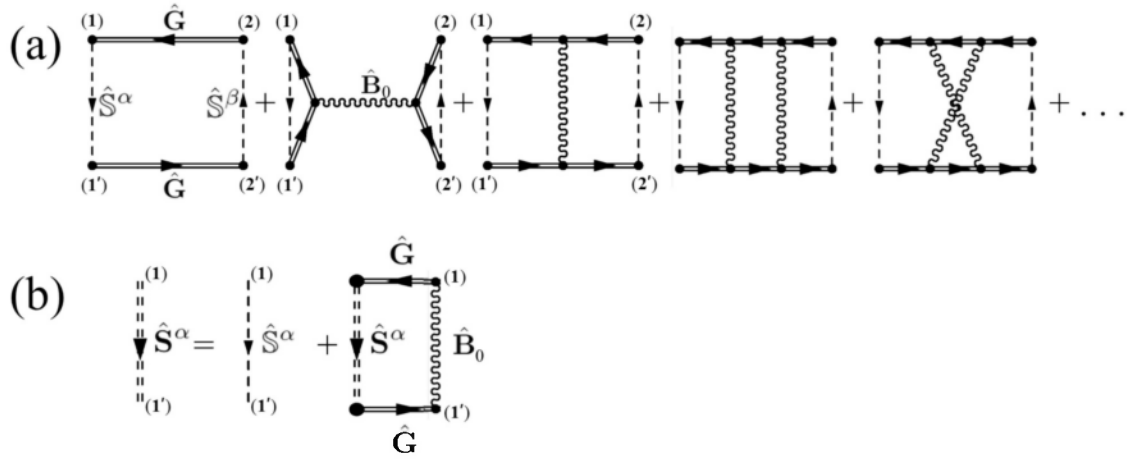

Figure 2.7: (a) Feynman diagrams for the lowest order corrections to the noise power due to the two-particle characteristics of the current-current correlation. (b) Diagrammatic representation of the self consistent expression, Eq .(2.127), for the noise power in Keldysh space taking into account the non-crossing ladder diagrams.

for the current. This approach can be generalized to the interacting systems as well, where we find the following for the noise power

$$S_{\alpha\beta} = \frac{\partial}{\partial\lambda_\beta} I^0_\alpha(\{\lambda_\beta\})|_{\{\lambda_\beta\}\to 0} \tag{2.126}$$
$$= \frac{e}{\hbar}\int dE \mathrm{Tr}\left[\delta_{\alpha\beta}\check{\mathbf{G}}\boldsymbol{\tau}_z\check{\mathbf{S}}^\alpha + \boldsymbol{\tau}_z\check{\mathbf{G}}\boldsymbol{\tau}_z\check{\mathbf{S}}^\alpha\boldsymbol{\tau}_z\check{\mathbf{G}}\boldsymbol{\tau}_z\check{\mathbf{S}}^\beta\right].$$

Here $\check{\mathbf{S}}^\alpha$ obeys the following Bethe-Salpeter equation

$$\check{\mathbf{S}}^\alpha(E) = \check{\mathbb{S}}^\alpha_0(E) + \check{\boldsymbol{\Sigma}}(\{\check{\mathbf{G}}\check{\mathbf{S}}^\alpha\check{\mathbf{G}}\})(E). \tag{2.127}$$

In Fig .2.7(a) we show the diagrams for noise power containing a few of the lowest order correction terms. Fig .2.7(b) shows the diagrammatic representation of Eq.(2.127) in order to take into account the non-crossing ladder diagrams appearing in the expression for the noise with interaction. We should mention that considering the self-consistent Fock diagrams for the single particle interacting electronic GFs and noninteracting bosonic GF, one has to take into account the previously mentioned non-crossing ladder diagrams in order to keep the fluctuation-dissipation theorem valid. We

postpone further investigation of this formalism including the numerical calculations of the noise in the presence of interaction to the future works.

Chapter 3

CHARGE PUMPING BY MAGNETIZATION DYNAMICS IN MAGNETIC AND SEMI-MAGNETIC TUNNEL JUNCTIONS WITH INTERFACIAL RASHBA OR BULK EXTRINSIC SPIN-ORBIT COUPLINGS

3.1 Motivation

Recent vigorous experimental efforts on pumping from MTJs under microwave radiation, have focused on the direct detection of pure spin current generated by coherent macrospin precession in both ferromagnetic metals [83, 84, 45] and insulators [85, 79] by converting it into dc voltage signal. For example, the experimental techniques employed for this purpose include the inverse spin Hall effect [83] or the second static F layer as detector within a magnetic tunnel junction (MTJ), [84] as well as the precessing F layer itself which can generate voltage [45] at the F|N interface by detecting the backflow spin current due to spin accumulation [37] driven by pumping into the N layers thinner than the spin-diffusion length.

The origin of the voltage signal of spin pumping in F|I|F MTJs can be easily understood [1, 86, 87] as a two step process: (i) the magnetization dynamics of the left F layer pumps pure spin current across the tunnel barrier (I-insulator) and (ii) the pumped spin current is then filtered by the analyzing right F layer where magnetization is static. This generates charge current or, equivalently, dc pumping voltage in an open circuit. [1, 86, 87] This voltage is proportional to the frequency $\propto \hbar\omega$ of microwaves due to adiabatic nature of pumping (in the adiabatic regime, formally $\omega \to 0$ since energy of microwave photons $\hbar\omega$ is smaller than other relevant energy scales in ferromagnetic solids).

On the other hand, surprisingly large voltage signal $\propto \hbar\omega$ observed [46] in F|I|N semi-MTJs, which do not contain the second analyzing F layer, has remained unexplained in virtually all recent theories [1, 86, 87, 88] of spin pumping in MTJs. Some of these theories [86, 87] actually predict tiny voltage signal, which, being non-adiabatic $\propto (\hbar\omega)^2$ is the second-order effect.

Also, there exists several orders of magnitude discrepancy between underestimated voltage signal of spin pumping in F|I|F MTJs obtained in the scattering theory, [1] experimental data, [84] and overestimated voltage signal obtained in the rotating frame approach [86, 87] or the tunneling Hamiltonian formalism combined with semiclassical modeling of the interplay of spin diffusion and self-consistent screening around interfaces. [88] This can be traced to different device setups where scattering approach was applied to MTJs assuming zero [1] spin accumulation in the F layers modeled as semi-infinite leads (justified through assumption that spin-flip rate in F is larger than the tunnel rate), while unrealistically large bulk [86, 87] or interfacial [88] spin accumulation appears in the other two approaches.

The MTJs employed in spin pumping experiments [84, 46] contain F layers of nanoscale thickness whose short spin-diffusion length [89] can be modeled by sufficiently strong extrinsic spin-orbit scattering. Most importantly, the very recent experiments [48] have unveiled a possibility of strong Rashba spin-orbit coupling (SOC) at the F|I interface due to structural inversion asymmetry of the multilayered device within which such interfaces reside (e.g., Rashba SOC was detected in N|F|I multilayers, but not in the N|F|N ones [48]).

However, SOCs have been traditionally neglected in a variety of approaches to spin and charge pumping by magnetization dynamics. [28, 1, 87, 90, 91] The SOCs in the bulk or on the surface of ferromagnetic materials play crucial role in other phenomena, such as the anomalous Hall effect [92] or the tunneling anisotropic magnetoresistance [63, 64, 93, 94, 95, 65] (TAMR). Moreover, the study of the interplay between SOC and STT has been recently initiated [96, 97, 98, 61] through theoretical proposals [99] and experimental realizations [48] that exploit SOCs for STT-driven

magnetization reversal of a single F layer with greatly reduced critical current required when compared to traditional spin valves or MTJs with two non-collinear magnetizations. [27]

In the "standard model" [28, 38] of spin pumping in magnetic multilayers containing many [38] F and N layers, the magnitude of pumped spin current by F|N interfaces is computed quantum-mechanically via the Brouwer scattering formula [100] which then serves as the boundary condition for the spin-diffusion equation [38] or enters into the so-called circuit theory [89] where device is split into nodes of characteristic size smaller than the spin-diffusion length. Thus, in these frameworks SOCs enter only phenomenologically through finite spin-diffusion length (a spin can be flipped by SOC and magnetic impurities in N or F layers, as well as by magnon scattering in the F layers).

However, these approaches are not applicable to MTJs since the spin accumulation is not well-defined in the insulating barrier. [38] Moreover, even the magnitude of pumped current cannot be obtained from the "standard model" formula, [28] governed by the interfacial spin-mixing conductance [89] $g^{\uparrow\downarrow}$, when *strong SOC is present immediately at the interface* which renders $g^{\uparrow\downarrow}$ an ill-defined quantity.

The recent alternative description [91] of spin pumping in F|N multilayers, based on nonequilibrium Green function (NEGF) expressions for the local spin and charge current densities, has encompassed both the earlier considered [101] nonlocal diffusion of the spin accumulation at the F|N interface generated by magnetization precession and the effective field described by the "standard model" (where spin accumulation does not build at the interface since spin-flip relaxation rate is assumed to be sufficiently larger than the spin injection rate). However, this framework [91] has treated SOCs only in the N layer away from the precessing F layer in order to analyze how each of these two pumped spin currents can be converted into charge current by the inverse spin Hall effect due to the extrinsic or intrinsic SOCs. That is, in this theory SOCs are not essential for the discussion of spin pumping effect itself.

We note that other groups have also recently identified the importance of adding

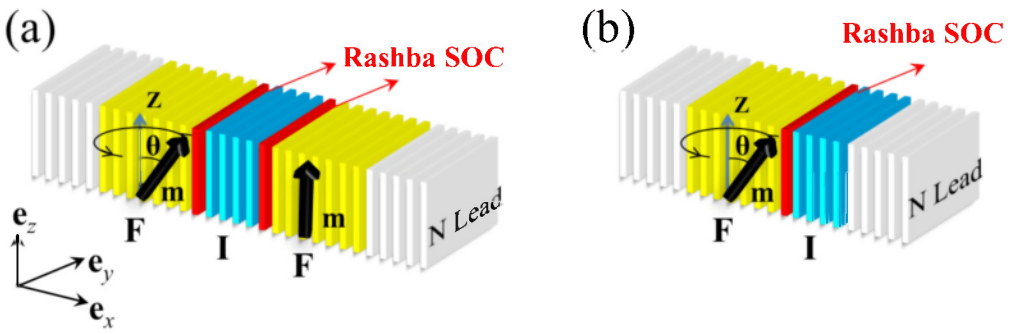

Figure 3.1: (a) F|I|F MTJ and (b) F|I|N semi-MTJ with precessing magnetization of a single F layer are modeled on a simple cubic finite-size tight-binding lattice attached to semi-infinite ideal (disorder and interaction free) N leads. The thicknesses of the ferromagnetic layers and thin insulating barrier is measured using the number of atomic monolayers d_F and d_I, respectively. For example, $d_F = 8$ and $d_I = 4$ in the illustration, while in the actual calculations we use $d_F = 50$ and $d_I = 5$ monolayers of cross section 20×20 lattice sites. The interfacial Rashba SOC due to structural inversion asymmetry of the junction is included in the last monolayer of the F slab that is in direct contact with the tunnel barrier I. The F layers can also include disorder modeled as a random on-site potential and the corresponding extrinsic SOC, while binary alloy disorder in the I layer models AlO_x-type tunnel barrier.

SOCs explicitly into the description of spin and charge pumping by magnetization dynamics. For example, a generalized scattering theory of adiabatic charge pumping by a single precessing F layer within N|F|N junctions containing SOCs has been formulated in Ref. [96]. Also, the pumping of current of magnetic monopoles and the associated (via Ampère law) charge current flowing in the plane of the Rashba SO-coupled interface (rather than perpendicular to it as is the focus of our study) between the precessing F layer and a nonmagnetic layer has been predicted in Ref. [102].

Here we develop a NEGF-based quantum transport theory of spin current pumping, its propagation, and conversion into electrically measurable signals in F|I|F and F|I|N junctions depicted in Fig. 3.1. The junctions are described by the microscopic time-dependent (due to precessing magnetization of one of the F layers) Hamiltonian which is tailored to take into account nanoscale thickness of F layers within which

we include terms describing disorder and extrinsic SOC in the F layers, as well as possibly strong Rashba SOC at the F|I interfaces. Our theory starts from the equations of motion generated by such Hamiltonian for NEGFs which depend on two time variables, and then finds a computationally efficient solution to such equations which physically describes processes where a specific number of microwave photons is absorbed or emitted by propagating electrons in the course of pumping. This solution for time-dependent NEGFs allows us to obtain time-averaged total charge current in the N leads of the junctions shown in Fig. 3.1 or the corresponding dc pumping voltage in the corresponding open circuits. The formulas which we derive for pumped currents are also applicable to any problem where a quantum-mechanical system is exposed to periodic time-dependent external field, independently of its frequency (i.e., including both adiabatic and non-adiabatic regimes) or amplitude (i.e., including both perturbative and non-perturbative regimes), as long as electron-electron, electron-phonon and electron-magnon interactions can be neglected.

This chapter is organized as follows. In Sec. 3.2 we discuss how to tune parameters of the microscopic Hamiltonian in order to reproduce properties of MTJs and semi-MTJs employed in experiments, [84, 46] such as their tunneling magnetoresistance, diffusive nature of transport within the F layers, finite spin-diffusion length in F layers and strong interfacial Rashba SOC. Section 3.3 discusses NEGF equations of motion and how to solve such equations after converting them into algebraic ones via double Fourier transform. In this section we also employ clean F|I|F junctions (with semi-infinite or finite thickness F layers) as a test bed to compare our theory to the scattering formulas for pumping in MTJs derived in Ref. [1], as well as to previously developed [103] solution to double-time-Fourier-transformed NEGF equations using continued fractions. In Sec. 3.4 we discuss properties of time-averaged pumped charge current and the corresponding dc voltage signal in open circuits for clean F|I|N and F|I|F junctions as a function of the strength of interfacial Rashba SOC. The effect of disorder in F and I layers, as well as the extrinsic SOC within F layers, on the dc pumping voltage in F|I|F MTJs is discussed in Sec. 3.5. We conclude in Sec. 3.6.

Readers seeking to understand physical effects of SOC on microwave-driven MTJs may wish to start with Sec. 3.2 and then jump to Sec. 3.4 and Sec. 3.5.

3.2 MTJ Device Setup and Hamiltonian

The MTJ and semi-MTJ we study are illustrated in Fig. 3.1(a) and (b), respectively. Each atomic monolayer shown in Fig. 3.1 is modeled on the square tight-binding lattice with single s-orbital per site. Since disorder is included as random potential in real space, atomic monolayers are of finite size 20×20 sites. This can also be viewed as the cross section of a supercell which is repeated periodically in the transverse direction, [89] while its size is sufficient to allow one to compute all quantities at the Γ point (i.e., without the need to perform k-point sampling). [104] We have checked that dc pumping voltage remains constant as one increases cross section size beyond 20×20 sites.

The ferromagnetic layers consist of $d_F = 50$ such monolayers, so that their thickness is $\simeq 15$ nm (assuming typical lattice spacing $a \simeq 3$ Å), which closely mimics F layers employed experimentally. [84, 46] The thickness of the insulating barrier is $d_I = 5$ atomic monolayers. The finite-size F|I|F or F|I|N multilayer is connected to macroscopic reservoirs via two semi-infinite ideal (i.e., disorder, spin and charge interaction-free) N leads to form a two-terminal device required for both NEGF and scattering theory analysis.

The general time-dependent Hamiltonian describing these two devices can be written as

$$\begin{aligned}\hat{H}(t) \;=\; & \sum_{\mathbf{i},ss'} \left(\varepsilon_{\mathbf{i}} \delta_{ss'} - \frac{\Delta_{\mathbf{i}}}{2} \mathbf{m}_{\mathbf{i}}(t) \cdot [\vec{\sigma}]_{ss'} \right) \hat{c}^{\dagger}_{\mathbf{i}s} \hat{c}_{\mathbf{i}s'} \\ & -\gamma \sum_{\langle \mathbf{i}\mathbf{i}' \rangle, ss'} \hat{c}^{\dagger}_{\mathbf{i}s} \hat{c}_{\mathbf{i}'s'} + i\lambda_{\mathrm{ESO}} \sum_{\mathbf{i}\mathbf{i}', ss'} \hat{c}^{\dagger}_{\mathbf{i}s} \mathbf{L}_{\mathbf{i}\mathbf{i}'} \cdot [\vec{\sigma}]_{ss'} \hat{c}_{\mathbf{i}s'} \\ & + \sum_{\langle \mathbf{i}\mathbf{i}' \rangle, ss'} \hat{c}^{\dagger}_{\mathbf{i}s} t^{ss'}_{\mathbf{i}\mathbf{i}'} \hat{c}_{\mathbf{i}'s'}. \end{aligned} \tag{3.1}$$

Its time-dependence stems from the unit vector $\mathbf{m}_{\mathbf{i}}(t)$ along the local magnetization direction within the left F layer, which is assumed to be spatially uniform and steadily

precessing around the z axis with a constant cone angle. The value of angle θ is controlled by the input microwave power (typically $\theta \lesssim 20°$ in the recent experiments [46]). The operators $\hat{c}^{\dagger}_{\mathbf{i}\sigma}$ ($\hat{c}_{\mathbf{i}\sigma}$) create (annihilate) electron with spin σ at site $\mathbf{i} = (i_x, i_y, i_z)$, and γ is the nearest neighbor hopping which sets the unit energy scale. The coupling of itinerant electrons to collective magnetization dynamics is described through the material-dependent exchange potential $\Delta_{\mathbf{i}}$, where $\vec{\sigma} = (\sigma_x, \sigma_y, \sigma_z)$ is the vector of the Pauli matrices and $[\hat{\sigma}]_{ss'}$ denotes the Pauli matrix elements.

The disorder within F layers can be introduced using the uniformly distributed random variable $\varepsilon^F_{\mathbf{i}} \in [-W/2, W/2]$ which models isotropic short-range static impurity potential. To account for the properties of amorphous AlO_x tunnel barrier in MTJs and semi-MTJs employed in the recent spin pumping experiments, [84, 46] the on-site potential on I monolayers is chosen as $\varepsilon^I_{\mathbf{i}} = U_b \pm \delta U_b$ where random fluctuations δU_b mimic binary alloy disorder. [105]

The impurity potential in the F layers also generates extrinsic SOC, as described by the third sum in Eq. (3.1). This can be viewed as the lattice version [106] of the Thomas term $\lambda(\vec{\sigma} \times \mathbf{p}) \cdot \nabla V_{\text{dis}}$ in the Pauli-Schrödinger equation so that

$$(\boldsymbol{L}_{\mathbf{ii}'})_x = \sum_{\nu,\nu'=\pm 1} \nu\nu' (\varepsilon^F_{\mathbf{i}+\nu\mathbf{e}_y} - \varepsilon^F_{\mathbf{i}+\nu'\mathbf{e}_z}) \delta_{\mathbf{i},\mathbf{i}'+\nu\mathbf{e}_y+\nu'\mathbf{e}_z}. \tag{3.2}$$

That is, on the tight-binding lattice the extrinsic SOC acts as additional spin-dependent hopping between both nearest neighbor and next nearest neighbor sites. Here $(\mathbf{e}_x, \mathbf{e}_y, \mathbf{e}_z)$ are the unit vectors along the x, y, z axis respectively and $\lambda_{\text{ESO}} = \lambda/4a$. The derivation of this term is presented in Appendix: C.

The fourth sum in Eq. (3.1) is the tight-binding representation [106] of the Rashba SOC written in terms of a generalized nearest neighbor hopping term that acts as 2×2 Hermitian matrix in the spin space:

$$\mathbf{t}_{\mathbf{ii}'} = \begin{cases} -i\gamma_{\text{RSO}}\sigma_z & (\mathbf{i} = \mathbf{i}' + \mathbf{e}_y) \\ +i\gamma_{\text{RSO}}\sigma_y & (\mathbf{i} = \mathbf{i}' + \mathbf{e}_z) \end{cases}, \tag{3.3}$$

The continuous version of the Rashba SOC, $\alpha_{\mathrm{RSO}}(\vec{\sigma} \times \hat{\mathbf{p}}) \cdot \mathbf{e}_x/\hbar$, has been traditionally studied in the context of two-dimensional electron gases (2DEGs) within semiconductor heterostructures with structural inversion asymmetry in the growth direction. [52] Nevertheless, several experiments have recently reported evidence of the Rashba SOC-induced splitting of the surface states in both non-magnetic and magnetic metals using angle-resolved photoelectron spectroscopy. [107] The very recent transport experiments [48] have demonstrated Rashba SOC-induced STT of a single thin F layer embedded between two asymmetric interfaces. For example, such effect was observed in Pt|Co|AlO_x multilayers, but not in the inversion symmetric ones Pt|Co|Pt. The experiment of Ref. [48] has also utilized heavy atoms and surface oxidation to create strong out-of-plane potential gradient in Pt|Co|AlO_x junctions and enhance the interfacial Rashba SOC.

This motivates the introduction of the Rashba SOC term of strength γ_{RSO} into the Hamiltonian in Eq. (3.1), which we set to be non-zero only on the last monolayer of the precessing F layer that is in the direct contact with the first monolayer of the tunnel barrier, as illustrated in Fig. 3.1. Note that the exact location of the interfacial Rashba SOC eventually requires fitting the Hamiltonian parameters to first-principles analysis. [93, 94, 95]

3.2.1 Tunning Hamiltonian Parameters to Reproduce Properties of MTJs Used in Experiments

The diffusive transport regime within F or N layers is defined semiclassically by the requirement that mean free path ℓ is smaller then the thickness of such layers, $\ell \ll d_F$ or $\ell \ll d_N$. In quantum transport calculations, the easiest way to select proper range of values for the disorder strength W which ensures diffusive regime is to compute the Fano factor $F = S/2eI$ of the shot noise whose zero-temperature and zero-frequency noise power S, is obtained from Eq. (2.89). For the diffusive metallic wires, $F = 1/3$ is universal in the sense of being independent of the impurity distribution, band structure, and shape of the conductor. [108] In Fig. 3.2 we plot the Fano factor

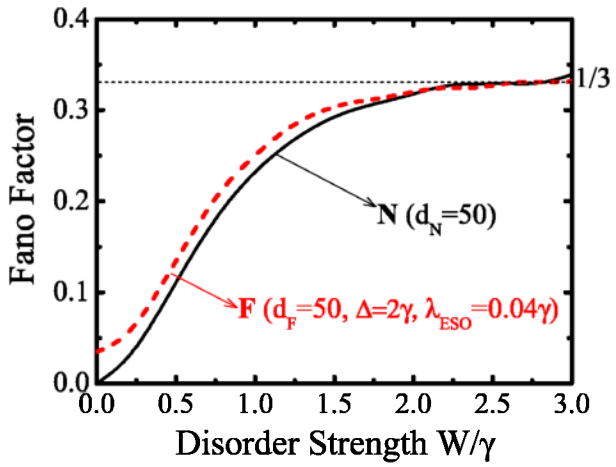

Figure 3.2: The Fano factor of the zero-temperature and zero-frequency shot noise vs. the disorder strength W in transport through N slab with static disorder or F slab with both static disorder and the corresponding extrinsic SOC of strength $\lambda_{\rm ESO} = 0.04\gamma$. Both slabs consists of 50 monolayers (containing 20×20 atoms per cross section) which are connected to two semi-infinite ideal N leads.

with increasing disorder strength W for both conventional disordered N layer attached to two ideal semi-infinite leads and F layer of the same dimensions with both disorder and extrinsic SOC. Using Fig. 3.2, we select $W = 3\gamma$ to ensure semiclassical diffusive transport regime.

Note that spin-dependent effects on the shot noise are reveled only when spin-polarized current is injected and the corresponding spin-resolved Fano factors are defined. [109] Thus, for unpolarized injected charge current, both F and N layers have virtually the same Fano factor in the diffusive regime, while larger Fano factor for the F layer in the quasi-ballistic regime is due to increased scattering at the N|F interfaces because of non-zero Δ.

3.2.1.1 Extrinsic SOC in the Bulk of F Layers

In both N and F layers, spin-flip scattering will destroy nonequilibrium spin accumulation which is typically accounted [89] through phenomenological spin-diffusion length $L_{\rm sf}$. Over this length scale, an injected spin accumulation loses its polarization

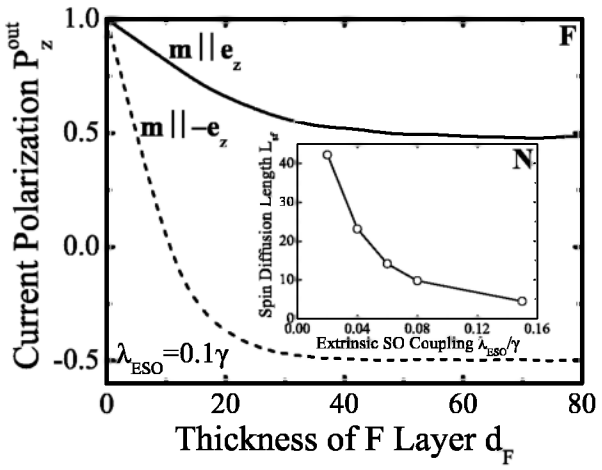

Figure 3.3: The decay of current polarization along the diffusive F layer with static disorder of strength $W = 3\gamma$ and the extrinsic SOC of strength $\lambda_{\rm ESO} = 0.1\gamma$. The F layer is attached to two semi-infinite ideal N leads where charge current which is 100 % spin-polarized along the z-axis, $\mathbf{P}^{\rm in} = (0, 0, 1)$, is injected from the left N lead and $P_z^{\rm out}$ is computed in the right N lead for F layer of thickness d_F. The unit vector of the magnetization in F is either parallel (solid line) or antiparallel (dashed line) to the z-axis. The inset shows spin-diffusion length as a function of $\lambda_{\rm ESO}$ when F layer is replaced by diffusive N layer with different strengths of extrinsic SOC, where each value of $L_{\rm sf}$ is extracted by fitting exponentially decaying function to $P_z^{\rm out}$ vs. d_N curves.

so that $L_{\rm sf}$ in ferromagnets defines the magnetoelectrically active region of F layer in contact with N layer. In metallic ferromagnetic materials, $L_{\rm sf}$ ranges [89] from 5 nm in $Ni_{80}Fe_{20}$ (permalloy), which is often employed as precessing F layer in spin pumping experiments, [84, 46] to 50 nm in Co.

To understand how to tune the strength $\lambda_{\rm ESO}$ of the extrinsic SOC term in Eq. (3.1) in order to generate different experimental situations in F layers of nanoscale thickness, such as $L_{\rm sf} < d_F$ or $L_{\rm sf} > d_F$ (where spin-flip processes essentially become unimportant), we compute the spin density matrix [4] of collected transported spins in the right lead 2 after fully spin-polarized charge current is injected from the left lead 1 across the F layer:

$$P_i^{\alpha,\text{out}} = \frac{I_\alpha^i(\overrightarrow{P}^{\text{in}})}{I_\alpha^0(\overrightarrow{P}^{\text{in}})}, \tag{3.4}$$

where, $I_\alpha^i(\overrightarrow{P}^{\text{in}})$, is obtained from Eq. (2.57). The spin current polarization vector $\mathbf{P}^{\text{out}} = (P_x^{\text{out}}, P_y^{\text{out}}, P_z^{\text{out}})$ whose magnitude $P^{\text{out}} = |\mathbf{P}^{\text{out}}|$ gives the so-called current polarization measured experimentally. [110] The spin polarization is computed for the two-terminal N|F|N device where F layer with static magnetization pointing along the z-axis and disorder of strength $W = 3\gamma$ is embedded between two semi-infinite N leads.

The measured current polarization of permalloy at room temperature ranges from $P = 0.32$ to $P = 0.5$, depending on the experimental technique employed. [110] Since we find only tiny fluctuations of $P_x,\ P_y \sim 10^{-3}$ in the presence of non-zero Δ and λ_{ESO}, we use $P^{\text{out}} = |P_z^{\text{out}}|$ as the measure of current polarization. We first tune $\Delta = 2\gamma$ of the F layer with $\lambda_{\text{ESO}} = 0$ to obtain $P^{\text{out}} \simeq 0.5$ at the Fermi energy $E_F = -3\gamma$. Then we compute the decay of P_z^{out} with increasing length of the diffusive F layer with non-zero λ_{ESO}, as shown in Fig. 3.3. For sufficiently thick F layer, these curves saturate at $|P_z^{\text{out}}| \simeq 0.5$. On the other hand, the same calculation for the diffusive N layer with non-zero λ_{ESO} gives usual exponentially decaying P_z^{out} vs. d_N curves due to spin diffusion, whose fitting establishes the correspondence between λ_{ESO} values used in our study and microscopically determined spin-diffusion length L_{sf}. The dependence $L_{\text{sf}} \propto 1/\lambda_{\text{ESO}}$ shown in the inset in Fig. 3.3 is expected for the diffusive transport regime.

With Δ and E_F specified in this fashion to ensure that current polarization of permalloy slab matches experimentally measured values, we finally tune the height of the potential barrier $U_b = 9\gamma$ in the tunnel barrier I of thickness $d_I = 5$ to tune the "optimistic" tunneling magnetoresistance (TMR) defined as

$$\text{TMR} = \frac{R_{\text{AP}} - R_{\text{P}}}{R_{\text{P}}}, \tag{3.5}$$

to TMR=50 % for the F|I|F MTJs employed experimentally. [84, 46] Here R_{AP} is the

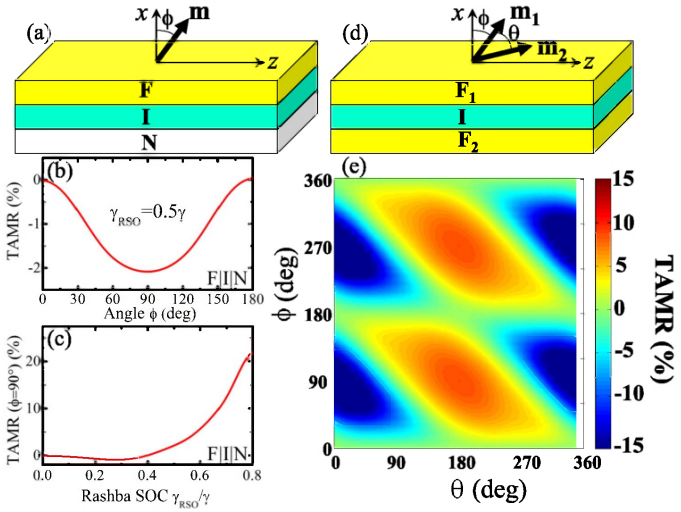

Figure 3.4: (a) The setup for the measurement of the out-of-plane TAMR in F|I|N semi-MTJ, defined by Eq. (3.6), as a function of the angle ϕ between the static magnetization of the F layer and the transport direction (the x-axis). In panel (b), the Rashba SOC at the F monolayer in contact with the tunnel barrier I is fixed at $\gamma_{\rm RSO} = 0.5\gamma$, while panel (c) shows TAMR ($\phi = 90°$) for different values of $\gamma_{\rm RSO}$. (d) The setup for the measurement of the out-of-plane TAMR in F|I|F MTJ, defined by Eq. (3.7), as a function of the magnetization orientation in each of the two F layers with respect to the transport direction. The TAMR depends on the absolute magnetization directions $\mathbf{m}_1$ and $\mathbf{m}_2$. In panel (e), the Rashba SOC of strength $\gamma_{\rm RSO} = 0.5\gamma$ is present at both F monolayers in contact with the tunnel barrier I. The F layers in both semi-MTJ and MTJ have finite thickness $d_F = 50$.

resistance with antiparallel configuration of magnetizations in the F layers of thickness $d_F = 50$, while $R_{\rm P}$ is the junction resistance when magnetizations are parallel. Since both of these resistances are dominated by the tunnel barrier potential, they are computed for clean junctions. [105] To model AlO_x tunnel barrier, we use binary alloy disorder characterized [105] by $\delta U_b = 0.5\gamma$.

3.2.1.2 TAMR and Spin Dephasing in Perpendicular Transport Through Interfaces with the Rashba SOC

To understand the correspondence between the strength of the Rashba SOC measured by the spin-dependent hopping parameter $\gamma_{\rm RSO}$ in Eq. (3.3) and the values

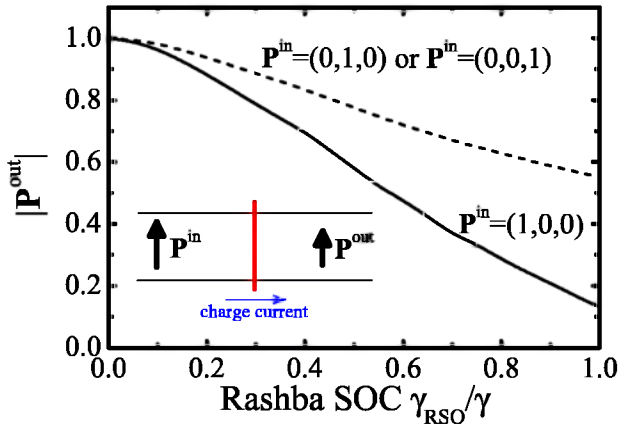

Figure 3.5: The magnitude $|\mathbf{P}^{\text{out}}|$ of the spin-polarization vector of outgoing charge current in the right N lead after fully $|\mathbf{P}^{\text{in}}| = 1$ spin-polarized current is injected from the left N lead traversing a monolayer with the Rashba SOC of strength γ_{RSO}. The spin-polarization vector $\mathbf{P}^{\text{in}}$ can point along three different axes of the coordinate system in Fig. 3.1, where $\mathbf{P}^{\text{in}} = (0,1,0)$ and $\mathbf{P}^{\text{in}} = (0,0,1)$ are parallel to the Rashba monolayer while $\mathbf{P}^{\text{in}} = (1,0,0)$ is orthogonal to the Rashba monolayer. The direction of $\mathbf{P}^{\text{out}}$ remains collinear with $\mathbf{P}^{\text{in}}$, as illustrated in the inset.

encountered in experimental devices, [48] we compute the so-called out-of-plane TAMR coefficient for F|I|N semi-MTJ which is defined as [65]

$$\text{TAMR}\,(\phi) = \frac{R(\phi) - R(0)}{R(0)}, \tag{3.6}$$

for the device setup illustrated in Fig. 3.4(a). In dc transport measurements of TAMR, the magnetization direction in F layer provides a control knob orienting the spin, while the magnetic anisotropy is determined by the interface symmetry rather than by the symmetry of the bulk materials. Here $R(0)$ is the resistance of semi-MTJ when static magnetization of its F layer is parallel to the x-axis as the direction of transport in Fig. 3.4(a), and $R(\phi)$ is the junction resistance when magnetization is rotated by an angle ϕ with respect to the x-axis within the xz-plane.

Figure 3.4(b) shows TAMR(ϕ) at fixed Rashba SOC, while the maximum TAMR($\phi = 90°$) vs. the strength of Rashba SOC is plotted in Fig. 3.4(c). Compared to the weak Rashba SOC in 2DEGs where typically $\gamma_{\text{RSO}} \simeq 0.01\gamma$, the interfacial Rashba SOC in

semi-MTJs has to be rather strong (as achieved in the recent experiments [48]) in order to generate observable TAMR. Since the interfacial SOI is linear in momentum, TAMR vanishes at the first order in $\gamma_{\rm RSO}$ after averaging over the Fermi sphere. However the ferromagnet contains local exchange field and a net transfer of angular momentum occurs at the second order, so that TAMR $\propto \gamma_{\rm RSO}^2$. This region of small TAMR occurs for $\gamma_{\rm RSO} \lesssim 0.4\gamma$ in Fig. 3.4(c), beyond which higher order processes start to play the role and TAMR increases faster with increasing $\gamma_{\rm RSO}$.

For F|I|F junctions, one can define the out-of-plane TAMR coefficient as [65]

$$\mathrm{TAMR}\,(\theta,\phi) = \frac{R(\theta,\phi) - R(\theta,0)}{R(\theta,0)}, \tag{3.7}$$

where the meaning of angles θ and ϕ is explained in Fig. 3.4(d). Since TAMR coefficient for F|I|N has only one angle argument, there is no ambiguity in using the same TAMR notation for both cases. The out-of-plane TAMR for F|I|F MTJ is shown in Fig. 3.4(e).

Unlike amply studied lateral spin transport in 2DEGs [4, 109] or interfaces [48] under the influence of the Rashba SOC, [4] very little is known about the effect of such interfaces on spin transport perpendicular to the plane, as illustrated by the measurement geometry in the inset of Fig. 3.5. We clarify their effect by using Eq. (3.4) to obtain the spin-polarization vector $\mathbf{P}^{\rm out}$ of the current in the right N lead after 100% spin-polarized charge current with $|\mathbf{P}^{\rm in}| = 1$ is injected from the left N lead. The result in Fig. 3.5 shows spin dephasing, where the outgoing spin polarization vector $\mathbf{P}^{\rm out}$ remains in the same direction as $\mathbf{P}^{\rm in}$, but with reduced magnitude $|\mathbf{P}^{\rm out}| < 1$. The degree of dephasing depends on the direction (perpendicular or parallel) of the initial spin polarization with respect to the Rashba interface.

3.3 NEGF Approach to Pumping by Precessing Magnetization

Theoretical studies of quantum charge pumping in noninteracting phase-coherent systems have been conducted using a variety of approaches. In the adiabatic regime, Brouwer scattering formula [100] is often used as an elegant geometrical description of the charge pumped per cycle in terms of the instantaneous scattering matrices of

the system. The adiabatic regime occurs when time-dependence of the driving field parameters is slow in comparison to the characteristic time scales of the system, such as the electron dwell time, so that electrons traverse the device as if the external potential landscape if frozen in time. Approaches beyond adiabatic regime include Floquet scattering theory, [111] iterative solutions of time-dependent states [112] and variations of the NEGF formalism. [103, 113] Moreover, the generality of the time-dependent NEGF framework [82] makes it a usual choice in the studies of pumping in the presence of strong Coulomb interactions. [114]

Among these approaches, Brouwer scattering formula [28] and NEGF formalism [87] have been employed to describe experiments on spin pumping by moving magnetization in magnetic multilayers. Unlike quantum charge pumping, the spin pumping in magnetic multilayers is *robust and ubiquitous* effect at room temperature. Nevertheless, the match between Brouwer scattering formula [28] and experiments on F|N multilayers is excellent due to pumped spin current being determined by the processes at the F|N interface. The scattering theory expresses pumped current by a remarkably simple formula

$$I^S\mathbf{P} = \frac{\hbar}{4\pi}\mathrm{Re}\, g^{\uparrow\downarrow}\, \mathbf{m}\times\frac{d\mathbf{m}}{dt}, \tag{3.8}$$

whose dc component is given by

$$I^{S_z} = \frac{\hbar\omega}{4\pi}\mathrm{Re}\, g^{\uparrow\downarrow}\sin^2\theta. \tag{3.9}$$

However, the derivation leading to this formula, as well as the very definition of the spin-mixing conductance [89] $g^{\uparrow\downarrow}$ (where $\mathrm{Re}\, g^{\uparrow\downarrow}$ is its real part) of the F|N interface, assumes absence of any spin-flips. [28]

Naively, one could numerically evaluate the Brouwer scattering formula for the whole device without introducing ill-defined $g^{\uparrow\downarrow}$ in the presence of interfacial SOCs. However, SOC renders all components of pumped spin or charge current time-dependent so that one has to compute the scattering matrix *at all times* within one period $\tau = 2\pi/\omega$ of the pumping cycle and then find the time-averaged value of pumped

currents. [96, 115] This is prohibitively expensive for 3D system composed of large number of atomic orbitals [such as the device in Fig. 3.1(a) whose Hamiltonian matrix is of the size 84000×84000], especially in the presence of disorder where additional averaging over impurity configurations is required. Although this could be achieved for smaller device sizes, we find that the maximum value of pumped current oscillating in time is orders of magnitude larger than its average value over one period in the case of MTJs which prevents the estimate of experimentally relevant time-averaged values from the numerical data.

The rotating frame approach, [86, 87] where pumping due to precessing magnetization is mapped onto a dc transport within a four-terminal device whose currents can be computed [87] using NEGFs, is also inapplicable in the presence of SOCs or other spin-flip mechanisms. This is due to the fact that the same unitary transformation (discussed in Sec. 3.3.2) which maps time-dependent Zeeman term in Eq. (3.1) to the one frozen at $t = 0$, generates new time-dependent SOC terms in the rotating frame.

As we showed in Chapter. 2, the retarded GF is governed by the following equation of motion [82]

$$i\frac{\partial}{\partial t}\mathbf{G}^r(t,t') - \mathbf{H}(t)\mathbf{G}^r(t,t') - \int_{-\infty}^{+\infty} dt''\, \mathbf{\Sigma}^r(t-t'')\mathbf{G}^r(t'',t') = \delta(t-t'), \tag{3.10}$$

where we use $\mathbf{G}^r$, $\mathbf{H}$(t), and $\mathbf{\Sigma}^r(t)$ notation to emphasize that these are matrices whose indices represent space and spin degrees of freedom. In noninteracting systems, the retarded self-energy $\mathbf{\Sigma}^r(t) = \sum_\beta \mathbf{\Sigma}^r_\beta(t)$ is simply the sum of self-energies $\mathbf{\Sigma}^r_\beta(t)$ due to leads β attached to the sample.

The lesser GF satisfies the Keldysh integral equation

$$\mathbf{G}^<(t,t') = \int_{-\infty}^{+\infty} dt_1 \int_{-\infty}^{+\infty} dt_2\, \mathbf{G}^r(t,t_1)\mathbf{\Sigma}^<(t_1,t_2)\mathbf{G}^a(t_2,t'), \tag{3.11}$$

where the advanced GF is related to the retarded one through $\mathbf{G}^r(t,t') = [\mathbf{G}^a(t',t)]^\dagger$. In the case of noninteracting systems, the lesser self-energy $\mathbf{\Sigma}^<(t) = \sum_\beta \mathbf{\Sigma}^<_\beta(t)$ is only due

to attached leads, which can be obtained from the retarded ones using $\mathbf{\Sigma}^{<}_{\alpha} = i f_{\alpha} \mathbf{\Gamma}_{\alpha}(t)$. Here f_{α} is the Fermi function of the macroscopic reservoir to which the lead α is attached at infinity and $\mathbf{\Gamma}_{\alpha}(t) = i(\mathbf{\Sigma}^{r}_{\alpha} - [\mathbf{\Sigma}^{r}_{\alpha}(t)]^{\dagger})$.

In stationary problems $\mathbf{G}^{r}(t,t')$ and $\mathbf{G}^{<}(t,t')$ depend on the time-difference $t-t'$, which allows to Fourier transform them into functions of a single energy argument and reduce the set of coupled integral and integro-differential equations to a set of algebraic equations. On the other hand, when the device Hamiltonian depends on time explicitly, one has to work with both times. Since directly solving equations Eq. (3.10) and (3.11) is cumbersome, it is advantageous to switch to a more convenient representation. The typical choices used for problems containing periodic time-dependent fields are: (*i*) the double-time Fourier transform [103, 116, 117]

$$\mathbf{G}^{r,<}(t,t') = \int\limits_{-\infty}^{+\infty} \frac{dE}{2\pi} \int\limits_{-\infty}^{+\infty} \frac{E'}{2\pi}\, e^{-iEt+iE't'}\, \mathbf{G}^{r,<}(E,E'); \tag{3.12}$$

(*ii*) the single Fourier transform [118] in the time difference $t-t'$

$$\mathbf{G}^{r,<}(t,t') = \int\limits_{-\infty}^{+\infty} \frac{dE}{2\pi}\, e^{-iE(t-t')}\, \mathbf{G}^{r,<}(t,E); \tag{3.13}$$

and (*iii*) the so-called Floquet matrix form $\mathbf{G}^{r,<}_{mn}(\omega)$ defined by [119]

$$\begin{aligned} \mathbf{G}^{r,<}_{n}(E) &= \int\limits_{-\infty}^{+\infty} dt_{\mathrm{rel}} \frac{1}{\tau} \int_{-\tau/2}^{\tau/2} dt_{\mathrm{av}} e^{iEt_{\mathrm{rel}}+in\Omega t_{\mathrm{av}}}\, \mathbf{G}^{r,<}(t,t'), \\ \mathbf{G}^{r,<}_{mn}(\omega) &= \mathbf{G}^{r,<}_{m-n}\left(E + \frac{m+n}{2}\Omega\right). \end{aligned} \tag{3.14}$$

The expressions in Eq. (3.14), where $t_{\mathrm{rel}} = t-t'$ and $t_{\mathrm{av}} = (t+t')/2$, exploit the periodicity condition $\mathbf{G}(t+\tau, t'+\tau) = \mathbf{G}(t,t')$ and are, therefore, GF counterpart of the Floquet matrix representation for periodically time-dependent Hamiltonian $\hat{H}(t+\tau) = \hat{H}(t)$ and its eigenstates (with the "Brillouin zone" of energies being $-\Omega/2 < E \leq \Omega/2$).

3.3.1 Exact Multiphoton Solution to Double-Time-Fourier-Transformed NEGFs

Here we adopt the double-time Fourier transform in Eq. (3.12), which has been used frequently to solve NEGF equations for non-adiabatic charge pumping [103] or spin pumping [116, 117] from the 2DEG with the Rashba SOC driven by time-periodic external fields. Due to the Floquet theorem, the double-time-Fourier-transformed retarded GF $\mathbf{G}^r(E,E')$ must take the form

$$\mathbf{G}^r(E,E') = \mathbf{G}^r(E,E+n\omega) = \mathbf{G}^r_n(E). \tag{3.15}$$

The coupling of energies E and $E+n\omega$ (n is integer) indicates how multiphoton exchange processes contribute toward the pumped current.

The double-time-Fourier-transformed Eq. (3.10) is given by:

$$\begin{aligned} &E\mathbf{G}^r(E,E+n\omega) - \int_{-\infty}^{+\infty} \frac{dE'}{2\pi}\, \mathbf{H}(E-E')\mathbf{G}^r(E',E+n\omega) \\ &-\mathbf{\Sigma}^r(E)\mathbf{G}^r(E,E+n\omega) = 2\pi\delta(n\omega) \end{aligned} \tag{3.16}$$

The Fourier transform of the Hamiltonian

$$\mathbf{H}(E) = 2\pi[\mathbf{H}_0\delta(E) + \mathbf{V}\delta(E+\omega) + \mathbf{V}^\dagger\delta(E-\omega)], \tag{3.17}$$

consists of the first term due to the time-independent part $\mathbf{H}_0$ of Eq. (3.1), while the other two terms are Fourier-transformed harmonic time-dependent part cast in the form $\mathbf{H}'(t) = \mathbf{V}e^{i\omega t} + \mathbf{V}^\dagger e^{-i\omega t}$. Here $\mathbf{V}$ is the matrix representation of the operator

$$\hat{V} = -\frac{1}{4}\sum_{\mathbf{i},ss'} \Delta_{\mathbf{i}} \sin\theta \left([\sigma_x]_{ss'} - i[\sigma_y]_{ss'}\right) \hat{c}^\dagger_{\mathbf{i}s}\hat{c}_{\mathbf{i}s'}, \tag{3.18}$$

extracted from Eq. (3.1) as the term carrying the periodic time-dependence.

By substituting Eq. (3.17) into Eq. (3.16) we arrive at the following equation:

$$[E\check{\mathbf{1}} + \check{\mathbf{\Omega}} - \check{\mathbf{H}} - \check{\mathbf{\Sigma}}^r(E+\check{\mathbf{\Omega}})]\check{\mathbf{G}}^r(E) = \hat{\mathbf{1}}. \tag{3.19}$$

To simplify the notation, we use

$$\check{\mathbf{H}} = \begin{pmatrix} \ddots & \cdots & \cdots & \cdots & \cdots & \cdots & \cdots \\ \cdots & \ddots & 0 & 0 & 0 & \cdots & \cdots \\ \cdots & \cdots & \mathbf{H}_0 & \mathbf{V} & 0 & \cdots & \cdots \\ \cdots & \cdots & \mathbf{V}^\dagger & \mathbf{H}_0 & \mathbf{V} & \cdots & \cdots \\ \cdots & \cdots & 0 & \mathbf{V}^\dagger & \mathbf{H}_0 & \cdots & \cdots \\ \cdots & \cdots & 0 & 0 & 0 & \ddots & \cdots \\ \cdots & \cdots & \cdots & \cdots & \cdots & \cdots & \ddots \end{pmatrix}, \tag{3.20}$$

and

$$\check{\mathbf{\Omega}} = \begin{pmatrix} \ddots & \cdots & \cdots & \cdots & \cdots & \cdots & \cdots \\ \cdots & -2\omega\mathbf{1} & 0 & 0 & 0 & \cdots & \cdots \\ \cdots & \cdots & -\omega\mathbf{1} & 0 & 0 & \cdots & \cdots \\ \cdots & \cdots & 0 & 0 & 0 & \cdots & \cdots \\ \cdots & \cdots & 0 & 0 & \omega\mathbf{1} & \cdots & \cdots \\ \cdots & \cdots & 0 & 0 & 0 & 2\omega\mathbf{1} & \cdots \\ \cdots & \cdots & \cdots & \cdots & \cdots & \cdots & \ddots \end{pmatrix}. \tag{3.21}$$

Here symbol $\check{\mathbf{A}}$ is used to denote a matrix which acts in the Hilbert space $\mathcal{H}_{\rm el} \otimes \mathcal{H}_{\rm ph}$, where the dimension of the Hilbert space of photons $\mathcal{H}_{\rm ph}$ is infinite. The unit matrix in the Hilbert space of a single electron $\mathcal{H}_{\rm el}$ is $\mathbf{1}$, and the unit matrix in $\mathcal{H}_{\rm el} \otimes \mathcal{H}_{\rm ph}$ is denoted by $\check{\mathbf{1}}$.

Since higher order multiphoton processes yield progressively smaller contribution to the pumped current, we restrict the dimension of $\mathcal{H}_{\rm ph}$ by considering up to $N_{\rm ph}$ photons. In this case, the dimensionality of $\mathcal{H}_{\rm ph}$ is $2N_{\rm ph}+1$ since one can have processes with no photon exchange $n = 0$ or the maximum of $n = N_{\rm ph}$ photons is absorbed or emitted. This means that if we keep only $N_{\rm ph} = 1$ processes, $\check{\mathbf{G}}(E)$ is a matrix of the dimension $l_{\rm sites} \times 2_s \times 3_{\rm ph}$ where $l_{\rm sites}$ is the number of lattice sites within the central region of devices in Fig. 3.1, 2_s takes into account the spin degrees of freedom, and $3_{\rm ph}$ is due to single (or no) photon exchange in the course of pumping.

The Keldysh equation (3.11) in this representation is written as:

$$\check{\mathbf{G}}^{<}(E) = \check{\mathbf{G}}^{r}(E)\check{\mathbf{\Sigma}}^{<}(E+\check{\mathbf{\Omega}})\check{\mathbf{G}}^{a}(E). \tag{3.22}$$

The knowledge of $\check{\mathbf{G}}^{<}(E)$ makes it possible to obtain the time-averaged total pumped charge current in lead α in the absence of any dc bias voltage

$$I_{\alpha} = \frac{e}{2N_{\mathrm{ph}}}\int_{-\infty}^{+\infty} dE\,\mathrm{Tr}\,[\check{\mathbf{\Gamma}}_{\alpha}\check{\mathbf{f}}\check{\mathbf{G}}^{r}\check{\mathbf{\Gamma}}\;\check{\mathbf{G}}^{a} - \check{\mathbf{\Gamma}}_{\alpha}\check{\mathbf{G}}^{r}\check{\mathbf{\Gamma}}\check{\mathbf{f}}\check{\mathbf{G}}^{a}], \tag{3.23}$$

where $\check{\mathbf{\Gamma}} = \sum_{\beta}\check{\mathbf{\Gamma}}_{\beta}$ and $\check{\mathbf{f}} = f(E+\check{\mathbf{\Omega}})$. Since the trace in the integrand, $\mathrm{Tr} \equiv \mathrm{Tr}_{\mathrm{el}}\mathrm{Tr}_{\mathrm{ph}}$, is summing over contributions from different photon exchange processes, the denominator includes $2N_{\mathrm{ph}}$ to avoid double counting. Note that the part of the trace operating in $\mathcal{H}_{\mathrm{ph}}$ space ensures the current conservation in our solution to NEGF equations. The analogous formula for the pumped spin current into lead α in the absence of any dc bias voltage is given by

$$I_{\alpha}^{S_i} = \frac{1}{4N_{\mathrm{ph}}}\int_{-\infty}^{+\infty} dE\,\mathrm{Tr}\,[\sigma_i(\check{\mathbf{\Gamma}}_{\alpha}\check{\mathbf{f}}\check{\mathbf{G}}^{r}\check{\mathbf{\Gamma}}\;\check{\mathbf{G}}^{a} - \check{\mathbf{\Gamma}}_{\alpha}\check{\mathbf{G}}^{r}\check{\mathbf{\Gamma}}\check{\mathbf{f}}\check{\mathbf{G}}^{a})]. \tag{3.24}$$

Equations (3.23) and (3.24) are the *central outcome* of our formalism and can be applied to arbitrary charge or spin pumping problem.

For the specific problem of pumping by precessing magnetization driven by microwaves, we take into account that $\hbar\omega \ll E_F$ and simplify Eq. (3.23) accordingly by expanding the Fermi function

$$\check{\mathbf{f}} = f(E_F)\check{\mathbf{1}} - \check{\mathbf{\Omega}}\partial f/\partial E. \tag{3.25}$$

This leads to the following *adiabatic* expression for pumped charge current:

$$I_{\alpha} = \frac{e}{2N_{\mathrm{ph}}}\mathrm{Tr}\,\{\check{\mathbf{\Gamma}}_{\alpha}(E_F)[\check{\mathbf{\Omega}}, \check{\mathbf{G}}^{r}(E_F)\check{\mathbf{\Gamma}}(E_F)]\check{\mathbf{G}}^{a}(E_F)\} \tag{3.26}$$

assuming zero temperature. The commutator

$$[\check{\mathbf{\Omega}}, \check{\mathbf{G}}^{r}(E_F)\check{\mathbf{\Gamma}}(E_F)] = \check{\mathbf{\Omega}}\check{\mathbf{G}}^{r}(E_F)\check{\mathbf{\Gamma}}(E_F) - \check{\mathbf{G}}^{r}(E_F)\check{\mathbf{\Gamma}}(E_F)\check{\mathbf{\Omega}} \tag{3.27}$$

allows us to make the notation more compact.

The time-averaged value of the pumped charge current is translated into the dc pumping voltage in an open circuit via

$$V_{\rm pump} = \frac{I_\alpha}{G(\theta)}, \tag{3.28}$$

which is the quantity measured in the recent experiments. [84, 46] Here $G(\theta)$ is the conductance of F|I|F or F|I|N junctions computed by tilting the *static* magnetization of the first F layer by an angle θ away from the z-axis and by applying the linear-response bias voltage between the N leads attached to the junction.

3.3.2 Comparison with the Rotating Frame Approach

In the absence of interactions causing spin-flips, such as the SOC, it is possible to convert the complicated time-dependent transport problem posed by the presence of precessing magnetization in the devices in Fig. 3.1 into the time-independent one by performing the unitary [86, 87, 120, 121] transformation of the Hamiltonian Eq. (3.1)

$$\hat{H}_{\rm rot} = \hat{U}\hat{H}(t)\hat{U}^\dagger - i\hbar\hat{U}\frac{\partial}{\partial t}\hat{U}^\dagger \equiv \hat{H}(t=0) - \frac{\omega}{2}\sigma_z. \tag{3.29}$$

Here the unitary operator is given by $\hat{U} = e^{i\omega\sigma_z t/2}$ for $\mathbf{m}(t)$ precessing counterclockwise. The transformed Hamiltonian $\hat{H}_{\rm rot}$ is time-independent in the frame rotating with the magnetization. The Zeeman term $\omega\sigma_z/2$, which emerges uniformly in the central region of devices in Fig. 3.1 and their N leads, will spin-split the bands of the N leads, thereby providing an intuitively appealing rotating frame [87] picture of pumping. In this picture, the N leads in the rotating frame are labeled by (α,σ) [$\alpha = L, R$ and $\sigma = \uparrow, \downarrow$] and they are biased by the electrochemical potential differences $\mu_L^\downarrow - \mu_R^\uparrow = \omega$ and $\mu_R^\downarrow - \mu_L^\uparrow = \omega$. Thus, these leads behave as effective half-metallic ferromagnets which emit or absorb only one spin species. The counter-propagating dc currents of spin-polarized electrons flowing from lead $\mu_\alpha^\downarrow$ to lead $\mu_\beta^\downarrow$, where electrons precess in the magnetic field of $\hat{H}(t=0)$ frozen at an angle θ with respect to the z-axis in order to enter into oppositely polarized lead, can be computed using NEGF, [87] transmission matrices, or the tunneling Hamiltonian approach. [86]

However, the rotating frame approach cannot be applied to systems containing SOCs (or any other source of spin flips) because unitary transformation would generate time-dependent SOC terms in Eq. (3.29). Nevertheless, it serves as a useful tool to compare the range of validity of different pumping formulas because the transport problem defined by Hamiltonian Eq. (3.1) with $\gamma_{\mathrm{RSO}} = \lambda_{\mathrm{ESO}} = 0$ can be solved exactly in the rotating frame. We start by first extending the NEGF-based formulas for pumped current in the rotating frame for devices with semi-infinite N leads treated in Ref. [87] to those with semi-infinite F leads. This eventually makes it possible to understand the origin of the orders of magnitude discrepancy between predictions made in Ref. [1] and Ref. [87] for the dc pumping voltages in the same type of MTJs.

Since the system in the rotating frame is stationary, NEGFs which depend there only on the time difference $t - t'$ can be Fourier transformed to work with functions of a single energy argument

$$\mathbf{G}^r_{\mathrm{rot}}(E) = [E\mathbf{1} - \mathbf{H}_{\mathrm{rot}} - \mathbf{\Sigma}^r_{\mathrm{rot}}(E)]^{-1}, \tag{3.30}$$

$$\mathbf{G}^<_{\mathrm{rot}}(E) = \mathbf{G}^r_{\mathrm{rot}}(E)\mathbf{\Sigma}^<_{\mathrm{rot}}(E)\mathbf{G}^a_{\mathrm{rot}}(E). \tag{3.31}$$

The retarded self energy in the rotating frame is obtained from the self-energy in the lab frame through a simple shift of its argument

$$\mathbf{\Sigma}^r_{\mathrm{rot},\alpha}(E) = \mathbf{\Sigma}^r_{\alpha}\left(E + \frac{1}{2}\omega\sigma_z\right). \tag{3.32}$$

The lesser self-energy in the rotating frame is then given by

$$\mathbf{\Sigma}^<_{\mathrm{rot},\alpha}(E) = if\left(E + \frac{1}{2}\omega\sigma_z\right)\mathbf{\Gamma}_{\alpha}\left(E + \frac{1}{2}\omega\sigma_z\right). \tag{3.33}$$

This leads to $\mathbf{G}^r_{\mathrm{rot}}(E) = \mathbf{G}^r(E+\omega\sigma_z/2)$ for the retarded GF and $\mathbf{G}^<_{\mathrm{rot}}(E) = i\sum_\beta \mathbf{G}^r_{\mathrm{rot}}\mathbf{f}\mathbf{\Gamma}_\beta(E+\omega\sigma_z/2)\mathbf{G}^a_{\mathrm{rot}}$ for the lesser one, where $\mathbf{f} = f(E+\omega\sigma_z/2)$ is the Fermi function in the rotating frame written as a 2×2 matrix in the spin space. Using $\mathbf{G}^r_{\mathrm{rot}}(E)$, $\mathbf{G}^<_{\mathrm{rot}}(E)$ and the following identity

$$i\mathbf{G}^r_{\mathrm{rot}}\mathbf{\Gamma}\left(E + \frac{1}{2}\omega\sigma_z\right)\mathbf{G}^a_{\mathrm{rot}} = \mathbf{G}^r_{\mathrm{rot}} - \mathbf{G}^a_{\mathrm{rot}}, \tag{3.34}$$

leads to an expression for pumped charge current in lead α

$$I_\alpha^{\mathrm{RF}} = e\int_{-\infty}^{+\infty} dE\,\frac{f_\downarrow - f_\uparrow}{2}\mathrm{Tr}\,[\mathbf{\Gamma}_\alpha\sigma_z\mathbf{G}^r_{\mathrm{rot}}(E)\mathbf{\Gamma}\mathbf{G}^a_{\mathrm{rot}}(E) - \mathbf{\Gamma}_\alpha\mathbf{G}^r_{\mathrm{rot}}(E)\mathbf{\Gamma}\sigma_z\mathbf{G}^a_{\mathrm{rot}}(E)], \tag{3.35}$$

where $\mathbf{\Gamma} = \sum_\alpha \mathbf{\Gamma}_\alpha$. Here $f_\uparrow = f(E+\omega/2)$ and $f_\downarrow = f(E-\omega/2)$ are the diagonal elements of $\mathbf{f}(E)$.

Thus, according to Eq. (3.35) only electrons whose energies fall into the interval $[E_F-\omega, E_F+\omega]$ participate in pumping (at zero temperature). Because of this, our more general solution Eq. (3.23), truncated $N_{\mathrm{ph}}=1$ to take into account only zero or single microwave photon exchange processes, gives identical result to Eq. (3.35) in the rotating frame approach assuming absence of spin-flip processes.

Similarly to Sec. 3.3.1, we can take into account that $\hbar\omega \ll E_F$ for microwave frequencies which yields pumped current in the adiabatic limit (where current is proportional to ω):

$$I_\alpha^{\mathrm{RF}} = \frac{e\omega}{2}\mathrm{Tr}\,\{\mathbf{\Gamma}_\alpha[\sigma_z, \mathbf{G}^r\mathbf{\Gamma}]\mathbf{G}^a\}. \tag{3.36}$$

Here all matrices are computed at E_F in the laboratory frame after we neglect their frequency dependence in the rotating frame by invoking the adiabatic condition $\omega \to 0$.

3.3.3 Comparison with Adiabatic Scattering Theory

In the adiabatic limit, one can also employ the Brouwer scattering formula [100] which gives the following expression for pumped charge current in terms of the derivatives of the instantaneous scattering matrix of the device:

$$I_\alpha^{\mathrm{ST}} = e\omega\int_0^\tau dt\,\mathrm{Tr}\left\{\sum_\beta \mathbf{S}_{\alpha\beta}(E_F,t)i\frac{\partial}{\partial t}\mathbf{S}^\dagger_{\alpha\beta}(E_F,t)\right\}. \tag{3.37}$$

We can recast Eq. (3.37) in terms of NEGFs for stationary transport (which depend on only one energy argument) by using the Fisher-Lee formula [122] for the scattering matrix

$$\mathbf{S}_{\alpha\beta}(E_F,t) = -\mathbf{1}\delta_{\alpha\beta} + i\sqrt{\mathbf{\Gamma}}_\alpha\cdot\mathbf{G}^r_{\alpha\beta}(E_F,t)\cdot\sqrt{\mathbf{\Gamma}}_\beta. \tag{3.38}$$

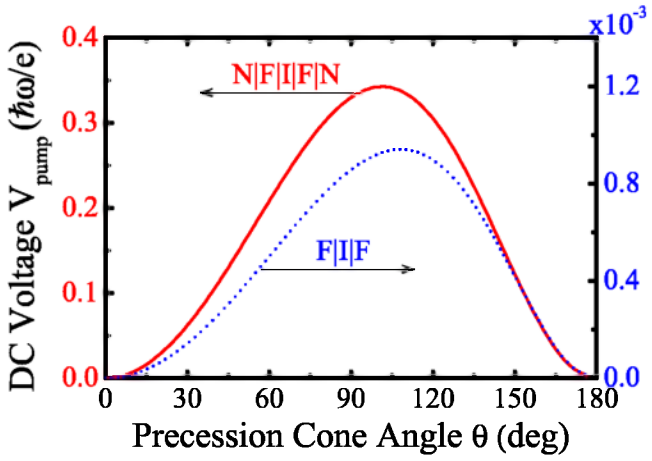

Figure 3.6: The comparison of the dc pumping voltage in a clean N|F|I|F|N junction with finite thickness F layers ($d_F = 50$) and a clean F|I|F junction whose F layers are semi-infinite. [1] The two curves can be computed using either the adiabatic NEGF formula in the rotating frame Eq. (3.36) or the adiabatic scattering formula Eq. (3.39). The parameters of these junction are chosen as $E_F = -2\gamma$, $\Delta = 2\gamma$, and $U_b = 9\gamma$.

Here $\mathbf{G}^r_{\alpha\beta}$ is the submatrix of $\mathbf{G}^r = [E - \mathbf{H}(t) - \mathbf{\Sigma}^r]^{-1}$ which connects edge monolayer of the device attached to lead α to the edge monolayer attached to lead β. The pumped current is then expressed as [103, 113]

$$I^{\mathrm{ST}}_{\alpha} = e\omega \int_0^{\tau} dt\, \mathrm{Tr}\left\{ \mathbf{\Gamma}_{\alpha} \mathbf{G}^r(E_F, t) i \frac{\partial}{\partial t} [\mathbf{\Gamma} \mathbf{G}^a(E_F, t)] \right\}. \tag{3.39}$$

This expression is equivalent to Eq. (3.36) due to the fact that frequency dependence of all NEGF quantities in the latter has been neglected.

Nevertheless, the application of Eq. (3.37) to clean MTJs with no spin-flip processes, where the scattering matrix was obtained directly by matching the wave functions across a simple model of Fe|MgO|Fe junction, has predicted [1] three orders of magnitude smaller pumping voltage than the rotating frame formula Eq. (3.36) applied to the same junction. [86, 87] Figure 3.6 explains that the origin of this discrepancy is not the particular formalism employed, but the assumed MTJ setup which contains semi-infinite F leads in Ref. [1] and finite thickness F layers in Ref. [86, 87]. Although the exact ratio of the voltage signals in these two models depends on the chosen values

of E_F and Δ at fixed U_b, the voltage signal in F|I|F MTJ model always remains below the one in the N|F|I|F|N model.

Both of these models describe unrealistic MTJs—there is no any kind of spin accumulation in the F layers in the F|I|F model, where semi-infinite F leads simply serve to define the spin-dependent scattering states, or spin accumulation persists throughout the finite thickness F layer in the N|F|I|F|N model. At the same time, the prediction of Ref. [1] is far below experimental values [84] ($\sim$ 1 nV predicted versus $\sim$ 1 μV measured at $\simeq$ 2 GHz FMR frequency), which points out to the need to take into account additional ingredients [88] in the MTJ model.

3.3.4 Comparison with Continued Fractions Solution to Double-Time-Fourier-Transformed NEGF Equations

The double-time-Fourier-transformed NEGF equations in Sec. 3.3.1 have been solved before for spin and charge pumping problems in an iterative manner using continued fractions. [103, 116, 117] Therefore, in this Section we discuss the advantage of our solution from Sec. 3.3.1 over continued fractions technique using the same F|I|F clean MTJs model (with F layers of finite thickness and no SOCs) from Fig. 3.6 as a test bed.

In the continued fractions method, one starts from the equation of motion for $\mathbf{G}^r_n(E)$ written as

$$\mathbf{G}^r_n(E) = 2\pi\delta(n\omega)\mathbf{g}^r_n(E) + \mathbf{G}^r_{n+1}(E)\mathbf{V}\mathbf{g}^r_n(E) + \mathbf{G}^r_{n-1}(E)\mathbf{V}^\dagger\mathbf{g}^r_n(E), \tag{3.40}$$

Here $\mathbf{g}^r(E) = [E - \mathbf{H}_0 - \mathbf{\Sigma}^r(E)]^{-1}$ is the Fourier transform of the retarded GF $\mathbf{g}^r(t-t')$ in the absence of the pumping potential $\mathbf{H}'(t) = 0$ which, therefore, depends only on the time difference $t - t'$ and can be Fourier transformed to a single energy argument. We also use notation $\mathbf{g}^r_n(E) = \mathbf{g}^r(E + n\omega)$, $\mathbf{G}^r_n = 2\pi\delta(0)\bar{\mathbf{G}}^r_n$ and $\mathbf{\Sigma}^r_0 = \mathbf{V}^\dagger\mathbf{g}^r_1\boldsymbol{\alpha}_1\mathbf{V} + \mathbf{V}\mathbf{g}^r_{-1}\boldsymbol{\beta}_{-1}\mathbf{V}^\dagger$. This equation is then solved [103, 116, 117] in an iterative manner using $\bar{\mathbf{G}}^r_0 = [(\mathbf{g}^r_0)^{-1} - \mathbf{\Sigma}^r_0]^{-1}$ for $n = 0$, $\bar{\mathbf{G}}^r_n = \bar{\mathbf{G}}^r_{n-1}\mathbf{V}^\dagger\mathbf{g}^r_n\boldsymbol{\alpha}_n$ for $n \geq 1$, and $\bar{\mathbf{G}}^r_n = \bar{\mathbf{G}}^r_{n+1}\mathbf{V}\mathbf{g}^r_n\boldsymbol{\beta}_n$ for $n \leq -1$. The coefficients $\boldsymbol{\alpha}_n$ and $\boldsymbol{\beta}_n$ are generated through continued fractions, $\boldsymbol{\alpha}_n(\mathbf{1} - \mathbf{V}^\dagger\mathbf{g}^r_{n+1}\boldsymbol{\alpha}_{n+1}\mathbf{V}\mathbf{g}^r_n) = \mathbf{1}$ and $\boldsymbol{\beta}_n(\mathbf{1} - \mathbf{V}\mathbf{g}^r_{n-1}\boldsymbol{\beta}_{n-1}\mathbf{V}^\dagger\mathbf{g}^r_n) = \mathbf{1}$.

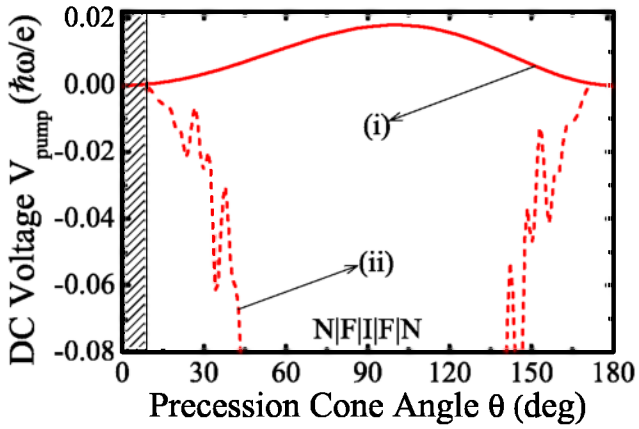

Figure 3.7: The dc pumping voltage in a clean F|I|F MTJ with finite thickness F layers ($d_F = 50$) in the absence of any SOCs computed using: (i) the exact solution Eq. (3.36) obtained via the rotating frame approach or, equivalently, full time-dependent solution Eq. (3.26) with one photon processes taken into account $N_{\rm ph} = 1$; and (ii) truncated (to $n = \pm 1$) continued fractions solution to double-time-Fourier-transformed NEGF equations which gives pumped charge current via Eq. (3.42). The shaded area marks the interval of precession cone angles $\theta \lesssim 10^\circ$ beyond which the continued fractions solution is not applicable anymore.

The knowledge of $\bar{\mathbf{G}}^r_n$ allows one to express the pumped charge current in lead α as [103, 117]

$$I^{\rm CF}_\alpha = \frac{1}{2\pi}\sum_{n=-\infty}^{+\infty}\int_{-\infty}^{+\infty} dE\, {\rm Tr}\left\{\mathbf{\Gamma}_\alpha(E)\bar{\mathbf{G}}^r_n(E)\mathbf{\Gamma}(E+n\omega)\bar{\mathbf{G}}^a_n(E)\right\}[f(E+n\omega)-f(E)]. \quad (3.41)$$

The summation over n in this formula shows how multiphoton exchange processes assist current pumping. This expression can be used for non-adiabatic external potentials, [103] while in the adiabatic regime $\omega \to 0$ and at zero temperature the difference of Fermi functions is replaced by $f(E+n\omega) - f(E) \approx \omega\delta(E - E_F)$, so that only the Fermi level states carry the pumped current.

Although one can in principle solve continued fractions for $\boldsymbol{\alpha}_n$ and $\boldsymbol{\beta}_n$ to arbitrary order n, this is virtually impossible to execute for sizable 3D devices (such as the ones in Fig. 3.1) due to the need to compute numerous submatrices of $\mathbf{G}^r_{n-1}$ required to obtain $\mathbf{G}^r_n$. Instead, most of recent applications [116, 117] of the continued fractions solution to spin pumping in 2DEGs with the Rashba SOC have utilized only a few fractions ($|n| \leq 3$). In other words, the convergence of the sum over n in Eq. (3.41)

can be achieved quickly only for small amplitude of the external potential $||\mathbf{V}|| \to 0$ which ensures that higher order fractions are negligible. The lowest order $n = 0, \pm 1$ version of Eq. (3.41) simplifies to [117]

$$I_\alpha^{\rm CF} = \frac{1}{2\pi}\int\limits_{-\infty}^{+\infty} dE\,{\rm Tr}\,\{\mathbf{\Gamma}_\alpha(E)\mathbf{g}^r(E)\mathbf{V}^\dagger\mathbf{A}_1(E)\mathbf{V}\mathbf{g}^a(E)\}[f(E+\omega)-f(E)] + \frac{1}{2\pi}\int\limits_{-\infty}^{+\infty} dE\,{\rm Tr}\,\{\mathbf{\Gamma}_\alpha(E)\mathbf{g}^r(E)\mathbf{V}\mathbf{A}_{-1}(E)\mathbf{V}^\dagger\mathbf{g}^a(E)\}[f(E-\omega)-f(E)], \tag{3.42}$$

where $\mathbf{A}_n(E) = \mathbf{g}_n^r(E)\mathbf{\Gamma}(E+n\omega)\mathbf{g}_n^a(E)$.

Figure 3.7 shows that Eq. (3.42) is insufficient to analyze pumping by magnetization dynamics in MTJs since it fails to reproduce the exact solution for dc pumping voltage in junctions with no spin flips given by Eq. (3.35) in the rotating frame approach. Because the strength of the pumping potential in Eq. (3.18) is determined by $\Delta\sin\theta$, pumping voltage computed from Eq. (3.42) can be valid only at small angles cone angles ($\theta \lesssim 10^\circ$ in Fig. 3.7; this interval would be somewhat larger in F|N multilayers). Even at small cone angles, the prediction $I_\alpha^{\rm CF} \propto \Delta^2\sin^2\theta$ stemming from Eq. (3.42), which is in accord with the "standard model" Eq. (3.9), becomes incorrect in the presence of SOC where I_α vs. θ turns out to be quite different (see Sec. 3.4). We note that one could try to use more general Eq. (3.41), but this would require to compute continued fractions $\boldsymbol{\alpha}_n$ and $\boldsymbol{\beta}_n$ to high order n, unlike our *non-perturbative* solution Eq. (3.23) which reproduces the exact result in the rotating frame using only $n = 0, \pm 1$ in the multiphoton GF in Eq. (3.15).

3.4 The Effect of Interfacial Rashba SOC on the Voltage Signal of Spin Pumping in F|I|N and F|I|F Junctions

Equation (3.26) applied to clean F|I|N junctions with interfacial Rashba SOC allows us to understand how the dc pumping voltage can appear in such semi-MTJs at the adiabatic level. The Rashba SOC is present at the F|I interface (i.e., at the last

monolayer of the precessing F layer that is in contact with the tunnel barrier I) and intrinsically participates in the pumping process. This is in contrast to other recent theories [91] of spin pumping in F|N multilayers where SOC is located away from the precessing F layer and, therefore, is not essential to understand the pumping effect itself.

Figure 3.8(a) demonstrates that dc pumping voltage $V_{\rm pump} \propto \hbar\omega$ in F|I|N junctions emerges as soon as the Rashba SOC is "turned on". This could explain signal observed experimentally [46] in F|I|N junctions, in contrast to previous attempts [86, 87] which have predicted $V_{\rm pump} \propto (\hbar\omega)^2$. For comparison, Fig. 3.8(b) shows how the presence of strong Rashba SOC directly at the F|I interface also enhances $V_{\rm pump}$ in conventional F|I|F MTJs.

Figure 3.8(d) provides additional insight into the charge pumping mechanism where we show that the dc pumping voltage in F|I|N semi-MTJs requires to include exchange of up to ten microwave photons in order to reach its asymptotic value. However, since that asymptotic value of $V_{\rm pump}$ is only about 10% higher than the result plotted in Figs. 3.8(a) and 3.8(c), where only zero or single microwave photon exchange processes are taken into account, we employ only this lowest order approximation in the rest of this chapter since [$N_{\rm ph} = 1$ in Eq. (3.26) is computationally much less expensive than $N_{\rm ph} = 10$].

The unique experimentally testable signature of charge pumping in F|I|N semi-MTJs that we predict in Fig. 3.8(c) is angular dependence of $V_{\rm pump}(\theta)$ which changes sign and it is, therefore, quite different from the usual $V_{\rm pump}(\theta)$ for F|I|F MTJs shown in Fig. 3.6. The charge pumping in semi-MTJs with weak interfacial Rashba SOC can be obtained analytically using the second-order perturbation expansion of GF entering Eq. (3.37) as the version of the Brouwer scattering formula:

$$\begin{aligned} I_L &= e\hbar\omega D^L \int_0^\tau dt\, \mathbf{e}_z \cdot \mathbf{m}(t) \left[\mathbf{m}(t) \times \frac{\partial \mathbf{m}(t)}{\partial t}\right] \\ &= e\hbar\omega D^L \left[\cos^2\chi - \frac{1}{2}\sin^2\chi\right] \sin^2\theta\cos\theta. \end{aligned} \tag{3.43}$$

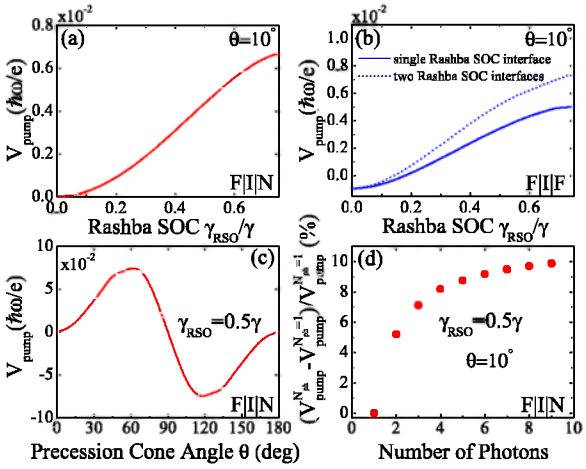

Figure 3.8: The dc pumping voltage in clean F|I|N semi-MTJ [panels (a),(c) and (d) and F|I|F MTJ [panel (b)] with finite thickness ($d_F = 50$) F layers and non-zero interfacial Rashba SOC. The Rashba SOC is located within the last monolayer of the precessing F layer that is in contact with the tunnel barrier I in (a),(c),(d) [as illustrated in Fig. 3.1(a)], or such edge monolayers are present in the left or both F layers [as illustrated in Fig. 3.1(b)] in panel (b). The data in panels (a),(b),(c) is computed by considering only one microwave photon exchange processes, while in panel (d) we show correction to this result when up to 9 microwave photons are taken into account in Eq. (3.26) applied to F|I|N semi-MTJ.

Here χ is the angle between the axis around which the magnetization precesses and the direction of transport [in the case of our device in Fig. 3.1(b), $\cos^2\chi - \frac{1}{2}\sin^2\chi = -1/2$]. The expression for $D^L \propto \gamma_{\rm RSO}^2$ determining the magnitude of the pumped current is obtained a follows. In the absence of Rashba SOC, the retarded GF of F|I|N semi-MTJ can be written as

$$\mathbf{G}_0^r = \mathbf{g}_0 + \mathbf{g}_1 \mathbf{m}\cdot\vec{\sigma}. \tag{3.44}$$

Starting from this expression, the second-order perturbation theory in the powers of $\gamma_{\rm RSO}$ applied to GF in the Brouwer scattering formula, recast as Eq. (3.37), yields

$$\begin{aligned} D^L \;=\; & 4\sum_\alpha \mathrm{Re}\,\{\mathrm{Tr}\,[\mathbf{\Gamma}_\alpha \mathbf{g}_0 V_\alpha \mathbf{g}_1 V_\alpha \mathbf{g}_1 \mathbf{\Gamma} \mathbf{g}_1^\dagger \\ & -\mathbf{\Gamma}_\alpha \mathbf{g}_1 V_\alpha \mathbf{g}_1 V_\alpha \mathbf{g}_0 \mathbf{\Gamma} \mathbf{g}_1^\dagger - \mathbf{\Gamma}_\alpha \mathbf{g}_1 V_\alpha \mathbf{g}_1 \mathbf{\Gamma} \mathbf{g}_0^\dagger V_\alpha \mathbf{g}_1^\dagger \\ & -\mathbf{\Gamma}^\alpha \mathbf{g}_1 V_\alpha \mathbf{g}_1 \mathbf{\Gamma} \mathbf{g}_1^\dagger V_\alpha \mathbf{g}_0^\dagger]\}, \end{aligned} \tag{3.45}$$

Here the vector $\mathbf{V} = (V_x, V_y, V_z)$, which contains the strength of the Rashba SOC $\gamma_{\rm RSO}$,

is defined by $\hat{H}_{\mathrm{RSO}} = \mathbf{e}_x \cdot (\mathbf{V} \times \vec{\sigma})$ where $\hat{H}_{\mathrm{RSO}}$ is the Rashba Hamiltonian [i.e., the fourth term in Eq. (3.1)].

In Fig. 3.8(c), we assume strong interfacial Rashba SOC ($\gamma_{\mathrm{RSO}} = 0.5\gamma$) so that $V_{\mathrm{pump}}(\theta)$ vs. θ plotted there deviates from this analytical expression $V_{\mathrm{pump}}(\theta) \propto \sin^2\theta\cos\theta/G(\theta)$. Note that for small TAMR [$\gamma_{\mathrm{RSO}} \lesssim 0.4$ according to Fig. 3.4(c)] $G(\theta)$ can be considered nearly constant, so that $V_{\mathrm{pump}}(\theta) \propto \sin^2\theta\cos\theta$ according to Eq. (3.43).

The second-order nature of this process can be illustrated using real space Feynman paths where electron impinging onto the tunnel barrier is reflected with rotation of its spin introduced by the Rashba interface. Therefore, it has to travel twice through this monolayer to reach the right N lead. This picture is encoded quantitatively in the expression for D^L in Eq. (3.45) which contains $\propto \gamma_{\mathrm{RSO}}^2$ dependence. We note that the same $\propto \gamma_{\mathrm{RSO}}^2$ and angular dependence has also been predicted [61] for linear-response STT in F|I|N semi-MTJs with the interfacial Rashba SOC, which is in accord with reciprocal nature of STT and spin pumping. That is, observation of one of these two effects implies, by Onsager reciprocal relations, the existence of the other effect. [96]

3.5 Disorder and Extrinsic SOC Effects on Charge Pumping in Magnetic Tunnel Junctions

In this Section, we analyze how disorder and the corresponding extrinsic SOC affects dc pumping voltage in conventional F|I|F MTJs. To isolate their effects only, we assume that interfacial intrinsic Rashba SOC studied in Sec. 3.4 is absent. When extrinsic SOC is negligible, we find that dc pumping voltage plotted in Fig. 3.9 (a) is increasing in the quasiballistic transport regime (characterized by the Fano factor $F < 1/3$ in Fig. 3.2) and then decreases once the diffusive regime (characterized by the Fano factor $F = 1/3$ in Fig. 3.2) is reached. At first sight, this initial increase of V_{pump} with increasing disorder is counterintuitive, even though conductance also decreases with disorder, since pumped current appears to be increasing with W. However, it can be explained qualitatively as being due to random electron scattering in real space which

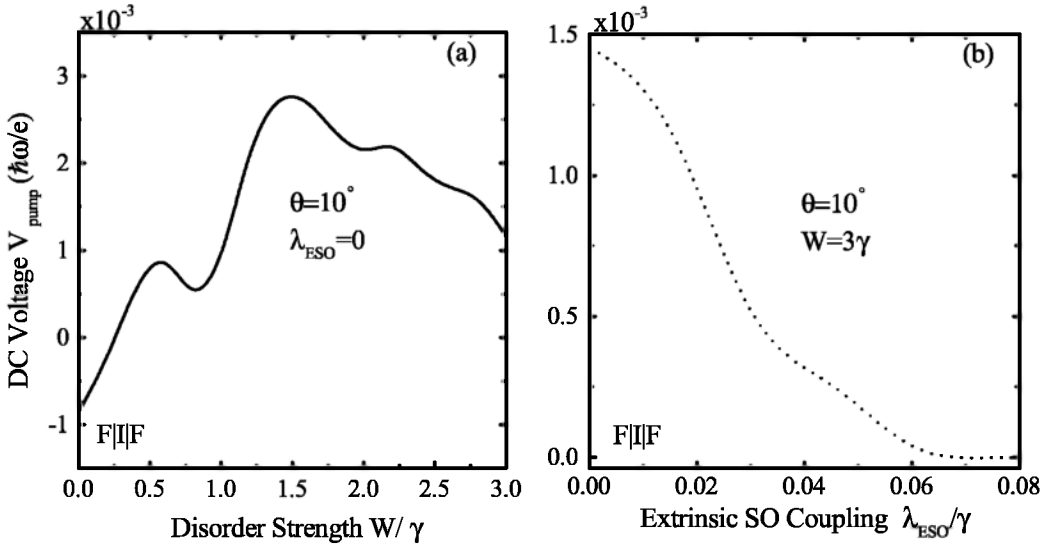

Figure 3.9: The dc pumping voltage in F|I|F MTJs of finite thickness F layers ($d_F = 50$) with: (a) static disorder of strength W within F layers; (b) static disorder of strength $W = 3\gamma$ ensuring diffusive transport regime (see Fig. 3.2) and the extrinsic SOC of strength $\lambda_{\rm ESO}$ determined by such disorder via Eq. (3.2). The tunnel barrier I in both panels contains binary alloy disorder $\delta U_b = 0.5\gamma$. The spin-diffusion length corresponding to the values of $\lambda_{\rm ESO}$ is shown in the inset of Fig. 3.3.

prolongs the average time an electron remains in the left F layer where it can interact with photons of the microwave pumping field. Similar enhancement of pure spin current pumping has been noticed in the diffusive regime in related device setups. [117, 120]

The same disorder used in Fig. 3.9(a) is related to the extrinsic SOC through Eq. (3.2), which becomes a relevant effect if $\lambda_{\rm ESO}$ is renormalized by the band structure effects to become stronger than its vacuum value by several orders of magnitude. [92] Unlike the interfacial Rashba SOC studied in Sec. 3.4 which brings novel effects into the pumping mechanism, the extrinsic SOC simply reduces the dc pumping voltage in F|I|F junctions, as shown in Fig. 3.9(b). Our unified quantum transport treatment of spin pumping [Fig. 3.9(b)] and spin diffusion (Fig. 3.3) shows that voltage signal of spin pumping in MTJs is brought to negligible value when the ratio of the F layer thickness to $L_{\rm sf}$ is $d_F/L_{\rm sf} \simeq 5$. We emphasize that our fully quantum-mechanical treatment of the conduction electrons is necessary to understand such interplay of spin pumping, spin accumulation around interfaces [88] and spin diffusion in MTJs since

conventional approach [28] developed for F|N multilayers, where pumping is treated quantum-mechanically while subsequent propagation of spins and charges is described semiclassically using phenomenological mean free path and spin-diffusion length, is inapplicable to systems containing tunnel barriers where spin accumulation is not well-defined. [38]

3.6 Summary of Chapter

In this chapter, we have derived an exact and efficient (for computational implementations) solution to the equations of motion for the double-time-Fourier-transformed NEGFs in the presence of time-periodic external potential. Unlike continued fractions solution [103] for the same equations, which is often applied to problems of spin [117] and charge pumping [103] by computing only a finite number of continued fractions while assuming that the amplitude of time-periodic external potential is small, our formulas for pumped charge Eq. (3.23) and spin Eq. (3.24) currents in the leads of a multiterminal devices can be used for *arbitrary* strength of periodic driving potential (thereby covering both perturbative [117, 116] and non-perturbative regimes) or frequency (thereby covering both adiabatic and non-adiabatic pumping regimes). They can also be applied to any noninteracting quantum system which is brought out of equilibrium by external field that exchanges photons with propagating electrons [123].

This fully quantum-mechanical treatment of pumping processes and subsequent propagation of electrons is applied to the problem of charge pumping by precessing magnetization in the single F layer of F|I|N semi-MTJ or F|I|F conventional MTJ in the presence of intrinsic Rashba SOC at the F|I interface. The non-zero interfacial Rashba SOC, located [95] within the edge monolayer of the precessing F in contact with the tunnel barrier I, generates non-zero dc pumping voltage in F|I|N semi-MTJ at the adiabatic level (i.e., pumping voltage is proportional to the microwave frequency ω). This could explain observations of voltage signal with such properties in the recent experiments [46] on microwave-driven F|I|N semi-MTJs where previously formulated theories [86, 87] have found only a very small non-adiabatic ($\propto \omega^2$) voltage

signal. We further predict a *unique signature* of this charge pumping phenomenon—the pumped charge current changes sign ($I \propto \sin^2\theta\cos\theta$ for small $\gamma_{\rm RSO}$) as the function of the precession cone angle θ so that measuring the corresponding dc pumping voltage ($V_{\rm pump} \propto \sin^2\theta\cos\theta$ for small $\gamma_{\rm RSO}$) would confirm our prediction.

Besides offering quantitative description of charge and spin pumping processes, our solution for NEGFs whose two energy arguments are connected by the Floquet theorem describing multiphoton emission and absorption processes also provides new physical insights: (*i*) in the absence of SOCs, emission or absorption of *one photon* is sufficient to match the exact solution in the rotating frame; [87, 120] (*ii*) in the presence of Rashba SOC, exchange of up to ten photons is required to reach asymptotic value of the pumped currents. Nevertheless, this asymptotic value is only about 10% larger than the value obtained using just one photon processes in the presence of SOCs.

We also find that static disorder can increase the dc pumping voltage in F|I|F MTJs with finite thickness F layers in the quasiballistic transport regime where scattered electrons spend more time within the precessing F layer to interact with microwave photons. The extrinsic SOC determined by the impurity potential responsible for the diffusive transport regime causes spin relaxation which ultimately diminishes the pumping voltage in F|I|F MTJs to zero when the spin-diffusion length is about five times shorter than the thickness of the F layers.

Chapter 4

MICROWAVE-DRIVEN FERROMAGNET–TOPOLOGICAL-INSULATOR HETEROSTRUCTURES: THE PROSPECT FOR GIANT SPIN BATTERY EFFECT AND QUANTIZED CHARGE PUMP DEVICES

4.1 Motivation

The recent experimental confirmation of two- (2D) and three-dimensional (3D) topological insulators [124] (TIs), such as HgTe/(Hg,Cd)Te quantum wells [24, 25] of certain width and compounds involving bismuth, [124] respectively, has attracted considerable attention from both basic and applied research communities. The TIs introduce an exotic quantum state of matter brought by spin-orbit (SO) coupling effects in solids which is characterized by a topological invariant that is insensitive to microscopic details and robust with respect to weak disorder. [124] Thus, although TIs have energy gap in the bulk, their topological order leads to quantized physical observables in the form of the number of gapless edge (in 2D) or surface (in 3D) states modulo two—TIs have an odd number of edge (surface) states in contrast to trivial band insulators with even (i.e., typically zero) number of such states.

As regards applications, the channeling of spin transport [125] through one-dimensional (1D) counter-propagating spin-filtered (i.e., "helical") edge states of 2D TIs, where the time-reversal invariance forces electrons of opposite spin to flow in opposite directions, opens new avenues to realize semiconductor spintronic devices based on manipulation of coherent spin states. [10] For example, fabrication of spin-field-effect transistor [126] (spin-FET), where spin precession in the presence of SO coupling is used to switch between on and off current state, requires to prevent entanglement of spin and orbital electronic degrees of freedom in wires with many conducting channels

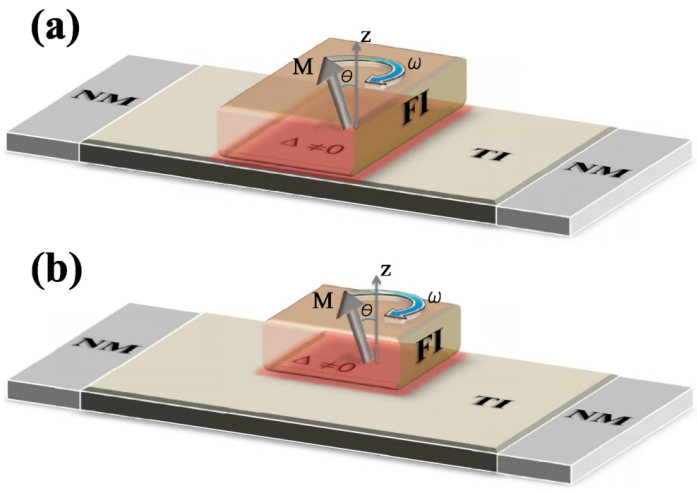

Figure 4.1: The proposed heterostructures consist of a 2D topological insulator (TI) attached to two normal metal (NM) electrodes where the ferromagnetic insulator (FI) with precessing magnetization (with cone angle θ) under the FMR conditions induces via the proximity effect a time-dependent exchange field $\Delta \neq 0$ in the TI region underneath. In the absence of any applied bias voltage, these devices pump pure spin current into the NM electrodes in setup (a) or both charge and spin current in setup (b).

or different amounts of spin precession along different trajectories, both of which make it impossible to achieve the perfect off state of spin-FET.

Some of the key questions posed by these rapid developments are: How can spintronic *heterostructures* [124] exploit TI edge or surface states in the presence of interfaces with other materials [127] or internal and external magnetic fields [73] used to manipulate spins while breaking the time-reversal invariance? How can the 2D TI phase be detected by conventional measurements of *quantized* charge [78] transport quantities?

For example, the 2D TI is operationally defined as a system which exhibits the quantum spin Hall effect (QSHE) with quantized spin conductance (ratio of transverse pure spin current to longitudinally applied bias voltage). However, this quantity is difficult to observe, and reported measurements [24, 25] of electrical quantities probing

the edge state transport in HgTe-based multiterminal devices have exhibited poor precision of quantization when contrasted with the integer quantum Hall effect—a close cousin of QSHE used in metrology.

In this chapter we propose two ferromagnet-TI (FM-TI) heterostructures, illustrated in Fig. 4.1, where an island of a ferromagnetic insulator (FI) is deposited over the surface of 2D TI modeled either as graphene nanoribbon (GNR) [128] with intrinsic SO coupling [95] or HgTe-based strip. [24, 25, 129] The precessing magnetization of FI under the ferromagnetic resonance conditions [85] (FMR) will induce a time-dependent exchange field in the TI region underneath via the magnetic proximity effect. [73] Using the nonequilibrium Green function (NEGF) approach [87, 130, 120] to pumping by precessing magnetization in the frame rotating with it, developed in Sec. 3.3.2, we demonstrate that setup in Fig. 4.1(a) makes possible efficient conversion of microwave radiation into *pure* spin current (Fig. 4.2) whose magnitude can reach a quantized value $eI^{S_z}/\hbar\omega = 2 \times e/4\pi$ even at small increase of the precession cone angle (i.e., microwave power input [46]) away from zero. On the other hand, the device in Fig. 4.1(b) generates charge current I (in addition to spin current) which is quantized $eI/\hbar\omega = e^2/h$ for a wide range of precession cone angles (Fig. 4.3). This offers an alternative operational definition of the 2D TI in terms of electrical measurements or a microwave detector which is more sensitive than conventional FM-NM spin pumping devices. [46] We also analyze the effect of disorder and device size on the quantization of pumped currents.

This chapter is organized as follows. In Sec. 4.2, we discuss how to compute pumped currents due to precessing magnetization by mapping such time-dependent quantum transport problem to an equivalent four-terminal DC circuit in the frame rotating with magnetization where steady-state spin and charge currents are evaluated using NEGFs in that frame. Section 4.3 covers pure spin current pumping in the heterostructure of Fig. 4.1(a), while Sec. 4.4 shows how charge current is pumped in the second type of proposed heterostructure in Fig. 4.1(b). We explain the origin and the corresponding requirements for these pumped currents to be quantized in Sec. 4.5.

We conclude in Sec. 4.6.

4.2 Rotating Frame Approach to Spin Pumping in FM-TI Heterostructures

The simplest model for the 2D TI central region of the device in Fig. 4.1 is GNR with intrinsic SO coupling, as described by the effective single π-orbital tight-binding Hamiltonian:

$$\hat{H}^{\text{lab}}_{\text{GNR}}(t) = \sum_{\mathbf{i}} \hat{c}^{\dagger}_{\mathbf{i}} \left(\varepsilon_{\mathbf{i}} - \frac{\Delta_{\mathbf{i}}}{2} \mathbf{m}_{\mathbf{i}}(t) \cdot \vec{\sigma} \right) \hat{c}_{\mathbf{i}} - \gamma \sum_{\langle \mathbf{ij} \rangle} \hat{c}^{\dagger}_{\mathbf{i}} \hat{c}_{\mathbf{j}} + \frac{2i}{\sqrt{3}} \gamma_{\text{SO}} \sum_{\langle\langle \mathbf{ij} \rangle\rangle} \hat{c}^{\dagger}_{\mathbf{i}} \vec{\sigma} \cdot (\mathbf{d_{kj}} \times \mathbf{d_{ik}}) \hat{c}_{\mathbf{j}}. \tag{4.1}$$

Here $\hat{c}_{\mathbf{i}} = (\hat{c}_{\mathbf{i}\uparrow}, \hat{c}_{\mathbf{i}\downarrow})^T$ is the vector of spin-dependent operators ($\uparrow$, $\downarrow$ denotes electron spin) which annihilate electron at site $\mathbf{i} = (i_x, i_y)$ of the honeycomb lattice, and $\vec{\sigma} = (\sigma_x, \sigma_y, \sigma_z)$ is the vector of the Pauli matrices. The nearest-neighbor hopping γ is assumed to be the same on the honeycomb lattice of GNR and square lattice of semi-infinite NM leads. The third sum in Eq. (4.1) is non-zero only in the GNR regions where it introduces the intrinsic SO coupling compatible with the symmetries of the honeycomb lattice. [128, 95] The SO coupling, which is responsible for the band gap [128] $\Delta_{\text{SO}} = 6\sqrt{3}\gamma_{\text{SO}}$, acts as spin-dependent next-nearest neighbor hopping where $\mathbf{i}$ and $\mathbf{j}$ are two next-nearest neighbor sites, $\mathbf{k}$ is the only common nearest neighbor of $\mathbf{i}$ and $\mathbf{j}$, and $\mathbf{d_{ik}}$ is a vector pointing from $\mathbf{k}$ to $\mathbf{i}$. For simplicity, [128, 130] we assume unrealistically [95] large value for $\gamma_{\text{SO}} = 0.03\gamma$. We use the on-site potential $\varepsilon_i \in [-W/2, W/2]$ as a uniform random variable to model the isotropic short-range spin-independent static impurities.

In both GNR and HgTe models, the coupling of itinerant electrons to collective magnetic dynamics is described through the exchange potential $\Delta_{\mathbf{i}}$. This is assumed to be non-zero only within the region of the TI which is covered by the FI island with precessing magnetization where the proximity effect [73] generates the time-dependent Zeeman term adiabatically. The magnitude of the effective exchange potential is selected to be $\Delta = 0.1\gamma$ in GNR model and $\Delta = 0.004$ eV in HgTe model for 2D TI.

The components of the rotating exchange field in the plane of the 2D TI, $\Delta_{\mathbf{i}} m_{\mathbf{i}}^{x}/2$ and $\Delta_{\mathbf{i}} m_{\mathbf{i}}^{y}/2$, generate energy gap by removing the edge states from the Δ_{SO} gap of the TI region below the FI island (in both models we assume $\Delta < \Delta_{\mathrm{SO}}$).

The effective tight-binding Hamiltonian [129] for the HgTe/CdTe quantum wells (applicable for small momenta around the Γ point) is defined on the square lattice with four orbitals per site:

$$\begin{aligned}
\hat{H}^{\mathrm{lab}}_{\mathrm{HgTe}}(t) &= \sum_{\mathbf{i}} \hat{c}_{\mathbf{i}}^{\dagger} \left[\begin{pmatrix} \varepsilon_{\mathbf{i}}^{s} & 0 & 0 & 0 \\ 0 & \varepsilon_{\mathbf{i}}^{p} & 0 & 0 \\ 0 & 0 & \varepsilon_{\mathbf{i}}^{s'} & 0 \\ 0 & 0 & 0 & \varepsilon_{\mathbf{i}}^{p'} \end{pmatrix} - \frac{\Delta_{\mathbf{i}}}{2} \mathbf{m}_{\mathbf{i}}(t) \cdot \vec{\sigma} \right] \hat{c}_{\mathbf{i}} \\
&+ \sum_{\mathbf{i}} \hat{c}_{\mathbf{i}}^{\dagger} \begin{pmatrix} V_{ss} & V_{sp} & 0 & 0 \\ -V_{sp}^{*} & V_{pp} & 0 & 0 \\ 0 & 0 & V_{ss} & V_{sp}^{*} \\ 0 & 0 & -V_{sp} & V_{pp} \end{pmatrix} \hat{c}_{\mathbf{i}+\mathbf{e}_x} + \mathrm{H.c.} \\
&+ \sum_{\mathbf{i}} \hat{c}_{\mathbf{i}}^{\dagger} \begin{pmatrix} V_{ss} & iV_{sp} & 0 & 0 \\ iV_{sp}^{*} & V_{pp} & 0 & 0 \\ 0 & 0 & V_{ss} & -iV_{sp}^{*} \\ 0 & 0 & -iV_{sp} & V_{pp} \end{pmatrix} \hat{c}_{\mathbf{i}+\mathbf{e}_y} + \mathrm{H.c.}
\end{aligned} \tag{4.2}$$

Here vector $\hat{c}_{\mathbf{i}} = (c_{\mathbf{i}}^{s}, c_{\mathbf{i}}^{p}, c_{\mathbf{i}}^{s'}, c_{\mathbf{i}}^{p'})^{T}$ contains four operators which annihilate an electron on site $\mathbf{i}$ in quantum states $|s,\uparrow\rangle$,$|p_x + ip_y,\uparrow\rangle$, $|s,\downarrow\rangle$, $|-(p_x - ip_y),\downarrow\rangle$, respectively. The Fermi energy is uniform throughout the device in Fig. 4.1, while the on-site matrix elements, $\varepsilon_{\mathbf{i}}^{s} = \varepsilon_{\mathbf{i}}^{s'} = E_s$ and $\varepsilon_{\mathbf{i}}^{p} = \varepsilon_{\mathbf{i}}^{p'} = E_p$, are tuned by the gate potential to ensure that TI regions are insulating and the NM electrodes described by the same Hamiltonian (4.2) are in the metallic regime. The unit vectors $\mathbf{e}_x$ and $\mathbf{e}_y$ are along the x and y directions, respectively. The parameters $E_s, E_p, V_{ss}, V_{pp}, V_{sp}$ characterizing the clean HgTe/CdTe quantum wells are defined as $V_{sp} = -iA/2a$, $V_{ss} = (B+D)/a^2$,

$V_{pp} = (D-B)/a^2$, $E_s = C + M - 4(B+D)/a^2$, and $E_p = C - M - 4(D-B)/a^2$ (a is the lattice constant) where A, B, C, D and M are controlled experimentally. [25]

The width of GNR regions with zigzag edges is measured in terms of the number of zigzag chains N_y comprising it, while its length is measured using the number of carbon atoms $d_{\rm TI}$ in the longitudinal direction. [130] The GNR-based devices studied in Figs. 4.2 and 4.7 are of the size $N_y = 20$, $d_{\rm TI} = 80$ where FI island of length $d_{\rm FI} = 40$ covers middle part of the TI, while in Figs. 4.3–4.6 the device is smaller, $N_y = 20$, $d_{\rm TI} = 45$ and $d_{\rm FI} = 15$, to allow for transparent images of local current profiles. The Fermi energy $E_F = 10^{-6}\gamma$ is within the TI gap.

The size of HgTe-based heterostructures is measured using the number of transverse lattice sites N_y and the number of sites $d_{\rm TI}$ in the longitudinal direction. The devices studied bellow have $N_y = 50$, $d_{\rm TI} = 200$ with FI island of length $d_{\rm FI} = 100$ covering middle part of the TI region (Fig. 4.2 also shows result for a larger device, $N_y = 100$, $d_{\rm TI} = 400$ and $d_{\rm FI} = 200$).

Hamiltonians (4.1) and (4.2) are time-dependent since the spatially uniform unit vector $\mathbf{m}(t)$ along the local magnetization direction is precessing steadily around the z-axis with a constant precession cone angle θ and frequency $f = \omega/2\pi$. This complicated time-dependent transport problem can be transformed into a simpler time-independent one via the unitary transformation of Hamiltonians (4.1) or (4.2) using $\hat{U} = e^{i\omega\sigma_z t/2}$ [for $\mathbf{m}(t)$ precessing counterclockwise]:

$$\hat{H}_{\rm rot} = \hat{U}\hat{H}^{\rm lab}(t)\hat{U}^\dagger - i\hbar\hat{U}\frac{\partial}{\partial t}\hat{U}^\dagger = \hat{H}^{\rm lab}(0) - \frac{\hbar\omega}{2}\sigma_z. \tag{4.3}$$

The Zeeman term $\hbar\omega\sigma_z/2$, which emerges uniformly in the sample and NM electrodes, will spin-split the bands of the NM electrodes, thereby providing a rotating frame picture of pumping based on the four-terminal DC device. [87, 130, 120] In the equivalent DC device, pumping by precessing magnetization can be understood [87] as a flow of spin-resolved charge currents between four spin-selective (i.e., effectively half-metallic FM) electrodes $\overset{\downarrow}{L}$, $\overset{\uparrow}{L}$, $\overset{\downarrow}{R}$ $\overset{\uparrow}{R}$ (L-left, R-right) biased by the electrochemical potential difference $\mu_p^\downarrow - \mu_p^\uparrow = \hbar\omega$.

The basic transport quantity for the DC circuit in the rotating frame is the spin-resolved bond charge current carrying spin-σ electrons from site $\mathbf{i}$ to site $\mathbf{j}$

$$J_{\mathbf{ij}}^{\sigma} = \frac{e}{h}\int_{-\infty}^{\infty} dE\,[\gamma_{\mathbf{ij}}\bar{G}_{\mathbf{ji}}^{<,\sigma\sigma}(E) - \gamma_{ji}\bar{G}_{\mathbf{ij}}^{<,\sigma\sigma}(E)]. \tag{4.4}$$

This is computed in terms of the lesser Green function in the rotating frame [87, 130, 120] $\bar{G}^{<}(E)$. Unlike $G^{<}(t,t')$ in the lab frame, $\bar{G}^{<}$ depends on only one time variable $\tau = t - t'$ (or energy E after the time difference τ is Fourier transformed). This finally yields local spin

$$J_{\mathbf{ij}}^{S} = \frac{\hbar}{2e}\left(J_{\mathbf{ij}}^{\uparrow} - J_{\mathbf{ij}}^{\downarrow}\right), \tag{4.5}$$

and local charge

$$J_{ij} = J_{\mathbf{ij}}^{\uparrow} + J_{\mathbf{ij}}^{\downarrow}, \tag{4.6}$$

currents flowing between nearest neighbor or next-nearest neighbor sites $\mathbf{i}$ and $\mathbf{j}$ connected by hopping $\gamma_{\mathbf{ij}}$. They can be computed within the device or within the NM electrodes.

The summation of all $J_{\mathbf{ij}}^{S}$ or $J_{\mathbf{ij}}$ at selected transverse cross section, $I^{S_z} = \sum_{ij} J_{ij}^{S_z}$ (assuming the z-axis for the spin quantization axis) and $I = \sum_{ij} J_{ij}$, yields total spin or charge current, respectively. The charge current I has to be the same at each cross section due to charge conservation, but the spin current I^{S_z} can vary in different regions of the device since spin does not have to be conserved. The magnitude of total currents pumped into, e.g., the left NM electrode (i.e., computed at any cross section within the left NM electrode) can also be expressed in terms of the transmission coefficients for the four-terminal DC device in the rotating frame [87]

$$\begin{aligned} I_L^{S_z} &= \frac{e}{h}\int dE\,\left(T_{RL}^{\uparrow\downarrow} + T_{LR}^{\uparrow\downarrow} + 2T_{LL}^{\uparrow\downarrow}\right) \\ &\quad \times \left[f^{\downarrow}(E) - f^{\uparrow}(E)\right], \end{aligned} \tag{4.7}$$

$$I = \frac{1}{4\pi}\int dE\,\left(T_{RL}^{\uparrow\downarrow} - T_{LR}^{\uparrow\downarrow}\right)\left[f^{\downarrow}(E) - f^{\uparrow}(E)\right], \tag{4.8}$$

Here the transmission coefficients $T_{pp'}^{\sigma\sigma'}$ determine the probability for σ' electrons injected through lead p' to emerge in electrode p as spin-σ electrons, and can be expressed

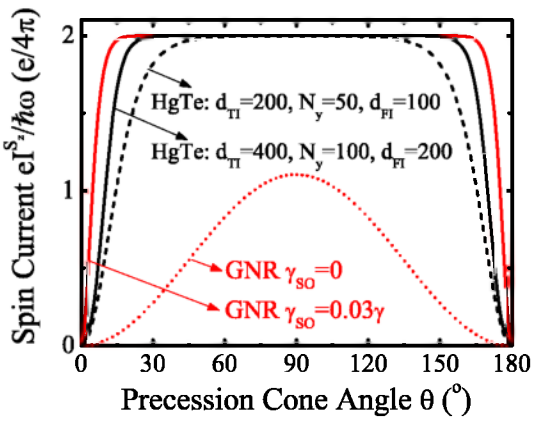

Figure 4.2: The total pure spin current pumped into the NM electrodes as a function of the precession cone angle in FM-TI heterostructures from Fig. 4.1(a). The TI region is modeled as GNR with zigzag edges and non-zero intrinsic SO coupling $\gamma_{SO} \neq 0$ or HgTe-based strip. For comparison, we also plot pumped spin current when TI is replaced by a zigzag GNR with zero intrinsic SO coupling $\gamma_{SO} = 0$. In the case of HgTe-based heterostructure, we show that increasing the size of the proximity induced magnetic region within TI widens the interval of cone angles within which pumped current is quantized.

in terms of the spin-resolved NEGFs. [87] The distribution function of electrons in the four electrodes of the DC device is given by $f^{\sigma}(E) = \{\exp[(E - E_F + \sigma\hbar\omega/2)/kT] + 1\}^{-1}$ where $\sigma = +$ for spin-$\uparrow$ and $\sigma = -$ for spin-$\downarrow$. Since the device is not biased in the laboratory frame (where all NM electrodes are at the same electrochemical potential $\mu_p = E_F$), this shifted Fermi function is uniquely specified by the polarization $\uparrow$ or $\downarrow$ of the electrode.

4.3 Quantized Pure Spin Current Pumping in FM-TI Heterostructures

The precessing magnetization of FM island in the device setup of Fig. 4.1(a) pumps pure (i.e., with no accompanying net charge flux) spin current symmetrically into the left and right NM electrodes in the absence of any bias voltage [if the device

is asymmetric, charge current is also pumped but only as the second order $\propto (\hbar\omega)^2$ effect [87]]. In the case of conventional NM in contact with precessing FM, different approaches predict [131, 87] that pumped spin current by the FM|NM interface behaves as $I^{S_z} \propto \sin^2\theta$. To understand the effect of the TI surrounding the precessing island, we first reproduce this feature in Fig. 4.2 for GNR with no SO coupling ($\gamma_{\rm SO} = 0$). When the intrinsic SO coupling [95] is "turned on" ($\gamma_{\rm SO} \neq 0$), the pumped pure spin current in Fig. 4.2 is substantially enhanced (by up to two orders of magnitude at small precession cone angles). In fact, pumping into helical edge states *profoundly modifies* I^{S_z} vs θ characteristics which becomes constant quantized quantity $eI^{S_z}/\hbar\omega = 2\times e/4\pi$ for large enough θ.

Figure 4.2 also confirms the same behavior for HgTe model of 2D TI. Moreover, it shows that interval of cone angles within which pumped current is quantized can be manipulated by using longer FI region. Exploiting this feature would enable giant spin battery effect where large pure spin current is induced by even very small microwave power input which experimentally [46] controls the precession cone angle.

Note that since $\hbar\omega \ll E_F$, we can use $f^{\downarrow}(E) - f^{\uparrow}(E) \approx \hbar\omega\delta(E - E_F)$ at low temperatures for the difference of the Fermi functions in Eqs. (4.7) and (4.8). This "adiabatic approximation" [120] is analogous to linear response calculations for biased devices, allowing us to define the pumping spin conductance $G_{\rm SP} = eI^{S_z}/\hbar\omega$. Its quantization in Fig. 4.2 is an alternative characterization of the 2D TI phase when compared to QSHE in four-terminal bridges [128, 130] where longitudinal charge current driven by the bias voltage V generates transverse spin current $I_T^{S_z}$ and corresponding quantized spin Hall conductance $G_{\rm SH} = I_T^{S_z}/V = 2 \times e/4\pi$. Thus, the spin battery in Fig. 4.1(a) would produce much larger pure spin currents than currently achieved through, e.g., conventional SHE in low-dimensional semiconductors while offering tunability that has been difficult to demonstrate for SHE-based devices. [10]

We recall that the original proposal [131] for spin battery operated by FMR was based on FM-NM heterostructures. However, experiments [37] performed on

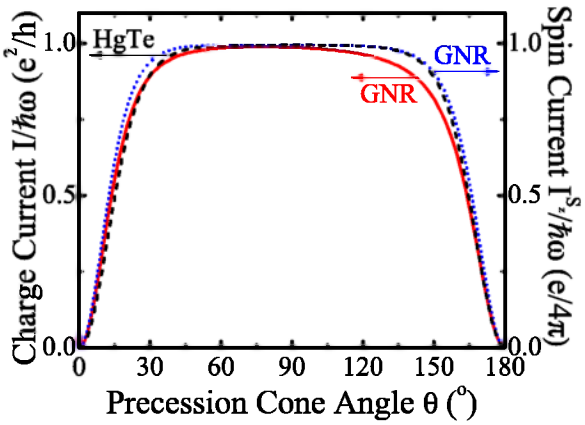

Figure 4.3: The total pumped charge current versus the precession cone angle in FM-TI heterostructures from Fig. 4.1(b). The TI region is modeled as GNR with zigzag edges and intrinsic SO coupling $\gamma_{SO} = 0.03\gamma$ or HgTe-based strip. In addition to charge current, these heterostructures pump spin current plotted explicitly for the GNR-based TI, while for HgTe-based device the two curves are virtually identical (due to larger device size).

$Ni_{80}Fe_{20}$|Cu bilayers have found that spin pumping by FM|NM interfaces is not an efficient scheme to drive spin accumulation in nonmagnetic materials (e.g., estimated [37] spin polarization is only 2×10^{-6} in 10-nm-thick Cu layer) because of the backflow of accumulated spins into the FM and the diffusion of polarized spins inside the NM. No such spin accumulation or spin dephasing exists in the device in Fig. 4.1(a) where bulk transport within the TI regions is completely suppressed (see Fig. 4.4) while 1D spin transport is guided by helical edge states.

4.4 Quantized Charge Current Pumping in FM-TI Heterostructures

While the most direct confirmation of the 2D TI phase would be achieved by measuring quantized G_{SH}, this is very difficult to perform experimentally. Thus, several recent studies [78, 130] have proposed experiments that would detect edge state transport in 2D TIs via simpler measurement of conventional electrical quantities in response to external probing fields.

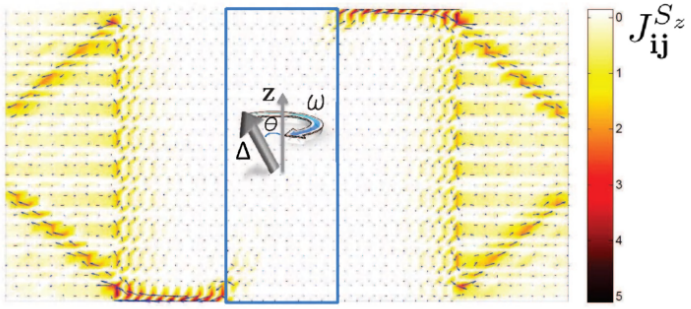

Figure 4.4: Spatial profile of local pumped pure spin current corresponding to total current in Fig. 4.2 at $\theta = 90°$ for GNR model of TI with $\gamma_{SO} = 0.03\gamma$. The corresponding total pumped currents are plotted in Figs. 4.2 and 4.6.

In particular, Ref. [78] has conjectured that a setup with two disconnected FM islands covering two lateral edges of 2D TI, where the magnetization of one of them is precessing while the other one is static, could pump quantized charge current counting the number of helical edge states. This proposal, based on intuitive arguments [78] rather than full quantum transport analysis of adiabatic pumping, concludes that charge pumping conductance $G_{CP} = eI/\hbar\omega = e^2/h$ would be 'universally' quantized for arbitrary device parameters or precession cone angle.

In order to induce quantized charge current response from the 2D TI phase, we propose an alternative heterostructure in Fig. 4.1(b) where FI island with precessing magnetization is covering portion of a *single* lateral edge of the TI. Figure 4.3 demonstrates that this device pumps both charge and spin currents into the NM electrodes. The pumping conductances G_{CP} plotted in Fig. 4.3 are quantized in a wide interval of precession cone angles, which can also be expanded by using longer FI island similarly to HgTe curves in Fig. 4.2.

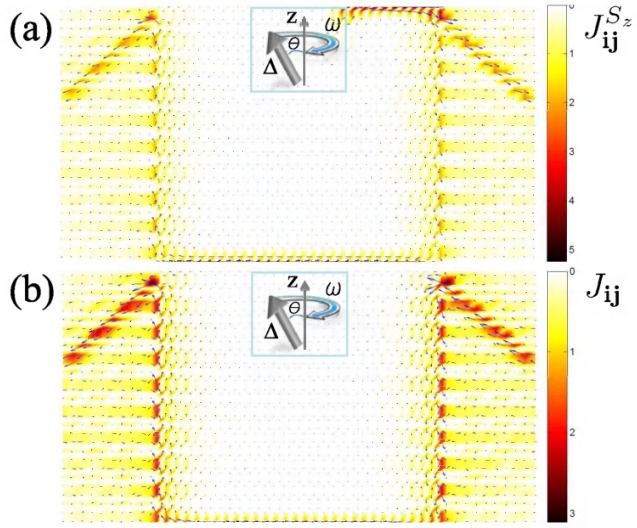

Figure 4.5: Spatial profile of (a) local pumped spin current and (b) local pumped charge current in the heterostructure shown in Fig. 4.1(b) at $\theta = 90°$. The corresponding total pumped currents are plotted in Fig. 4.3.

4.5 Origin and Requirements for Quantized Pumping in FM-TI Heterostructures

To explain the origin of quantized spin and charge pumping in the proposed FM-TI heterostructures, we compute spatial profiles of local pure spin current in Fig. 4.4 and local charge and spin currents in Fig. 4.5 for devices in Fig. 4.1(a) and Fig. 4.1(b), respectively. In the four-terminal DC device picture of pumping, [87] these local *nonequilibrium* currents are generated by the spin flow from electrode $\downarrow_p$ at higher $\mu_p^{\downarrow}$ into electrode $\uparrow_{p'}$ at lower $\mu_{p'}^{\uparrow}$. The role of the central island with static (in the rotating frame) noncollinear magnetization, for which the incoming spins are not the eigenstates of the corresponding Zeeman term, is to allow for transmission with spin precession or reflection accompanied by spin rotation (for transport between $\downarrow_p$ and $\uparrow_p$ electrodes). The spin precession or rotation is necessary for spin to be able to enter electrode at a lower electrochemical potential (accepting spins opposite to the originally injected ones) while flowing through the edge state moving in proper direction compatible with their chirality.

The quantization of the pumped pure spin current in Fig. 4.2 is ensured by

the absence of flow through the bulk of the magnetic island within TI underneath FI in Fig. 4.4(a). In this case, only perfect reflection with spin rotation at the interface between TI region with proximity induced $\Delta \neq 0$ and TI itself takes place redirecting spins from one helical edge state to the other one at the same edge. Thus, the transmission coefficient [87] $T_{LL}^{\uparrow\downarrow} = 1$ in Eq. (4.7) becomes quantized since it is governed by local ballistic transport through edge states on the top right lateral edge in Fig. 4.4(a), while the other two coefficients are zero $T_{RL}^{\uparrow\downarrow} = T_{LR}^{\uparrow\downarrow} = 0$. This also explains why the range of precession cone angles within which $G_{\rm SP}$ in Fig. 4.2 or $G_{\rm CP}$ in Fig. 4.3 is quantized can be expanded by increasing the length of the magnetic island within TI (i.e., the corresponding FI island on the top) or the proximity induced exchange potential Δ—both tunings diminish overlap of evanescent modes from the two TI|magnetic-island interfaces. This is further clarified by Fig. 4.6 where spin current emerges also in the bulk of the magnetic island in the non-quantized case for small $\theta = 5°$. As discussed in Sec. 4.2, spin current is in general not conserved, which is exemplified in Fig. 4.6 by different values of the total pumped spin current at different cross sections (including zero in the middle of the magnetic island at large precession cone angle $\theta = 90°$; the non-zero current around interfaces is due to evanescent modes).

Analogously, quantized charge current in Fig. 4.3 is driven by the same reflection process discussed above which then generates flow of rotated spin along the right TI|NM interface and the bottom lateral edge in Fig. 4.5(b) while utilizing only one of the two helical edge states. In the lab frame picture of pumping, the emission of currents in the absence of bias voltage can be viewed as a flow of spins, driven by absorption of microwave photons, from the region around the interface between the magnetic island and TI where edge states penetrate as evanescent modes into the island. However, this framework does not offer simple explanation of why pumped currents can become quantized.

Figures 4.4 and 4.5 also provide answer to the following question: What happens to current, which is confined to a narrow region of space along the samples edges within TI, as it exits from the TI region into the NM electrodes? The local charge or spin

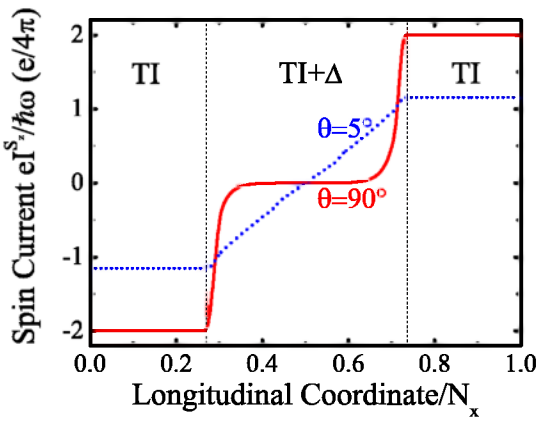

Figure 4.6: Total pure spin current at each transverse cross section along the heterostructure in Fig. 4.1(a) for two different precession cone angles. The total spin current for cone angle $\theta = 90°$ is obtained by summing local currents shown in Fig. 4.4.

fluxes remain confined to a narrow "flux tube" even within the NM electrodes which is refracted at the TI|NM interface by an angle 45°. This feature is explained by the fact that at the TI|NM interface the helical edge state in the, e.g., upper right corner changes direction (to flow downward along the TI|NM interface) so that at this region of space at which current penetrates from TI into NM the quantum state carrying it has wavevector $k_y = k_x$. By continuity of wavefunctions, this relation is preserved within the NM electrodes leading to the observed refraction of the guiding center for electron quantum-mechanical propagation.

Figure 4.7 shows that pumped currents remain precisely quantized in the presence of weak static (spin-independent) disorder simulating short-range impurity scattering. Further increasing of the disorder strength diminishes pumped charge current much faster than the spin current.

Finally, our analysis clarifies that the second FM island with static magnetization covering the opposite edge of the device in the proposal of Ref. [78] for quantized

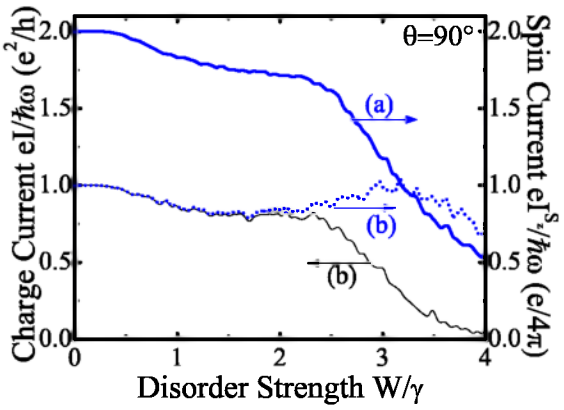

Figure 4.7: The effect of the static impurity potential on pumped currents at precession cone angle $\theta = 90°$ for GNR-based TI, where pure spin current curve labeled with (a) is generated by the spin battery device in Fig. 4.1(a) while curves labeled with (b) are for the device in Fig. 4.1(b).

charge pump is redundant. Moreover, in the case of FM island with precessing magnetization deposited directly on the top of TI to generate proximity effect and pumping, quantization would be lost [130] if electrons can penetrate into the metallic region provided by such islands so that transport ceases to be governed purely by the helical edge states.

4.6 Summary of Chapter

In conclusion, in this chapter we proposed two types of FM-TI heterostructures shown in Fig. 4.1 which can pump quantized spin or charge current in the absence of any applied bias voltage. The device in Fig. 4.1(a) emits pure spin current I^{S_z} toward both the left and the right NM electrodes. Its quantized value $eI^{S_z}/(\hbar\omega) = 2 \times e/4\pi$ can be attained even at very small microwave power input (determining the precession cone angle [46]) driving the magnetization precession, thereby offering a very efficient spin battery device that would surpass any battery [131, 37] based on pumping by

conventional FM|NM interfaces. On the other hand, the device in Fig. 4.1(b) generates quantized charge current $eI/(\hbar\omega) = e^2/h$ in response to absorbed microwaves, which can be utilized either for electrical detection of the 2D TI phase via measurement of precisely quantized quantity (that survives weak disorder) directly related to the number of helical edge states or as a sensitive detector of microwave radiation.

Chapter 5

SPIN-TO-CHARGE CONVERSION IN VERTICAL AND LATERAL TOPOLOGICAL-INSULATOR/FERROMAGNET HETEROSTRUCTURES WITH MICROWAVE-DRIVEN PRECESSING MAGNETIZATION

5.1 Motivation

One of the central goals of second generation spintronics [10] is to generate and manipulate pure spin currents with no net charge flux. The pure spin currents make possible transport of information encoded in electron spin with much less dissipation than generated when using spin-polarized charge current of first generation spintronics. However, their detection and measurement requires to convert them into conventional charge currents and voltages. Over the past decade or so, the inverse spin Hall effect [132] (SHE)—where pure spin current injected longitudinally into a material with spin-orbit coupling (SOC) induces [133, 134] transverse charge current—has emerged as the standard detector which has often been coupled to generators of pure spin currents like spin pumping by precessing magnetization, [83, 135, 136] nonlocal spin diffusion, [137, 138] direct SHE, [139, 140] magnon-spin transmutation, [85] and laser pulses. [141]

5.2 Device Setup

The very recent experiments on lateral heterostructures illustrated in Fig. 5.1(a)—where ferromagnetic (F) layer with precessing magnetization, driven by microwaves of frequency ω under the ferromagnetic resonance (FMR) condition, is brought into a contact with a two-dimensional (interfacial) gas of either conventional electrons with

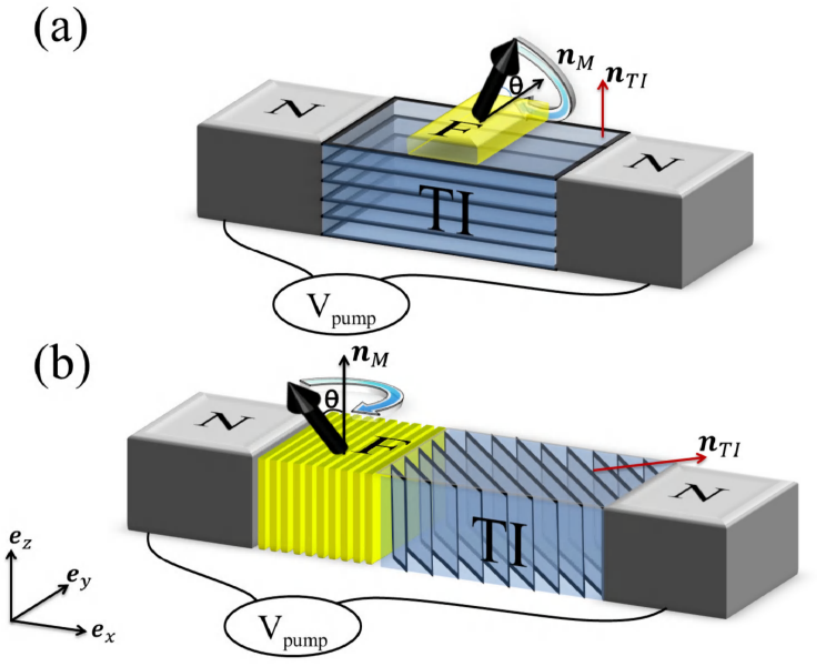

Figure 5.1: Schematic of (a) lateral and (b) vertical F/TI heterostructures where magnetization dynamics, driven by the absorption of microwaves of frequency ω under the FMR conditions, pumps pure spin current along the z- or x-axis, respectively, in the absence of any dc bias voltage between the N leads. The strong interfacial converts pumped spins into charge current flowing along the x-axis in both panels, which is measured as the voltage signal V_{pump} in an open circuit. Besides lateral heterostructures of F/TI type (explored in the experiments of Ref. [2]), we also analyze lateral F/2DEG heterostructures with conventional Rashba SOC at the interface (explored in the experiments of Ref. [3]) for comparison. Due to the magnetic proximity effect, $\Delta_{\text{surf}}(t)$ energy gap appear on the surface of TI or 2DEG due to the component of magnetization $\mathbf{m}(t)$ which is perpendicular to the interface. The unit vector $mathbfn_M$ specifies the axis around which magnetization is precessing, while the unit vector $\mathbf{n}_{\text{TI}}$ is perpendicular to QLs of 3D TI slab.

parabolic energy-momentum dispersion (as formed at Ag/Bi interface) [3] described by the Hamiltonian [52]

$$\hat{H}_{\mathrm{2DEG}} = \frac{\hat{\mathbf{p}}^2}{2m^*} + \frac{\alpha}{\hbar}(\vec{\sigma} \times \hat{\mathbf{p}}) \cdot \mathbf{e}_z, \tag{5.1}$$

or massless Dirac electrons with linear energy-momentum dispersion on the surface of three-dimensional topological insulators (3D TIs) [2] described by the Hamiltonian

$$\hat{H}_{\mathrm{TIS}} = v_F(\vec{\sigma} \times \hat{\mathbf{p}}) \cdot \mathbf{e}_z, \tag{5.2}$$

both of which exhibit spin-momentum locking due to Rashba-type SOC [52]—have observed voltage V_{pump} along the x-direction in the absence of any applied dc bias voltage. Here $\hat{\mathbf{p}} = (\hat{p}_x, \hat{p}_y)$ is the momentum operator, m^* is the effective mass ($m^* \simeq 0.35m$ at the Ag/Bi interface) and v_F is the Fermi velocity. This effect has been interpreted as the "inverse Edelstein effect" [142] (IEE) where *nonequilibrium* spin accumulation in spin-split diffusive two-dimensional electron gas (2DEG) creates an electric field perpendicular to the spin direction, which drives charge current or induces dc voltage signal V_{pump} in an open circuit.

In the case of heterostructures in Fig. 5.1(a), the nonequilibrium spin accumulation is due to spin current I^S pumped along the z-axis, whose dc component carries spins along the y-axis, which is redirected to flow within the interface along the x-axis because of highly resistive Bi or TI layers. Thus, it is unrelated to the inverse SHE which would generate charge current in direction $\mathbf{S} \times \mathbf{I}^S$. It has also been speculated [2] that the efficiency of conversion in the case of F/TI heterostructures could reach 100% due to spin-momentum locking along the single circle (at the intersection of the Dirac cone and Fermi energy plane), rather than two circles [3, 142] in the case of conventional massive electrons which counter the effect of each other.

However, these explanations do not [2, 142] operate directly with time-dependent pumped spin current, so it remains unclear how much of it is actually converted into charge current and how efficient [91, 115] are different types of SOC in this conversion process. Another mechanism of pumped-spin-to-charge conversion was predicted

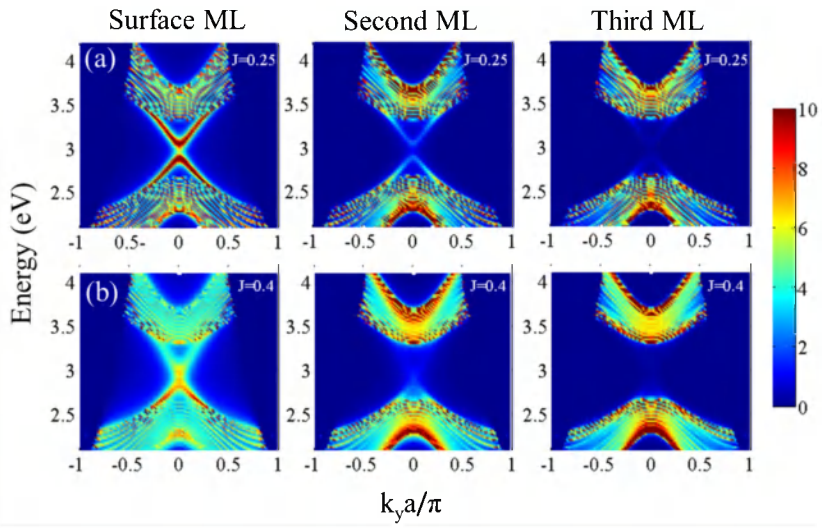

Figure 5.2: The local density of states $g(E, k_y, k_z = 0)$ on first ML of TI in contact with F layer within vertical heterostucture illustrated in Fig. 5.1(b), as well as on adjacent second and third MLs. The TI layer is either weakly (top row with F-TI hopping $J = 0.25$ eV) or strongly (bottom row with F-TI hopping $J = 0.4$ eV) coupled to the neighboring F layer whose magnetization perpendicular to the F/TI interface is assumed to induce energy gap on surface of TI via the magnetic proximity effect.

theoretically in Ref. [30] for vertical F/I heterostructures, such as those illustrated in Fig. 5.1(b) using F/TI system, where pumped spins and reflected and transmitted *perpendicularly* through the interface with strong SOC which leads to charge current (or voltage in open circuit) along the x-axis in Fig. 5.1(b).

5.3 Models and Hamiltonians

The F/TI and F/2DEG lateral heterostuctures illustrated in Fig. 5.1(a) are modeled on a simple cubic or square tight-binding lattice with lattice spacing a, respectively. The TI central region has finite length $L_x^{\mathrm{TI}} = 50a$ and thickness $L_z^{\mathrm{TI}} = 8a$, while it is assumed to be infinite in the y-direction, with each site hosting four spin-dependent orbitals of the minimal effective Hamiltonian. [143]

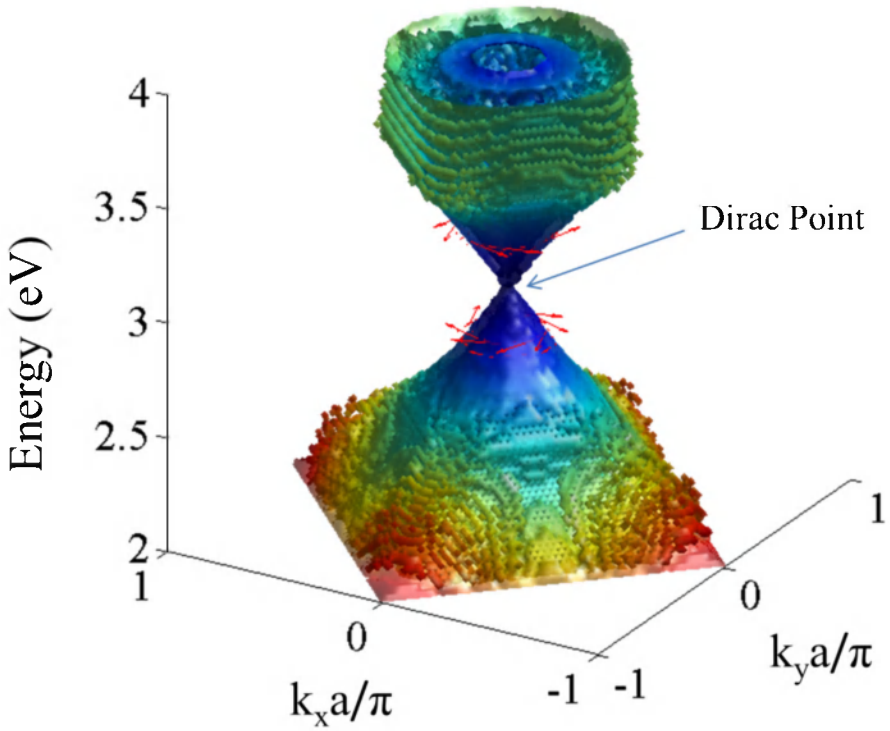

Figure 5.3: The peak of local density of states $g(E, k_y, k_z)$ on first ML of TI in contact with N layer within vertical N/TI/N heterostucture and the corresponding spin texture of the state. The TI layer is weakly coupled to the neighboring N layer, $J = 0.05$ eV.

$$\hat{H}_{\rm TI} = U_{\mathbf{n}}^{\dagger} \sum_{n,\mathbf{k}_{\parallel}} \left\{ \mathbf{c}_{n,\mathbf{k}_{\parallel}}^{\dagger} \left(\frac{B}{a^2} \mathbf{\Gamma}_0 - i \frac{A}{2a} \mathbf{\Gamma}_3 \right) \mathbf{c}_{n+1,\mathbf{k}_{\parallel}} + \text{H.c.} \right.$$
$$\left. + \mathbf{c}_{n,\mathbf{k}_{\parallel}}^{\dagger} \left[C\mathbf{1} + d(\mathbf{k}_{\parallel}) \mathbf{\Gamma}_0 + \frac{A}{a} (\mathbf{\Gamma}_1 \sin k_x a + \mathbf{\Gamma}_2 \sin k_y a) \right] \mathbf{c}_{n,\mathbf{k}_{\parallel}} \right\} U_{\mathbf{n}}, \tag{5.3}$$

where,

$$U_{\mathbf{n}} = \begin{pmatrix} \mathbf{1} & \mathbf{0} \\ \mathbf{0} & \boldsymbol{\tau}_p \end{pmatrix}, \tag{5.4}$$

with,

$$\boldsymbol{\tau}_p = \begin{pmatrix} i n_{TI}^z & (i n_{TI}^x + n_{TI}^y) \\ (i n_{TI}^x - n_{TI}^y) & -i n_{TI}^z \end{pmatrix}. \tag{5.5}$$

This Hamiltonian yields the correct gap size in the bulk and surface dispersion of Bi_2Se_3 based 3DTI while reducing to the continuum $\mathbf{k}\cdot\mathbf{p}$ Hamiltonian in the small k limit. In Fig. 5.3 we present the peak of local density of states $g_l(E, k_y, k_z) = -\sum_\alpha \Im(\mathbf{G}^r_{l\alpha,l\alpha})/\pi$ calculated for the N/TI/N heterostructure at the N/TI interface layer l where the sum is over the atomic orbitals α. In the calculation we consider $\mathbf{n}_{TI} = (1, 0, 0)$. The cone structure and the spin texture is in consistence with the expected dispersion relation for the surface state of the TIs. Here $\mathbf{n}_{TI}$ is the unit vector normal to the QLs of the TI shown in Fig. 5.1 and $\hat{\mathbf{c}} = (\hat{c}_{+\uparrow}, \hat{c}_{+\downarrow}, \hat{c}_{-\uparrow}, \hat{c}_{-\downarrow})^T$ annihilates electron in different orbitals, $d(\mathbf{k})_\parallel = M - 2B/a^2 + 2B(\cos k_x a + \cos k_y a - 2)/a^2$, $\mathbf{\Gamma}_i$ $(i = 0, 1, 2, 3)$ are 4×4 Dirac matrices and $\mathbf{1}$ is the unit matrix of the same size. The numerical values of parameters are chosen as: $M = 0.3$ eV; $A = 0.5$ aeV; and $B = 0.25$ a^2eV. The Fermi energy of the whole device is set at $E_F = 3.1$ eV, and the bottom of the band of the TI layer is shifted by $C = 3.0$ eV.

The F and N layers are described by a tight-binding Hamiltonian with a single s- orbital per site

$$\begin{aligned}\hat{H}_F &= \sum_{n,\sigma\sigma',\mathbf{k}_\parallel} \hat{c}^\dagger_{n\sigma,\mathbf{k}_\parallel} \left(\varepsilon_{n,\mathbf{k}_\parallel}\delta_{\sigma\sigma'} - \frac{\Delta_n}{2}\mathbf{m}\cdot[\vec{\sigma}]_{\sigma\sigma'}\right) \hat{c}_{n\sigma',\mathbf{k}_\parallel} \\ &\quad - \gamma \sum_{n,\sigma,\mathbf{k}_\parallel} (\hat{c}^\dagger_{n\sigma,\mathbf{k}_\parallel}\hat{c}_{n+1,\sigma,\mathbf{k}_\parallel} + \text{H.c.}). \end{aligned} \tag{5.6}$$

The operators $\hat{c}^\dagger_{\mathbf{n}\sigma}$ $(\hat{c}_{\mathbf{n}\sigma})$ create (annihilate) electron with spin σ on monolayer n with transverse momentum $\mathbf{k}_\parallel$ within the monolayer. The in-monolayer kinetic energy $\varepsilon_{n,\mathbf{k}_\parallel} = -2\gamma(\cos k_y a + \cos k_z a)$ is equivalent to an increase in the on-site energy, and the nearest neighbor hopping is $\gamma = 1.0$ eV. The coupling of itinerant electrons to collective magnetization dynamics is described through the material-dependent exchange potential Δ_n ($\Delta_n \equiv 0$ within semi-infinite ideal N leads), where $\vec{\sigma} = (\sigma_x, \sigma_y, \sigma_z)$ is the vector of the Pauli matrices and $[\sigma_\alpha]_{\sigma\sigma'}$ denotes the Pauli matrix elements. Coupling of the two-orbital normal metal to the four-orbital TI at the interface of the two materials

is modeled by the following hopping matrix,

$$\boldsymbol{T}_{F/TI} = \begin{pmatrix} \gamma_c \mathbf{1} & \gamma_c \mathbf{1} \end{pmatrix}. \tag{5.7}$$

The 2DEG central region has finite length $L_x^{\text{2DEG}} = 100a$ and it is assumed to be infinite in the y-direction, with each site hosting two spin-dependent orbitals of the discretized version [144] of Hamiltonian in Eq. 5.1. We do not model explicitly the presence of the F overlayer with precessing magnetization in Fig. 5.1(a), but instead add term $-\Delta\mathbf{m}(t)\cdot\vec{\sigma}/2$ in the region of length L_x^{F} residing in the center of the top plane of TI or plane of 2DEG. Here Δ is the mean-field exchange splitting induced by the F overlayer through magnetic proximity effect, $\mathbf{m}(t)$ is the unit vector along the precessing magnetization. In the numerical calculations for the case of F/TI heterostructure we choose $L_x^{\text{F}} = 20a$ and $\Delta = 0.28$ eV, while in the case of F/2DEG we consider $L_x^{\text{F}} = 50a$, $\Delta = 0.2$ eV and $\alpha_{SOC} = 0.1$aeV.

The vertical F/TI heterostructures in Fig. 5.1(b) are modeled on the simple cubic lattice composed of 2D monolayers (MLs) that are infinite in the yz-plane. The length of F layer is $d_{\text{F}} = 50$ MLs and of TI layer is $d_{\text{TI}} = 5$ MLs. In the case of vertical heterostructures, we add $-\Delta_{\text{surf}}\mathbf{m}(t)\cdot\vec{\sigma}/2$ on the first monolayer of TI layer in contact with F layer, where both $\Delta_{\text{surf}} \equiv 0$ and $\Delta_{\text{surf}} = \Delta = 0.28$ eV (where Δ is exchange splitting in the F layer) are considered for the results presented in the next section. Figure 5.2 shows the local density of states (LDOS) on the MLs of TI that are the closest to F layer within the vertical heterostructure in Fig. 5.1(b). When the hopping parameter between lattice sites of F and TI is large ($J = 0.4$ eV), the energy-momentum relation in the bottom row of Fig. 5.2 bears little resemblance to the Dirac cone because of flooding [145] of F/TI interface by evanescent wavefunctions which originate from the F layer and penetrate into the bulk gap of TI while exponentially decaying in space. To avoid this effect, we assume smaller hopping $J = 0.25$ eV which leads to LDOS shown in the top row of Fig. 5.2. The weak F to TI coupling can be achieved by growing an ultrathin layer of a conventional band insulator, such as In_2Se_3 with large bandgap and good chemical and structural compatibility with Bi_2Se_3 where

sharp heterointerfaces have already been demonstrated by molecular-beam epitaxy growth [146]. This dielectric layer will also affect the value of the proximity induced surface energy gap Δ_{surf}. In addition, Fig. 5.2 demonstrates how gapped surface state of TI can penetrate into the bulk of TI as evanescent wavefunction decaying over the first few MLs and effectively doping the bulk.

Since pumped charge and all components of pumped spin current tensor are time-dependent in the presence of SOC, [30] the nonequilibrium Green function formalism [147] is advantageous choice for the computation because it gives from the outset experimentally measurable current averaged over one period. In contrast, standard scattering approach to adiabatic pumping [100, 28] requires to compute current at all times (or, in practice, over a discrete time grid) during one period of microwave oscillations and then find its average, [115, 96] which can be computationally expensive [especially for tunneling structures, like vertical F/TI ones in Fig. 5.1(b), where current amplitude can be several orders of magnitude larger than its average value].

5.4 Results and Discussion

In this section, we apply the Floquet-nonequilibrium Green function (Floquet-NEGF) formalism [30, 148] introduced in section. 3.3.1, to time-dependent Hamiltonian of lateral and vertical heterostructures depicted in Figs. 5.1(a) and 5.1(b), respectively, assuming *ballistic* transport regime. For lateral heterostructures in Fig. 5.1(a), we demonstrate in Fig. 5.4 that both charge I and spin I^{S_α} currents will flow within the plane of F/TI or F/2DEG interface in the direction of the x-axis denoted in Fig. 5.1. The charge current in Fig. 5.4(a),(c) is non-zero only when magnetization is precessing around the y-axis—this setup injects dc component of spin current into the interface with spins pointing along the y-axis, which is partially converted into charge current along the x-axis. On the other hand, when F layer magnetization is precessing around the x- or the y-axis, the charge current along the x-axis is identically zero $I \equiv 0$, while non-zero pure spin currents I^{S_x} and I^{S_y} continue to flow along the x-axis as shown in Fig. 5.4(b),(d). Note that in open circuits one would measure [3, 2] the voltage signal

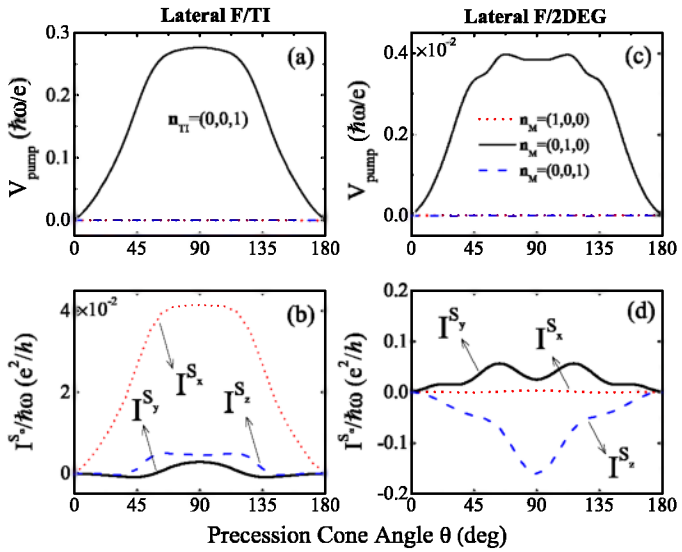

Figure 5.4: (a), (c) The dc pumping voltage in lateral F/TI and F/2DEG heterostructures for different orientation of the axis $\mathbf{n}_M$ around which magnetization of the F layer precesses with cone angle θ. Panels (b) and (c) plot the spin current I^{S_α} which accompanies the charge current $I = V_{\rm pump}G$ in (a) and (b), respectively, where both I^{S_α} and I flow along the x-axis in Fig. 5.1. Note that charge current is non-zero only when magnetization is precessing around the y-axis in Fig. 5.1(a).

$V_{\rm pump} = I/G$, which is plotted in Fig. 5.4(a),(c) with G being the conductance of the two-terminal system.

While this picture is fully compatible with the one based on IEE, [142] our approach finding both charge and spin currents makes it possible to quantify the spin-to-charge conversion efficiency by using the ratio I/I^{S_α}. Note that we employ the same units for charge current, $I = I^{\uparrow} + I^{\downarrow}$, and spin current, $I^{S_\alpha} = I^{\uparrow} - I^{\downarrow}$, expressed in terms of spin-resolved charge currents $I^{\uparrow}$ and $I^{\downarrow}$ carrying spins pointing along the α-axis. To quantify total spin angular momentum emitted by the central region of systems in Fig. 5.1 into two N leads, we sum up spin currents in the left (L) and right (R) N lead to get $I^{S_\alpha} = I_L^{S_\alpha} - I_R^{S_\alpha}$. Thus, the ratio I/I^{S_α} is a pure number which we show in Fig. 5.5. It reaches $I/I^{S_\alpha} \simeq$ 2–8% for F/2DEG interface, increasing to $I/I^{S_\alpha} \simeq$ 40–60% on the F/TI interface due to perfect spin-momentum locking. Note that in the case of conventional spin-polarized charge current, $I^{S_\alpha}/I \leq 1$ would signify spin-polarization along the α-axis. In Fig. 5.5 this number can be bigger than 1 because spin current was initially generated by pumping in the absence of dc bias voltage and without any

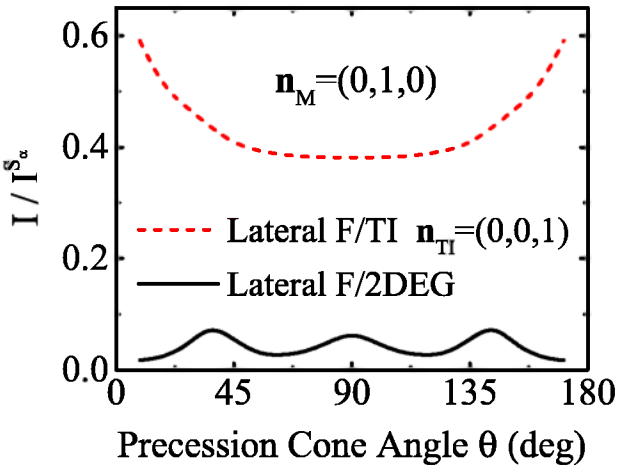

Figure 5.5: Efficiency of spin-to-charge conversion in lateral F/TI and F/2DEG heterostructures quantified by computing the ratio of charge I and spin I^{S_α} currents from Fig. 5.4 for magnetization precessing around the y-axis $[\mathbf{n}_M = (0,1,0)]$ in Fig. 5.1(a).

net charge flux, and subsequently only partially converted into charge current by the SO-coupled interface.

Figure 5.6(a),(c) shows charge current along the x-axis in vertical heterostructures depicted in Fig. 5.1(b) whose magnetization is precessing along the z-axis. In conventional F/N layers, magnetization dynamics pumps time-dependent pure spin current into N layer in the absence of any bias voltage which has been amply explored as a robust and ubiquitous pumping effect at room temperature [28]. However, no charge pumping at the adiabatic level $\propto \omega$ is expected in multilayers with a *single* precessing F layer [87]. In section. 3.4 we showed that, this outcome changes if strong SOC is present directly at the interface, as predicted to occur in F/I junctions with the Rashba SOC at the interface. [30] While the angular dependence of pumped charge current for F/TI interface in Fig. 5.6(a) is the same $\propto \sin^2\theta\cos\theta$ as for the F/I interface with the Rashba SOC, the magnitude of the voltage signal is very sensitive to opening of time-dependent energy gap $\Delta_{\text{surf}}(t)$ on the surface of TI due to magnetic proximity effect. That is, as soon as the cone angle θ becomes non-zero due to microwave

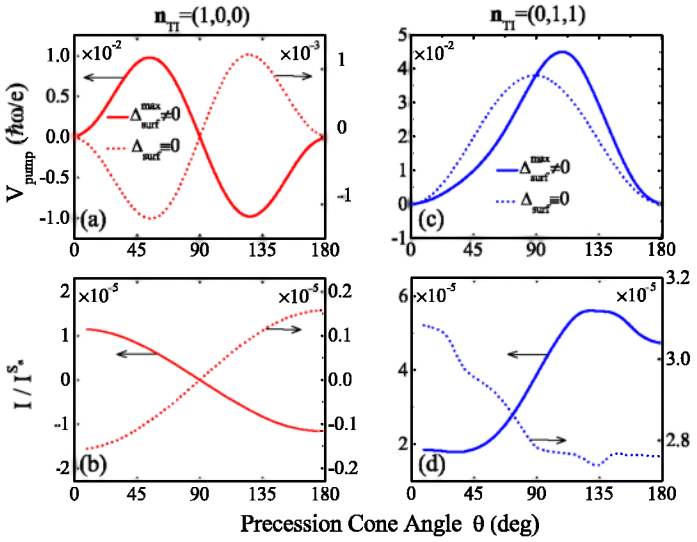

Figure 5.6: The angular dependence of dc pumping voltage in F/TI vertical heterostructures from Fig. 5.1(b) whose magnetization is precessing around the z-axis, $\mathbf{n}_M = (0,0,1)$. The QLs of 3D TI slab are oriented perpendicular to $\mathbf{n}_{\rm TI} = (1,0,0)$ in panels (a) and (b), or to $\mathbf{n}_{\rm TI} = (0,1,1)$ in panels (c) and (d).

absorption, the time-dependent exchange field acquires a component $(\Delta \sin\theta \sin\omega t)\mathbf{e}_x$ which is perpendicular to the surface of the TI and induces the corresponding surface gap $\Delta_{\rm surf}(t)$. The value of $\Delta^{\rm max}_{\rm surf}$ is not necessarily related to $\Delta|\sin\theta|$ because magnetic proximity effect can be influenced by the properties of the F/TI interface, [149] so that in Fig. 5.6 we consider both $\Delta_{\rm surf}(t) \neq 0$ and $\Delta_{\rm surf}(t) = 0$ cases.

The Bi_2Se_3 realization of TI is a strongly anisotropic material composed of quintuple layers (QLs) of Bi and Se atoms, where one QL consists of three Se layers strongly bonded to two Bi layers in between. [124] The electrons on the metallic surface of Bi_2Se_3 are routinely described by the massless Rashba Hamiltonian in Eq. (5.2) which describes spin-orthogonal-to-momentum locking for both Bi and Si sublattices, as observed in spin-ARPES experiments. [124] However, such description is valid only when the surface of TI crystal coincides with the plane of QL, while for other orientations of QLs the two sublattices generate different spin textures. [150, 151] To illustrate their effect, we also show in Fig. 5.6(c) charge current when QLs are oriented

perpendicularly to the unit vector $\mathbf{n}_{TI} = (0, 1, 1)$ drawn in Fig. 5.1. The corresponding ratios I/I^{S_α} are plotted in Figs. 5.6(b) and 5.6(d) for two different orientations of QLs (denoted on the top of the left and right column in Fig. 5.6).

The recent theoretical [149] and experimental [152, 153, 154] efforts have vigorously pursued F/TI heterostructures with non-zero (time-independent) Δ_{surf}, as well as without complicated hybridization [149] of bulk and surface states so that split Dirac-cone remains easily identifiable. Such gapped surface state of TIs due to time-reversal breaking makes possible experimental probing of generic properties of 3D TIs like the topological magnetoelectric effect (where magnetization is generated by an electric field E with a quantized coefficient), half-integer quantum Hall effect and magnetic monopole. [124] It has also been predicted [76] that F/TI heterostructure in Fig. 5.1(a) with precession axis lying within the TI surface will pump charge current which jumps abruptly every time the z-component of the precession magnetization touches zero due to counterpart of parity anomaly effect from high energy physics. However, observation of such effects requires perfectly insulating bulk of TI and Fermi energy tuned close to the Dirac point (DP). On the other hand, sensitivity of charge current pumped vertically through the TI surface on the presence of $\Delta_{\text{surf}}(t)$ does not require either of these two conditions.

The non-zero pumping voltage at the adiabatic level $\propto \omega$ in vertical F/I junctions with interfacial SOC [30] (in the absence of interfacial SOC, simple F/I junctions pump [87] charge current $\propto \omega^2$ which is, therefore, nonadiabatic) is closely related to the tunneling anisotropic magnetoresistance (TAMR). The out-of-plane TAMR for F/TI vertical heterostructures is defined [30] as $\text{TAMR}\,(\theta) = [R(\theta) - R(\theta = 0°)]/R(\theta = 0°)$ using conventional dc resistances $R(\theta)$ measured by tilting the static magnetization of the F layer in Fig. 5.1(b) towards the transport direction. The TAMR curves plotted in Fig. 5.7 show that change in the conductance $G(\theta) = 1/R(\theta)$ is too small to account for the enormous difference between $V_{\text{pump}}(\Delta_{\text{surf}}^{\text{max}} \neq 0)$ and $V_{\text{pump}}(\Delta_{\text{surf}}^{\text{max}} \equiv 0)$ cases. Although TAMR differentiates between massless and massive Dirac fermions on the surface of the TI, it cannot be used to reliably detect the latter since it would diminish

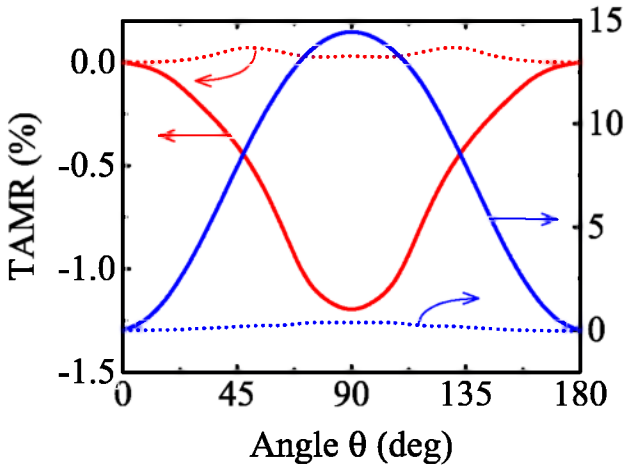

Figure 5.7: The TAMR of F/TI vertical heterostructures from Fig. 5.1(b) for gapless ($\Delta_{\text{surf}} \equiv 0$ for dotted lines) and gapped ($\Delta_{\text{surf}} \neq 0$ for solid lines) surface of TI that is in direct contact with the F layer. The QLs of 3D TI slab are oriented perpendicular to $\mathbf{n}_{\text{TI}} = (1, 0, 0)$ for red lines or to $\mathbf{n}_{\text{TI}} = (0, 1, 1)$ for blue lines.

if bulk charge carriers are present within the TI slab.

5.5 Summary of Chapter

In this chapter, using the charge-conserving Floquet-Green function approach to quantum systems driven by periodic time-dependent potential, we analyzed how spin current pumped (in the absence of any bias voltage) by the precessing magnetization of a ferromagnetic (F) layer is injected *laterally* and converted into charge current flowing in the same direction within interfaces with strong spin-orbit coupling (SOC). In the case of metallic interface with the Rashba SOC used in recent experiments [Nature Comm. **4**, 2944 (2013)], both spin I^{S_α} and charge I current flow within the interface with $I/I^{S_\alpha} \simeq 2$–8% (depending on the precession cone angle), while for F/topological-insulator (F/TI) interface employed in recent experiments (arXiv:1312.7091) this conversion efficiency is much higher $I/I^{S_\alpha} \simeq 40$–60% due to perfect spin-momentum locking. The spin-to-charge conversion occurs also when spin current is pumped *vertically* through F/TI interface, where we predicted that charge

current (or dc pumping voltage in an open circuit) will be sensitive to whether the Dirac fermions at the interface are massive or massless.

Chapter 6

SPIN-TRANSFER AND SPIN-ORBIT INDUCED TORQUES

6.1 Density Matrix in Steady-State Nonequilibrium

The stationary nonequilibrium density matrix $\boldsymbol{\rho}_{\mathrm{neq}}$ of current carrying steady states is one of the most fundamental objects of nonequilibrium quantum statistical mechanics and quantum transport theory. [155, 156, 157, 158] It yields the expectation values of any single-particle observables, while its diagonal elements give directly the particle density within the device. [159, 160, 161] For example,

$$A = \mathrm{Tr}\left[\boldsymbol{\rho}_{\mathrm{neq}}\mathbf{A}\right], \tag{6.1}$$

gives charge current, spin current, and spin density in system out of equilibrium when the corresponding operators (i.e., their matrix representation) are inserted as $\mathbf{A}$.

In the case of steady-state transport of non-interacting quasiparticles described using popular tight-binding Hamiltonians,[157] one can obtain charge or spin currents in the linear response regime using the nonequilibrium Green function (NEGF)-based expressions[155, 157, 162] that do not invoke $\boldsymbol{\rho}_{\mathrm{neq}}$ explicitly. However, the inclusion of atomistic details of the device through self-consistent Hamiltonians, typically obtained[159, 161] from or fitted[163] to density functional theory (DFT), requires the knowledge of equilibrium density matrix $\boldsymbol{\rho}_{\mathrm{eq}}$ to describe the charge transfer between different atomic species[160] or $\boldsymbol{\rho}_{\mathrm{neq}}$ to describe the charge redistribution due to the current flow at finite bias voltage. [159, 160, 161] Otherwise, without computing the charge redistribution and the corresponding self-consistent electric potential profile across the device the current-voltage characteristics violates[164, 165] gauge invariance, i.e., invariance with respect to the global shift of electric potential by a constant,

$V \to V + V_0$. It is worth mentioning that $\boldsymbol{\rho}_{\rm neq}$ plays an essential role in describing steady-state transport in interacting quantum systems far from equilibrium, where recent efforts[156] have tried to construct an effective equilibrium-like (i.e., written in the usual Boltzmann form) density matrix, $\boldsymbol{\rho}_{\rm neq} = \exp[-\beta(\mathbf{H} - \mathbf{Y})]$, using the device Hamiltonian $\mathbf{H}$ and $\mathbf{Y}$ operator that encodes information about the finite bias voltage.

One of the key issues in applying Eq. (6.1) to specific problem is to remove possible equilibrium contribution to a physical quantity of interest, if such quantity has a non-zero expectation value in the absence of bias voltage that is compatible with the time-reversal invariance. For example, spintronic systems are abundant in such situations: (*i*) since spin current operator is time-reversal invariant, it can have non-zero expectation values in the thermodynamic equilibrium, as highlighted[162, 166] by the case of equilibrium local currents in two-dimensional electron gases (2DEGs) with the Rashba spin-orbit coupling (SOC); (*ii*) the spin operator is not time-reversal invariant, so spin density can be non-zero in thermodynamic equilibrium on the proviso that time-reversal invariance is broken by internal or external magnetic fields.

Another example of equilibrium quantities that appear in the formalism, but are not measured in standard transport experiments, are the circulating or diamagnetic currents which always exist in the presence of a magnetic field. They contribute to the local charge current density, $\mathbf{j}(\mathbf{r}) = \int d\mathbf{r}'\, \underline{\sigma}(\mathbf{r}, \mathbf{r}')\mathbf{E}(\mathbf{r}')$, as signified by the Kubo non-local conductivity tensor $\underline{\sigma}(\mathbf{r}, \mathbf{r}')$ being dependent on *all* states below the Fermi energy.[167] Thus, theoretical description of charge transport in multiterminal Hall bridges must remove diamagnetic currents in order to produce experimentally measurable quantities, such as conductance coefficients connecting voltages and total charge currents in different terminals, which depend only on the states in some shell (defined by the temperature) around the Fermi surface.[167]

Similarly, naïve application of the Kubo formula to the thermal Hall coefficient always yields unphysical result due to the presence of the equilibrium circulating energy flow.[168] That is, in a system breaking the time-reversal invariance, either by applying an external magnetic or due to the spontaneous magnetization, the temperature

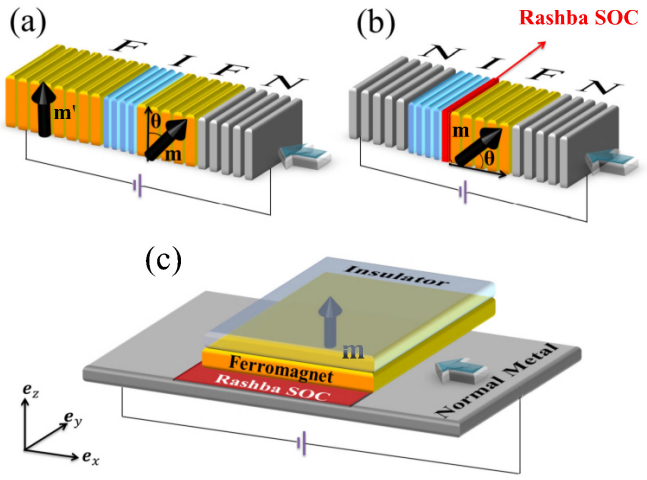

Figure 6.1: Schematic view of junctions exhibiting spin torque that we employ in Sec. 6.4 to illustrate applications of our gauge-invariant nonequilibrium density matrix derived in Sec. 6.3: (a) conventional MTJ containing spin-polarizing F′ layer with fixed magnetization and F layer with free magnetization which are separated by a thin insulating layer; (b) semi-MTJ containing a single F layer with free magnetization and the Rashba SOC at the I/F interface; and (c) N/F/I heterostructure (realized in the recent experiments as Pt/Co/AlO_x heterostructure) where the Rashba SOC is presumed to exist at the N/F interface. In all three cases, the unpolarized charge current driving spin torque is injected along the x-axis. We assume that each layer in panels (a), (b) and (c) is composed of atomic monolayers modeled on an infinite square tight-binding lattice.

gradient not only drives the transport heat current, but also drives the circulating heat current. Although both contributions are present in the microscopic current density calculated by the standard linear response theory, a proper subtraction of circulating component is necessary since such quantity is *not observable* in the transport experiment.

On the other hand, spintronics literature has often utilized putative expressions[169, 170, 171] for $\boldsymbol{\rho}_{\rm neq}$ which actually do not obey gauge invariance and, therefore, can lead to ambiguous results for the expectation values quantities such as spin density, spin-transfer torque (STT), and local spin current. This is due to the fact that, depending on the chosen way of splitting the bias voltage between the source and drain electrodes of the device, one gets different results because of improperly subtracted expectation value in equilibrium (i.e., at zero bias voltage).

6.2 Spin-Transfer Torque

The spin-transfer torque (STT) is a phenomenon in which spin current of large enough density injected into a ferromagnetic (F) layer either switches its magnetization from one static configuration to another or generates a dynamical situation with steady-state precessing magnetization [27]. The origin of STT is absorption of itinerant flow of angular momentum components normal to the magnetization direction. It represents one of the *central phenomena* of the second-generation spintronics, focused on manipulation of coherent spin states, since reduction of current densities (currently of the order 10^6-10^8 A/cm^2) required for STT-based magnetization switching is expected to bring commercially viable magnetic random access memory (MRAM) [41]. The rich nonequilibrium physics [42] arising in the interplay of spin currents carried by fast conduction electrons and collective magnetization dynamics, viewed as the slow classical degree of freedom, is of great fundamental interest.

Very recent experiments [48, 50] and theoretical studies [99] have sought STT in nontraditional setups which do not involve the usual two (spin-polarizing and free) F layers with noncollinear magnetizations [42], but rely instead on the spin-orbit coupling (SOC) effects in structures lacking inversion symmetry. Such "SO torques" [56] have been detected [48] in Pt/Co/AlO_x lateral devices where current flows in the plane of Co layer. Concurrently, the recent discovery [124] of three-dimensional (3D) topological insulators (TIs), which possess a usual band gap in the bulk while hosting metallic surfaces whose massless Dirac electrons have spins locked with their momenta due to the strong Rashba-type SOC, has led to theoretical proposals to employ these exotic states of matter for spintronics [17] and STT in particular [72]. For example, magnetization of a ferromagnetic film with perpendicular anisotropy deposited on the TI surface could be switched by interfacial quantum Hall current [72]. However, very little is known about STT in setups where *spin transport is perpendicular* to interfaces with strong SOC [30, 61, 75], as exemplified by the vertical TI-based heterostructure in Fig. 6.7. Such heterostructures could exploit strong interfacial SOC without requiring [75, 145] perfectly insulating bulk whose unintentional doping in present experiments

obscures [172] topological properties anticipated for lateral transport along the TI surface.

For conventional F′/I/F magnetic tunnel junctions (MTJs) illustrated in Fig. 6.1(a), where the reference F′ layer with fixed magnetization $\mathbf{m}'$ plays the role of an *external spin-polarizer*, it is customary to analyze the in-plane (originally considered by Slonczewski[173]) and perpendicular (also called "field-like") components of the STT vector,[42]

$$\mathbf{T} = \mathbf{T}_{\parallel} + \mathbf{T}_{\perp}. \tag{6.2}$$

The in-plane torque

$$\mathbf{T}_{\parallel} = \tau_{\parallel}\mathbf{m} \times (\mathbf{m} \times \mathbf{m}'), \tag{6.3}$$

is purely nonequilibrium and competes with the damping. The perpendicular torque

$$\mathbf{T}_{\perp} = \tau_{\perp}\mathbf{m} \times \mathbf{m}', \tag{6.4}$$

arises from spin reorientation at the interfaces and possesses both the equilibrium (i.e., interlayer exchange coupling) and the nonequilibrium contributions which act like an effective magnetic field on the magnetization $\mathbf{m}$ of the free F layer.

The often assumed bias voltage dependence of STT components in MTJs, $\tau_{\parallel} = a_1 V_b + a_2 V_b^2$ and $\tau_{\perp} = b_0 + b_1 V_b^2$, is violated in asymmetrically designed MTJs (where the bias dependence of $\tau_{\perp}$ acquires a linear contribution[174]) or at larger V_b where recent experiments[42] have uncovered more complicated dependency. The most accurate STT experiments (such as those based on spin-transfer-driven ferromagnetic resonance[42]) have access only to the derivatives of $\mathbf{T}_{\parallel}$ and $\mathbf{T}_{\perp}$ with respect to V_b (the so-called "torkance" [175]). Thus, only the nonequilibrium contributions driven by the nonzero bias voltage $V_b = V_L - V_R$ between the left and the right electrode are accessed experimentally. Accordingly, equilibrium contribution[176, 177] to $\mathbf{T}_{\perp}$ at $V_b = 0$ should be removed when comparing theoretical predictions with experimental results.

At finite bias voltage, one can simply compute $\mathbf{T}_{\perp}(V_b) - \mathbf{T}_{\perp}(V_b = 0)$ to extract numerically the purely nonequilibrium perpendicular torque.[177, 178] However, this

fails at small V_b due to substantial numerical errors accumulated when subtracting two nearly equal numbers. In symmetric MTJs with identical F and F′ layers, one can eliminate equilibrium value of $\mathbf{T}_\perp$ by using the special gauge (i.e., the reference level for the electric potential) where voltage $-V_b/2$ is applied to the left and $V_b/2$ to the right electrode.[176] This trick, however, is not applicable to setups with F and F′ layers of different thickness or when they are made of different materials.[174, 179]

Moreover, it cannot be applied to recently predicted[61, 62] unconventional STT driven by SOC in asymmetric N/I/F or N/TI/F vertical heterostructures, where TI is a thin slab of three-dimensional topological insulator[124] and strong Rasba SOC exists at I/F or TI/F interface, as illustrated in Fig. 6.1(b). In the case of such "semi-MTJs", current flowing perpendicularly through the I/F or TI/F interface will induce both $\mathbf{T}_\perp$ and $\mathbf{T}_\parallel$ on the free F layer even in the linear-response regime. This happens in the absence of any additional spin-polarizing F′ layer through a mechanism closely related to tunneling anisotropic magnetoresistance[65, 30] (TAMR) in the case of N/I/F junctions,[61, 62] or a combination of TAMR-based effect and spin-polarizing action of the TI slab (where current becomes polarized in the direction of transport) in the case of N/TI/F junctions.[62]

Finally, the so-called spin-orbit torques have attracted a lot of attention recently.[56] They occur in laterally patterned N/F/I heterostructures with a single F layer whose interfaces contain Rashba SOC, as illustrated in Fig. 6.1(c). It has been known for a long time,[54, 55] and confirmed in recent experiments,[180] that in-plane longitudinal steady-state charge current flowing through the Rashba spin-split 2DEG will induce nonequilibrium transverse spin accumulation. This mechanism—the so-called Edelstein effect—provides one of the two possible explanations [57, 99, 181, 182, 183] for the very recent experimental observations[48, 49, 50] of magnetization switching of the Co layer within structurally inversion asymmetric Pt/Co/AlO_x junction where current flows in the plane of Pt/Co and Co/AlO_x interfaces [in Fig. 6.1(c) we assume that SOC is located at the N/F interface, but the other choice with SOC at F/I interface is also possible[57]]. The key quantity that has to be calculated in the theoretical analysis[183]

of SO torques is the nonequilibrium spin density within the Rashba 2DEG with an additional Zeeman term due to the magnetization of the F layer (like Co). Thus, usage of gauge-noninvariant $\boldsymbol{\rho}_{\rm neq}$ expressions[169, 170, 171] for this task would give an incorrect result due to the fact that this system has non-zero spin density in equilibrium allowed by the time-reversal invariance breaking due to the Zeeman term.

Here we demonstrate in Sec. 6.3 how to construct the proper gauge-invariant nonequilibrium density matrix, in terms of the widely used NEGFs for devices[155, 157] attached to two macroscopic reservoirs, which ensures that no equilibrium contribution is included in the current-induced nonequilibrium expectation values of physical quantities. Section 6.4 shows three applications of this formalism in the computation of the components of spin torque vector for junctions illustrated in Fig. 6.1. We conclude in Sec. 6.5.

6.3 Gauge-Invariant Nonequilibrium Density Matrix for Steady-State Transport in the Linear-Response and Elastic Regime

Let us consider a finite-size open quantum system described on a tight-binding lattice[157, 162] where the operator $\hat{c}^{\dagger}_{n\sigma}$ ($\hat{c}_{n\sigma}$) creates (annihilates) electron with spin σ on site n (specific examples of such Hamiltonians $\mathbf{H}$ are given in Sec. 6.4). The system is opened by being attached to two macroscopic reservoirs—left (L) and right (R)—which drive charge current when they have different electrochemical potentials and, thereby, different Fermi functions $f_{L,R}(E) = f(E - eV_{L,R})$. The reservoirs and dissipation they are responsible for do not have to be modeled explicitly. Instead, one introduces the left and the right ideal semi-infinite leads through their retarded self-energies[184] $\mathbf{\Sigma}^{r}_{L,R}(E)$, so that Hamiltonian $\mathbf{H} + \mathbf{\Sigma}^{r}_{L,R}(E) + \mathbf{\Sigma}^{r}_{L,R}(E)$ of a finite-size but open quantum system acquires a continuous spectrum. Such spectrum is sufficient to bring the system into a true nonequilibrium steady-state with a finite value of the dc current at long enough times (as demonstrated by, e.g., real-time diagrammatic Monte Carlo simulations of nonequilibrium quantum transport[185]).

In stationary situations, either due to thermodynamic equilibrium or steady-state current flow, the density matrix ρ can be expressed[186] in terms of the lesser GF:

$$\rho = \frac{1}{2\pi i}\int dE\, \mathbf{G}^{<}(E). \tag{6.5}$$

In the case of elastic transport regime (i.e., when electron-electron, electron-phonon, and electron-spin dephasing processes can be neglected), from Eq. (2.43), the lesser GF

$$\mathbf{G}^{<}(E) = \mathbf{G}^{r}(E)[if_L(E)\mathbf{\Gamma}_L(E) + if_R(E)\mathbf{\Gamma}_R(E)]\mathbf{G}^{a}(E), \tag{6.6}$$

is given solely in terms of the retarded GF, $\mathbf{G}^{r}(E)$. Here $\mathbf{G}^{a}(E) = [\mathbf{G}^{r}(E)]^{\dagger}$ is the advanced GF, and $\mathbf{\Gamma}_{L,R}(E) = i[\mathbf{\Sigma}^{r}_{L,R}(E) - \mathbf{\Sigma}^{a}_{L,R}(E)]$ are the level broadening operators which quantify escape rates of electrons into the semi-infinite lead.

For purely computational purposes,[159, 160] one usually separates "equilibrium" and "nonequilibrium" contributions to ρ in the elastic transport regime:

$$\begin{aligned}\rho \;\; = \;\; & -\frac{1}{\pi}\int_{-\infty}^{+\infty} dE\, \mathrm{Im}\left[\mathbf{G}^{r}(E)\right] f_R(E) \\ & + \frac{1}{2\pi}\int_{-\infty}^{+\infty} dE\, \mathbf{G}^{r}(E)\cdot\mathbf{\Gamma}_L(E-eV_L)\cdot\mathbf{G}^{a}(E)\left[f_L(E) - f_R(E)\right].\end{aligned} \tag{6.7}$$

Here the first "equilibrium" term is typically computed via the semicircular path combined with the path in the complex plane parallel to the real axis,[159, 160] while the integration in the second "nonequilibrium" term is bounded between $E_F - eV_R$ and $E_F - eV_L$ by the difference of the Fermi functions (E_F is the Fermi energy for the whole device in equilibrium) and has to be done directly along the real axis.[160, 161]

While the second "nonequilibrium" term in Eq. (6.7) contains information about the bias voltage [through $f_L(E) - f_R(E)$], as well as about the lead assumed to be injecting electrons into the device (through $\mathbf{\Gamma}_L$), it cannot be used as the proper nonequilibrium density matrix that is defined by

$$\rho_{\mathrm{neq}} = \rho - \rho_{\mathrm{eq}} = \rho + \frac{1}{\pi}\int_{-\infty}^{+\infty} dE\, \mathrm{Im}\,\left[\mathbf{G}^{r}(E)\right] f(E). \tag{6.8}$$

This is due to the fact that second term in Eq. (6.8), which is the NEGF expression for the equilibrium density matrix ρ_{eq}, does not cancel the gauge-noninvariant first term in Eq. (6.7) which depends explicitly [through $f_R(E)$] on the arbitrarily set V_R and implicitly on the voltages applied to both reservoirs [through $\mathbf{G}^r(E)$].

Nevertheless, the second term in Eq. (6.7), written in the linear-response and zero-temperature limit (where it becomes the Fermi surface property)

$$\frac{1}{2\pi}\int_{-\infty}^{+\infty} dE\, \mathbf{G}^r(E)\cdot\mathbf{\Gamma}_L(E-eV_L)\cdot\mathbf{G}^a(E)[f_L(E)-f_R(E)] \longrightarrow \frac{eV_b}{2\pi}\mathbf{G}^r(E_F)\cdot\mathbf{\Gamma}_L(E_F)\cdot\mathbf{G}^a(E_F), \tag{6.9}$$

is often used in spintronics literature[169, 170, 171] as the putative (but improper due to being gauge-noninvariant) expression for ρ_{neq}. This gives ambiguous (i.e., dependent on the chosen V_R) nonequilibrium expectation values through $\text{Tr}[\rho_{\text{neq}}\ldots]$.

To derive the proper gauge-invariant ρ_{neq} in the linear-response limit, we first expand the retarded GF

$$\mathbf{G}^r(E) = \frac{1}{E-\mathbf{H}-eU-\mathbf{\Sigma}_L(E-eV_L)-\mathbf{\Sigma}_R(E-eV_R)}, \tag{6.10}$$

to linear order in the bias voltage. Here $\mathbf{H}$ is the Hamiltonian of the active region of the device and eU is the potential profile across the active region of the device when current is flowing. This is achieved in two steps, where we first rewrite Eq. (6.10) using the exact Dyson equation[165]

$$\begin{aligned}\mathbf{G}^r(E) =& \mathbf{G}_0^r(E)+\mathbf{G}_0^r(E)\left[eU+\mathbf{\Sigma}_L(E-eV_L)\right.\\ &\left.-\mathbf{\Sigma}_L(E)+\mathbf{\Sigma}_R(E-eV_R)-\mathbf{\Sigma}_R(E)\right]\mathbf{G}^r(E),\end{aligned} \tag{6.11}$$

in terms of the retarded GF at zero bias voltage

$$\mathbf{G}_0^r(E) = \left[E-\mathbf{H}-\mathbf{\Sigma}_L(E)-\mathbf{\Sigma}_R(E)\right]^{-1}. \tag{6.12}$$

In the second step, we expand the self-energies

$$\mathbf{\Sigma}_{L,R}(E-eV_L) \approx \mathbf{\Sigma}_{L,R}(E) - eV_{L,R}\frac{\partial\mathbf{\Sigma}_{L,R}}{\partial E}\bigg|_{V_{L,R}=0}, \tag{6.13}$$

to linear order in voltage. Combining Eqs. (6.11) and (6.13) gives

$$\mathbf{G}^r(E) \approx \mathbf{G}_0^r(E) + \mathbf{G}_0^r(E) \left[eU - eV_L \frac{\partial \mathbf{\Sigma}_L}{\partial E}\bigg|_{V_L=0} - eV_R \frac{\partial \mathbf{\Sigma}_R}{\partial E}\bigg|_{V_R=0} \right] \mathbf{G}_0^r(E). \tag{6.14}$$

By plugging Eq. (6.14) into Eq. (6.8), together with the expansion of the Fermi function

$$f_{L,R}(E) \approx f(E) - eV_{L,R} \frac{\partial f}{\partial E}\bigg|_{V_{L,R}=0}, \tag{6.15}$$

and expansion of the level broadening operator

$$\mathbf{\Gamma}_L(E - eV_L) \approx \mathbf{\Gamma}_L(E) - eV_L \frac{\partial \mathbf{\Gamma}_L}{\partial E}\bigg|_{V_L=0}, \tag{6.16}$$

and by keeping only the terms linear in the applied voltage, we finally obtain the gauge-invariant nonequilibrium density matrix for the steady-state transport in the linear-response regime

$$\begin{aligned} \rho_{\text{neq}} = &-\frac{eV_R}{\pi} \int_{-\infty}^{+\infty} dE \, \text{Im}\left[\mathbf{G}_0^r\right] \left(-\frac{\partial f}{\partial E}\right) \\ &- \frac{1}{\pi} \int_{-\infty}^{+\infty} dE \, \text{Im}\left[\mathbf{G}_0^r \left(eU - eV_L \frac{\partial \mathbf{\Sigma}_L}{\partial E} - eV_R \frac{\partial \mathbf{\Sigma}_R}{\partial E} \right) \mathbf{G}_0^r \right] f(E) \\ &+ \frac{eV_b}{2\pi} \int_{-\infty}^{+\infty} dE \, \mathbf{G}_0^r \mathbf{\Gamma}_L \mathbf{G}_0^a \left(-\frac{\partial f}{\partial E}\right). \end{aligned} \tag{6.17}$$

In the zero-temperature limit, this expression simplifies further

$$\begin{aligned} \rho_{\text{neq}} = &-\frac{eV_R}{\pi} \text{Im}\left[\mathbf{G}_0^r(E_F)\right] \\ &- \frac{1}{\pi} \int_{-\infty}^{E_F} dE \, \text{Im}\left[\mathbf{G}_0^r \left(eU - eV_L \frac{\partial \mathbf{\Sigma}_L}{\partial E} - eV_R \frac{\partial \mathbf{\Sigma}_R}{\partial E} \right) \mathbf{G}_0^r \right] f(E) \\ &+ \frac{eV_b}{2\pi} \mathbf{G}_0^r(E_F) \cdot \mathbf{\Gamma}_L(E_F) \cdot \mathbf{G}_0^a(E_F), \end{aligned} \tag{6.18}$$

We note that expansions discussed above could be performed further[165] to obtain ρ_{neq} order-by-order in the applied bias voltage.

The third term in Eq. (6.17), when traced with the total current operator[157] $\mathbf{I} = 2e\mathbf{\Gamma}_R/\hbar$ in the right lead, gives the usual Landauer-type conductance formula (derived by Caroli *et al.* in Ref. [187]):

$$\begin{aligned} G &= \frac{I}{V_b} = \mathrm{Tr}[\rho_{\mathrm{neq}}\mathbf{I}] \\ &= \frac{2e^2}{h}\int_{-\infty}^{+\infty} dE\,\mathrm{Tr}\left[\mathbf{\Gamma}_R\mathbf{G}_0^r\mathbf{\Gamma}_L\mathbf{G}_0^a\right]\left(-\frac{\partial f}{\partial E}\right). \end{aligned} \tag{6.19}$$

The same trace with the first two terms in Eq. (6.17) is identically equal to zero because no total charge current can flow into the leads in thermodynamic equilibrium, even if time-reversal invariance is broken by magnetic field.[167]

The first two terms in Eq. (6.18) makes this expression for ρ_{neq} quite different from often[169, 170] used but incorrect Eq. (6.9). Their role is to properly subtract any non-zero expectation value that exists in thermodynamic equilibrium. For example, the first term in Eq. (6.18) is easily interpreted using ρ_{eq} in Eq. (6.8)—when traced with an operator this term will give equilibrium expectation value at the Fermi energy which must be removed [so the sign in front of the first term different from the sign in front of the third term in Eq. (6.18)]. The second term in Eq. (6.18) ensures the gauge invariance of the nonequilibrium expectation values, while making the whole expression non-Fermi-surface property. It also renders usage of Eq. (6.18) computationally demanding due to the requirement to perform integration from the bottom of the band up to the Fermi energy, as discussed in more detail in Sec. 6.4.

6.4 Applications to Spin Torque Calculations

The NEGF formalism offers three different algorithms[169, 178, 62] to compute STT at finite bias voltage in F′/I/F MTJs, which are delineated below, as well as an additional algorithm for STT in the linear response (suitable for F′/N/F spin valves) using the GF expressions for the so-called spin-mixing conductance.[175] We start by explaining first the often employed[177, 178] model for MTJs in Fig. 6.1(a) defined

on a cubic tight-binding lattice, with lattice constant a and unit area $a^2 \equiv \square$, where monolayers of different materials (F, N, I) are infinite in the transverse to transport direction yz-planes. The F, N, and I layers are described by a tight-binding Hamiltonian with a single s-orbital per site defined in Eq. (5.6). In the numerical calculations we choose the exchange splitting to be $\Delta_n = 1.0$ eV, where $\Delta_n \equiv 0$ within semi-infinite ideal N leads or within the tunnel barrier region I (the corresponding Hamiltonians are labeled by $\hat{H}_F$, $\hat{H}_N$, and $\hat{H}_I$). Here $\vec{\sigma} = (\sigma_x, \sigma_y, \sigma_z)$ is the vector of the Pauli matrices and $[\vec{\sigma}_\alpha]_{\sigma\sigma'}$ denotes the Pauli matrix elements.

The simplest route[177, 178] to STT is to compute the vector of spin current between two neighboring monolayers n and $n+1$ coupled by the hopping parameter γ

$$\mathbf{I}^S_{n,n+1} = \frac{\gamma}{4\pi} \int dE d\mathbf{k}_\parallel \, \mathrm{Tr}_\sigma \left[\vec{\sigma}(\mathbf{G}^<_{n+1,n} - \mathbf{G}^<_{n,n+1})\right]. \tag{6.20}$$

The integration over $\mathbf{k}_\parallel$ is required because of the assumed translational invariance in the transverse direction. For conserved total spin, when SOC and other spin-flipping interactions can be neglected, the monolayer-resolved[188] STT is given by

$$\mathbf{T}_n = -\nabla \cdot \mathbf{I}^S = \mathbf{I}^S_{n-1,n} - \mathbf{I}^S_{n,n+1}, \tag{6.21}$$

which is a discrete form of the divergence of the spin current. The total torque on the free magnetization of the F layer is then obtained from

$$\mathbf{T} = \sum_{n=0}^{\infty} (\mathbf{I}^S_{n-1,n} - \mathbf{I}^S_{n,n+1}) = \mathbf{I}^S_{-1,0} - \mathbf{I}^S_{\infty,\infty} = \mathbf{I}^S_{-1,0}. \tag{6.22}$$

Here the subscripts -1 and 0 refer to the last monolayer of the I barrier (or N spacer in the case of F′/N/F spin valves) and the first monolayer of the free F layer, respectively. This methodology *requires* that the free F layer is semi-infinite. Furthermore, it cannot be applied to semi-MTJ in Fig. 6.1(b) since $\mathbf{I}^S_{-1,0}$ is *insufficient* to get STT if strong SOC is present directly at the I/F interface. Also, spin current will not decay, $\mathbf{I}^S_{\infty,\infty} \neq 0$, if SOC is present in the bulk of the free F layer.[96, 98] We note that interfacial SOC also renders the spin-mixing conductance an ill-defined quantity.[175]

A more general approach to compute the STT vector in the presence of SOC or other spin-nonconserving interactions is to use the torque operator[169, 175, 179]

$$\mathbf{T} = \frac{d\mathbf{S}}{dt} = \frac{1}{2i}[\vec{\sigma}, \mathbf{H}_F] \tag{6.23}$$

and find its expectation value $\mathbf{T} = [\mathbf{T}\rho_{\text{neq}}]$. Here $\mathbf{S} = \hbar\vec{\sigma}/2$ is the electron spin operator. Using $\mathbf{H}_F$ in Eq. (5.6), gives $\mathbf{T} = \Delta(\vec{\sigma} \times \mathbf{m})/2$. The torque operator approach is applicable to *finite thickness* free F layers, where it gives the layer-resolved[169, 188] STT whose sum over all monolayers comprising the free F layer gives the total STT.

For conventional F′/I/F MTJs, where the reference F′ layer with fixed magnetization $\mathbf{m}'$ plays the role of an external spin-polarizer, it is customary to analyze the in-plane (originally considered by Slonczewski [173]) and perpendicular (also called "field-like torque" [27]) components of the STT vector [42], $\mathbf{T} = \mathbf{T}_{\parallel} + \mathbf{T}_{\perp}$. The in-plane torque $\mathbf{T}_{\parallel} = \tau_{\parallel}\mathbf{m} \times (\mathbf{m} \times \mathbf{m}')$ is purely nonequilibrium and competes with the damping. The perpendicular torque $\mathbf{T}_{\perp} = \tau_{\perp}\mathbf{m} \times \mathbf{m}'$ arises from spin reorientation at the interfaces and possesses both equilibrium (i.e., interlayer exchange coupling) and nonequilibrium contributions which act like an effective magnetic field on the magnetization $\mathbf{m}$ of the free F layer. While $\mathbf{T}_{\perp}$ component is vanishingly small in metallic spin valves [189, 188], it can be substantial [42] in MTJs due to the momentum filtering imposed by the tunnel barrier [176, 177].

The third[62] NEGF-based approach to the computation of STT vector is also applicable to F layers of finite thickness with bulk or interfacial SOC, while offering additional physical insights. If the device Hamiltonian depends on a variable q, which corresponds to slow collective classical degrees of freedom, the expectation value of the corresponding canonical force $\mathbf{Q} = -\partial\mathbf{H}/\partial q$ can obtained from

$$Q = -\frac{1}{2\pi i}\int_{-\infty}^{+\infty} dE\,\mathrm{Tr}\left[\frac{\partial \mathbf{H}}{\partial q}\mathbf{G}^{<}\right] = -\left\langle \frac{\partial \mathbf{H}}{\partial q}\mathbf{G}^{<}\right\rangle. \tag{6.24}$$

Here we used the density matrix Eq. (6.5) expressed in terms of $\mathbf{G}^{<}(E, q)$ as adiabatic lesser GF computed for a frozen-in-time variable q. By exchanging the derivative

between the Hamiltonian and $\mathbf{G}^<(E,q)$,

$$Q = -\frac{\partial \langle \mathbf{H}\mathbf{G}^< \rangle}{\partial q} + \left\langle \frac{\mathbf{H}\partial \mathbf{G}^<}{\partial q} \right\rangle, \tag{6.25}$$

and by using Eqs. (6.6) and (6.10) for the retarded and lesser GFs, respectively, we obtain

$$Q = i\left\langle \frac{\partial \mathbf{G}^r}{\partial q}\mathbf{\Sigma}^<\mathbf{G}^a\mathbf{\Gamma} \right\rangle - \left\langle \mathbf{\Sigma}^<\frac{\partial \mathbf{G}^r}{\partial q} \right\rangle. \tag{6.26}$$

We note that Eq. (6.26) is akin to the mean value of time-averaged force in nonequilibrium Born-Oppenheimer approaches[190, 43] to current-induced forces exerted by conduction electrons on ions in nanojunctions or mechanical degrees of freedom in nanoelectromechanical systems whose collective modes are slow compared to electronic time scales. Furthermore, the same derivation that leads to Eq. (6.26) can be extended to obtain[43] the noise and damping terms, expressed solely in terms of electronic NEGFs, which enter into the nonequilibrium Langevin equation (taking the form of a generalized Landau-Lifshitz-Gilbert equation) for the free magnetization of the F layer. Equation (6.26) also allows us to establish the Onsager-type[96] reciprocal relation between STT and spin pumping,[30] where microwave driven precessing magnetization of a single F layer pumps pure spin current into adjacent normal metal layers.

This can be proven easily by choosing $q = \omega t$ in which case the average of $Q(t)$ in linear bias approximation will be $\frac{\delta Q}{\delta V_b} = \frac{e}{2\pi\omega}\Im Tr(\frac{\partial \mathbf{G}^r}{\partial t}\mathbf{\Gamma}^L\mathbf{G}^a\mathbf{\Gamma}) = I_{pumping}/\omega$

The application of Eq. (6.26) to get T_α ($\alpha = x, y, z$) component of the STT vector acting on the magnetization of the free F layer within, e.g., F′/I/F MTJ proceeds by first computing $\mathbf{G}^r$ for the device described by the Hamiltonian $\hat{H} = \hat{H}_{F'} + \hat{H}_I + \hat{H}_F$. In the second step, the Hamiltonian of the F layer is modified

$$\hat{H}_F^q = \hat{H}_F + q\sum_{n,\sigma\sigma',\mathbf{k}_\parallel} \hat{c}^\dagger_{n\sigma,\mathbf{k}_\parallel}[\mathbf{e}_\alpha \cdot (\mathbf{m}\times\vec{\sigma})]_{\sigma\sigma'}\hat{c}_{n\sigma',\mathbf{k}_\parallel}, \tag{6.27}$$

and $\mathbf{G}^r[\mathbf{H}^q]$ is computed for the new Hamiltonian $\mathbf{H}^q = \mathbf{H}_{F'} + \mathbf{H}_I + \mathbf{H}_F^q$. This yields

$$\frac{\partial \mathbf{G}^r}{\partial q} \approx \frac{\mathbf{G}^r[\mathbf{H}^q] - \mathbf{G}^r[\mathbf{H}]}{q}, \tag{6.28}$$

where we typically employ $q = 10^{-7}$ as the infinitesimal. The derivative $\partial \mathbf{G}^r/\partial q$ plugged into Eq. (6.26) yields $Q = T_\alpha$.

Equation (6.26) includes both the equilibrium[169, 176, 177] $\mathbf{T}_\perp(V_b = 0)$ and experimentally measured[42] *nonequilibrium* $\mathbf{T}_\perp(V_b) - \mathbf{T}_\perp(V_b = 0)$ contribution to $\mathbf{T}_\perp$. The linear-response contribution at zero temperature can be extracted by using $\rho_{\rm neq}$ in Eq. (6.18)

$$Q_{\rm neq} = -\sum_p V_p \mathrm{Tr}\left[\frac{\partial \mathbf{G}_0^r}{\partial q}\mathbf{\Gamma}_p \mathbf{G}_0^a \mathbf{\Gamma} - i\frac{\partial \mathbf{G}_0^r}{\partial q}\mathbf{\Gamma}_p\right] \\ -\sum_p V_p \mathrm{Im}\left\{\int_{-\infty}^{E_F} dE\, \mathrm{Tr}\left[\frac{\partial \mathbf{G}_0^r}{\partial q}\frac{\partial \mathbf{H}}{\partial V_p} - \frac{\partial \mathbf{G}_0^r}{\partial q}\frac{\partial \mathbf{\Sigma}_p^r}{\partial E}\right]\right\}. \tag{6.29}$$

Since $\mathbf{T}_\parallel$ is zero in equilibrium, the second sum in Eq. (6.8) has to be computed only for $\mathbf{T}_\perp$.

Thus, Eq. (6.29) is more efficient than the torque operator method when computing $\mathbf{T}_\parallel$ since the former requires to know only the submatrix of the retarded GF which couples the first and last monolayer of the active device region, while the later requires to obtain the retarded GF on each monolayer of the free F layer. When computing $\mathbf{T}_\perp$, both methods have similar computational complexity since they require knowledge of the full retarded GF matrix.

When computing the nonequilibrium $\mathbf{T}_\perp$, we use the fact that the integrand in the second term of Eq. (6.29) [which stems from the second term in Eq. (6.18)] is analytic function in the upper complex plane. Then, as demonstrated in Fig. 6.2, the integration can proceed along the contour composed of an infinite semi-circle, along which the trace is zero due to $\partial \mathbf{G}^r/\partial q \sim 1/E^2$, and the vertical line at $E = E_F$. We note that adaptive integration is required very close to E_F. For junctions with transverse translational symmetry, such as the ones in Fig. 6.1(a) and (b), one has to perform additional integration over $\mathbf{k}_\parallel$. This requires adaptive scheme (or very dense k-point sampling in brute force schemes[188]) to converge the integrand because of the fact that STT can change fast in specific regions of the 2D Brillouin zone.

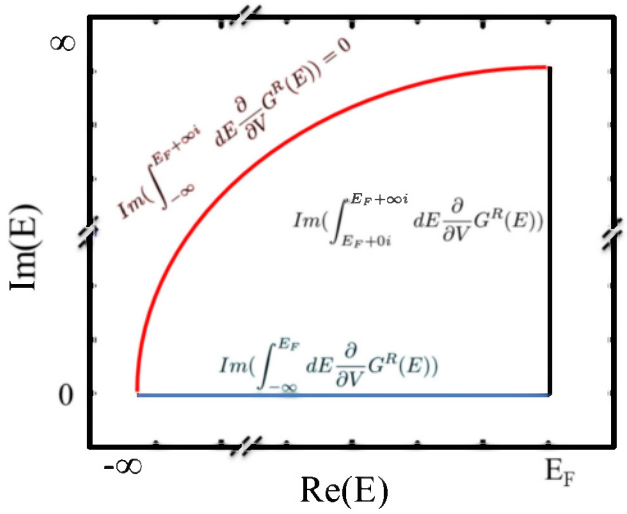

Figure 6.2: Complex plane integration contour for the derivative of retarded Green function which shows the integration over energy can be performed over the imaginary axis where (unlike the real axis integration which suffers from singularities) the integrand depends smoothly on the integration variable.

6.4.1 Application to Spin-Transfer Torque in MTJs

The MTJ in Fig. 6.1(a) is modeled by Hamiltonian in Eq. (5.6) where the I layer has thickness $d_{\rm I} = 5$ monolayers and $d_{\rm F} = 20$ for both the fixed F′ and free F layers. The potential barrier within the I layer is modeled using $\varepsilon_n = 6$ eV within that layer. The Fermi energy of this device in equilibrium is set at $E_F = 3.1$ eV. In such symmetric MTJs, whose ferromagnetic layers are of the same thickness and with the same mean-field exchange splitting $\Delta = 1.0$ eV, the linear-response $\mathbf{T}_\perp \propto V_b$ component of the STT vector is is identically zero. [42, 176, 177, 179]

This is confirmed in Fig. 6.3(a) using the proper gauge-invariant nonequilibrium density matrix in Eq. (6.18). On the other hand, using the improper gauge-noninvariant expression Eq. (6.9) for $\rho_{\rm neq}$ gives non-zero value for $\mathbf{T}_\perp \propto V_b$

which changes with the way the voltage bias is chosen and gives zero for symmetric bias of $(-V_b/2, V_b/2)$.

. Since $\mathbf{T}_\parallel$ does not have non-zero expectation value in equilibrium, both the proper and improper expressions for $\rho_{\rm neq}$ give the same result, where Fig. 6.3 reproduces

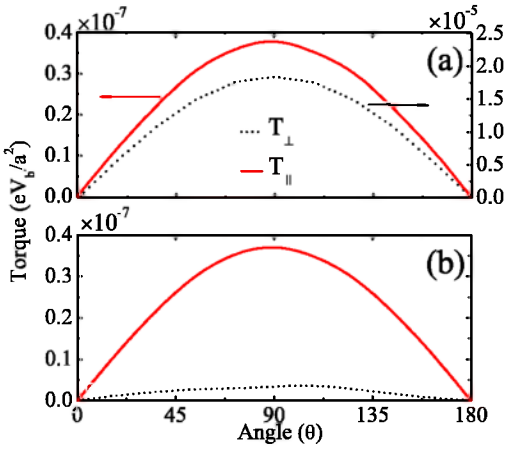

Figure 6.3: Angular dependence of the in-plane and perpendicular components of STT vector in symmetric F′/I/F MTJs, illustrated in Fig. 6.1(a), computed at zero temperature and for linear-response bias voltage V_b using: (a) the proper gauge-invariant expression Eq. (6.18) for $\rho_{\rm neq}$; and (b) the improper gauge-noninvariant expression Eq. (6.9) for $\rho_{\rm neq}$.

the well-known $\propto \sin\theta$ angular dependence.

6.4.2 Application to Spin-Transfer Torque in Semi-MTJs with Interfacial Rashba SOC

To account for the Rashba SOC at the I/F interface in N/I/F semi-MTJ in Fig. 6.1(b), we add the following term

$$\varepsilon_{0,\mathbf{k}_\parallel} \mapsto \varepsilon_{0,\mathbf{k}_\parallel} + \alpha(\vec{\sigma} \times \mathbf{k}_\parallel) \cdot \mathbf{e}_x, \tag{6.30}$$

to the on-site energy [see Eq. 5.6] of first monolayer 0 of the F layer which is coupled to the I layer. Here $\gamma_{\rm SO} = \alpha/2a$ quantifies the strength of the Rashba SOC, which we set at $\gamma_{\rm SO} = 0.1$ eV. The potential barrier within the I layer is modeled using $\varepsilon_n = 6$ eV within that layer. The Fermi energy of this device in equilibrium is set at $E_F = 3.1$ eV.

The standard experiments to detect the presence of Rashba SOC at F/I interfaces of N/I/F junctions involve measurement[63, 64, 93, 94, 95] of the so-called out-of-plane TAMR coefficient,[65, 30] $\mathrm{TAMR}\,(\phi) = [R(\phi) - R(0)]/R(0)$. Here $R(0)$ is

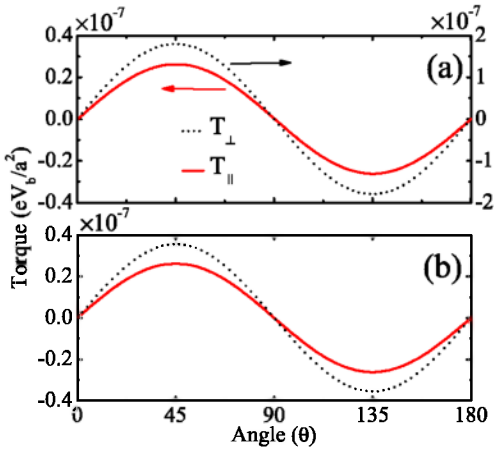

Figure 6.4: Angular dependence of the in-plane and perpendicular components of STT vector in N/I/F semi-MTJs, illustrated in Fig. 6.1(b), computed at zero temperature and for linear-response bias voltage V_b using: (a) the proper gauge-invariant expression Eq. (6.18) for $\rho_{\rm neq}$; and (b) the improper gauge-noninvariant expression Eq. (6.9) for $\rho_{\rm neq}$.

the resistance of semi-MTJ when static magnetization of its F layer is parallel to the x-axis, as the direction of transport in Fig. 6.1, and $R(\phi)$ is the junction resistance when magnetization is rotated by an angle ϕ with respect to the x-axis within the xz-plane.

Since the interfacial SOC is linear in momentum, TAMR vanishes at the first order in $\gamma_{\rm SO}$ after averaging over the Fermi sphere. However the ferromagnet contains local exchange field and a net transfer of angular momentum occurs at the second order, so that TAMR $\propto \gamma_{\rm SO}^2$. This is also the origin of recently predicted[61, 62] unconventional TAMR-related STT in semi-MTJs in Fig. 6.1(b). Although semi-MTJs lack the conventional spin-polarizing F$'$ layer, whose magnetization $\mathbf{m}'$ together with free magnetization $\mathbf{m}$ define the plane with respect to which STT vector is decomposed, the usual torque components can be defined[61, 62] as

$$\mathbf{T} = \mathbf{T}_{\parallel} + \mathbf{T}_{\perp} = \tau_{\parallel}\mathbf{m}\times(\mathbf{m}\times\mathbf{e}_x) + \tau_{\perp}\mathbf{m}\times\mathbf{e}_x. \tag{6.31}$$

Here the direction of transport ($\mathbf{e}_x$ in Fig. 6.1) replaces $\mathbf{m}'$.

Since semi-MTJs in Fig. 6.1(b) are always structurally asymmetric, $\mathbf{T}_\perp \propto V_b$ torque component is necessarily non-zero. To get its correct value requires to properly remove the equilibrium contribution $\mathbf{T}_\perp(V_b = 0)$, which is accomplished using the proper gauge-invariant ρ_{neq} in Eq. (6.18) with the result being shown in Fig. 6.4(a). Comparing this with incorrectly computed $\mathbf{T}_\perp$, using gauge-noninvariant ρ_{neq} in Eq. 6.9, shows an order of magnitude discrepancy which is over-estimated/under-estimated when a $(V_b, 0)/(0, V_b)$ (where the first lead is conncted to the ferromagnet) bias is chosen.

Unlike the symmetric angular dependence of conventional STT in MTJs discussed in Sec. 6.4.1, both $\mathbf{T}_\perp$ and $\mathbf{T}_\parallel$ exhibit $\propto \sin 2\theta$ angular dependence due to the existence of four stable magnetic states—two perpendicular to the I/F interface ($\theta = 0, 180°$) and two parallel to that interface ($\theta = \pm 90°$). The existence of both in-plane and perpendicular torque components in Eq. (6.2) is analogous to conventional STT in MTJs discussed in Sec. 6.4.1, where $\mathbf{T}_\perp \propto \mathbf{m} \times \mathbf{e}_x$ competes with the demagnetizing field and the perpendicular anisotropy while $\mathbf{T}_\parallel \propto \mathbf{m} \times (\mathbf{m} \times \mathbf{e}_x)$ competes with the damping. Thus, the unconventional TAMR-related STT can induce magnetization switching from out of plane to in plane and vice versa, as well as the current-driven magnetization precessions (for more details about predicted manifestations and its potential applications see Refs. [61, 191, 62]).

6.4.3 Application to Spin-Orbit Torques in Laterally Patterned Heterostructures with Strong Interfacial Rashba Coupling

The early experimental confirmation[192, 193] of the spin Hall effect in semiconductor devices with extrinsic (due to impurities) or intrinsic (due to band structure) SOC—where longitudinal unpolarized charge current generates transverse pure spin current or spin accumulation at the lateral edges—has ignited theoretical studies of spin accumulation around the device edges in the diffusive[194, 195, 196] and ballistic[171, 197, 198, 199, 200] transport regimes. Since the prediction of the Edelstein effect, [54] there has been also a lot of interest to understand how *nonequilbrium*

spin density emerges in the interior of diffusive 2D systems with SOC within inversion asymmetric semiconductor heterostructures.[55, 194] Most of such calculations have been focused on 2DEGs or 2D hole gases (2DHGs) with the Rashba SOC (linear in momentum[171, 194, 196, 197, 198, 199, 200] in the case of 2DEGs, or cubic[195] in momentum in the case of 2DHGs) in different geometries where 2D system is attached to two or more electrodes. For analytical calculations, it is advantageous to make one[194, 198, 199, 200] or both[55] dimensions of 2D systems infinite. These studies have been typically conducted using either the Kubo formula[195, 55] or the NEGF formalism.[171, 197, 194]

The analogous problem arises in the case of SO torques in the laterally patterned N/F/I heterostructures in Fig. 6.1(c), except that the effective mass Hamiltonian of 2D system at the N/F interface

$$\mathbf{H} = \frac{\hat{\mathbf{p}}}{2m^*} + \frac{\alpha}{\hbar}(\hat{\mathbf{p}} \times \mathbf{e}_z) \cdot \vec{\sigma} - \frac{\Delta}{2}\mathbf{m} \cdot \vec{\sigma}, \tag{6.32}$$

has both the Rashba (second) and Zeeman (third) term. Here $\hat{\mathbf{p}} = (\hat{p}_x, \hat{p}_y)$ is the momentum operator and Δ is the mean-field exchange splitting due to the magnetization of the F layer pointing along the unit $\mathbf{m}$ vector. We recall that Hamiltonian in Eq. (6.32) (with an additional term for static impurity potential) is also often used to study fundamental aspects of the anomalous Hall effect in itinerant metallic ferromagnets.[92]

While α in 2DEGs within typical semiconductor heterostructures is in the range 0.001–0.1 eVÅ, it is estimated to reach[56] $\simeq$ 1 eVÅ in laterally patterned Pt/Co/AlO_x heterostructures in Fig. 6.1(c). The very recent transport experiments[48] have suggested that Rashba SOC could be responsible for the observed magnetization switching in a single F layer embedded between two asymmetric interfaces. For example, such effect was observed in Pt/Co/AlO_x multilayers, but not in the inversion symmetric ones Pt/Co/Pt. The experiments reported in Refs. [48, 49] have also utilized heavy atoms and surface oxidation to create strong out-of-plane potential gradient in Pt/Co/AlO_x junctions and enhance the interfacial Rashba SOC.

When unpolarized current is injected into such 2DEG along the x-axis in Fig. 6.1(c), the ensuing nonequilibrium spin density can be obtained from

$$\mathbf{S}^{\rm neq} = \frac{\hbar}{2}{\rm Tr}\left[\rho_{\rm neq}\vec{\sigma}\right]. \tag{6.33}$$

If the trace here is taken over the spin Hilbert space $\mathcal{H}_S$, one obtains the local spin density $\mathbf{S}^{\rm neq}(\mathbf{r})$, while taking trace over the full Hilbert space $\mathcal{H}_{\rm O}\otimes\mathcal{H}_{\rm S}$ (where $\mathcal{H}_{\rm O}$ is the orbital space) gives total spin $\int d\mathbf{r}\,\mathbf{S}^{\rm neq}(\mathbf{r})$ [or $\sum_{\mathbf{r}}\mathbf{S}^{\rm neq}(\mathbf{r})$ in some discrete representation].

The knowledge of $\mathbf{S}^{\rm neq}$ makes it possible to compute[56, 99, 181, 182] the SO torque per unit volume acting on the magnetization of the F layer, $\mathbf{T}_{\rm SO} = \Delta(\mathbf{m}\times\mathbf{S}^{\rm neq})/2$. Since Edelstein effect produces transverse nonequilibrium spin density, it has been considered that $\mathbf{T}_{\rm SO}$ acts as an effective magnetic field that cannot excite self-sustained magnetization precession because $\mathbf{T}_{\rm SO}$ does not compete with the damping. [56] Microscopically, SO torque transfers orbital momentum from the lattice to the spin system, unlike conventional STT which operates by transferring spin angular momentum between two non-collinear magnetic layers or domains.

Below we use $\mathbf{m}\equiv\mathbf{e}_z$ as in the experiments.[48, 49, 56] The nonequilbrium spin density $\mathbf{S}^{\rm neq}(\mathbf{r})$ has been computed for 2DEG wires[183] described by the Hamiltonian Eq. (6.32), but confined in the y-direction and including scattering of static impurities to generate the diffusive transport regime. Here we choose to analyze ballistic 2DEG which offers simplicity in illustrating the application of Eq. (6.18). Our 2DEG is infinite in the transverse (the y-axis in Fig. 6.1) direction while being $L_x = 100$ sites long in the x-direction of transport (which is the same two-terminal device geometry employed in Ref. [194]). Due to the periodicity in the y-direction, we perform additional integration over k_y to obtain

$$\mathbf{S}^{\rm neq}(x) = \frac{\hbar}{2}\int dk_y\,{\rm Tr}\left[\rho_{\rm neq}(k_y)\vec{\sigma}\right]. \tag{6.34}$$

The discretization[162] of Eq. (6.32) leads to a tight-binding like Hamiltonian

defined on the square lattice of sites $\mathbf{n} = (n_x, n_y)$

$$\begin{aligned}\hat{H} &= \sum_{\mathbf{n},\sigma\sigma'} \hat{c}^{\dagger}_{\mathbf{n}\sigma} \left(\varepsilon_{\mathbf{n}} \delta_{\sigma\sigma'} - \frac{\Delta}{2} \mathbf{m} \cdot [\vec{\sigma}]_{\sigma\sigma'} \right) \hat{c}_{\mathbf{n}\sigma'} \\ &+ \sum_{\mathbf{n}\mathbf{n}'\sigma\sigma'} \hat{c}^{\dagger}_{\mathbf{n}\sigma} t^{\sigma\sigma'}_{\mathbf{n}\mathbf{n}'} \hat{c}_{\mathbf{n}'\sigma'}. \end{aligned} \tag{6.35}$$

whose nearest-neighbor hopping parameters are non-trivial 2×2 Hermitian matrices $\mathbf{t}_{\mathbf{n}'\mathbf{n}} = (\mathbf{t}_{\mathbf{n}\mathbf{n}'})^{\dagger}$ in the spin space:

$$\mathbf{t}_{\mathbf{n}\mathbf{n}'} = \begin{cases} -\gamma \mathbf{I}_{\mathrm{s}} - i\gamma_{\mathrm{SO}} \sigma_y & (\mathbf{n} = \mathbf{n}' + \mathbf{e}_x) \\ -\gamma \mathbf{I}_{\mathrm{s}} + i\gamma_{\mathrm{SO}} \sigma_x & (\mathbf{n} = \mathbf{n}' + \mathbf{e}_y) \end{cases}, \tag{6.36}$$

Here $\gamma = 1$ eV is the orbital hopping, $\gamma_{\mathrm{SO}} = \alpha/2a$ is SO hopping which we set at $\gamma_{\mathrm{SO}} = 0.1$ eV, and we chose $\Delta = 0.6$ eV for exchange splitting. The Fermi energy in this model is chosen close to the bottom of the band $E_F = -3.5$ eV in order to maintain the parabolic energy-momentum dispersion of the original effective mass Hamiltonian Eq. (6.32). While the on-site potential $\varepsilon_{\mathbf{n}}$ can be used to introduce disorder, we set $\varepsilon_{\mathbf{n}} = 0$ for our ballistic 2DEG.

In some of the prior studies of current-driven nonequilibrium spin density in 2DEGs with the Rashba SOC, as described by Eq. (6.35) with $\Delta = 0$, one can find naïve attempts to derive a linear-response formula for $\mathbf{S}^{\mathrm{neq}}(\mathbf{r})$ based on NEGFs. For example, Ref. [171] starts from the general expression $\mathbf{S}^{\mathrm{neq}}(\mathbf{r}) = \frac{\hbar}{4\pi i} \int dE \, \mathrm{Tr}_{\mathrm{S}}[\vec{\sigma} \mathbf{G}^{<}(E)]$, obtained by combining Eqs. (6.1) and (6.5), and then expands $\mathbf{G}^{<}(E)$ to linear order in small bias voltage

$$\mathbf{G}^{<}(E) = \mathbf{G}^{<}(E)\Big|_{V_b=0} - i\frac{eV_b}{2} \frac{\partial f(E)}{\partial E} [\mathbf{G}^{r}(E)(\mathbf{\Gamma}_L - \mathbf{\Gamma}_R)\mathbf{G}^{a}] + \mathcal{O}(V_b^2), \tag{6.37}$$

to arrive at the following formula

$$\mathbf{S}^{\mathrm{neq}}(\mathbf{r}) = \frac{\hbar e V_b}{4} \mathrm{Tr}_{\mathrm{S}}[\vec{\sigma} \{ \mathbf{G}^{r}(E_F)(\mathbf{\Gamma}_L - \mathbf{\Gamma}_R)\mathbf{G}^{a}(E_F)]. \tag{6.38}$$

This derivation assumes that the bias voltage is split using $V_L = -eV_b/2$ and $V_R = V_b/2$. However, this expression is not gauge-invariant since using $V_L = -V_b/2$ and $V_R = 0$

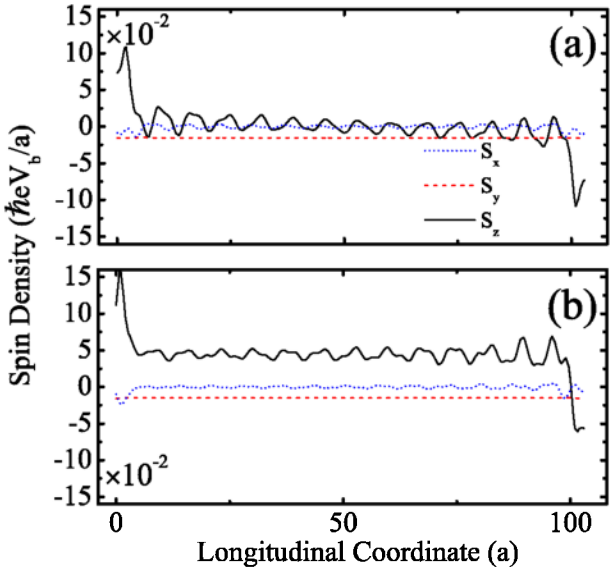

Figure 6.5: The current-driven nonequilibrium spin density $\mathbf{S}^{\rm neq}(x)$ in the ferromagnetic 2DEG with the Rashba SOC, described by the Hamiltonian Eq. (6.32) with $\gamma_{\rm SO} = 0.1$ eV and $\Delta = 0.6$ eV, which is infinite in the y-direction and of finite-size in the transport x-direction. This quantity is computed at zero temperature and for linear-response bias voltage V_b using: (a) the proper gauge-invariant expression Eq. (6.18) for $\rho_{\rm neq}$; and (b) the improper gauge-noninvariant expression Eq. (6.9) for $\rho_{\rm neq}$.

(or, equivalently, shifting the potential everywhere by a constant $-V_b/2$) would give different expansion

$$\mathbf{G}^<(E) = \mathbf{G}^<(E)\Big|_{V_b=0} - ieV_b\frac{\partial f(E)}{\partial E}[\mathbf{G}^r(E)\mathbf{\Gamma}_L\mathbf{G}^a] + \mathcal{O}(V_b^2), \tag{6.39}$$

and different corresponding formula for $\mathbf{S}^{\rm neq}(\mathbf{r})$.

While the usage of such gauge-noninvariant expressions [note that Eq. (6.39) is equivalent to employing Eq. (6.9)] does not affect previous results [162, 171, 197] obtained for the Rashba spin-split 2DEG in the absence of magnetization or external magnetic field, where equilibrium spin density is zero due to the fact that SOC alone does not break time-reversal invariance, it will lead to ambiguous results if applied to a 2D system described by the Hamiltonian Eq. (6.32). We illustrate this in Fig. 6.5, where the difference between the results computed using improper Eq. (6.9) and proper Eq. (6.18) expressions for $\rho_{\rm neq}$ is less dramatic than in the case of $\mathbf{T}_\perp$ discussed in Secs. 6.4.1 and 6.4.2.

For comparison, we also plot $\mathbf{S}^{\rm neq}(x)$ in Fig. 6.6 for the case $\Delta = 0$. This system exhibits large transverse nonequilibrium spin density $S_y^{\rm neq}(x) \neq 0$ (while $S_x^{\rm neq}(x) =$

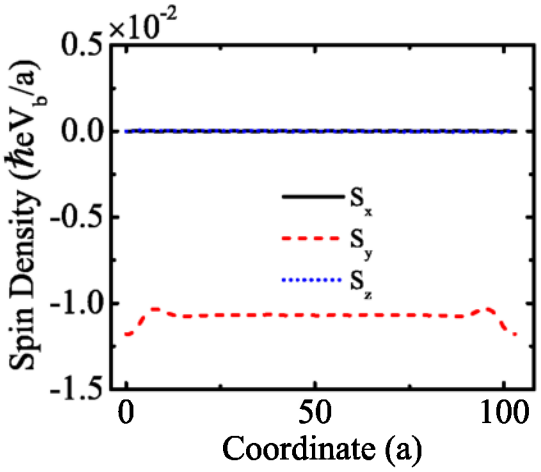

Figure 6.6: The current-driven nonequilibrium spin density $\mathbf{S}^{\rm neq}(x)$ in 2DEG with the Rashba SOC, described by the Hamiltonian Eq. (6.32) with $\gamma_{\rm SO} = 0.1$ eV and $\Delta = 0$ eV, which is infinite in the y-direction and of finite-size in the transport x-direction. This quantity is computed at zero temperature and for linear-response bias voltage V_b using: (a) the proper gauge-invariant expression Eq. (6.18) for $\rho_{\rm neq}$; and (b) the improper gauge-noninvariant expression Eq. (6.9) for $\rho_{\rm neq}$. The vertical lines mark interfaces between the 2DEG and semi-infinite normal metal leads without any SOC.

$S_z^{\rm neq}(x) = 0$), similarly to the Edelstein effect studied in infinite homogeneous diffusive 2DEGs.[54, 55] Introduction of non-zero magnetization into the Rashba Hamiltonian Eq. (6.32) leads to smaller $S_y^{\rm neq}(x)$, while also generating non-zero $S_x^{\rm neq}(x)$ and $S_z^{\rm neq}(x)$ with oscillatory spatial dependence in Fig. 6.5(a) which is made possible by the ballistic nature of transport between the contacts. Thus, $\mathbf{T}_{\rm SO}$ in laterally patterned N/F/I heterostructure with clean N/F interface will be dominated by the field-like term along $\mathbf{m} \times \mathbf{e}_y$ direction since spatial integration of $S_x^{\rm neq}(x)$, which gives rise to (anti)damping torque component along $\mathbf{m} \times (\mathbf{m} \times \mathbf{e}_y)$, yields only a small correction.

We note that recent experiments detecting current-driven magnetization switching in Pt/Co/AlO_x heterostructures can be interpreted using two different mechanisms: (*i*) current-induced $\mathbf{S}^{\rm neq}(\mathbf{r})$ at Pt/Co or Co/AlO_x interfaces due to the Rashba SOC present at those interfaces;[48, 49]; (*ii*) or spin Hall current generated within the Pt layer which then flows perpendicularly through Pt/Co interface to induce STT on Co magnetization[50] [the latter case is equivalent to a conventional torque in MTJs studied in Sec. 6.4.1 arising from a polarizing layer that would be located below the Co layer with its magnetization along the y-axis and the current injection along the z-axis in

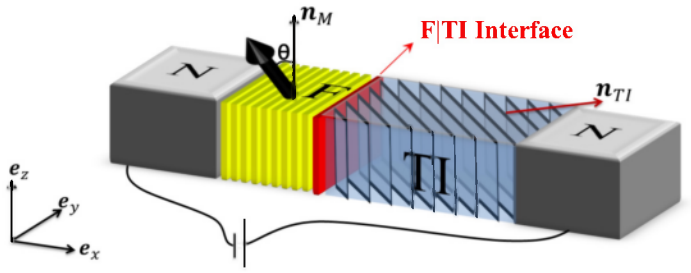

Figure 6.7: Schematic view of the topological-insulator-based vertical heterostructure operated by spin-transfer torque. The junction contains a *single* F layer of finite thickness with free magnetization $\mathbf{m}$, and the N leads are semi-infinite. We assume that each layer is composed of atomic monolayers (modeled on an infinite square tight-binding lattice).

Fig. 6.1(c)]. In principle, both torque mechanisms can be present and operate largely independent of each other. However, experimentally observed large sensitivity of torque on the thickness of Co layer is presently difficult to reconcile with predictions[57] based on either of these mechanisms computed for simplistic model Hamiltonians such as the one in Eq. (6.32). Thus, first-principles studies investigating how structural and electronic properties depend on the thickness of layers within such heterostructures are called for.

6.4.4 Application to Spin-Orbit Torques in 3D Topological Insulator Heterostructures

In this section, we predict that heterostructure in Fig. 6.7 will exhibit an *unconventional* STT, driven both by the surface SOC and spin-polarizing effect of the bulk of TI slab on current flowing perpendicularly through it. Its unusual features depicted in Fig. 6.8(a) could also open new avenues in the design of STT-MRAM [67] and spin torque oscillators [66]. For example, in conventional collinearly magnetized STT-MRAM devices [41], the initial current-induced STT is zero so that one has to rely on thermal fluctuations or small misalignments of the layer magnetizations to initiate the switching. Such undesirable long mean switching times and broad switching time distributions can be avoided by adding a TI capping layer onto the standard

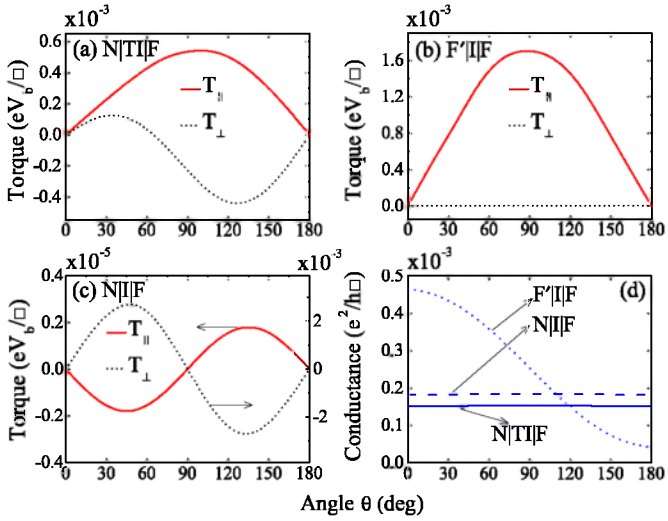

Figure 6.8: (a) The angular dependence of torque components, $\mathbf{T}_{\parallel} = \tau_{\parallel}\mathbf{m} \times (\mathbf{m} \times \mathbf{e}_z)$ and $\mathbf{T}_{\perp} = \tau_{\perp}\mathbf{m} \times \mathbf{e}_z$, acting on the free magnetization $\mathbf{m}$ within N/TI/F heterostructure in Fig. 6.7. (b) The torque components, $\mathbf{T}_{\parallel} = \tau_{\parallel}\mathbf{m} \times (\mathbf{m} \times \mathbf{m}')$ and $\mathbf{T}_{\perp} = \tau_{\perp}\mathbf{m} \times \mathbf{m}'$, acting on the free-layer magnetization $\mathbf{m} = (\sin\theta\cos\phi, \sin\theta\sin\phi, \cos\theta)$ in conventional F′/I/F symmetric MTJ where magnetization of the reference layer F′ is fixed at $\mathbf{m}' = \mathbf{e}_z$. (c) The torque components in N/I/F junction, defined in the same fashion as in panel (a), with the Rashba SOC of strength $\alpha_R/2a = 0.1$ eV located on the last monolayer of F which is in contact with I barrier. (d) The angular dependence of conductances for N/TI/ F, F′/I/F and N/I/F junctions. The bias voltage V_b in all panels is sufficiently small to ensure the linear-response regime.

F/I/F′ magnetic tunnel junction (MTJ), to form a TI/F/I/F′ vertical heterostructure, where TI layer will initiate fast switching of the F layer magnetization in accord with Fig. 6.8(a).

To understand the origin of torque components in Fig. 6.8(a), we first elucidate the effect of TI slab on unpolarized charge current injected from the left N lead by computing the spin polarization of outgoing current in the right normal metal (N) lead of N/TI/N junction with an unpolarized input current. The expression for the spin-polarization vector $\mathbf{P}^{\rm out} = P^{\rm out}\mathbf{n}_{TI} \times \mathbf{e}_x$, was derived as Eq. (3.4) in terms of the spin and charge current in the system. Its evaluation for N/TI/N junction is plotted in Fig. 6.9, which shows how TI slab polarizes the incoming current in the direction perpendicular to both of the transport and normal to the QLs of the 3DTI. The polarizing effect of the TI slab comes from the effective momentum-dependent magnetic field encoded by the $\mathbf{\Gamma}_i$ terms in the TI Hamiltonian in Eq. (5.3). This requires sufficient

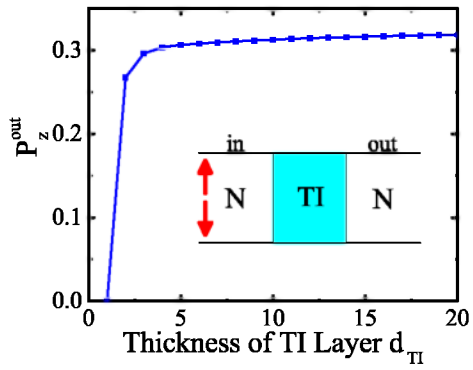

Figure 6.9: The spin-polarization vector $\mathbf{P}^{\rm out} = P^{\rm out}\mathbf{n}_{TI} \times \mathbf{e}_x$ of current [4] in the right N lead of N|TI|N junction as a function of the thickness $d_{\rm TI}$ of the 3D TI layer with $\mathbf{n}_{TI} = \mathbf{e}_y$, after unpolarized charge current is injected from the left N lead.

thickness of the TI slab, as well as that the Fermi energy of the device E_F is within the bulk gap of TI. The spin-polarization of charge current induced by its flow through a finite-size region with SOC has been discussed previously for low-dimensional systems (such as the two-dimensional electron gas with the Rashba SOC [201]). Due to constraints imposed by the time-reversal invariance, such SOC-induced polarization cannot [201] be detected via current or voltage measurement on standard two-terminal ferromagnetic circuits, as exemplified by Fig. 6.8(d) where conductance of N/TI/F junction is the same for $\mathbf{m} \parallel \mathbf{e}_z$ and $\mathbf{m} \nparallel \mathbf{e}_z$ configurations.

Following this analysis, the meaning of torque components in Fig. 6.8(a) for N/TI/F junction is explained by

$$\mathbf{T} = \mathbf{T}_{\parallel} + \mathbf{T}_{\perp} = \tau_{\parallel}\mathbf{m} \times (\mathbf{m} \times \mathbf{e}_z) + \tau_{\perp}\mathbf{m} \times \mathbf{e}_z. \tag{6.40}$$

The non-zero values of both $\mathbf{T}_{\parallel}$ and $\mathbf{T}_{\perp}$ in N/TI/F junction make this SOC-driven STT quite different from recently explored "SO torques" [56, 99] which lack anti-damping (i.e., equivalent to our $\mathbf{T}_{\parallel}$) component and, therefore, cannot induce precession of magnetization in the single F layer. We note that the same definition of torque components is applicable [61] also to N/I/F vertical heterostructures with strong Rashba SOC, $\alpha_R(\vec{\sigma} \times \mathbf{k}_{\parallel}) \cdot \mathbf{e}_z$, at the I/F interface [56, 48] even though current does not become polarized along $\mathbf{e}_z$ there. The torque components for N/I/F junction plotted in Fig. 6.8(c) are driven purely by the surface Rashba SOC, which is the second order

effect $\propto \alpha_R^2$ characterized by torque asymmetry [61] around the stable magnetic state $\theta = 90°$. On the other hand, $\mathbf{T}_\parallel$ and $\mathbf{T}_\perp$ in Fig. 6.8(a) are non-zero at $\theta = 90°$ in N/TI/F junctions due to the summation of an asymmetric contribution driven by the strong SOC on the surface of TI layer and a symmetric one [akin to conventional torque in MTJs shown in Fig. 6.8(b)] driven by spin-polarization [Fig. 6.9] of current flowing through the bulk of the TI layer.

Figures 6.8(a),(b) show that linear-response $\mathbf{T}_\parallel$ in N/TI/F junctions is comparable to the one in symmetric F′/I/F MTJs tuned (via the on-site potential in the I layer) to have similar conductance, which points to unforeseen [17] spintronics applications of TIs. The angular dependence of conductances for N/TI/F, N/I/F, and F′/I/F junctions are compared in Fig. 6.8(d).

We now turn to details of our formalism. The junction in Fig. 6.7 is modeled on a cubic lattice, with lattice constant a and unit area $a^2 \equiv \square$, where monolayers of different materials (N, F, TI) are infinite in the transverse xy-direction. The TI layer has thickness $d_{\rm TI} = 5$ and the free F layer has thickness $d_F = 70$ monolayers. The F and N layers are described by a tight-binding Hamiltonian presented in Eq. (5.6). In the numerical calculations we consider exchange potential $\Delta_n = 1.0$ eV. The hopping $\gamma_c = 0.25$ eV between F or N monolayers and the TI monolayer is chosen to ensure that the Dirac cone on the surface of TI is not distorted [75, 145] by the penetration of evanescent modes from these neighboring metallic layers. The weak F to TI coupling can be achieved by growing an ultrathin layer of a conventional band insulator, such as In_2Se_3 with large bandgap and good chemical and structural compatibility with Bi_2Se_3 where sharp heterointerfaces have already been demonstrated by molecular-beam epitaxy growth [146]. We assume that such layer is present and suppresses the magnetic proximity effect so that $\Delta_n = 0$ on the TI monolayer (denoted as F/TI interface in Fig. 6.7) that is closest to the F layer.

The early phenomenological modeling [173] of STT in noncollinear ferromagnetic multilayers was succeeded by more microscopic theories [40, 189, 169, 188, 177, 176], often in combination with first-principles input about real materials [40, 189, 169, 188].

These theories have been focused on devices without SOC where STT is directly connected to the divergence of spin current as a consequence of the conservation of total spin. Thus, STT vector can be obtained simply from the local spin current at the N/F or I/F interface within F′/N/F spin valves or F′/I/F magnetic tunnel junctions (MTJs). Such local spin currents are typically computed using the Landauer-Bütikker scattering approach [40, 188] or the NEGF formalism [189, 169, 177]. However, these methodologies are *inapplicable* to junctions with SOC within the free F layer, which has recently ignited search for efficient algorithms [169, 96, 98] that can compute STT in the presence of spin non-conserving interactions. The SOC can be introduced into the device by either bulk ferromagnets (as in F layers based on ferromagnetic semiconductors [56, 96, 98]) or due to the Rashba SOC at the I/F interface in devices with structural inversion asymmetry [56].

The application of Eq. (6.26) to get T_α ($\alpha = x, y, z$) component of the STT vector acting on the magnetization of the free F layer within N/TI/F junction proceeds by first computing $\mathbf{G}^r(E)$ for the device described by the Hamiltonian $\mathbf{H} = \mathbf{H}_{\rm TI} + \mathbf{H}_F$. In the second step, the Hamiltonian of the F layer is modified

$$\hat{H}_F^q = \hat{H}_F + q \sum_{n,\sigma\sigma',\mathbf{k}_\parallel} \mathbf{c}^\dagger_{n\sigma,\mathbf{k}_\parallel} [\mathbf{e}_\alpha \cdot (\mathbf{m} \times \vec{\sigma})]_{\sigma\sigma'} \hat{c}_{n\sigma',\mathbf{k}_\parallel}, \tag{6.41}$$

and $\mathbf{G}^r(E)[\hat{H}^q]$ is computed for the new Hamiltonian $\hat{H}^q = \hat{H}_{\rm TI} + \hat{H}_F^q$. This yields $\partial \mathbf{G}^r / \partial q \approx (\mathbf{G}^r[\hat{H}^q] - \mathbf{G}^r[\hat{H}])/q$ where we use $q = 10^{-7}$ as the infinitesimal. The derivative $\partial \mathbf{G}^r / \partial q$ plugged into Eq. (6.26) yields $Q = T_\alpha$.

6.5 Summary of Chapter

In conclusion, within the framework of nonequilibrium Green functions, we show how to construct the proper *gauge-invariant* (i.e., independent of the reference level for electric potential) density matrix in steady-state nonequilibrium for an active region attached to two macroscopic reservoirs whose small electrochemical potential difference drives linear-response dc current in the absence of inelastic processes in the active

region. Our central expression in this chapter—Eq. (6.18) at zero temperature or Eq. (6.17) at non-zero temperature—contains three terms. One of those terms yields the usual two-terminal Landauer-type conductance formula when computing expectation value for the total charge current in the electrodes, which is always a purely nonequilibrium quantity. The two additional terms ensure that any non-zero equilibrium expectation value of a physical quantity is properly removed from the formalism in gauge invariant fashion.

We illustrate the usage of the proper nonequilibrium density matrix by computing the field-like, which is non-zero even in equilibrium, and (anti)damping components of the conventional torque in F′/I/F MTJs or unconventional torque in N/I/F semi-MTJs with strong Rashba SOC at the I/F interface. The third application evaluates current-driven nonequilibrium spin density in the ferromagnetic Rashba model, which yields the SO torque as one of the possible mechanisms behind mangetization switching of a single F layer recently observed[48, 49, 50] in laterally patterned N/F/I heterostructures with in-plane injected charge current. We compare these results with those obtained using the gauge-noninvariant expressions for the nonequilibrium density matrix found in spintronics literature to show how they lead to incorrect prediction for the current-driven field-like torque or nonequilibrium spin density due to improper removal of the corresponding equilibrium expectation values.

Furthermore we note that although STT we predict in N/TI/F junctions does not require F′ layer with fixed magnetization as polarizer, its measurement necessitates usage of the second reference F′ layer in order to detect magnetization switching or precession in the free F layer. Nevertheless, the experimental setups we propose for this purpose, consisting of MTJ capped with TI layer to form TI/F/I/F ′ stacking, require much lesser total number of layers than recently fabricated orthogonal ST-MRAM [67] or ST oscillators [66] (containing F″ polarizer whose fixed magnetization must be kept perpendicular to in-plane magnetized F and F′ layers).

Chapter 7

ELECTRON-MAGNON INTERACTION EFFECTS ON ELECTRONIC TRANSPORT IN MTJS

7.1 Motivation

Magnetic tunnel junctions (MTJ) are layered heterostructures in which an insulating tunnel barrier (I) separates two ferromagnetic layers (F). They have been the subject of vigorous research in both fundamental and applied physics since they exhibit effects like tunneling magneto-resistance (TMR) [202] and spin-transfer torque (STT), [27, 12] as well as quantum size effects in electron transport (even at room temperature) when normal metal (N) layer is inserted. [203] From the fundamental viewpoint, these effects represent examples of nonequilibrium quantum many-body systems with an interplay of fast conduction electrons carrying spin current and slow collective magnetization, while from the viewpoint of applications they play an essential role in developing magnetic sensors, random access memory, novel programmable logic devices, resonant-tunneling spin transistors and nanoscale microwave oscillators with ultrawide operating frequency ranges. [41]

A majority of theoretical studies of TMR or STT effects has assumed phase-coherent tunneling of non-interacting quasiparticles. For example, such approaches [44, 204] have led to a remarkable prediction of very large TMR ratio $\simeq 4000\%$ at zero bias voltage for clean epitaxial MgO-based MTJs. The TMR ratio is defined by $\mathrm{TMR} = (R_{\mathrm{AP}} - R_{\mathrm{P}})/R_{\mathrm{P}}$, where R_{P} is the resistance for parallel orientations of two magnetizations in F/I/F MTJ and R_{AP} is the resistance when they are antiparallel. These predictions have ignited large experimental efforts that have eventually reached TMR ratios of more than 1000% at low temperatures and $\simeq 600\%$ at room

temperature for well-oriented MgO barriers with stress relaxation. [205] The phase-coherent calculations—such as numerical ones based on the nonequilibrium Green function (NEGF) formalism [147] combined with simplistic tight-binding Hamiltonians [178, 206] or first-principles obtained Hamiltonians; [179] as well as analytical ones [176] based on the scattering approach—have been able to capture the dependence of a_J and b_J on the bias voltages $V_b \lesssim 0.2$ V in MgO-based MTJs. [207] However, such theories [178, 206, 176] including *only* elastic electron tunneling start to deviate from experimental findings at higher bias voltages, which is particularly pronounced [208, 209, 42] for b_J (playing a significant role during magnetization switching at $V_b \simeq 1.0$ V).

The inelastic electron-magnon (e-m) or electron-phonon (e-ph) scattering could account for these discrepancies. [208, 209] In particular, since magnon bandwidth is usually of the order of $\simeq$ 100 meV, at high bias voltages multiple magnon scattering events can be excited. [210] Also, energy dependence of the magnon density of states (DOS) probed [210] at finite bias voltage is intimately linked to the evolution of the magnetization during current-driven switching when going beyond the macrospin approximation. [211, 212]

In fact, even at small bias voltage thermally excited magnons affect TMR (e.g., emission or absorption of magnon at F/I interface reduces the effective spin polarization of electrons incoming from F leads in Fig. 7.1), so that TMR decreases with increasing temperature. [213, 214] Although thermally induced change of the resistance is different for AlO_x- and MgO-based MTJs, their inelastic tunneling spectra [215] (IETS) shows very similar properties. That is, plotting the second derivative d^2I/dV_b^2 of current vs. bias voltage in MTJs reveals zero bias anomaly (ZBA) where peaks (see, e.g., Fig. 2 in Ref. [213]) of opposite sign appear at $V_b \simeq \pm 10$ mV and are related to magnons. Also, additional phonon peaks are found [213] at $V_b \simeq \pm 81$ mV for the MgO-based MTJs or at $V_b \simeq \pm 120$ mV for AlO_x-based MTJs.

Theoretical efforts to capture e-m inelastic scattering effects on TMR, ZBA and STT have thus far utilized simplified frameworks [216, 217] which *cannot* deal

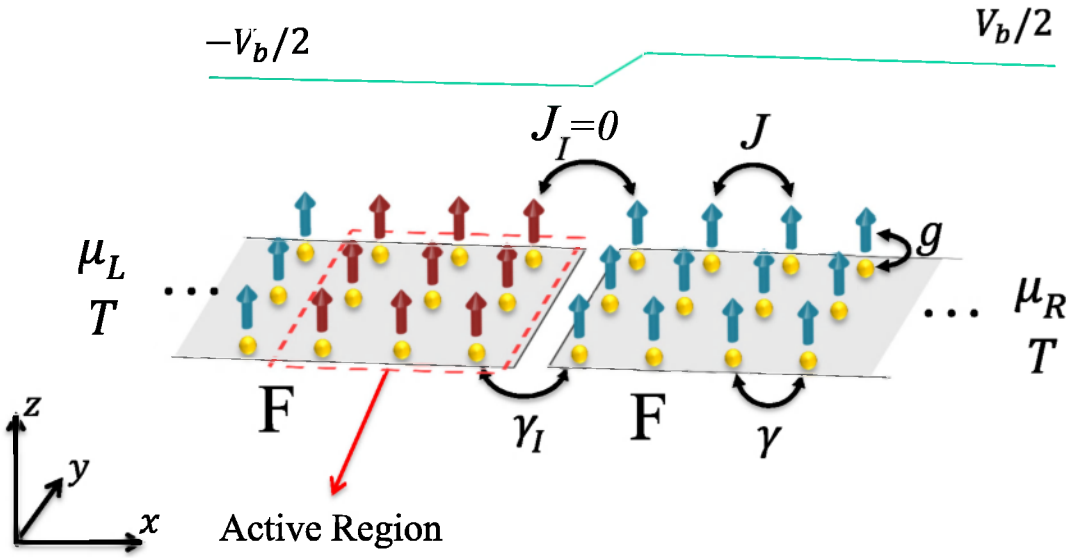

Figure 7.1: Schematic view of a quasi-1D model of F/I/F MTJ where the left semi-infinite ideal F lead, modeled as spin-split tight-binding lattice of size $\infty \times N_y$, is attached via hopping γ to an active region consisting of $N_x \times N_y$ lattice sites (we use $N_x = 3$ and $N_y = 1$ or $N_y = 3$ in the calculations below). The right semi-infinite lead is attached to the active region via smaller hopping $\gamma_I = 0.1\gamma$ that simulates the tunnel barrier I. The same sites also host localized spins which are coupled to each other via the ferromagnetic coupling $J > 0$ in the Heisenberg model. The local coupling between the spin of conduction electrons and localized spin on each site is of strength g. The left and right semi-infinite leads are assumed to terminate into macroscopic Fermi liquid reservoirs held at electrochemical potentials μ_L and μ_R, respectively, whose difference sets the bias voltage $eV_b = \mu_L - \mu_R$. The voltage profile across MTJ is shown on the top. The left F layer is assumed to be attached at infinity to a macroscopic reservoir of magnons held at temperature T.

with multiple scattering events, backaction of magnons driven far from equilibrium and energy dependence of magnonic DOS. Such effects can be taken systematically and rigorously into account at arbitrary temperature or bias voltage by using the NEGF formalism coupled with perturbation expansion of electron or magnon self-energies in the presence of their mutual interaction in terms of the respective Feynman diagrams. [147] In equilibrium problems, like that of magnetic polaron, electronic self-energy has been constructed by considering large set of diagrams involving an arbitrary number of e-m scattering vertices between the emission and absorption vertices. [218] However, using the same diagrams within the NEGF framework would violate charge conservation, yielding different charge currents in the left and right lead of a two-terminal device at finite bias voltage.

One of the conserving approximations is the so-called self-consistent Born approximation (SCBA) where one considers Hartree and Fock diagrams for the electronic self-energy which corresponds to perturbation in the order $\mathcal{O}(g^2)$ where g is the strength of e-m interaction. Evaluation of these diagrams for a systems defined on the lattice hosting orbitals in real space is computationally very demanding due to the fact that GF lines in the diagrams of nonequilibrium many-body perturbation theory (MBPT) are fully interacting (or dressed), so that self-energy matrix becomes a functional of the GF matrix. This generates a coupled system of nonlinear integral equations which has to be solved by performing multiple integrations over each matrix element until the self-consistency is achieved. Such route has been undertaken in only a handful of studies where further simplifications (such as using dispersionless magnons, $\omega_{\mathbf{k}} = \omega_0$) were utilized. [219]

Here we discuss in Sec. 7.3 how to construct the electronic self-energy and GF within SCBA, together with the magnonic self-energy within the electron-hole (e-h) polarization bubble approximation which takes into account influence of electrons on magnons while inserting the dressed magnonic GF into SCBA diagrams. Thus, consideration of such diagrams is akin to the self-consistent GW treatment of the one-particle electronic self-energy due to electron-electron interaction out of equilibrium. [220] Our

approach treats these quantities as matrices [221] in the Keldysh space, rather than following the commonly used route based on Langreth rules to manipulate expressions involving products of their submatrices. [147] This formalism is then applied to a many-body Hamiltonian, introduced in Sec. 7.2, of an interacting e-m system defined on the real-space lattice describing MTJ that is brought out of equilibrium by the applied finite bias voltage. Despite using a quasi-one-dimensional (quasi-1D) model for MTJ illustrated in Fig. 7.1, where e-m interaction is treated diagrammatically only within few lattice sites (denoted as "active region" in Fig. 7.1) of the left F layers, charge current versus bias voltage and its second derivative obtained in Sec. 7.4 capture essential features of ZBA observed in realistic junctions. The sum of spin currents carried by electrons in the non-interacting F leads attached to this active region is non-zero which, therefore, allows us to quantify in Sec. 7.4 the amount of lost angular momentum of electronic subsystem that is carried away by magnonic spin current. We conclude in Sec. 7.5.

7.2 Hamiltonian for Coupled Electron-Magnon System within MTJ

To make the discussion transparent, we focus on the particular example of e-m interacting many-body system out of equilibrium which emerges within the quasi-1D model of a two-terminal F/I/F MTJ depicted in Fig. 7.1. This can be described by the following Hamiltonian

$$\begin{aligned}\hat{H} = &\sum_{i\sigma}\left(\varepsilon_i + \frac{\Delta}{2} m_z^i [\sigma_z]_{\sigma\sigma}\right) \hat{c}_{i\sigma}^{\dagger}\hat{c}_{i\sigma} \\ &+ \sum_{\langle ij\rangle,\sigma} (\gamma_{ij}\hat{c}_{i\sigma}^{\dagger}\hat{c}_{j\sigma} + \text{H.c.}) \\ &- \frac{1}{2}\sum_{\langle ij\rangle} J_{ij}\hat{\vec{S}}_i \cdot \hat{\vec{S}}_j - \frac{1}{2}E_Z \sum_i (\hat{S}_i^z)^2 + g\sum_j \hat{\vec{S}}_j \cdot \hat{\vec{s}}_j\end{aligned} \tag{7.1}$$

The first term in Eq. (7.1) accounts for the on-site potential due to the voltage profile shown in Fig. 7.1, as well as for the coupling of itinerant electrons to collective magnetization described by the material-dependent exchange potential $\Delta = 0.75$ eV. We use the standard notation $\vec{\sigma} = (\sigma_x, \sigma_y, \sigma_z)$ for the vector of the Pauli matrices, where

$[\sigma_{x,y,z}]_{\sigma\sigma'}$ are their matrix elements. Here $m_z^i = 1$ or $m_z^i = -1$ depending on whether the magnetization of the left or right F layer is parallel or antiparallel to the z-axis, respectively. The second term in Eq. (7.1) describes hopping of electrons between single s-orbitals located on the tight-binding lattice sites, where $\hat{c}_{i\sigma}^\dagger$ ($\hat{c}_{i\sigma}$) creates (annihilates) electron on site i in spin state $\sigma = \uparrow, \downarrow$ and γ_{ij} is the nearest-neighbor hopping parameter. We set $\gamma_{ij} = \gamma = 1$ eV for all pairs of lattice sites, except for the last row of sites of the left F layer and the first row of sites of the right F layer where $\gamma_{ij} = \gamma_I = 0.1$ eV (in the case of $N_x \times N_y \equiv 3 \times 1$ active region in Fig. 7.1) or $\gamma_{ij} = \gamma_I = 0.3$ eV (in the case of $N_x \times N_y \equiv 3 \times 3$ active region in Fig. 7.1) simulates the presence of the tunnel barrier I.

The third term is the Heisenberg model [222] describing interaction between spin operators $\hat{\vec{S}}_i$ and $\hat{\vec{S}}_j$ localized on the nearest-neighbor sites of the same tight-binding lattice, where ferromagnetic coupling is set as $J_{ij} = J = 1 \times 10^{-3}$ eV, except for the I region where $J_{ij} = J_I \equiv 0$. The fourth term with $E_Z = 2 \times 10^{-3}$ eV is introduced to select energetically favorable direction (i.e., an easy-axis) for the spontaneous magnetization in the ferromagnetic layers along the z-axis. Finally, the fifth term describes interaction of the spin operator $(\hat{\vec{s}}_j)_{\sigma\sigma'} = \frac{1}{2}\vec{\sigma}_{\sigma\sigma'}\hat{c}_{j\sigma}^\dagger\hat{c}_{j\sigma'}$ of conduction electrons with the localized spin operators $\hat{\vec{S}}_j$, where the coupling constant is set as $g = 0.045$ eV.

The active region of MTJ in Fig. 7.1, within which NEGFs and self-energies due to e-m interaction are computed, consists of $N_x \times N_y$ sites enclosed in Fig. 7.1. The rest of the tight-binding sites belong to the left and right semi-infinite leads (taken into account through lead self-energies discussed in Sec. 7.3). The leads are assumed to terminate at infinity into macroscopic Fermi liquid reservoirs held at electrochemical potentials $\mu_L = E_F + eV_L$ and $\mu_R = E_F + eV_R$ (the Fermi energy is chosen as $E_F = 0.5$ eV for $N_x \times N_y \equiv 3 \times 1$ active region and $E_F = 2.65$ eV for $N_x \times N_y \equiv 3 \times 3$ active region), whose difference sets the bias voltage $eV_b = \mu_L - \mu_R$. Concurrently, the left F layer is assumed to be attached at infinity to a macroscopic reservoir of magnons held at temperature T.

Using the approximate version of the Holstein-Primakoff transformations [222]

$$\hat{S}_i^+ \approx \sqrt{2S}\hat{b}_i^\dagger, \tag{7.2a}$$

$$\hat{S}_i^- \approx \sqrt{2S}\hat{b}_i, \tag{7.2b}$$

$$\hat{S}_i^z = \hat{b}_i^\dagger \hat{b}_i - m_z^i S, \tag{7.2c}$$

we can replace the spin operators by bosonic operators. The approximation in Eq. (7.2) is a valid when the occupation number of bosonic states at temperature T is low, $\langle \hat{b}_i^\dagger \hat{b}_i \rangle \ll S$, where we select $S = 10$. This is equivalent to saying that the left or right F layer is near its ferromagnetic ground state where $\langle \hat{S}_i^z \rangle = S$ on all lattice sites within both the left and right F layers for the parallel (P) configuration of magnetizations in MTJ, or $\langle \hat{S}_i^z \rangle = S$ within the left F layer and $\langle \hat{S}_i^z \rangle = -S$ within the right F layer for antiparallel (AP) configuration of magnetizations in MTJ.

This replacement allows us to rewrite the Hamiltonian in Eq. (7.1) as $\hat{H} = \hat{H}_\mathrm{e} + \hat{H}_\mathrm{m} + \hat{H}_\mathrm{e-m}$, where all three terms are now given in the second quantization

$$\begin{aligned}\hat{H}_\mathrm{e} &= \sum_{i,\sigma} \left(\varepsilon_i + \frac{1}{2}\left(gS + \Delta\right) m_z^i \sigma_z \right)_{\sigma\sigma} \hat{c}_{i\sigma}^\dagger \hat{c}_{i\sigma} \\ &\quad + \sum_{\langle ij \rangle, \sigma} (\gamma_{ij} \hat{c}_{i\sigma}^\dagger \hat{c}_{j\sigma} + \mathrm{H.c.}), \end{aligned} \tag{7.3a}$$

$$\begin{aligned}\hat{H}_\mathrm{m} &= -S \sum_{\langle ij \rangle} J_{ij} \hat{b}_i^\dagger \hat{b}_j \\ &\quad + S(E_Z + 2zJ) \sum_i \hat{b}_i^\dagger \hat{b}_i, \end{aligned} \tag{7.3b}$$

$$\begin{aligned}\hat{H}_\mathrm{e-m} &= \sqrt{\frac{S}{2}} \sum_i g(\hat{b}_i^\dagger \hat{c}_{i\downarrow}^\dagger \hat{c}_{i\uparrow} + \hat{b}_i \hat{c}_{i\uparrow}^\dagger \hat{c}_{i\downarrow}), \\ &\quad + \frac{1}{2} \sum_{i\sigma} g [\sigma_z]_{\sigma\sigma} \hat{b}_i^\dagger \hat{b}_i \hat{c}_{i\sigma}^\dagger \hat{c}_{i\sigma}. \end{aligned} \tag{7.3c}$$

Here $2z$ is the number of nearest neighbor sites. The many-body interaction is encoded by $\hat{H}_\mathrm{e-m}$ in Eq. (7.3c), which is assumed to be non-zero only in the active device region in Fig. 7.1. Its first term has a clear physical interpretation—the spin of a conduction electron is flipped when magnon is absorbed or emitted. Since its second term (in the lowest order, its role is to renormalize the effective Zeeman splitting for electrons) is

much smaller than the first term due to assumed $\langle \hat{b}_i^\dagger \hat{b}_i \rangle \ll S$, we ignore it in subsequent discussion.

In the rest of the system depicted in Fig. 7.1, electrons and magnons are assumed to behave as non-interacting quasiparticles. For example, in the case of $N_x \times N_y \equiv 3 \times 1$ active region, the left and right semi-infinite F leads are 1D chains whose electrons in equilibrium ($\varepsilon_i = 0$) are described by $\hat{H}_\mathrm{e}$ in Eq. (7.3a) generating dispersion $E_k = -2\gamma \cos(ka) \pm (gS + \Delta)/2$ which is spin split both by the mean-field treatment of $g \sum_j \hat{\vec{S}}_j \cdot \hat{\vec{s}}_j$ interaction term and Δ. The left semi-infinite lead [223] for the magnonic subsystem is described by $\hat{H}_\mathrm{m}$ in Eq. (7.3b), where non-interacting magnons have dispersion $\omega_k = 2JS[1 - \cos(ka)] + E_Z S$.

7.3 Nonequilibrium Diagrammatics for Electron-Magnon Interacting System

7.3.1 Compact Analytical Expressions in the Keldysh Space

In Sec. 2.4 we showed that the NEGF formalism [147] operates with two central one-particle quantities— the retarded GF ($\mathbf{G}^r$ for fermions or $\mathbf{B}^r$ for bosons), describing the density of available quantum states; and the lesser GF ($\mathbf{G}^<$ for fermions or $\mathbf{B}^<$ for bosons), describing how quasiparticles occupy those states. One can also use two additional GFs, advanced [$\mathbf{G}^a = (\mathbf{G}^r)^\dagger$ for fermions or $\mathbf{B}^a = (\mathbf{B}^r)^\dagger$ for bosons] and greater ($\mathbf{G}^>$ for fermions or $\mathbf{B}^>$ for bosons), describing the properties of the corresponding empty states. These four GFs, which generally depend on two time arguments (t, t'), are connected by the fundamental relation

$$\mathbf{A}^> - \mathbf{A}^< = \mathbf{A}^r - \mathbf{A}^a, \tag{7.4}$$

for electronic ($\mathbf{A} \equiv \mathbf{G}$) or bosonic ($\mathbf{A} \equiv \mathbf{B}$) GFs. Keldysh-space matrix GF for fermions is defined by

$$\check{\mathbf{G}} = \begin{pmatrix} \mathbf{G}^< + \mathbf{G}^r & \mathbf{G}^> \\ \mathbf{G}^< & \mathbf{G}^> - \mathbf{G}^r \end{pmatrix} = i \begin{pmatrix} \theta_{t'-t} \langle \hat{c}_{1'}^\dagger \hat{c}_1 \rangle - \theta_{t-t'} \langle \hat{c}_1 \hat{c}_{1'}^\dagger \rangle & -\langle \hat{c}_1 \hat{c}_{1'}^\dagger \rangle \\ \langle \hat{c}_{1'}^\dagger \hat{c}_1 \rangle & \theta_{t'-t} \langle \hat{c}_1 \hat{c}_{1'}^\dagger \rangle - \theta_{t-t'} \langle \hat{c}_{1'}^\dagger \hat{c}_1 \rangle \end{pmatrix}, \tag{7.5}$$

and for bosons it is defined by

$$\check{\mathbf{B}} = \begin{pmatrix} \mathbf{B}^{<} + \mathbf{B}^{r} & \mathbf{B}^{>} \\ \mathbf{B}^{<} & \mathbf{B}^{>} - \mathbf{B}^{r} \end{pmatrix} = -i \begin{pmatrix} \theta_{t'-t}\langle \hat{b}_{1}^{\dagger}, \hat{b}_{1} \rangle + \theta_{t-t'}\langle \hat{b}_{1}\hat{b}_{1'}^{\dagger} \rangle & \langle \hat{b}_{1}\hat{b}_{1'}^{\dagger} \rangle \\ \langle \hat{b}_{1}^{\dagger}, \hat{b}_{1} \rangle & \theta_{t'-t}\langle \hat{b}_{1}\hat{b}_{1'}^{\dagger} \rangle + \theta_{t-t'}\langle \hat{b}_{1'}^{\dagger}, \hat{b}_{1} \rangle \end{pmatrix}. \tag{7.6}$$

Here $1 \equiv (t, i, \sigma)$ and $1' \equiv (t', j, \sigma')$; θ_x is the Heaviside step function ($\theta_x = 1$ for $x \geq 0$ and $\theta_x = 0$ for $x < 0$); and $\langle \cdots \rangle \equiv \mathrm{Tr}[\mathcal{T}_C \cdots \hat{\rho}_0]/\mathrm{Tr}[\hat{\rho}_0]$ is the nonequilibrium expectation value [147] with $\mathcal{T}_C$ being the contour ordering operator and the initial density matrix of the system $\hat{\rho}_0$ is usually taken at $-\infty$ for the steady-state formulations within the NEGF.

In stationary problems GFs depend only on the time difference $t - t'$, so that they can be Fourier transformed to energy E or frequency ω. Using Hamiltonian in Eq. (7.3) and performing such Fourier transform leads to the following Keldysh-space Dyson equation for electrons

$$\check{\mathbf{G}}(E) = \boldsymbol{\tau}^{z} \frac{1}{(E - \mathbf{H}_{\mathrm{e}})\boldsymbol{\tau}^{z} - \check{\boldsymbol{\Sigma}}_{\mathrm{e-m}}(E) - \check{\boldsymbol{\Sigma}}_{\mathrm{leads}}(E)} \boldsymbol{\tau}^{z}, \tag{7.7}$$

or magnons

$$\check{\mathbf{B}}(\omega) = \boldsymbol{\tau}^{z} \frac{1}{(\omega - \mathbf{H}_{\mathrm{m}})\boldsymbol{\tau}^{z} - \check{\boldsymbol{\Omega}}_{\mathrm{m-e}}(\omega) - \check{\boldsymbol{\Omega}}_{\mathrm{leads}}(\omega)} \boldsymbol{\tau}^{z}. \tag{7.8}$$

This approach allows for compact notation by avoiding the widespread route [147] where one starts from the Dyson equation for the contour-ordered GF containing convolution integrals on the two-branch Keldysh-Schwinger contour, and then applies the so-called Langreth rules [147] to find the lengthy expressions involving the lesser and retarded GFs with two time arguments located on the single real-time axis (or their Fourier transforms). The Dyson equation for the Keldysh-space matrix GFs in energy, like Eqs. (7.7) and (7.8), is rarely used in the literature due to redundancy expressed by Eq. (7.4). For example, such equation can be found in the NEGF-based calculations of the full counting statistics [224, 225, 226] where the presence of the counting field results in the nonunitary evolution on the Keldysh-Schwinger contour, thereby requiring to work with all four submatrices in Eqs. (7.5) or (7.6) because the relation like Eq. (7.4) is not valid anymore. Nevertheless, even when Eq. (7.4) holds, it can

be advantageous to work directly with the matrices in the Keldysh space—this greatly simplifies writing the analytical expressions that the Feynman diagrams of nonequilibrium MBPT represent and, moreover, it makes possible to derive expressions for the perturbation expansion of more complicated quantities like the current noise obtained from the two-particle nonequilibrium correlation function.

The self-energies due to many-body interaction, $\check{\mathbf{\Sigma}}_{\mathrm{e-m}}(E)$ for electron and $\check{\mathbf{\Omega}}_{\mathrm{m-e}}(\omega)$ for magnon, can be simply added to the self-energies introduced by the attached semi-infinite leads, $\check{\mathbf{\Sigma}}_{\mathrm{leads}}$ for electron and $\check{\mathbf{\Omega}}_{\mathrm{leads}}(\omega)$ for magnons, respectively. This is due to the fact that e-m interaction is assumed to be localized within the active region in Fig. 7.1, so that the leads do not involve many-body interactions. Thus, the self-energies of the leads for the junction in Fig. 7.1

$$\check{\mathbf{\Sigma}}_{\mathrm{leads}} = \sum_{\alpha=L,R} \begin{pmatrix} (1-f_\alpha)\mathbf{\Sigma}^r_\alpha + f_\alpha \mathbf{\Sigma}^a_\alpha & (1-f_\alpha)(\mathbf{\Sigma}^r_\alpha - \mathbf{\Sigma}^a_\alpha) \\ -f_\alpha(\mathbf{\Sigma}^r_\alpha - \mathbf{\Sigma}^a_\alpha) & -f_\alpha \mathbf{\Sigma}^r_\alpha - (1-f_\alpha)\mathbf{\Sigma}^a_\alpha \end{pmatrix} \tag{7.9}$$

$$\check{\mathbf{\Omega}}_{\mathrm{leads}} = \sum_{\alpha=L} \begin{pmatrix} (1+n_\alpha)\mathbf{\Omega}^r_\alpha - n_\alpha \mathbf{\Omega}^a_\alpha & (1+n_\alpha)(\mathbf{\Omega}^r_\alpha - \mathbf{\Omega}^a_\alpha) \\ n_\alpha(\mathbf{\Omega}^r_\alpha - \mathbf{\Omega}^a_\alpha) & n_\alpha \mathbf{\Omega}^r_\alpha - (1+n_\alpha)\mathbf{\Omega}^a_\alpha \end{pmatrix} \tag{7.10}$$

are single-particle quantities which can always be computed in an exact fashion, either analytically [227] for simple models like Eqs. (7.3a) and (7.3b) or numerically for more complicated lead Hamiltonians. [228] The effect of the bias voltage is introduced by a rigid shift in energy, $\mathbf{\Sigma}^r_{L,R}(E, V_b) = \mathbf{\Sigma}^r_{L,R}(E \mp eV_b/2, 0)$. The Fermi function of the macroscopic reservoir to which lead α is attached is denoted by $f_\alpha(E) = f(E - eV_\alpha)$. The Bose-Einstein distribution function of the macroscopic reservoir of magnons to which the left F layer is attached is denoted by $n_\alpha(\omega)$.

The one-particle self-energies due to e-m interaction, $\check{\mathbf{\Sigma}}_{\mathrm{e-m}}$ and magnon $\check{\mathbf{\Omega}}_{\mathrm{m-e}}$, are formally obtained by summing all irreducible diagrams, i.e., those diagrams that cannot be taken apart by cutting a single line. The self-energies are actually *functionals* of the respective electronic or magnonic GF, so that they have to be approximated in

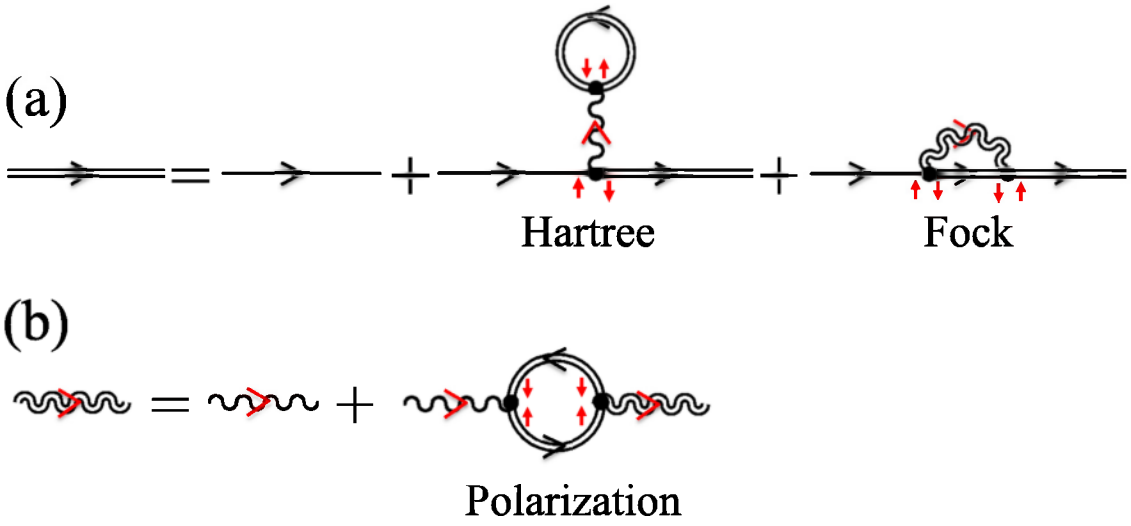

Figure 7.2: Diagrammatic representation of the Dyson equation in the Keldysh space: (a) the electron case, $\check{\mathbf{G}} = \check{\mathbf{G}}_0 + \check{\mathbf{G}}_0\check{\mathbf{\Sigma}}_{\mathrm{e-m}}\check{\mathbf{G}}$, in Eq. (7.7); and (b) the magnon case, $\check{\mathbf{B}} = \check{\mathbf{B}}_0 + \check{\mathbf{B}}_0\check{\mathbf{\Omega}}_{\mathrm{m-e}}\check{\mathbf{B}}$, in Eq. (7.8). The perturbation expansion for the electronic self-energy $\check{\mathbf{\Sigma}}_{\mathrm{e-m}}$ in (a) retains Hartree and Fock diagrams, while the expansion in (b) for the magnonic self-energy $\check{\mathbf{\Omega}}_{\mathrm{m-e}}$ retains e-h polarization bubble diagram. The single straight line denotes the non-interacting electronic GF, $\check{\mathbf{G}}_0$ [which includes the self-energies due to the leads in Eq. (7.9)]; the single wavy line denotes the non-interacting magnonic GF, $\check{\mathbf{B}}_0$ [which includes the self-energy due to the left lead in Eq. (7.10)]; double straight line denotes the interacting electronic GF, $\check{\mathbf{G}}$; and double wavy line denotes the interacting magnonic GF, $\check{\mathbf{B}}$. The solid circles denote vertices that are integrated out. The electron spin is flipped at each vertex, which is illustrated by spin-$\uparrow$ (before the vertex) being flipped into spin-$\downarrow$ (after the vertex), while a magnon is being created. The same process applies to flipping of spin-$\downarrow$ to spin-$\uparrow$, where the direction of magnon propagation (indicated by arrow on the wavy lines) is reversed. Note that the Hartree diagram in panel (a) contains a single (rather than double) wavy line in order to avoid double counting.

practical calculations. Diagrammatic techniques provide a natural scheme for generating approximate self-energies, as well as for systematically improving these approximations. While there are no general prescriptions on how to select the relevant diagrams, this process can be guided by physical intuition. In addition, unlike equilibrium [218] MBPT, the diagrams selected in nonequilibrium [147] MBPT must generate GFs that yield expectation value for charge current which is conserved. For example, the final current in the left and right leads of the device in Fig. 7.1 must be the same in any chosen approximation for the self-energies.

Here we select one of the conserving approximations, [147] where the Feynman diagrams retained for the electron or magnon self-energies are displayed in Figs. 7.2(a) and 7.2(b), respectively. The diagrams in Figs. 7.2(a) are equivalent to the so-called self-consistent Born approximation (SCBA) for the electronic self-energy considered in problems like e-ph interacting systems. [229, 230, 231, 232, 233, 234, 235, 236, 237] However, in the case of e-m interaction, one has to introduce additional bookkeeping in such diagrams to account for flipping of electron spin together with magnon emission or absorption, as illustrated in Fig. 7.2. The Keldysh-space expression for the electronic self-energy read from the Fock diagram in Fig. 7.2(a) is given by

$$\check{\mathbf{\Sigma}}^F_{mn,\uparrow\uparrow}(E) = \frac{i}{2} g^2 S \int d\omega\, \check{\mathbf{B}}_{mn}(\omega) \check{\mathbf{G}}_{mn,\downarrow\downarrow}(E-\omega), \tag{7.11a}$$

$$\check{\mathbf{\Sigma}}^F_{mn,\downarrow\downarrow}(E) = \frac{i}{2} g^2 S \int d\omega\, [\check{\mathbf{B}}^T]_{mn}(\omega) \check{\mathbf{G}}_{mn,\uparrow\uparrow}(E+\omega). \tag{7.11b}$$

Here m and n are matrix indices which include the Keldysh space and real (i.e., orbital) space, so that $\check{\mathbf{\Sigma}}^F_{mn,\sigma\sigma}(E)$ selects a submatrix of $\check{\mathbf{\Sigma}}^F$.

Finding the proper expression for the Hartree diagram in Fig. 7.2(a) in the Keldysh space requires extra care [238] because t and t' for the inner electronic GF along the loop are equal, so that $\theta_{t-t'}$ in Eq. (7.5) gives 1 or 0 depending on whether $t-t' \to 0^+$ or $t-t' \to 0^-$, respectively. Therefore, $\check{\mathbf{G}}(t, t' \to t+0^+) = \begin{pmatrix} \mathbf{G}^<(t,t) & 0 \\ 0 & \mathbf{G}^<(t,t) \end{pmatrix}$ in

terms of which we obtain the following expressions

$$\check{\mathbf{\Sigma}}^{H}_{mn,\uparrow\downarrow} = \frac{-i\delta_{mn}}{2} g^2 S \sum_{p} \int dE\, [\check{\mathbf{B}}_0]_{mp}(\omega = 0) \boldsymbol{\tau}^{z}_{pp} \check{\mathbf{G}}_{pp,\downarrow\uparrow}(E), \tag{7.12a}$$

$$\check{\mathbf{\Sigma}}^{H}_{mn,\downarrow\uparrow} = \frac{-i\delta_{mn}}{2} g^2 S \sum_{p} \int dE\, [\check{\mathbf{B}}^{T}_0]_{mp}(\omega = 0) \boldsymbol{\tau}^{z}_{pp} \check{\mathbf{G}}_{pp,\uparrow\downarrow}(E). \tag{7.12b}$$

Note that the off-diagonal (i.e., lesser and greater) components of $\check{\mathbf{\Sigma}}^{H}_{\mathrm{m-e}}$ vanish, and the remaining retarded component on the diagonal is energy independent.

Although $\check{\mathbf{\Sigma}}_{\mathrm{e-m}}(E) = \check{\mathbf{\Sigma}}^{H} + \check{\mathbf{\Sigma}}^{F}(E)$ in SCBA, we retain only the Fock term in the actual calculations below. We note that in SCBA for e-ph interacting systems, $\check{\mathbf{\Sigma}}^{H}$ is often neglected [232, 236] due to being small and, therefore, having little effect on the final current (this becomes unwarranted for larger e-ph interaction strengths where SCBA breaks down [236]). For the e-m interacting systems, the situation is much more complex because direct evaluation of Eq. (7.12) leads to numerical instabilities. This stems from the fact that our MTJ is invariant with respect to the rotation around the z-axis (see Fig. 7.1), so that spin-flip rate which appears in Eq. (7.12) can acquire arbitrary phase thereby requiring to consider full double time dependence of $\check{\mathbf{\Sigma}}^{H}$. We relegate this to future studies, while here we retain $\check{\mathbf{\Sigma}}_{\mathrm{e-m}}(E) = \check{\mathbf{\Sigma}}^{F}(E)$ which is termed [236] Fock-only SCBA (F-SCBA).

In the case of e-ph many-body systems driven far from equilibrium, phonon heating due to propagating electrons has been considered either phenomenologically using a rate equation for the phonon occupation, [231, 232, 239] or microscopically by using phonon GF with interacting self-energy truncated to the e-h polarization bubble diagram. [229, 230, 233, 234, 235, 225, 226] It is worth mentioning that the two approaches yield virtually identical results for time-averaged current in the limit of weak e-ph coupling, but they start differing significantly in the case of the current noise due to the feedback of the phonon dynamics on the statistics of the transmitted electrons which cannot be captured by the phenomenological rate equation approach. [226] Since magnon bandwidth ($\simeq$ 100 meV) is relatively small, [210] they can be easily driven into far from equilibrium state by charge current at finite bias voltage. For the purpose

of describing such state, we retain in Fig. 7.2(b) the e-h polarization bubble diagram for the magnonic self-energy whose analytical expression is given by

$$\check{\mathbf{\Omega}}^{\mathrm{pol}}_{mn}(\omega) = -\frac{i}{2} g^2 S \int dE\, \check{\mathbf{G}}_{\downarrow\downarrow,nm}(E) \check{\mathbf{G}}_{\uparrow\uparrow,mn}(E+\omega). \tag{7.13}$$

Thus, the dressed magnonic GF which includes this self-energy through Eq. (7.8) will be inserted into the electronic self-energy diagrams in Fig. 7.2(a), thereby generating an infinite resummation of diagrams until the mutual self-consistency is achieved. Note that this is analogous to the self-consistent GW treatment of the one-particle electronic self-energy due to electron-electron interaction out of equilibrium. [220]

7.3.2 Numerical Implementation in Keldysh Space

Equations (7.7), (7.8), (7.11) and (7.13) form a system of coupled nonlinear integral equations that has to be solved iteratively until the convergence criterion is met. We use expectation value of charge current (see Sec. 7.4) to define one such criterion, $\sum_{\alpha=L,R} |I_\alpha^{\mathrm{new}} - I_\alpha^{\mathrm{old}}| < \delta$. Here I_α^{old} is charge current in lead α at the beginning of an iteration, I_α^{new} denotes charge current at the end of the same iteration and we select $\delta = 10^{-6}$.

The Keldysh-space electronic GF and self-energies in these coupled equations are matrices of the size $N_{\mathrm{sites}} \times 2_{\mathrm{spin}} \times 2_{\mathrm{Keldysh}}$ (if $n_{\mathrm{orb}} > 1$ orbitals are used per site then $N_{\mathrm{sites}} \mapsto N_{\mathrm{sites}} \times n_{\mathrm{orb}}$), while the magnonic GF and self-energies are matrices of the size $N_{\mathrm{sites}} \times 2_{\mathrm{Keldysh}}$. The most time-consuming part of solving the coupled equations is the integration in Eq. (7.11) for $\check{\mathbf{\Sigma}}^F(E)$, which can be viewed as the convolution

$$\check{\mathbf{C}}(x) = \check{\mathbf{A}}(x) * \check{\mathbf{B}}(x) = \int_{-\infty}^{\infty} dy\, \check{\mathbf{A}}(x-y) \circ \check{\mathbf{B}}(y), \tag{7.14}$$

where $[\check{\mathbf{A}} \circ \check{\mathbf{B}}]_{mn} = [\check{\mathbf{A}}]_{mn}[\check{\mathbf{B}}]_{mn}$ is the elementwise product of matrices. The fact that matrix elements of the retarded and advanced components of GFs in Eqs. (7.7) and (7.8) are nonzero in the whole range of integration would make the numerical computation of this convolution prohibitively expensive. However, this obstacle can be removed by using the fact that retarded and advanced GFs are analytic functions

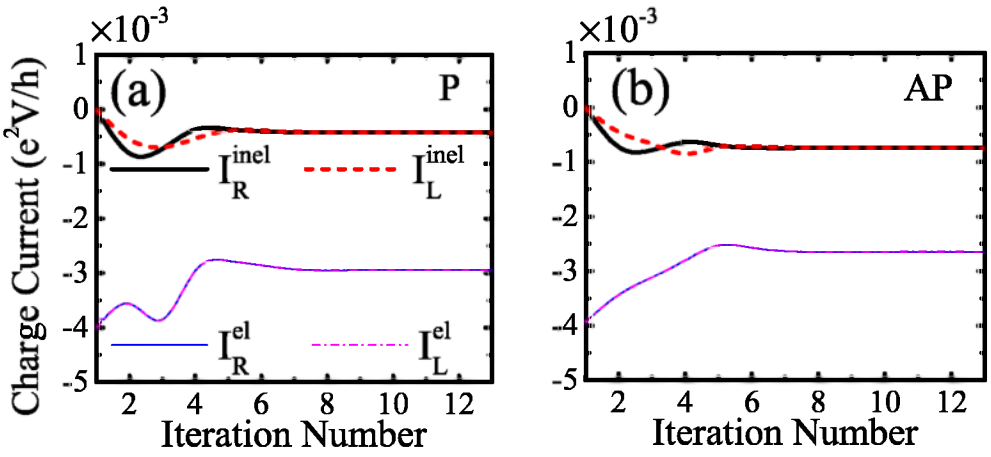

Figure 7.3: Elastic and inelastic contributions to charge current in the left and right lead of MTJ in Fig. 7.1 with $N_x \times N_y \equiv 3 \times 1$ active region at different iteration number within the self-consistent loop for solving coupled Eqs. (7.7), (7.8), (7.11) and (7.13). The orientation of the magnetizations of two F layers in Fig. 7.1 is parallel in (a) and antiparallel in (b). The bias voltage is set as $V_b = -60$ mV and temperature is $T = 12$ K.

in the upper and lower half of the complex plane, respectively. Thus, the real ($\Re$) and imaginary ($\Im$) parts of their matrix elements must obey the following relation

$$\Re\{\mathbf{A}^r(x)\} = \mathcal{H}[\Im\{\mathbf{A}^r(x)\}] = \frac{1}{\pi}\mathcal{P}\int dy\,\frac{\Im\{\mathbf{A}^r(y)\}}{x-y}. \tag{7.15}$$

Here $\mathcal{H}$ is the Hilbert transform, whose implementation in our scheme is discussed in more details in Appendix A, and $\mathcal{P}$ stands for the Cauchy principal value. This makes it possible to decompose Keldysh-space matrices as follows

$$\check{\mathbf{A}} = \begin{pmatrix} \mathbf{A}_{11} & \mathbf{A}_{12} \\ \mathbf{A}_{21} & \mathbf{A}_{22} \end{pmatrix} = \begin{pmatrix} \mathbf{A}^< + \mathbf{A}^r & \mathbf{A}^> \\ \mathbf{A}^< & \mathbf{A}^> - \mathbf{A}^r \end{pmatrix}$$
$$= \check{\mathbf{A}}^{\mathrm{sym}} + \mathcal{H}[\check{\mathbf{A}}^{\mathrm{asym}}], \tag{7.16}$$

where

$$\check{\mathbf{A}}^{\mathrm{sym}} = \begin{pmatrix} \Re(\mathbf{A}_{21}) + i\Im(\mathbf{A}_{11}) & \mathbf{A}_{12} \\ \mathbf{A}_{21} & \Re(\mathbf{A}_{12}) + i\Im(\mathbf{A}_{22}) \end{pmatrix}, \tag{7.17a}$$

$$\check{\mathbf{A}}^{\mathrm{asym}} = \begin{pmatrix} 1 & 0 \\ 0 & -1 \end{pmatrix} \Im(\mathbf{A}_{11} - \mathbf{A}_{21}), \tag{7.17b}$$

are labeled as "symmetric" and "asymmetric" part. We note that all the relevant information is already contained in $\check{\mathbf{A}}^{\mathrm{sym}}$, so that one can find $\check{\mathbf{A}}^{\mathrm{asym}}$ from it by using

$$\check{\mathbf{A}}^{\mathrm{asym}} = \frac{1}{i} \begin{pmatrix} 1 & 0 \\ 0 & -1 \end{pmatrix} (\mathbf{A}_{11}^{\mathrm{sym}} - \mathbf{A}_{21}^{\mathrm{sym}}). \tag{7.18}$$

This idea allows us to restrict the range of integration in the convolution in Eq. (7.14) to the energy bandwidth of electrons and magnons. Once the decomposition is done for both matrices $\check{\mathbf{A}}$ and $\check{\mathbf{B}}$, the convolution in Eq. (7.14) can be evaluated using

$$\check{\mathbf{C}} = \check{\mathbf{A}} * \check{\mathbf{B}} = \check{\mathbf{C}}^{\mathrm{sym}} + \mathcal{H}[\check{\mathbf{C}}^{\mathrm{asym}}], \tag{7.19}$$

with

$$\check{\mathbf{C}}^{\mathrm{sym}} = \check{\mathbf{A}}^{\mathrm{sym}} * \check{\mathbf{B}}^{\mathrm{sym}} - \check{\mathbf{A}}^{\mathrm{asym}} * \check{\mathbf{B}}^{\mathrm{asym}}, \tag{7.20a}$$

$$\check{\mathbf{C}}^{\mathrm{asym}} = \check{\mathbf{A}}^{\mathrm{sym}} * \check{\mathbf{B}}^{\mathrm{asym}} + \check{\mathbf{A}}^{\mathrm{asym}} * \check{\mathbf{B}}^{\mathrm{sym}}. \tag{7.20b}$$

Here we used the following properties of the Hilbert transform and the convolution operator

$$\mathcal{H}[\check{\mathbf{A}}] * \check{\mathbf{B}} = \check{\mathbf{A}} * \mathcal{H}[\check{\mathbf{B}}] = \mathcal{H}[\check{\mathbf{A}} * \check{\mathbf{B}}], \tag{7.21}$$

$$\mathcal{H}[\mathcal{H}[\check{\mathbf{A}}]] = -\check{\mathbf{A}}. \tag{7.22}$$

Note that one has to actually calculate only $\check{\mathbf{C}}^{\mathrm{sym}}$, after which the asymmetric part is obtained from Eq. (7.18).

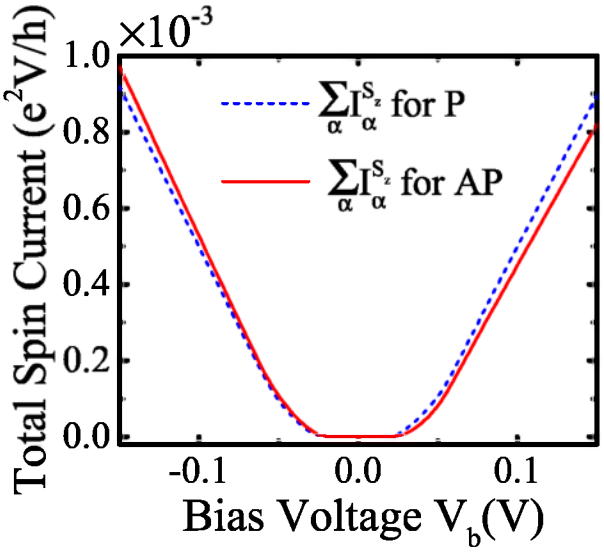

Figure 7.4: Total spin current dissipated (at $T = 12$ K) inside $N_x \times N_y \equiv 3 \times 1$ active region of MTJ in Fig. 7.1 as a function of the bias voltage for parallel and antiparallel orientation of the magnetizations of two F layers. The spin current is obtained from Eq. (7.28) using electronic GF computed by solving coupled Eqs. (7.7), (7.8) and (7.11).

7.4 Application to Charge and Spin Currents in MTJ Driven by Finite Bias Voltage

The charge current in lead α can be viewed as the sum of two spin-resolved charge currents, $I_\alpha = I_\alpha^\uparrow + I_\alpha^\downarrow$. For an interacting active region attached to two non-interacting semi-infinite leads, lead currents can be obtained directly from $\check{\mathbf{G}}(E)$ and $\check{\mathbf{\Sigma}}_\alpha$

$$\begin{aligned} I_\alpha &= \frac{e}{h}\int dE\, \mathrm{Tr}\left[\boldsymbol{\tau}_{11}(\check{\mathbf{G}}\boldsymbol{\tau}^z\check{\mathbf{\Sigma}}_\alpha - \check{\mathbf{\Sigma}}_\alpha\boldsymbol{\tau}^z\check{\mathbf{G}})\right] \\ &= \frac{e}{h}\int dE\, \mathrm{Tr}\left[\mathbf{G}^>(E)\mathbf{\Sigma}_\alpha^<(E) - \mathbf{G}^<(E)\mathbf{\Sigma}_\alpha^>(E)\right], \end{aligned} \tag{7.23}$$

where we employ the following notation

$$\boldsymbol{\tau}_{11} = \begin{pmatrix} 1 & 0 \\ 0 & 0 \end{pmatrix}. \tag{7.24}$$

The second line in Eq. (7.23) is the well-known Meir-Wingreen formula. [240] Similarly, the spin current $I_\alpha^S = I_\alpha^\uparrow - I_\alpha^\downarrow$ (in the same units as for the charge current) in lead α is obtained from

$$\begin{aligned} I_\alpha^{S_{x,y,z}} &= \frac{e}{h}\int dE\,\mathrm{Tr}\left[\boldsymbol{\tau}_{11}\sigma_{x,y,z}(\check{\mathbf{G}}\boldsymbol{\tau}^z\check{\boldsymbol{\Sigma}}_\alpha - \check{\boldsymbol{\Sigma}}_\alpha\boldsymbol{\tau}^z\check{\mathbf{G}})\right] \\ &= \frac{e}{h}\int dE\,\mathrm{Tr}\left[\sigma_{x,y,z}\left(\mathbf{G}^>(E)\boldsymbol{\Sigma}_\alpha^<(E) - \mathbf{G}^<(E)\boldsymbol{\Sigma}_\alpha^>(E)\right)\right]. \end{aligned} \tag{7.25}$$

It is instructive to check if charge current is conserved, $\sum_\alpha I_\alpha \stackrel{?}{=} 0$, after electronic GF in F-SCBA is inserted into Eq. (7.23)

$$\begin{aligned} &\sum_\alpha I_\alpha = \frac{e}{h}\int dE\,\mathrm{Tr}\left[(\boldsymbol{\tau}^z\check{\mathbf{G}}(E)\boldsymbol{\tau}^z\check{\boldsymbol{\Sigma}}_{\text{leads}}(E) - \check{\boldsymbol{\Sigma}}_{\text{leads}}(E)\boldsymbol{\tau}^z\check{\mathbf{G}}(E)\boldsymbol{\tau}^z)\boldsymbol{\tau}_{11}\right] \\ &= -\frac{e}{h}\int dE\,\mathrm{Tr}\left[(\boldsymbol{\tau}^z\check{\mathbf{G}}(E)\boldsymbol{\tau}^z\check{\boldsymbol{\Sigma}}^F(E) - \check{\boldsymbol{\Sigma}}^F(E)\boldsymbol{\tau}^z\check{\mathbf{G}}(E)\boldsymbol{\tau}^z)\boldsymbol{\tau}_{11}\right] \\ &= \frac{eg^2S}{2ih}\int dE dE'\,\mathrm{Tr}\left[(\boldsymbol{\tau}^z\check{\mathbf{G}}_{\uparrow\uparrow}(E)\boldsymbol{\tau}^z\check{\mathbf{B}}(E-E')\circ\check{\mathbf{G}}_{\downarrow\downarrow}(E') - \check{\mathbf{G}}_{\downarrow\downarrow}(E')\circ\check{\mathbf{B}}(E'-E)\boldsymbol{\tau}^z\check{\mathbf{G}}_{\uparrow\uparrow}(E)\boldsymbol{\tau}^z\right. \\ &\quad \left.+\boldsymbol{\tau}^z\check{\mathbf{G}}_{\downarrow\downarrow}(E')\boldsymbol{\tau}^z\check{\mathbf{B}}^T(E'-E)\circ\check{\mathbf{G}}_{\uparrow\uparrow}(E) - \check{\mathbf{G}}_{\uparrow\uparrow}(E)\circ\check{\mathbf{B}}^T(E-E')\boldsymbol{\tau}^z\check{\mathbf{G}}_{\downarrow\downarrow}(E')\boldsymbol{\tau}^z)\boldsymbol{\tau}_{11}\right] \\ &\equiv 0. \end{aligned} \tag{7.26}$$

We use $\check{\mathbf{G}}\boldsymbol{\tau}^z(\check{\boldsymbol{\Sigma}}_{\text{leads}}+\check{\boldsymbol{\Sigma}}^F)-(\check{\boldsymbol{\Sigma}}_{\text{leads}}+\check{\boldsymbol{\Sigma}}^F)\boldsymbol{\tau}^z\check{\mathbf{G}}=0$ to write the second line in Eq. (7.26). To show that the third line is identically zero, we use the fact that three arbitrary matrices $\check{\mathbf{A}}$, $\check{\mathbf{B}}$ and $\check{\mathbf{C}}$ satisfy $\mathtt{diag}(\check{\mathbf{A}}\circ\check{\mathbf{B}}\check{\mathbf{C}} - \check{\mathbf{A}}\check{\mathbf{B}}^T\circ\check{\mathbf{C}}) = 0$, where $\mathtt{diag}(\ldots)$ returns the main diagonal of its matrix argument. Note that in all of the above expressions the elementwise products of the matrices are performed prior to the matrix products. This demonstrates that no matter what approximation is employed for the magnonic GF and self-energy, the charge current will be conserved as long as the self-consistency is achieved when computing electronic GF and self-energy within F-SCBA.

The charge current in Eq. (7.23) can be conveniently separated [235, 241] into two terms, $I_\alpha = I_\alpha^{\text{el}} + I_\alpha^{\text{inel}}$

$$I_\alpha^{\text{el}} = \frac{e}{h}\sum_\beta\int dE\,\mathrm{Tr}\left[\boldsymbol{\Gamma}_\alpha\mathbf{G}^r\boldsymbol{\Gamma}_\beta\mathbf{G}^a\right](f_\beta - f_\alpha), \tag{7.27a}$$

$$I_\alpha^{\text{inel}} = \frac{e}{h}\int dE\,\mathrm{Tr}\left[\mathbf{G}^r\boldsymbol{\Sigma}^{>,F}\mathbf{G}^a\boldsymbol{\Sigma}_\alpha^< - \mathbf{G}^r\boldsymbol{\Sigma}^{<,F}\mathbf{G}^a\boldsymbol{\Sigma}_\alpha^>\right]. \tag{7.27b}$$

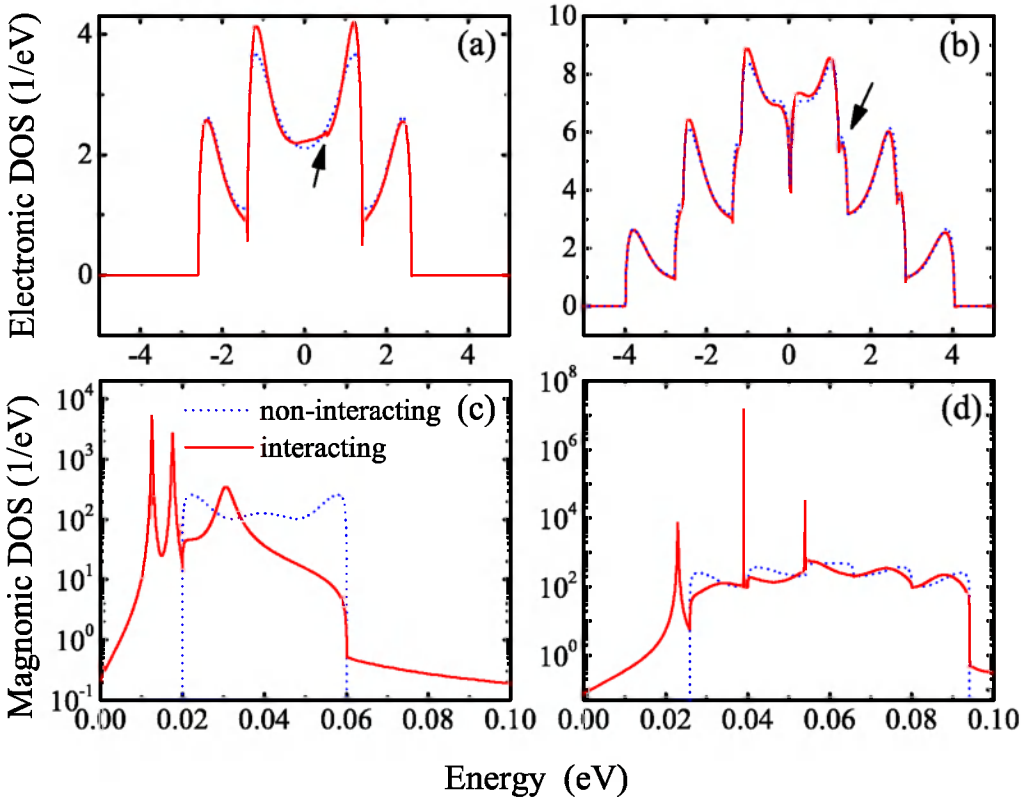

Figure 7.5: The electronic density of states within the active region of MTJ model in Fig. 7.1 of size: (a) $N_x \times N_y \equiv 3 \times 1$; and (b) $N_x \times N_y \equiv 3 \times 3$. The magnonic density of states within the same active regions is shown in panels (c) and (d), respectively. These quantities are computed at finite bias voltage $V_b = -60$ mV and at temperature $T = 12$ K, in the absence ($g = 0$ for dashed line) or the presence ($g \neq 0$ for solid line) of e-m interaction in the Hamiltonian in Eq. (7.3c). The respective DOS is obtained from the retarded electronic GF, using $-\mathrm{Tr}[\Im(\mathbf{G}^r)]/\pi$, or the retarded magnonic GF, using $-\mathrm{Tr}[\Im(\mathbf{B}^r)]/\pi$, after solving coupled Eqs. (7.7), (7.8), (7.11) and (7.13) which take into account influence of electrons on magnons. The arrows in panels (a) and (b) point at the kinks (located at the Fermi energies of MTJ model with two different sizes of the active region, respectively) in the interacting electronic DOS (solid line) due to e-m coupling.

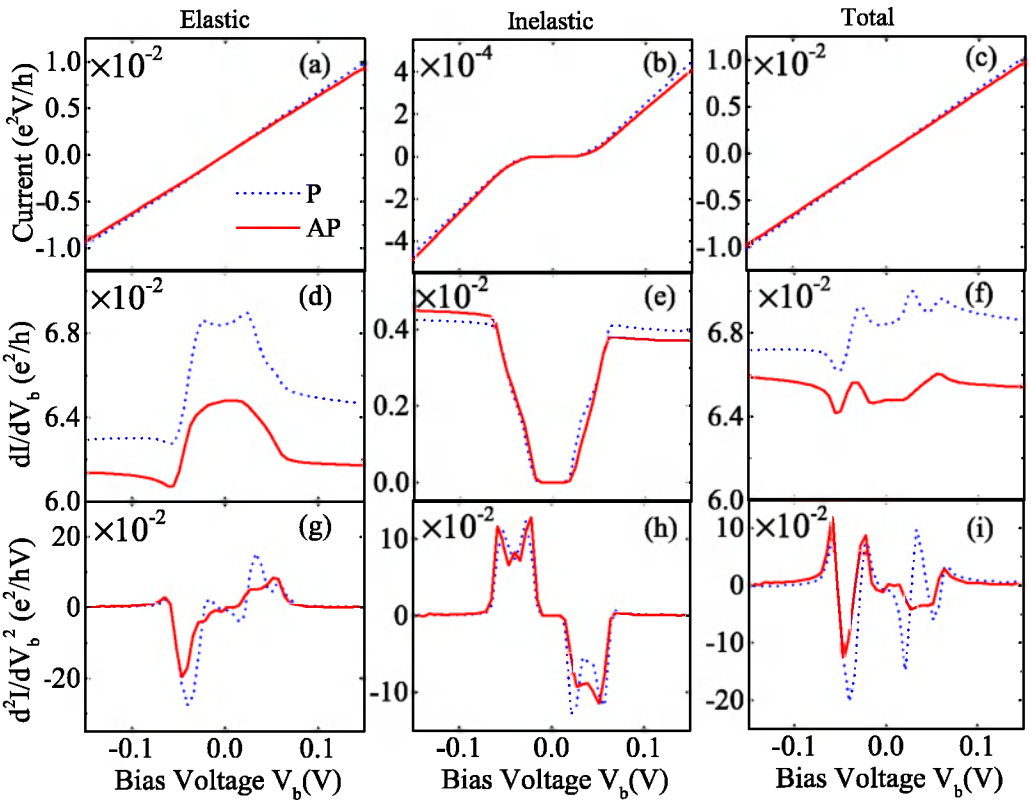

Figure 7.6: Elastic and inelastic charge currents in Eq. (7.27) and their sum, as well as the corresponding first and second derivatives, versus the bias voltage in the model of MTJ in Fig. 7.1 with active region $N_x \times N_y \equiv 3 \times 1$ for parallel and antiparallel orientation of its magnetizations. These charge currents are obtained from the electronic GF computed in F-SCBA which includes (in self-consistent fashion) the non-interacting magnonic GF. The temperature is set as $T = 12$ K.

We label the first term as "elastic" current $I_\alpha^{\rm el}$ since it has the form of the Landauer-like formula for elastic transport of non-interacting quasiparticles whose effective transmission function is expressed [187] in terms of NEGF quantities, $T(E) = \mathrm{Tr}[\mathbf{\Gamma}_\alpha \mathbf{G}^r \mathbf{\Gamma}_\beta \mathbf{G}^a]$. The second term appears as the nonequilibrium corrections due to many-body interactions, which we label as "inelastic" current. Plotting separately elastic and inelastic current components makes it possible to provide additional insights when interpreting our results in Sec. 7.4.

Note that apparent connection of Eq. (7.27a) to the Landauer formula should not be pushed too far since the effective transmission $T(E)$ in $I_\alpha^{\rm el}$ already contains part of e-m interaction. That is, the standard Landauer formula [187] for single-particle elastic scattering uses the retarded and advanced GFs which include the self-energies due to the semi-infinite leads only. On the other hand, $\mathbf{G}^r$ and $\mathbf{G}^a$ in $I_\alpha^{\rm el}$ include additional self-energy due to e-m interaction which renormalizes the non-interacting reference system, and for strong enough interaction can go even beyond the quasiparticle description of the many-body interacting quantum system. Even when quasiparticles are well-defined, the presence of self-energy that is functional of the retarded GF itself means that $I_\alpha^{\rm el}$ includes dephasing effects due to many-body interaction [242] and is, therefore, different from phase-coherent tunneling current that would be obtained from the the standard Landauer formula. [187]

Here we illustrate in Fig. 7.3 that $I_\alpha^{\rm el}$ is conserved at each iteration, while the conservation of $I_\alpha^{\rm inel}$ component requires to reach the self-consistency in the computation of electronic GF and self-energy in F-SCBA, as discussed in Eq. (7.26). Note that the magnonic GF and self-energy used to obtain Fig. 7.3 also include e-h polarization bubble diagram from Fig. 7.2(b).

The spin current can analogously be separated into the elastic and inelastic

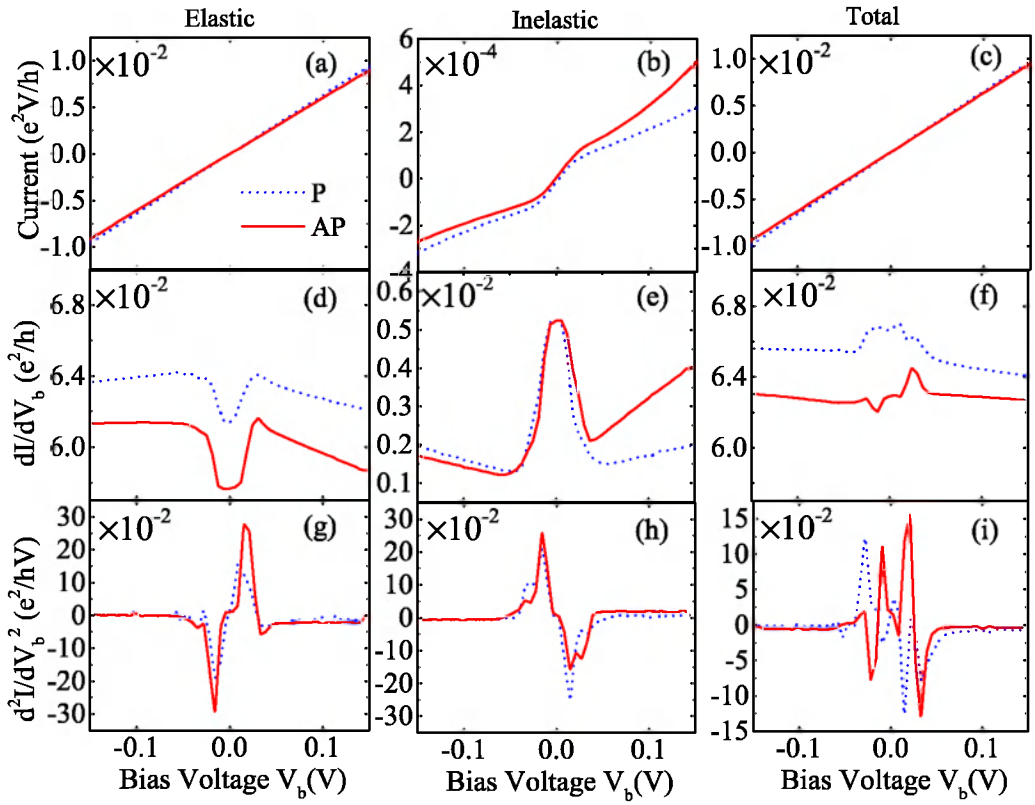

Figure 7.7: Elastic and inelastic charge currents in Eq. (7.27) and their sum, as well as the corresponding first and second derivatives, versus the bias voltage in the model of MTJ in Fig. 7.1 with active region $N_x \times N_y \equiv 3 \times 1$ for parallel and antiparallel orientation of its magnetizations. These charge currents are obtained from the electronic GF computed in F-SCBA, which includes (in self-consistent fashion) the interacting magnonic GF with the e-h polarization bubble diagram in Fig. 7.2(b). The temperature is set as $T = 12$ K.

contributions, $I_\alpha^{S_z} = I_\alpha^{S_z,\mathrm{el}} + I_\alpha^{S_z,\mathrm{inel}}$

$$I_\alpha^{S_z,\mathrm{el}} = \frac{e}{h}\sum_\beta \int dE\, \mathrm{Tr}\left[\sigma_z \mathbf{\Gamma}_\alpha \mathbf{G}^r \mathbf{\Gamma}_\beta \mathbf{G}^a\right](f_\beta - f_\alpha), \tag{7.28a}$$

$$I_\alpha^{S_z,\mathrm{inel}} = \frac{e}{h}\int dE\, \mathrm{Tr}\left[\sigma_z\left(\mathbf{G}^r \mathbf{\Sigma}^{>,F} \mathbf{G}^a \mathbf{\Sigma}_\alpha^< - \mathbf{G}^r \mathbf{\Sigma}^{<,F} \mathbf{G}^a \mathbf{\Sigma}_\alpha^>\right)\right]. \tag{7.28b}$$

We find that $\sum_\alpha I_\alpha^{S_z,\mathrm{el}} \equiv 0$ vanishes at *all* bias voltages, so that the total spin current $\sum_\alpha I_\alpha^{S_z} = \sum_\alpha I_\alpha^{S_z,\mathrm{inel}}$ is governed by the inelastic component only which is plotted in Fig. 7.4. Thus, this quantity measures the loss of angular momentum of electrons within the interacting active region of MTJ in Fig. 7.1, which is then carried away by magnonic spin current (through the left semi-infinite lead toward the left magnonic macroscopic reservoir). Although spin current carried by electrons or magnons individually is not conserved, the total angular moment in this process is conserved. This finding further justifies the separation of currents into elastic and inelastic contributions since $\sum_\alpha I_\alpha^{S_z,\mathrm{el}} \equiv 0$ does not participate in the loss of angular momentum.

Due to the fact that the e-m interaction strength g is comparable to the magnonic bandwidth, the single particle and many-body properties of magnons within the active region in Fig. 7.1 are governed largely by the collective quasiparticles rather than the bare (non-interacting) magnons we started from. This is demonstrated by plotting the magnon density of states (DOS) in Fig. 7.5 within the active region versus energy. The DOS is obtained from $-\mathrm{Tr}[\Im(\mathbf{B}^r)]/\pi$ with e-m interactions turned off ($g = 0$) or turned on ($g \neq 0$). In Fig. 7.5(c), we can clearly distinguish three peaks corresponding to the quasibound states suggesting the formation of long-lived quasiparticles. They can be interpreted as a magnon dressed by the cloud of electron-hole pair excitations out of equilibrium. Importantly for ZBA discussed below, the DOS of interacting magnons extends all the way to zero energy, thereby enabling e-m scattering even at vanishingly small bias voltage. On the other hand, the electronic DOS obtained from $-\mathrm{Tr}[\Im(\mathbf{G}^r)]/\pi$ and plotted in Figs. 7.5(a) and 7.5(b) is only slightly perturbed when e-m interaction is turned on due to much larger electronic bandwidth.

Figure 7.6 plots the elastic, inelastic and total charge currents, together with their first derivative dI/dV_b (i.e., differential conductance) and second derivative d^2I/dV_b^2

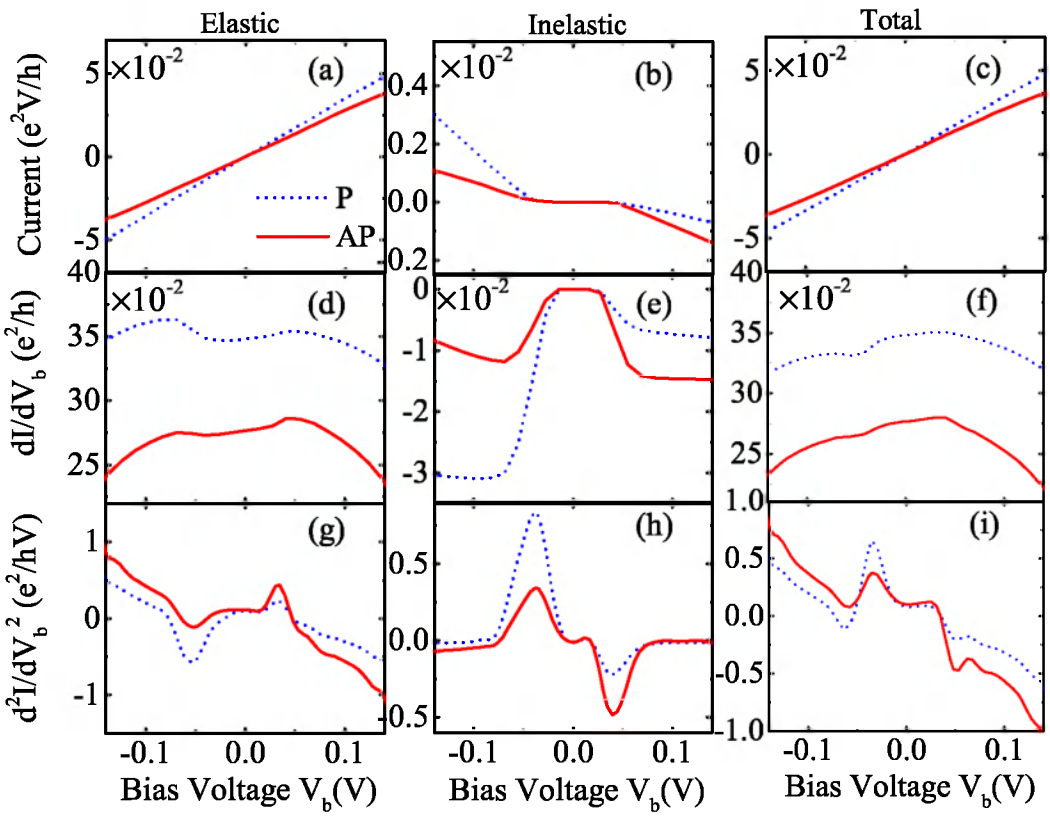

Figure 7.8: Elastic and inelastic charge currents in Eq. (7.27) and their sum, as well as the corresponding first and second derivatives, versus the bias voltage in the model of MTJ in Fig. 7.1 with active region $N_x \times N_y \equiv 3 \times 3$ for parallel and antiparallel orientation of its magnetizations. These charge currents are obtained from the electronic GF computed in F-SCBA, which includes (in self-consistent fashion) the non-interacting magnonic GF. The temperature is set as $T = 12$ K.

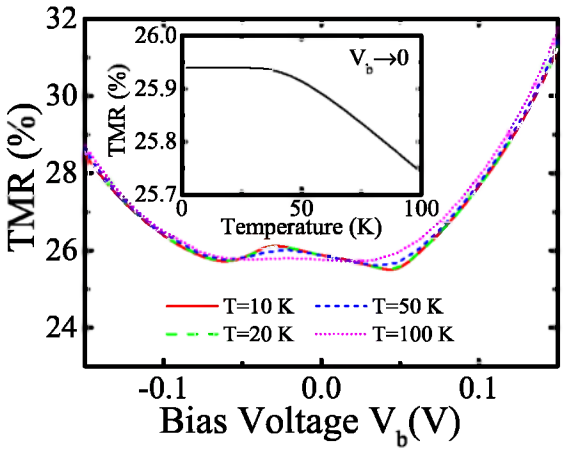

Figure 7.9: The TMR vs. bias voltage V_b in the model of MTJ in Fig. 7.1 with active region $N_x \times N_y \equiv 3 \times 3$. The inset shows TMR as a function of temperature in the linear-response limit $V_b \to 0$. These results are obtained from electronic GF computed by solving coupled Eqs. (7.7), (7.8) and (7.11).

(i.e., IETS), as a function of the applied bias voltage V_b. The currents in Fig. 7.6 are computed using F-SCBA for the electronic GF and self-energy of $N_x \times N_y \equiv 3 \times 1$ active region in Fig. 7.1, while the magnonic GF is used as the non-interacting one by setting $\check{\mathbf{\Omega}}_{\mathrm{m-e}} \equiv 0$ in Eq. (7.8). The inelastic current in Fig. 7.6(b) is zero until the threshold bias voltage is reached ($\simeq \pm 20$ mV according to dashed line in Fig. 7.5) at which magnons can be excited. Above the threshold voltage, inelastic current displays Ohmic behavior. This is simply due to the fact that the rate of energy (and angular momentum) loss is proportional to the rate of electrons being injected into the active region. Although elastic current in Fig. 7.6(a) shows apparent Ohmic behavior for all bias voltages, the corresponding differential conductance in Fig. 7.6(d) deviates strongly from the straight line within the energy rage where magnons can be excited. This can be explained by the fact that the effective electronic DOS inside the active region can be changed through e-m scattering. The elastic differential conductance in Fig. 7.6(d) decreases once the magnons are excited, but this is compensated by the

increase of inelastic differential conductance in Fig. 7.6(e) such that the total differential conductance in Fig. 7.6(f) has less pronounced features. The IETS plotted in Figs. 7.6(g) and 7.6(h) shows a clear signature of the non-interacting magnonic DOS from Fig. 7.5 with two peaks emerging slightly away from $V_b = 0$. Nevertheless, when these two contributions are summed up in Fig. 7.6(i), IETS for total current shows more than just two peaks.

In order to see the effect of DOS of interacting magnons (solid line in Fig. 7.5), or possible magnon heating due to tunneling electrons, Fig. 7.7 presents the same information as in Fig. 7.6 but recomputed by including e-h polarization bubble diagram in Fig. 7.2(b) for the magnonic self-energy $\check{\mathbf{\Omega}}_{\mathrm{m-e}} \neq 0$. Since DOS of interacting magnons in Fig. 7.5 is sufficiently broadened to reach low frequencies, the inelastic current in Fig. 7.7(b) is now non-zero even for very small bias voltage $V_b \to 0$. The presence of magnons dressed by the cloud of e-h pair excitations in this calculation forces elastic conductance in Fig. 7.7(d) to increase around $V_b = 0$, or inelastic conductance in Fig. 7.7(e) to decrease, which is opposite to the behavior of the same quantities in the case of non-interacting magnons analyzed in Fig. 7.6. The two peaks of opposite sign around $V_b = 0$ in partial IETS plotted in Figs. 7.7(g) and 7.7(h) look very similar to ZBA peaks observed experimentally [213] in realistic MTJs.

Due to opposite effect of e-m interaction on the two partial IETS, their sum in both Figs. 7.6(i) and 7.7(i) looses the simple two peak structure around $V_b = 0$ observed experimentally. [213] To investigate whether this complexity in the total IETS could be an artifact of 1D nature of MTJ model (with active region $N_x \times N_y \equiv 3 \times 1$ attached to 1D leads) considered in Figs. 7.6 and 7.7, we recompute the same quantities for the active region $N_x \times N_y \equiv 3 \times 3$ in Fig. 7.8. For this case, both the partial IETS in Figs. 7.8(g) and 7.8(h) and the total IETS in Fig. 7.8(i) exhibit simple two peak structure. However, the two peaks appear slightly away from the zero bias voltage $V_b = 0$ because we do not include (due to substantial computational expense) e-h polarization bubble diagram from Fig. 7.2(b) which is needed to introduce non-zero magnonic DOS at low energies in Fig. 7.5(d) enabling e-m scattering at $V_b \to 0$.

The usage of $N_x \times N_y \equiv 3 \times 3$ active region introduces non-negligible TMR ratio which can be extracted from Fig. 7.8(c) as TMR $\simeq 26\%$ for $V_b \in (-0.1\text{ V}, 0.1\text{ V})$. Its detailed dependence on V_b plotted in Fig. 7.9 shows how ZBA vanishes for temperatures $T \gtrsim 100$ K. Also, the TMR ratio (at $V_b \to 0$) vs. temperature shown in the inset of Fig. 7.9 agrees with experimentally observed [213, 214] TMR decrease with increasing temperature.

Considering fully 3D model of MTJs, where additional k-point sampling is required for the transverse direction, would require carefully crafted approximations to evade prohibitively expensive five-dimensional integrals in the systems of coupled nonlinear integral equations for the electronic and magnonic GFs. Also, we note that dI/dV_b in experiments [213] has a dip at $V_b = 0$, and its absolute value increases with increasing $|V_b|$ due to opening of new conducting channels by inelastic e-m scattering. This is not seen in Figs. 7.6(f), 7.7(f) and 7.8(f) due to small number of spin-resolved conducting channels (up to six for $N_x \times N_y \equiv 3 \times 3$ active region) present in our model of MTJ.

7.5 Summary of Chapter

The e-ph interaction in nanostructures driven out of equilibrium, as the example of nonequilibrium electron-boson quantum-many body system, has been amply studied [229, 230, 231, 232, 233, 236, 237, 225, 226] over the past decade using NEGF formalism. This approach, which makes it possible to rigorously model microscopic details of inelastic scattering processes, has been typically implemented using the SCBA diagrams for the electronic self-energy, and sometimes also including e-h polarization bubble diagram for the phonon self-energy in the nonequilibrium MBPT. On the other hand, the same level of description of e-m scattering has received far less attention, [219] despite its great relevance for a plethora of problems in spintronics. [216, 217]

In this chapter, we have shown how to obtain analytical expressions for SCBA and e-h polarization bubble diagrams describing e-m scattering. This is achieved in a particularly compact form by using matrix GFs in the Keldysh space (which are

functions of energy for electrons or frequency for magnons in steady-state nonequilibrium), thereby simplifying tracking of electron spin flips and direction of magnon propagation required to conserve angular momentum at each vertex of the Feynman diagrams. The self-consistent solution of the corresponding system of coupled nonlinear integral equations, which is equivalent to infinite resummation of certain classes of diagrams (akin to the self-consistent GW treatment of the one-particle electronic self-energy due to electron-electron interaction out of equilibrium [220]), is obtained via several intertwined numerical algorithms that reduce the computational complexity of this task.

Using this framework, we have computed charge and spin currents at finite bias voltage in quasi-1D models of F/I/F MTJ illustrated in Fig. 7.1. Our *key results* are summarized as follows: (*i*) while elastic component of the sum of spin currents in all attached leads is zero at all bias voltages, the inelastic one is non-zero thereby measuring the loss of spin angular momentum carried by magnons away from the active region (see Fig. 7.4); (*ii*) turning on the e-m interaction strongly modifies magnonic DOS, which acquires larger bandwidth while exhibiting peaks due to quasibound states of *magnons dressed by the cloud of electron-hole pair excitations* [see Figs. 7.5(c) and 7.5(d)]; (*iii*) using F-SCBA for the electronic self-energy in Fig. 7.2(a), coupled with e-h polarization bubble diagram for the magnonic self-energy in Fig. 7.2(b), generates two peak structure around zero bias voltage in the second derivative (i.e., IETS [215]) of both elastic and inelastic charge currents (see Fig. 7.7).

We emphasize that e-h polarization bubble diagram in Fig. 7.2(b) is responsible for the substantial change of magnonic DOS (encoded by the retarded magnonic GF) in equilibrium, as well as for magnon heating (encoded by the lesser magnonic GF) in nonequilibrium due to tunneling electrons where heated magnons can also exert backaction [226] onto electrons. Since ZBA occurs at very small bias voltages, the former effect is more important because the broadened magnonic DOS in Figs. 7.5(c) and 7.5(d) extends to low energies (in contrast to DOS of non-interacting magnons),

thereby making possible inelastic e-m scattering even at zero bias. It is worth mentioning that the effect of electron-boson interaction on bosonic DOS has been rarely discussed in prior NEGF studies [219, 229, 230, 231, 232, 233, 236, 237, 225, 226] of coupled electron-boson systems, either due to simplicity of bosonic spectrum assumed or because of not inserting dressed magnonic GF lines (which include e-h polarization bubble diagram) into SCBA for electronic GF.

While partial IETS in Figs. 7.7(g) and 7.7(h) obtained from elastic or inelastic components of charge current, respectively, are quite similar to experimentally observed [213] ZBA, their sum in Fig. 7.7(i) is more complicated due to usage of strictly 1D model with active region $N_x \times N_y \equiv 3 \times 1$ in those Figures. Switching to $N_x \times N_y \equiv 3 \times 3$ active region attached to quasi-1D leads (supporting more than two spin-resolved conducting channels) makes total IETS in Fig. 7.8(i) exhibiting only two peaks, albeit shifted slightly away from $V_b = 0$ due to exclusion of e-h polarization bubble diagram in this calculation in order to reduce computational expense.

We believe that extension of our approach to 3D MTJs [by adding computationally expensive k-point sampling in the y and z directions while keeping real space Hamiltonian from Eq. (7.1) in the x direction] would be able to describe not just ZBA in realistic junctions, but also TMR and STT effects as a function of temperature and bias voltage, thereby opening a path to understand how to optimize these effects for applications in spintronics by *tailoring magnon spectrum*.

BIBLIOGRAPHY

[1] J. Xiao, G. E. W. Bauer, and A. Brataas, "Charge pumping in magnetic tunnel junctions: Scattering theory," *Physical Review B (Condensed Matter and Materials Physics)* **77** (2008), no. 18, 180407.

[2] Y. Shiomi, K. Nomura, Y. Kajiwara, K. Eto, M. Novak, K. Segawa, Y. Ando, and E. Saitoh, "Bulk topological insulators as inborn spintronics detectors," *arXiv:1312.1111* (2013).

[3] J. C. R. Sánchez, L. Vila, G. Desfonds, S. Gambarelli, J. P. Attané, J. M. D. Teresa, C. Magén, and A. Fert, "Spin-to-charge conversion using rashba coupling at the interface between non-magnetic materials," *Nat. Commun.* **4** (2013) 2944.

[4] B. K. Nikolić and S. Souma, "Decoherence of transported spin in multichannel spin-orbit-coupled spintronic devices: Scattering approach to spin-density matrix from the ballistic to the localized regime," *Phys. Rev. B* **71** (2005), no. 19, 195328.

[5] E. Y. Tsymbal and I. Žutić, eds., *Handbook of Spin Transport and Magnetism.* Chapman and Hall/CRC, Boca Raton, 2012.

[6] H. Ohno, "A window on the future of spintronics," *Nature Materials* **9** (2010) 952.

[7] T. Dietl, "A ten-year perspective on dilute magnetic semiconductors and oxides," *Nature Materials* **9** (2010) 965.

[8] T. Maruyama, Y. Shiota, T. Nozaki, K. Ohta, N. Toda, M. Mizuguchi, A. A. Tulapurkar, T. Shinjo, M. Shiraishi, S. Mizukami, Y. Ando, and Y. Suzuki, "Large voltage-induced magnetic anisotropy change in a few atomic layers of iron," *Nature Nanotech.* **4** (2009) 158.

[9] I. Žutić, J. Fabian, and S. Das Sarma, "Spintronics: Fundamentals and applications," *Rev. Mod. Phys.* **76** (2004) 323, arXiv:cond-mat/0405528.

[10] D. D. Awschalom and M. E. Flatté, "Challenges for semiconductor spintronics," *Nat. Phys.* **3** (Mar., 2007) 153–159.

[11] N. Nagaosa, "Spin currents in semiconductors, metals, and insulators," *J. Phys. Soc. Jpn.* **77** (2008) 031010.

[12] A. Brataas, A. D. Kent, and H. Ohno, "Current-induced torques in magnetic materials," *Nature Mater.* **11** (2012) 372.

[13] T. Jungwirth, J. Wunderlich, and K. Olejník, "Spin hall effect devices," *Nature Mater.* **11** (2012) 382.

[14] G. E. W. Bauer, E. Saitoh, and B. J. van Wees, "Spin caloritronics," *Nature Materials* **11** (2012) 391.

[15] B. Huang, D. J. Monsma, and I. Appelbaum, "Coherent spin transport through a 350 micron thick silicon wafer," *Physical Review Letters* **99** (2007), no. 17, 177209.

[16] R. Jansen, "Silicon spintronics," *Nature Materials* **11** (2012) 400.

[17] D. Pesin and A. H. MacDonald, "Spintronics and pseudospintronics in graphene and topological insulators," *Nature Mater.* **11** (2012) 409.

[18] H. Zhang, C.-X. Liu, X.-L. Qi, X. Dai, Z. Fang, and S.-C. Zhang, "Topological insulators in bi_2se_3, bi_2te_3 and sb_2te_3 with a single dirac cone on the surface," *Nature Phys.* **5** (2009) 438.

[19] H. Zhang and S.-C. Zhang, "Topological insulators from the perspective of first-principles calculations," *Phys. Status Solidi RRL.* **doi: 10.1002/pssr.201206414** (2012).

[20] D. Kim, S. Cho, N. P. Butch, P. Syers, K. Kirshenbaum, S. Adam, J. Paglione, and M. S. Fuhrer, "Surface conduction of topological dirac electrons in bulk insulating bi_2se_3," *Nature Physics* **8** (2012) 459.

[21] F. Xiu, L. He, Y. Wang, L. Cheng, L.-T. Chang, M. Lang, G. Huang, X. Kou, Y. Zhou, X. Jiang, Z. Chen, J. Zou, A. Shailos, and K. L. Wang, "Manipulating surface states in topological insulator nanoribbons," *Nature Nanotechnology* **6** (2011) 216.

[22] M. Z. Hasan and J. E. Moore, "Three-dimensional topological insulators," *Annual Review of Condensed Matter Physics* **2** (2011) 55.

[23] C. Weeks, J. Hu, J. Alicea, M. Franz, and R. Wu, "Engineering a robust quantum spin hall state in graphene via adatom deposition," *Phys. Rev. X* **1** (Oct, 2011) 021001.

[24] M. König, S. Wiedmann, C. Brüne, A. Roth, H. Buhmann, L. W. Molenkamp, X.-L. Qi, and S.-C. Zhang, "Quantum Spin Hall Insulator State in HgTe Quantum Wells," *Science* **318** (2007), no. 5851, 766–770, http://www.sciencemag.org/cgi/reprint/318/5851/766.pdf.

[25] A. Roth, C. Brüne, H. Buhmann, L. W. Molenkamp, J. Maciejko, X.-L. Qi, and S.-C. Zhang, "Nonlocal edge state transport in the quantum spin hall state," *Science* **325** (2009) 294.

[26] C. Brune, A. Roth, H. Buhmann, E. M. Hankiewicz, L. W. Molenkamp, J. Maciejko, X.-L. Qi, and S.-C. Zhang, "Spin polarization of the quantum spin hall edge states," *arXiv:1107.0585* (2011).

[27] D. Ralph and M. Stiles, "Spin transfer torques," *Journal of Magnetism and Magnetic Materials* **320** (Apr., 2008) 1190–1216.

[28] Y. Tserkovnyak, A. Brataas, G. E. W. Bauer, and B. I. Halperin, "Nonlocal magnetization dynamics in ferromagnetic heterostructures," *Rev. Mod. Phys.* **77** (2005) 1375, arXiv:cond-mat/0409242.

[29] B. Heinrich and G. Woltersdorf, "Intrinsic spin relaxation processes in metallic magnetic multilayers," *Journal of Superconductivity and Novel Magnetism* **20** (Feb., 2007) 83–89.

[30] F. Mahfouzi, J. Fabian, N. Nagaosa, and B. K. Nikolić, "Charge pumping by magnetization dynamics in magnetic and semimagnetic tunnel junctions with interfacial rashba or bulk extrinsic spin-orbit coupling," *Phys. Rev. B* **85** (Feb, 2012) 054406.

[31] D. J. Thouless, "Quantization of particle transport," *Phys. Rev. B* **27** (May, 1983) 6083–6087.

[32] P. W. Brouwer, "Scattering approach to parametric pumping," *Phys. Rev. B* **58** (Oct, 1998) R10135–R10138.

[33] M. Büttiker, A. Prêtre, and H. Thomas, "Dynamic conductance and the scattering matrix of small conductors," *Phys. Rev. Lett.* **70** (Jun, 1993) 4114–4117.

[34] M. Switkes, C. M. Marcus, K. Campman, and A. C. Gossard, "An Adiabatic Quantum Electron Pump," *Science* **283** (1999), no. 5409, 1905–1908, http://www.sciencemag.org/cgi/reprint/283/5409/1905.pdf.

[35] S. K. Watson, R. M. Potok, C. M. Marcus, and V. Umansky, "Experimental realization of a quantum spin pump," *Phys. Rev. Lett.* **91** (Dec, 2003) 258301.

[36] F. Giazotto, P. Spathis, S. Roddaro, S. Biswas, F. Taddei, M. Governale, and L. Sorba, "A josephson quantum electron pump," *Nature Physics* **7** (2011) 857.

[37] T. Gerrits, M. L. Schneider, and T. J. Silva, "Enhanced ferromagnetic damping in permalloy/cu bilayers," *Journal of Applied Physics* **99** (2006), no. 2, 023901.

[38] T. Taniguchi and H. Imamura, "Critical current of spin-transfer-torque-driven magnetization dynamics in magnetic multilayers," *Physical Review B (Condensed Matter and Materials Physics)* **78** (2008), no. 22, 224421.

[39] W. Chen, M. J. Rooks, N. Ruiz, J. Z. Sun, and A. D. Kent, "Spin transfer in bilayer magnetic nanopillars at high fields as a function of free-layer thickness," *Phys. Rev. B* **74** (Oct, 2006) 144408.

[40] M. D. Stiles and A. Zangwill, "Anatomy of spin-transfer torque," *Phys. Rev.* **B 66** (2002) 014407.

[41] J. Katine and E. E. Fullerton, "Device implications of spin-transfer torques," *Journal of Magnetism and Magnetic Materials* **320** (2008) 1217.

[42] C. Wang, Y.-T. Cui, J. A. Katine, R. A. Buhrman, and D. C. Ralph, "Time-resolved measurement of spin-transfer-driven ferromagnetic resonance and spin torque in magnetic tunnel junctions," *Nature Physics* **7** (2011) 496.

[43] N. Bode, L. Arrachea, G. S. Lozano, T. S. Nunner, and F. von Oppen, "Current-induced switching in transport through anisotropic magnetic molecules," *Phys. Rev. B* **85** (Mar, 2012) 115440.

[44] W. H. Butler, X.-G. Zhang, T. C. Schulthess, and J. M. MacLaren, "Spin-dependent tunneling conductance of Fe|MgO|Fe sandwiches," *Phys. Rev. B* **63** (Jan, 2001) 054416.

[45] M. V. Costache, M. Sladkov, S. M. Watts, C. H. van der Wal, and B. J. van Wees, "Electrical detection of spin pumping due to the precessing magnetization of a single ferromagnet," *Physical Review Letters* **97** (2006), no. 21, 216603.

[46] T. Moriyama, R. Cao, X. Fan, G. Xuan, B. K. Nikolić, Y. Tserkovnyak, J. Kolodzey, and J. Q. Xiao, "Tunnel barrier enhanced voltage signal generated by magnetization precession of a single ferromagnetic layer," *Physical Review Letters* **100** (2008), no. 6, 067602.

[47] B. Heinrich, C. Burrowes, E. Montoya, B. Kardasz, E. Girt, Y.-Y. Song, Y. Sun, and M. Wu, "Spin pumping at the magnetic insulator (yig)/normal metal (au) interfaces," *Phys. Rev. Lett.* **107** (Aug, 2011) 066604.

[48] I. M. Miron, G. Gaudin, S. Auffret, B. Rodmacq, A. Schuhl, S. Pizzini, J. Vogel, and P. Gambardella, "Current-driven spin torque induced by the rashba effect in a ferromagnetic metal layer," *Nature Materials* **9** (2010) 230.

[49] I. M. Miron, K. Garello, G. Gaudin, P.-J. Zermatten, M. V. Costache, S. Auffret, S. Bandiera, B. Rodmacq, A. Schuhl, and P. Gambardella, "Perpendicular switching of a single ferromagnetic layer induced by in-plane current injection," *Nature* **476** (2011) 189.

[50] L. Liu, O. J. Lee, T. J. Gudmundsen, D. C. Ralph, and R. A. Buhrman, "Current-induced switching of perpendicularly magnetized magnetic layers using spin torque from the spin hall effect," *Phys. Rev. Lett.* **109** (Aug, 2012) 096602.

[51] L. Liu, C.-F. Pai, Y. Li, H. W. Tseng, D. C. Ralph, and R. A. Buhrman, "Spin-torque switching with the giant spin hall effect of tantalum," *Science* **336** (2012) 555.

[52] R. Winkler, *Spin-Orbit Coupling Effects in Two-Dimensional Electron and Hole Systems.* Springer, Berlin, 2003.

[53] T. Suzuki, S. Fukami, N. Ishiwata, M. Yamanouchi, S. Ikeda, N. Kasai, and H. Ohno, "Current-induced effective field in perpendicularly magnetized ta/cofeb/mgo wire," *Applied Physics Letters* **98** (2011), no. 14, 142505.

[54] V. M. Edelstein, "Spin polarization of conduction electrons induced by electric current in two-dimensional asymmetric electron systems," *Solid State Comm.* **73** (1990) 233.

[55] J. Inoue, G. E. W. Bauer, and L. W. Molenkamp, "Diffuse transport and spin accumulation in a rashba two-dimensional electron gas," *Phys. Rev. B* **67** (2003) 033104.

[56] P. Gambardella and I. M. Miron, "Current-induced spin-orbit torques," *Philos. Transact. A Math. Phys. Eng. Sci.* **369** (2011) 3175.

[57] A. Manchon, "Spin hall effect versus rashba torque: A diffusive approach," *arXiv:1204.4869* (2012).

[58] D. A. Pesin and A. H. MacDonald, "Quantum kinetic theory of current-induced torques in rashba ferromagnets," *Phys. Rev. B* **86** (Jul, 2012) 014416.

[59] P. M. Haney, H.-W. Lee, K.-J. Lee, A. Manchon, and M. D. Stiles, "Current induced torques and interfacial spin-orbit coupling: Semiclassical modeling," *Phys. Rev. B* **87** (May, 2013) 174411.

[60] J.-H. Park, C. H. Kim, H.-W. Lee, and J. H. Han, "Orbital chirality and rashba interaction in magnetic bands," *Phys. Rev. B* **87** (Jan, 2013) 041301.

[61] A. Manchon, "Interfacial spin-orbit splitting and current-driven spin torque in anisotropic tunnel junctions," *Phys. Rev. B* **83** (May, 2011) 172403.

[62] F. Mahfouzi, N. Nagaosa, and B. K. Nikolić, "Spin-orbit coupling induced spin-transfer torque and current polarization in topological-insulator/ferromagnet vertical heterostructures," *Phys. Rev. Lett.* **109** (Oct, 2012) 166602.

[63] C. Gould, C. Rüster, T. Jungwirth, E. Girgis, G. M. Schott, R. Giraud, K. Brunner, G. Schmidt, and L. W. Molenkamp, "Tunneling anisotropic magnetoresistance: A spin-valve like tunnel magnetoresistance using a single magnetic layer," *Phys. Rev. Lett.* **93** (2004) 117203, arXiv:cond-mat/0407735.

[64] J. Moser, A. Matos-Abiague, D. Schuh, W. Wegscheider, J. Fabian, and D. Weiss, "Tunneling anisotropic magnetoresistance and spin-orbit coupling in Fe/GaAs/Au tunnel junctions," *Phys. Rev. Lett.* **99** (Aug, 2007) 056601.

[65] A. Matos-Abiague and J. Fabian, "Anisotropic tunneling magnetoresistance and tunneling anisotropic magnetoresistance: Spin-orbit coupling in magnetic tunnel junctions," *Phys. Rev. B* **79** (Apr, 2009) 155303.

[66] D. Houssameddine, U. Ebels, B. Delaët, B. Rodmacq, I. Firastrau, F. Ponthenier, M. Brunet, C. Thirion, J.-P. Michel, L. Prejbeanu-Buda, M.-C. Cyrille, O. Redon, , and B. Dieny, "Spin-torque oscillator using a perpendicular polarizer and a planar free layer," *Nature Mater.* **6** (2007) 447.

[67] H. Liu, D. Bedau, D. Backes, J. A. Katine, J. Langer, and A. D. Kent, "Ultrafast switching in magnetic tunnel junction based orthogonal spin transfer devices," *Applied Physics Letters* **97** (2010), no. 24, 242510.

[68] T. Devolder, J. Hayakawa, K. Ito, H. Takahashi, S. Ikeda, P. Crozat, N. Zerounian, J.-V. Kim, C. Chappert, and H. Ohno, "Single-shot time-resolved measurements of nanosecond-scale spin-transfer induced switching: Stochastic versus deterministic aspects," *Phys. Rev. Lett.* **100** (Feb, 2008) 057206.

[69] D. Bedau, H. Liu, J. Z. Sun, J. A. Katine, E. E. Fullerton, S. Mangin, and A. D. Kent, "Spin-transfer pulse switching: From the dynamic to the thermally activated regime," *Applied Physics Letters* **97** (2010), no. 26, 262502.

[70] W. L. Lim, N. Ebrahim-Zadeh, H. G. E. Hentschel, and S. Urazhdin, "Temperature-dependent proximity magnetism in pt," *arXiv:1209.1802* (2012).

[71] X.-L. Qi and S.-C. Zhang, "Topological insulators and superconductors," *Rev. Mod. Phys.* **83** (Oct, 2011) 1057–1110.

[72] I. Garate and M. Franz, "Inverse spin-galvanic effect in the interface between a topological insulator and a ferromagnet," *Phys. Rev. Lett.* **104** (Apr, 2010) 146802.

[73] T. Yokoyama, Y. Tanaka, and N. Nagaosa, "Anomalous magnetoresistance of a two-dimensional ferromagnet/ferromagnet junction on the surface of a topological insulator," *Phys. Rev. B* **81** (Mar, 2010) 121401.

[74] T. Yokoyama, "Current-induced magnetization reversal on the surface of a topological insulator," *Phys. Rev. B* **84** (Sep, 2011) 113407.

[75] F. Mahfouzi, N. Nagaosa, and B. K. Nikolić, "Charge pumping through the interface between topological insulator with massive surface dirac fermions and a precessing ferromagnet," *arXiv:1112.2314* (2011).

[76] H. T. Ueda, A. Takeuchi, G. Tatara, and T. Yokoyama, "Topological charge pumping effect by the magnetization dynamics on the surface of three-dimensional topological insulators," *Phys. Rev. B* **85** (Mar, 2012) 115110.

[77] F. Mahfouzi, B. K. Nikolić, S.-H. Chen, and C.-R. Chang, "Microwave-driven ferromagnet–topological-insulator heterostructures: The prospect for giant spin battery effect and quantized charge pump devices," *Phys. Rev. B* **82** (Nov, 2010) 195440.

[78] X.-L. Qi, T. L. Hughes, and S.-C. Zhang, "Fractional charge and quantized current in the quantum spin hall state," *Nat Phys* **4** (Apr., 2008) 273–276.

[79] H. Kurebayashi, O. Dzyapko, V. E. Demidov, D. Fang, A. J. Ferguson, and S. O. Demokritov, "Controlled enhancement of spin-current emission by three-magnon splitting," *Nature Materials* **10** (2011) 660.

[80] N. Ashcroft and N. Mermin, *Solid State Physics.* Saunders College, Philadelphia, 1976.

[81] N. Marzari, A. A. Mostofi, J. R. Yates, I. Souza, and D. Vanderbilt, "Maximally localized wannier functions: Theory and applications," *Rev. Mod. Phys.* **84** (Oct, 2012) 1419–1475.

[82] A.-P. Jauho, N. S. Wingreen, and Y. Meir, "Time-dependent transport in interacting and noninteracting resonant-tunneling systems," *Phys. Rev. B* **50** (Aug, 1994) 5528–5544.

[83] E. Saitoh, M. Ueda, H. Miyajima, and G. Tatara, "Conversion of spin current into charge current at room temperature: Inverse spin-hall effect," *Appl. Phys. Lett.* **88** (2006) 182509.

[84] R. Cao, T. Moriyama, W. G. Wang, X. Fan, J. Kolodzey, S.-H. Chen, C.-R. Chang, Y. Tserkovnyak, B. K. Nikolić, and J. Q. Xiao, "Spin-polarized transport and dynamics in magnetic tunneling structures," *IEEE Transactions on Magnetics* **45** (2009) 3434.

[85] Y. Kajiwara, K. Harii, S. Takahashi, J. Ohe, K. Uchida, M. Mizuguchi, H. Umezawa, H. Kawai, K. Ando, K. Takanashi, S. Maekawa, and E. Saitoh, "Transmission of electrical signals by spin-wave interconversion in a magnetic insulator," *Nature* **464** (Mar., 2010) 262–266.

[86] Y. Tserkovnyak, T. Moriyama, and J. Q. Xiao, "Tunnel-barrier-enhanced dc voltage signals induced by magnetization dynamics in magnetic tunnel junctions," *Physical Review B (Condensed Matter and Materials Physics)* **78** (2008), no. 2, 020401.

[87] S.-H. Chen, C.-R. Chang, J. Q. Xiao, and B. K. Nikolić, "Spin and charge pumping in magnetic tunnel junctions with precessing magnetization: A nonequilibrium green function approach," *Physical Review B (Condensed Matter and Materials Physics)* **79** (2009), no. 5, 054424.

[88] S. T. Chui and Z. F. Lin, "Large voltage from spin pumping in magnetic tunnel junctions," *Physical Review B (Condensed Matter and Materials Physics)* **77** (2008), no. 9, 094432.

[89] A. Brataas, G. E. W. Bauer, and P. J. Kelly, "Non-collinear magnetoelectronics," *Physics Reports* **427** (2006) 157.

[90] Y.-H. Zhu, B. Hillebrands, and H. C. Schneider, "Spin-signal propagation in time-dependent noncollinear spin transport," *Phys. Rev. B* **79** (2009) 214412.

[91] A. Takeuchi, K. Hosono, and G. Tatara, "Diffusive versus local spin currents in dynamic spin pumping systems," *Phys. Rev. B* **81** (Apr, 2010) 144405.

[92] N. Nagaosa, J. Sinova, S. Onoda, A. H. MacDonald, and N. P. Ong, "Anomalous hall effect," *Rev. Mod. Phys.* **82** (May, 2010) 1539–1592.

[93] M. Wimmer, M. Lobenhofer, J. Moser, A. Matos-Abiague, D. Schuh, W. Wegscheider, J. Fabian, K. Richter, and D. Weiss, "Orbital effects on tunneling anisotropic magnetoresistance in fe/gaas/au junctions," *Phys. Rev. B* **80** (Sep, 2009) 121301.

[94] A. N. Chantis, K. D. Belashchenko, E. Y. Tsymbal, and M. van Schilfgaarde, "Tunneling anisotropic magnetoresistance driven by resonant surface states: First-principles calculations on an fe(001) surface," *Phys. Rev. Lett.* **98** (2007) 046601, arXiv:cond-mat/0610061.

[95] M. Gmitra, S. Konschuh, C. Ertler, C. Ambrosch-Draxl, and J. Fabian, "Band-structure topologies of graphene: Spin-orbit coupling effects from first principles," *Phys. Rev. B* **80** (Dec, 2009) 235431.

[96] K. M. D. Hals, A. Brataas, and Y. Tserkovnyak, "Scattering theory of charge-current induced magnetization dynamics," *EPL (Europhysics Letters)* **90** (2010), no. 4, 47002.

[97] K. Obata and G. Tatara, "Current-induced domain wall motion in rashba spin-orbit system," *Phys. Rev. B* **77** (Jun, 2008) 214429.

[98] P. M. Haney and M. D. Stiles, "Current-induced torques in the presence of spin-orbit coupling," *Phys. Rev. Lett.* **105** (Sep, 2010) 126602.

[99] A. Manchon and S. Zhang, "Theory of nonequilibrium intrinsic spin torque in a single nanomagnet," *Physical Review B* **78** (2008) 212405.

[100] P. W. Brouwer, "Scattering approach to parametric pumping," *Phys. Rev. B* **58** (Oct, 1998) R10135–R10138.

[101] R. H. Silsbee, A. Janossy, and P. Monod, "Coupling between ferromagnetic and conduction-spin-resonance modes at a ferromagnetic—normal-metal interface," *Phys. Rev. B* **19** (May, 1979) 4382–4399.

[102] A. Takeuchi and G. Tatara, "Spin damping monopole," *arXiv:1104.4215* (2011).

[103] B. Wang, J. Wang, and H. Guo, "Current plateaus of nonadiabatic charge pump: Multiphoton assisted processes," *Phys. Rev. B* **68** (Oct, 2003) 155326.

[104] K. S. Thygesen and K. W. Jacobsen, "Interference and k -point sampling in the supercell approach to phase-coherent transport," *Phys. Rev. B* **72** (Jul, 2005) 033401.

[105] H. Itoh, J. Inoue, A. Umerski, and J. Mathon, "Quantum oscillation of magnetoresistance in tunneling junctions with a nonmagnetic spacer," *Phys. Rev. B* **68** (Nov, 2003) 174421.

[106] B. K. Nikolić and L. P. Zârbo, "Extrinsically vs. intrinsically driven spin hall effect in disordered mesoscopic multiterminal bars," *Europhysics Letters* **77** (2007), no. 4, 47004 (5pp).

[107] H. Bentmann, F. Forster, G. Bihlmayer, M. G. E. V. Chulkov and, L. Moreschin and, and F. Reinert, "Origin and manipulation of the rashba splitting in surface alloys," *EPL (Europhysics Letters)* **87** (2009) 37003.

[108] Y. M. Blanter and M. Büttiker, "Shot noise in mesoscopic conductors," *Physics Reports* **336** (Sept., 2000) 1–166, cond-mat/9910158.

[109] B. K. Nikolić and R. L. Dragomirova, "What can we learn about the dynamics of transported spins by measuring shot noise in spin-orbit-coupled nanostructures?," *Semiconductor Science and Technology* **24** (2009), no. 6, 064006.

[110] M. Zhu, C. L. Dennis, and R. D. McMichael, "Temperature dependence of magnetization drift velocity and current polarization in $ni_{80}fe_{20}$ by spin-wave doppler measurements," *Phys. Rev. B* **81** (Apr, 2010) 140407.

[111] M. Moskalets and M. Büttiker, "Floquet scattering theory of quantum pumps," *Phys. Rev. B* **66** (Nov, 2002) 205320.

[112] O. Entin-Wohlman, A. Aharony, and Y. Levinson, "Adiabatic transport in nanostructures," *Phys. Rev. B* **65** (Apr, 2002) 195411.

[113] L. Arrachea and M. Moskalets, "Relation between scattering-matrix and keldysh formalisms for quantum transport driven by time-periodic fields," *Physical Review B (Condensed Matter and Materials Physics)* **74** (2006), no. 24, 245322.

[114] D. Fioretto and A. Silva, "Phase coherence, inelastic scattering, and interaction corrections in pumping through quantum dots," *Phys. Rev. Lett.* **100** (Jun, 2008) 236803.

[115] J. ichiro Ohe, A. Takeuchi, G. Tatara, and B. Kramer, "Inverse spin hall effect in the rashba spin-orbit system," *Physica E: Low-dimensional Systems and Nanostructures* **40** (2008), no. 5, 1554. 17th International Conference on Electronic Properties of Two-Dimensional Systems.

[116] C. Li, Y. Yu, Y. Wei, and J. Wang, "Nonadiabatic quantum spin pump: Interplay between spatial interference and photon-assisted tunneling in two-dimensional rashba systems," *Phys. Rev. B* **75** (Jan, 2007) 035312.

[117] K. Hattori, "Spin pumping from rashba spin-orbit-coupled electron systems driven by electric dipole spin resonance," *Journal of the Physical Society of Japan* **77** (2008) 034707.

[118] L. Arrachea, "Exact green's function renormalization approach to spectral properties of open quantum systems driven by harmonically time-dependent fields," *Phys. Rev. B* **75** (2007) 035319.

[119] N. Tsuji, T. Oka, and H. Aoki, "Correlated electron systems periodically driven out of equilibrium: $floquet + dmft$ formalism," *Phys. Rev. B* **78** (Dec, 2008) 235124.

[120] K. Hattori, "Spin pumping from finite-sized electron systems in ballistic and diffusive transport regimes," *Physical Review B (Condensed Matter and Materials Physics)* **75** (2007), no. 20, 205302.

[121] P. Zhang, Q.-K. Xue, and X. C. Xie, "Spin current through a quantum dot in the presence of an oscillating magnetic field," *Phys. Rev. Lett.* **91** (Nov, 2003) 196602.

[122] D. S. Fisher and P. A. Lee, "Relation between conductivity and transmission matrix," *Phys. Rev. B* **23** (Jun, 1981) 6851–6854.

[123] T. Kitagawa, T. Oka, A. Brataas, L. Fu, and E. Demler, "Transport properties of nonequilibrium systems under the application of light: Photoinduced quantum hall insulators without landau levels," *Phys. Rev. B* **84** (Dec, 2011) 235108.

[124] M. Z. Hasan and C. L. Kane, "Colloquium: Topological insulators," *Rev. Mod. Phys.* **82** (Nov, 2010) 3045–3067.

[125] A. R. Akhmerov, C. W. Groth, J. Tworzydło, and C. W. J. Beenakker, "Switching of electrical current by spin precession in the first landau level of an inverted-gap semiconductor," *Phys. Rev. B* **80** (Nov, 2009) 195320.

[126] S. Datta and B. Das, "Electronic analog of the electro-optic modulator," *Applied Physics Letters* **56** (1990), no. 7, 665–667.

[127] T. Yokoyama, Y. Tanaka, and N. Nagaosa, "Giant spin rotation in the junction between a normal metal and a quantum spin hall system," *Phys. Rev. Lett.* **102** (Apr, 2009) 166801.

[128] C. L. Kane and E. J. Mele, "Quantum spin hall effect in graphene," *Physical Review Letters* **95** (Nov., 2005) 226801, cond-mat/0411737.

[129] B. A. Bernevig, T. L. Hughes, and S.-C. Zhang, "Quantum spin hall effect and topological phase transition in hgte quantum wells," *Science* **314** (2006) 1757, arXiv:cond-mat/0611399.

[130] S.-H. Chen, B. K. Nikolić, and C.-R. Chang, "Inverse quantum spin hall effect generated by spin pumping from precessing magnetization into a graphene-based two-dimensional topological insulator," *Phys. Rev. B* **81** (Jan, 2010) 035428.

[131] A. Brataas, Y. Tserkovnyak, G. E. W. Bauer, and B. I. Halperin, "Spin battery operated by ferromagnetic resonance," *Phys. Rev. B* **66** (Aug, 2002) 060404(R).

[132] J. E. Hirsch, "Spin hall effect," *Phys. Rev. Lett.* **83** (1999) 1834.

[133] E. M. Hankiewicz, L. W. Molenkamp, T. Jungwirth, and J. Sinova, "Manifestation of the spin-hall effect through transport measurements in the mesoscopic regime," *Phys. Rev. B* **70** (2004) 241301, arXiv:cond-mat/0409334.

[134] C.-L. Chen, C.-R. Chang, and B. K. Nikolić, "Quantum coherence and its dephasing in the giant spin hall effect and nonlocal voltage generated by magnetotransport through multiterminal graphene bars," *Phys. Rev. B* **85** (Apr, 2012) 155414.

[135] O. Mosendz, J. E. Pearson, F. Y. Fradin, G. E. W. Bauer, S. D. Bader, and A. Hoffmann, "Quantifying spin hall angles from spin pumping: Experiments and theory," *Phys. Rev. Lett.* **104** (Jan, 2010) 046601.

[136] K. Ando, S. Takahashi, J. Ieda, Y. Kajiwara, H. Nakayama, T. Yoshino, K. Harii, Y. Fujikawa, M. Matsuo, S. Maekawa, and E. Saitoh, "Inverse spin-hall effect induced by spin pumping in metallic system," *Journal of Applied Physics* **109** (2011), no. 10, –.

[137] S. O. Valenzuela and M. Tinkham, "Direct electronic measurement of the spin hall effect," *Nature* **442** (2006) 176, arXiv:cond-mat/0605423.

[138] T. Seki, Y. Hasegawa, S. Mitani, S. Takahashi, H. Imamura, S. Maekawa, J. Nitta, and K. Takanashi, "Giant spin hall effect in perpendicularly spin-polarized fept/au devices," *Nat Mater* **7** (Feb., 2008) 125–129.

[139] C. Brüne, A. Roth, E. G. Novik, M. König, H. Buhmann, E. M. Hankiewicz, W. Hanke, J. Sinova, and L. W. Molenkamp, "Evidence for the ballistic intrinsic spin hall effect in hgte nanostructures," *Nature Phys.* **6** (June, 2010) 448–454.

[140] D. A. Abanin, S. V. Morozov, L. A. Ponomarenko, R. V. Gorbachev, A. S. Mayorov, M. I. Katsnelson, K. Watanabe, T. Taniguchi, K. S. Novoselov, L. S. Levitov, and A. K. Geim, "Giant nonlocality near the dirac point in graphene," *Science* **332** (2011) 328.

[141] L. K. Werake, B. A. Ruzicka, and H. Zhao, "Observation of intrinsic inverse spin hall effect," *Phys. Rev. Lett.* **106** (Mar, 2011) 107205.

[142] K. Shen, G. Vignale, and R. Raimondi, "Microscopic theory of the inverse edelstein effect," *Phys. Rev. Lett.* **112** (Mar, 2014) 096601.

[143] C.-X. Liu, X.-L. Qi, H. Zhang, X. Dai, Z. Fang, and S.-C. Zhang, "Model hamiltonian for topological insulators," *Phys. Rev. B* **82** (Jul, 2010) 045122.

[144] F. Mahfouzi and B. K. Nikolić, "How to construct the proper gauge-invariant density matrix in steady-state nonequilibrium: Applications to spin-transfer and spin-orbit torques," *SPIN* **03** (2013), no. 02, 1330002, http://www.worldscientific.com/doi/pdf/10.1142/S2010324713300028.

[145] E. Zhao, C. Zhang, and M. Lababidi, "Mott scattering at the interface between a metal and a topological insulator," *Phys. Rev. B* **82** (Nov, 2010) 205331.

[146] Z. Y. Wang, X. Guo, H. D. Li, T. L. Wong, N. Wang, and M. H. Xie, "Superlattices of bi[sub 2]se[sub 3]/in[sub 2]se[sub 3]: Growth characteristics and structural properties," *Appl. Phys. Lett.* **99** (2011), no. 2, 023112.

[147] G. Stefanucci and R. van Leeuwen, *Nonequilibrium Many-Body Theory of Quantum Systems: A Modern Introduction.* Cambridge University Press, Cambridge, 2013.

[148] C.-R. C. S.-H. Chen, C.-L. Chen and F. Mahfouzi, "Spin-charge conversion in a multiterminal aharonov-casher ring coupled to precessing ferromagnets: A charge-conserving floquet nonequilibrium green function approach," *Phys. Rev. B* **87** (2013) 045402.

[149] W. Luo and X.-L. Qi, "Massive dirac surface states in topological insulator/magnetic insulator heterostructures," *Phys. Rev. B* **87** (Feb, 2013) 085431.

[150] P. G. Silvestrov, P. W. Brouwer, and E. G. Mishchenko, "Spin and charge structure of the surface states in topological insulators," *Phys. Rev. B* **86** (Aug, 2012) 075302.

[151] N. N. P.-H. Chang, F. Mahfouzi and B. K. Nikolić, "Spin-seebeck effect on the surface of a topological insulator due to nonequilibrium spin-polarization parallel to the direction of thermally driven electronic transport," *Phys. Rev. B* **89** (2014) 195418.

[152] Q. I. Yang, M. Dolev, L. Zhang, J. Zhao, A. D. Fried, E. Schemm, M. Liu, A. Palevski, A. F. Marshall, S. H. Risbud, and A. Kapitulnik, "Emerging weak localization effects on a topological insulator-insulating ferromagnet (bi_2se_3-eus) interface," *Phys. Rev. B* **88** (Aug, 2013) 081407.

[153] P. Wei, F. Katmis, B. A. Assaf, H. Steinberg, P. Jarillo-Herrero, D. Heiman, and J. S. Moodera, "Exchange-coupling-induced symmetry breaking in topological insulators," *Phys. Rev. Lett.* **110** (Apr, 2013) 186807.

[154] A. Kandala, A. Richardella, D. W. Rench, D. M. Zhang, T. C. Flanagan, and N. Samarth, "Growth and characterization of hybrid insulating ferromagnet-topological insulator heterostructure devices," *Applied Physics Letters* **103** (2013), no. 20, 202409.

[155] M. D. Ventra, *Electrical Transport in Nanoscale Systems.* Cambridge University Press, 2008.

[156] P. Dutt, J. Koch, J. E. Han, and K. L. Hur, "Effective equilibrium theory of nonequilibrium quantum transport," *Annals of Physics* **326** (2011) 2963.

[157] S. Datta, "Nanoscale device modeling: the green's function method," *Superlattices and Microstructures* **28** (2000) 253.

[158] A. Dhar, K. Saito, and P. Hänggi, "Nonequilibrium density-matrix description of steady-state quantum transport," *Phys. Rev. E* **85** (Jan, 2012) 011126.

[159] M. Brandbyge, J.-L. Mozos, P. Ordejón, J. Taylor, and K. Stokbro, "Density-functional method for nonequilibrium electron transport," *Physical Review B* **65** (Apr., 2002) 165401, cond-mat/0110650.

[160] D. A. Areshkin and B. K. Nikolić, "Electron density and transport in top-gated graphene nanoribbon devices: First-principles green function algorithms for systems containing a large number of atoms," *Phys. Rev. B* **81** (Apr, 2010) 155450.

[161] S. Sanvito, "Chapter 7 electron transport theory for large systems," in *Computational Nanoscience*, pp. 179–224. The Royal Society of Chemistry, 2011.

[162] B. K. Nikolić, L. P. Zârbo, and S. Souma, "Imaging mesoscopic spin hall flow: Spatial distribution of local spin currents and spin densities in and out of multiterminal spin-orbit coupled semiconductor nanostructures," *Phys. Rev. B* **73** (2006) 075303, arXiv:cond-mat/0506588.

[163] S. Barraza-Lopez, M. Vanević, M. Kindermann, and M. Y. Chou, "Effects of metallic contacts on electron transport through graphene," *Phys. Rev. Lett.* **104** (Feb, 2010) 076807.

[164] T. Christen and M. Büttiker, "Gauge-invariant nonlinear electric transport in mesoscopic conductors," *Europhys. Lett.* **35** (1996), no. 7, 523–528.

[165] A. R. Hernández and C. H. Lewenkopf, "Nonlinear electronic transport in nanoscopic devices: Nonequilibrium green's functions versus scattering approach," *arXiv:0907.2073* (2009).

[166] E. I. Rashba, "Spin currents in thermodynamic equilibrium: The challenge of discerning transport currents," *Phys. Rev. B* **68** (Dec, 2003) 241315.

[167] H. U. Baranger and A. D. Stone, "Electrical linear-response theory in an arbitrary magnetic field: A new Fermi-surface formation," *Phys. Rev. B* **40** (1989) 8169.

[168] T. Qin, Q. Niu, and J. Shi, "Energy magnetization and the thermal hall effect," *Phys. Rev. Lett.* **107** (Nov, 2011) 236601.

[169] P. M. Haney, D. Waldron, R. A. Duine, A. S. Núñez, H. Guo, and A. H. MacDonald, "Current-induced order parameter dynamics: Microscopic theory applied to co/cu/co spin valves," *Phys. Rev. B* **76** (Jul, 2007) 024404.

[170] C. Heiliger, M. Czerner, B. Y. Yavorsky, I. Mertig, and M. D. Stiles, "Implementation of a nonequilibrium green's function method to calculate spin-transfer torque," *Journal of Applied Physics* **103** (2008), no. 7, 07A709.

[171] A. Reynoso, G. Usaj, and C. A. Balseiro, "Spin hall effect in clean two-dimensional electron gases with rashba spin-orbit coupling," *Phys. Rev. B* **73** (2006), no. 11, 115342.

[172] N. P. Butch, K. Kirshenbaum, P. Syers, A. B. Sushkov, G. S. Jenkins, H. D. Drew, and J. Paglione, "Strong surface scattering in ultrahigh-mobility bi_2se_3 topological insulator crystals," *Phys. Rev. B* **81** (Jun, 2010) 241301.

[173] J. C. Slonczewski, "Current-driven excitation of magnetic multilayers," *J. Magn. Magn. Mater.* **159** (1996) L1.

[174] S.-C. Oh, S.-Y. P. A. Manchon, M. Chshiev, J.-H. Han, H.-W. Lee, J.-E. Lee, K.-T. Nam, Y. Jo, Y.-C. Kong, B. Dieny, and K.-J. Lee, "Bias-voltage dependence of perpendicular spin-transfer torque in asymmetric mgo-based magnetic tunnel junctions," *Nature Phys.* **5** (2009) 898.

[175] K. Carva and I. Turek, "Landauer theory of ballistic torkances in noncollinear spin valves," *Phys. Rev. B* **80** (Sep, 2009) 104432.

[176] J. Xiao, G. E. W. Bauer, and A. Brataas, "Spin-transfer torque in magnetic tunnel junctions: Scattering theory," *Physical Review B (Condensed Matter and Materials Physics)* **77** (2008), no. 22, 224419.

[177] Y.-H. Tang, N. Kioussis, A. Kalitsov, W. H. Butler, and R. Car, "Influence of asymmetry on bias behavior of spin torque," *Phys. Rev. B* **81** (Feb, 2010) 054437.

[178] I. Theodonis, N. Kioussis, A. Kalitsov, M. Chshiev, and W. H. Butler, "Anomalous bias dependence of spin torque in magnetic tunnel junctions," *Physical Review Letters* **97** (2006), no. 23, 237205.

[179] C. Heiliger and M. D. Stiles, "*Ab Initio* studies of the spin-transfer torque in magnetic tunnel junctions," *Phys. Rev. Lett.* **100** (May, 2008) 186805.

[180] S. D. Ganichev, S. N. Danilov, P. Schneider, V. V. Bel'Kov, L. E. Golub, W. Wegscheider, D. Weiss, and W. Prettl, "Electric current-induced spin orientation in quantum well structures," *J. Magn. Magn. Mater* **300** (2006) 127.

[181] A. Manchon and S. Zhang, "Theory of spin torque due to spin-orbit coupling," *Physical Review B* **79** (2009) 094422.

[182] I. Garate and A. H. MacDonald, "Influence of a transport current on magnetic anisotropy in gyrotropic ferromagnets," *Phys. Rev. B* **80** (Oct, 2009) 134403.

[183] X. Wang and A. Manchon, "Diffusive spin dynamics in ferromagnetic thin films with a rashba interaction," *Phys. Rev. Lett.* **108** (Mar, 2012) 117201.

[184] J. Velev and W. Butler, "On the equivalence of different techniques for evaluating the green function for a semi-infinite system using a localized basis," *Journal of Physics: Condensed Matter* **16** (2004), no. 21, R637–R657.

[185] M. Schiró and M. Fabrizio, "Real-time diagrammatic monte carlo for nonequilibrium quantum transport," *Phys. Rev. B* **79** (Apr, 2009) 153302.

[186] H. Haug and A.-P. Jauho, *Quantum kinetics in transport and optics of semiconductors*. Springer-Verlag, Berlin, 2008.

[187] C. Caroli, R. Combescot, P. Nozieres, and D. Saint-James, "Direct calculation of the tunneling curre," *Journal of Physics C: Solid State Physics* **4** (1971), no. 8, 916–929.

[188] S. Wang, Y. Xu, and K. Xia, "First-principles study of spin-transfer torques in layered systems with noncollinear magnetization," *Phys. Rev. B* **77** (May, 2008) 184430.

[189] D. M. Edwards, F. Federici, J. Mathon, and A. Umerski, "Self-consistent theory of current-induced switching of magnetization," *Phys. Rev. B* **71** (Feb, 2005) 054407.

[190] N. Bode, S. V. Kusminskiy, R. Egger, and F. von Oppen, "Scattering theory of current-induced forces in mesoscopic systems," *Phys. Rev. Lett.* **107** (Jul, 2011) 036804.

[191] A. Manchon, "Voltage-driven versus current-driven spin torque in anisotropic tunneling junctions," *IEEE Trans. Magn.* **47** (2011) 2735.

[192] Y. K. Kato, R. C. Myers, A. C. Gossard, and D. D. Awschalom, "Observation of the spin hall effect in semiconductors," *Science* **306** (2004) 1910.

[193] J. Wunderlich, B. Kaestner, J. Sinova, and T. Jungwirth, "Experimental observation of the spin-hall effect in a two dimensional spin-orbit coupled semiconductor system," *Phys. Rev. Lett.* **94** (2005) 047204, arXiv:cond-mat/0410295.

[194] E. G. Mishchenko, A. V. Shytov, and B. I. Halperin, "Spin current and polarization in impure 2d electron systems with spin-orbit coupling," *Phys. Rev. Lett.* **93** (2004) 226602, arXiv:cond-mat/0406730.

[195] K. Nomura, J. Wunderlich, J. Sinova, B. Kaestner, A. H. MacDonald, and T. Jungwirth, "Edge spin accumulation in semiconductor two-dimensional hole gases," *Phys. Rev. B* **72** (2005) 245330, arXiv:cond-mat/0508532.

[196] I. Adagideli and G. E. W. Bauer, "Intrinsic spin hall edges," *Phys. Rev. Lett.* **95** (2005) 256602, arXiv:cond-mat/0506531.

[197] B. K. Nikolić, S. Souma, L. P. Zârbo, and J. Sinova, "Nonequilibrium spin hall accumulation in ballistic semiconductor nanostructures," *Physical Review Letters* **95** (2005), no. 4, 046601.

[198] V. A. Zyuzin, P. G. Silvestrov, and E. G. Mishchenko, "Spin hall edge spin polarization in a ballistic 2d electron system," *Physical Review Letters* **99** (2007), no. 10, 106601.

[199] E. B. Sonin, "Edge spin accumulation: Spin hall effect without bulk spin current," *Phys. Rev. B* **81** (Mar, 2010) 113304.

[200] A. Khaetskii and E. Sukhorukov, "Edge spin accumulation in a ballistic regime," *JETP Lett.* **92** (2010) 244.

[201] I. Adagideli, G. E. W. Bauer, and B. I. Halperin, "Detection of current-induced spins by ferromagnetic contacts," *Phys. Rev. Lett.* **97** (2006) 256601, arXiv:cond-mat/0606193.

[202] E. Y. Tsymbal, O. N. Mryasov, and P. R. LeClair, "Spin-dependent tunnelling in magnetic tunnel junctions," *J. Phys.: Condens. Matter* **15** (2003) R109.

[203] S. Yuasa, T. Nagahama, and Y. Suzuki, "Spin-polarized resonant tunneling in magnetic tunnel junctions," *Science* **297** (2002) 234.

[204] J. Mathon and A. Umerski, "Theory of tunneling magnetoresistance of an epitaxial fe/mgo/fe(001) junction," *Phys. Rev. B* **63** (May, 2001) 220403.

[205] S. Ikeda, J. Hayakawa, Y. Ashizawa, Y. M. Lee, K. Miura, H. Hasegawa, M. Tsunoda, F. Matsukura, and H. Ohno, "Tunnel magnetoresistance of 604300 k by suppression of ta diffusion in cofeb/mgo/cofeb pseudo-spin-valves annealed at high temperature," *Applied Physics Letters* **93** (2008), no. 8, 082508.

[206] Y.-H. Tang, N. Kioussis, A. Kalitsov, W. H. Butler, and R. Car, "Controlling the nonequilibrium interlayer exchange coupling in asymmetric magnetic tunnel junctions," *Phys. Rev. Lett.* **103** (Jul, 2009) 057206.

[207] H. Kubota, A. Fukushima, K. Yakushiji, T. Nagahama, S. Yuasa, K. Ando, H. Maehara, Y. Nagamine, K. Tsunekawa, D. D. Djayaprawira, N. Watanabe, and Y. Suzuki, "Quantitative measurement of voltage dependence of spin-transfer torque in mgo-based magnetic tunnel junctions," *Nature Physics* **4** (2008) 37.

[208] Z. Li, S. Zhang, Z. Diao, Y. Ding, X. Tang, D. M. Apalkov, Z. Yang, K. Kawabata, and Y. Huai, "Perpendicular spin torques in magnetic tunnel junctions," *Phys. Rev. Lett.* **100** (Jun, 2008) 246602.

[209] S.-Y. Park, Y. Jo, and K.-J. Lee, "Measurement of perpendicular spin torque at high bias via the pulsed switching phase diagram," *Phys. Rev. B* **84** (Dec, 2011) 214417.

[210] T. Balashov, A. F. Takács, M. Däne, A. Ernst, P. Bruno, and W. Wulfhekel, "Inelastic electron-magnon interaction and spin transfer torque," *Phys. Rev. B* **78** (Nov, 2008) 174404.

[211] J. P. Strachan, V. Chembrolu, Y. Acremann, X. W. Yu, A. A. Tulapurkar, T. Tyliszczak, J. A. Katine, M. J. Carey, M. R. Scheinfein, H. C. Siegmann, and J. Stöhr, "Direct observation of spin-torque driven magnetization reversal through nonuniform modes," *Phys. Rev. Lett.* **100** (Jun, 2008) 247201.

[212] A. Brataas, Y. Tserkovnyak, and G. E. W. Bauer, "Current-induced macrospin versus spin-wave excitations in spin valves," *Phys. Rev. B* **73** (Jan, 2006) 014408.

[213] V. Drewello, J. Schmalhorst, A. Thomas, and G. Reiss, "Evidence for strong magnon contribution to the tmr temperature dependence in mgo based tunnel junctions," *Phys. Rev. B* **77** (Jan, 2008) 014440.

[214] A. A. Khan, J. Schmalhorst, G. Reiss, G. Eilers, M. Münzenberg, H. Schuhmann, and M. Seibt, "Elastic and inelastic conductance in co-fe-b/mgo/co-fe-b magnetic tunnel junctions," *Phys. Rev. B* **82** (Aug, 2010) 064416.

[215] M. A. Reed, "Inelastic electron tunneling spectroscopy," *Materials Today* **11** (2008) 46.

[216] P. M. Levy and A. Fert, "Spin transfer in magnetic tunnel junctions with hot electrons," *Phys. Rev. Lett.* **97** (Sep, 2006) 097205.

[217] A. Manchon and S. Zhang, "Influence of interfacial magnons on spin transfer torque in magnetic tunnel junctions," *Phys. Rev. B* **79** (May, 2009) 174401.

[218] P. Richmond, "An electron in a ferromagnetic crystal (the magnetic polaron)," *J. Phys. C* **3** (1970) 2402.

[219] F. Reininghaus, T. Korb, and H. Schoeller, "Fingerprints of the magnetic polaron in nonequilibrium electron transport through a quantum wire coupled to a ferromagnetic spin chain," *Phys. Rev. Lett.* **97** (Jul, 2006) 026803.

[220] K. S. Thygesen and A. Rubio, "Conserving gw scheme for nonequilibrium quantum transport in molecular contacts," *Physical Review B (Condensed Matter and Materials Physics)* **77** (2008), no. 11, 115333.

[221] T. Kita, "Introduction to nonequilibrium statistical mechanics with quantum field theory," *Prog. Theor. Phys.* **123** (2010) 581.

[222] E. Rastelli, *Statistical Mechanics of Magnetic Excitations: From Spin Waves to Stripes and Checkerboards.* World Scientific, Singapore, 2013.

[223] F. Meier and D. Loss, "Magnetization transport and quantized spin conductance," *Phys. Rev. Lett.* **90** (2003) 167204.

[224] A. O. Gogolin and A. Komnik, "Towards full counting statistics for the anderson impurity model," *Phys. Rev. B* **73** (May, 2006) 195301.

[225] D. F. Urban, R. Avriller, and A. Levy Yeyati, "Nonlinear effects of phonon fluctuations on transport through nanoscale junctions," *Phys. Rev. B* **82** (Sep, 2010) 121414.

[226] T. Novotný, F. Haupt, and W. Belzig, "Nonequilibrium phonon backaction on the current noise in atomic-sized junctions," *Phys. Rev. B* **84** (Sep, 2011) 113107(R).

[227] S. Datta, *Electronic transport in mesoscopic systems.* Cambridge University Press, Cambridge, 1995.

[228] I. Rungger and S. Sanvito, "Algorithm for the construction of self-energies for electronic transport calculations based on singularity elimination and singular value decomposition," *Phys. Rev. B* **78** (Jul, 2008) 035407.

[229] A. Mitra, I. Aleiner, and A. J. Millis, "Phonon effects in molecular transistors: Quantal and classical treatment," *Phys. Rev. B* **69** (Jun, 2004) 245302.

[230] J. K. Viljas, J. C. Cuevas, F. Pauly, and M. Häfner, "Electron-vibration interaction in transport through atomic gold wires," *Phys. Rev. B* **72** (Dec, 2005) 245415.

[231] J. Koch, M. Semmelhack, F. von Oppen, and A. Nitzan, "Current-induced nonequilibrium vibrations in single-molecule devices," *Phys. Rev. B* **73** (Apr, 2006) 155306.

[232] T. Frederiksen, M. Paulsson, M. Brandbyge, and A.-P. Jauho, "Inelastic transport theory from first principles: Methodology and application to nanoscale devices," *Phys. Rev. B* **75** (May, 2007) 205413.

[233] M. Galperin, M. A. Ratner, and A. Nitzan, "Molecular transport junctions: vibrational effects," *J. Phys.: Condens. Matter* **19** (2007) 103201.

[234] H.-F. Lü and Y. Guo, "Kondo effect and spin-polarized transport through a quantum dot with rashba spin-orbit interaction," *Physical Review B (Condensed Matter and Materials Physics)* **76** (2007), no. 4, 045120.

[235] Y. Asai, "Nonequilibrium phonon effects on transport properties through atomic and molecular bridge junctions," *Phys. Rev. B* **78** (Jul, 2008) 045434.

[236] W. Lee, N. Jean, and S. Sanvito, "Exploring the limits of the self-consistent born approximation for inelastic electronic transport," *Phys. Rev. B* **79** (Feb, 2009) 085120.

[237] L. K. Dash, H. Ness, and R. W. Godby, "Nonequilibrium inelastic electronic transport: Polarization effects and vertex corrections to the self-consistent born approximation," *Phys. Rev. B* **84** (Aug, 2011) 085433.

[238] A. Oguri and R. Sakano, "Exact interacting green's function for the anderson impurity at high bias voltages," *Phys. Rev. B* **88** (Oct, 2013) 155424.

[239] L. Siddiqui, A. W. Ghosh, and S. Datta, "Phonon runaway in carbon nanotube quantum dots," *Phys. Rev. B* **76** (Aug, 2007) 085433.

[240] Y. Meir and N. S. Wingreen, "Landauer formula for the current through an interacting electron region," *Phys. Rev. Lett.* **68** (Apr, 1992) 2512–2515.

[241] H. Ness, L. K. Dash, and R. W. Godby, "Generalization and applicability of the landauer formula for nonequilibrium current in the presence of interactions," *Phys. Rev. B* **82** (Aug, 2010) 085426.

[242] X. Chen, I. Rungger, C. D. Pemmaraju, U. Schwingenschlögl, and S. Sanvito, "First-principles study of high-conductance dna sequencing with carbon nanotube electrodes," *Phys. Rev. B* **85** (Mar, 2012) 115436.

Appendix A

HILBERT TRANSFORMATION

The Hilbert transform of a function $f(x)$ is defined as

$$H\{f\}(y) = \frac{1}{\pi} p.v. \int_{-\infty}^{\infty} dy \frac{f(x)}{y-x} \tag{A.1}$$

with $p.v.$ being the Cauchy principal value integral. One can see that performing a direct integration on an equidistant or even adaptive grid is going to be numerically very time consuming and inefficient. Instead other approaches such as using FFT seem to be more practical with the requirement that f to be defined on an equidistant grid. But since the function f in our calculations are given at adaptive points with second order polynomial interpolation , here we try to develope an algorithm that uses this type of input and calculates Hilbert transform of the corresponding array. To do this lets say the function f is defined on $2N+1$ adaptive points x_ns such that the value of the function inside the range (x_{2n-1}, x_{2n+1}) is obtained by a second order polynomial interpolation using three points $(x_{2n-1}, x_{2n}, x_{2n+1})$. In this case the above integral can be written as

$$H\{f\}(x) = \frac{1}{\pi} \sum_{n=1}^{N} p.v. \int_{x_{2n-1}}^{x_{2n+1}} dy \frac{a_n(y) f_{2n-1} + b_n(y) f_{2n} + c_n(y) f_{2n+1}}{x-y} \tag{A.2}$$

with

$$a_n(y) = \frac{(y-x_{2n})(y-x_{2n+1})}{(x_{2n-1}-x_{2n})(x_{2n-1}-x_{2n+1})} \tag{A.3}$$

$$b_n(y) = \frac{(y-x_{2n-1})(y-x_{2n+1})}{(x_{2n}-x_{2n-1})(x_{2n}-x_{2n+1})} \tag{A.4}$$

$$c_n(y) = \frac{(y-x_{2n-1})(y-x_{2n})}{(x_{2n+1}-x_{2n-1})(x_{2n+1}-x_{2n})} \tag{A.5}$$

We can now perform the integrations analytically and get

$$H\{f\}(y) = \frac{1}{\pi}\sum_{n=1}^{N} f_{2n-1}a_n^h(y) + f_{2n}b_n^h(y) + f_{2n+1}c_n^h(y) \tag{A.6}$$

where

$$a_n^h(y) = \frac{\frac{1}{2}(x_{2n+1} - x_{2n-1}) - (y - x_{2n}) - \frac{(y-x_{2n})(y-x_{2n+1})}{x_{2n+1}-x_{2n-1}}L_n}{x_{2n} - x_{2n-1}} \tag{A.7}$$

$$b_n^h(y) = \frac{\frac{1}{2}(x_{2n+1} - x_{2n-1})^2 - (x_{2n+1} - x_{2n-1})(y - x_{2n-1}) - (y - x_{2n-1})(y - x_{2n+1})L_n}{(x_{2n} - x_{2n-1})(x_{2n} - x_{2n+1})} \tag{A.8}$$

$$c_n^h(y) = \frac{-\frac{1}{2}(x_{2n+1} - x_{2n-1}) - (y - x_{2n}) - \frac{(y-x_{2n-1})(y-x_{2n})}{x_{2n+1}-x_{2n-1}}L_n}{x_{2n+1} - x_{2n}} \tag{A.9}$$

$$L_n = \log(\frac{y - x_{2n+1}}{y - x_{2n-1}}) \tag{A.10}$$

One can redefine the above arrays in a single array $h_n(y)$ as follows

$$\begin{aligned} &h_1(y) = a_1^h(y) \quad , \quad h_{2N+1}(y) = c_N^h(y), \\ &h_{2n}(y) = b_n^h(y) \quad , \quad h_{2n+1}(y) = a_{n+1}^h(y) + c_n^h(y) \end{aligned} \tag{A.11}$$

and write down

$$H\{f\}(y) = \frac{1}{\pi}\sum_{n=1}^{2N+1} f_n h_n(y) \tag{A.12}$$

Appendix B

AN EFFICIENT ALGORITHM TO FIND CERTAIN ELEMENTS OF INVERSE OF A SPARSE MATRIX

In this note our aim is to find certain elements of the inverse of a symmetric sparse matrix. When the size of the matrix is too large one might not be interested to know all elements of the inverse of the matrix. In fact it's not efficient at all to find all elements of inverse of the matrix and then filter out the required elements. Instead we can see in the following that for the case of sparse matrices it's possible to find efficiently only required blocks of the inverse of matrix. The idea is to reorder the indices of the matrix such that at the end we'll have a block tridiagonal matrix(in general with different dimensions). Then we use a recursive method and try to find the required blocks of the inverse which is in fact first block of the matrix. Therefore in this method one should first specify the elements that are required. One can do this by introducing a vector array $x = [x_1, x_2, ..., x_n]$, where xi shows the index of the required elements. Therefore if the size of whole symmetric matrix A is N, x_i would lie between 1 and N. As the first step we construct an n by n matrix using these elements and put it as first block of our block diagonal matrix B. Then we try to construct the whole block diagonal matrix B, using this base. In order to do this we try to find the next block by finding the indices that are connected directly to first block. For example if $x = x_1 = 1$ then , all js such that $A(1, j)$ are nonzero will give me the indices of my next block (i.e. $x' = [j_1, j_2, ...]$). In order to do this in Matlab we wrote following function

```
1 function x=neighbours_sites(ix,iy,m)
2   yp=find(ix==m);
```

```
3    for j=1:size(yp)
4      x(j)=iy(yp(j));
5    end
```

where,

```
1   [ix,iy,z]=find(A);
```

m in this function is index of one site and x would be in general an array showing all indices coupled to index m. Now we can use this function and find indices of the next block using following Matlab function;

```
1  function [x1,fs1,nfs1]=next_block(ix,iy,x,fs,nfs)
2    Nb=size(x,2);
3    fs1=fs;
4    nfs1=nfs;
5    Counter=0;
6    for j=1:Nb
7      nx=neighbours_sites(ix,iy,x(j));
8      for k=1:size(nx,2)
9        new=1;
10       for l=1:nfs1
11     if(nx(k)==fs1(l))
12       new=0;
13       end
14       end
15       if(new==1)
16     Counter=Counter+1;
17     nfs1=nfs1+1;
18     fs1(nfs1)=nx(k);
19     x1(Counter)=nx(k);
20       end
21     end
```

```
22    end
23    if(Counter==0)
24      x1=0;
25    end
```

'fs' in this function represents found sites (indices) and 'nfs' is the number of found sites. We have introduced such variables to put only new indices for the next block. As a result x1 in this function gives indices of the next block. Now using this function we can also put as input the indices of second block and get the indices of third block. Continuing this procedure we can construct the whole matrix as blocked matrix. In fact in this method we find a new ordering for our original matrix A which is now in a form of block diagonal matrix. As the following code we present the function that performs this procedure.

```
1  function [T1,H,T2,s]=sparse_to_block(A,x)
2    [ix,iy,z]=find(A);
3    Nt=size(A,1);
4    fs=zeros(Nt);
5    Nb=size(x,2);
6    nfs=Nb;
7    fs(1:nfs)=x(:);
8    l_n=1;
9    s(l_n)=Nb;
10   while nfs<Nt
11     nfs1=nfs;
12     [x1,fs,nfs]=next_cell(ix,iy,x,fs,nfs);
13     if(nfs1==nfs)
14       break;
15     end
16     Nb1=size(x1,2);
17     for j=1:Nb
18       for k=1:Nb
19     H(j,k,l_n)=A(x(j),x(k));
```

```
20        end
21        for k=1:Nb1
22      T1(j,k,l_n)=A(x(j),x1(k));
23      T2(k,j,l_n)=A(x1(k),x(j));
24        end
25      end
26      l_n=l_n+1;
27      x=x1;
28      Nb=Nb1;
29      s(l_n)=Nb;
30    end
31    for j=1:Nb
32      for k=1:Nb
33        H(j,k,l_n)=A(x(j),x(k));
34      end
35    end
```

The outputs of this function are three arrays of matrices which form upper diagonal blocks (T1) and diagonal blocks (H) and lower diagonal blocks (T2) and a one dimensional array s which represents the dimensions of the block matrices. As an example we consider a 200 × 200 random sparse matrix and put x=[1,2,3]. Now we use this three blocked diagonal matrix and using following function try to find the elements of inverse of first block. We can see the result of direct inversion and our method are completely in agreement.

```
1  function invA=invb(T1,H,T2,s)
2    Nz=size(H,3);
3    N=size(H,1);
4    if(s==0)
5      s(1:Nz)=N;
6    end
7    i=1:s(Nz);
8    B(i,i)=inv(H(i,i,Nz));
```

```
 9    for k=1:Nz-2
10      i=1:s(Nz-k);
11      j=1:s(Nz-k+1);
12      B(i,i)=inv(H(i,i,Nz-k)-T1(i,j,Nz-k)*B(j,j)*T2(j,i,Nz-k));
13    end
14    i=1:s(1);
15    j=1:s(2);
16    invA(i,i)=inv(H(i,i,1)-T1(i,j,1)*B(j,j)*T2(j,i,1));
```

Appendix C

SPIN-ORBIT INTERACTION HAMILTONIAN

Spin-orbit Hamiltonian reads

$$H_{SO} = \frac{1}{2m_e c}(\nabla V \times \overrightarrow{p}).\overrightarrow{S} \tag{C.1}$$

where V can be due to atomic potential (leading to $L.S$ terms in Hamiltonian), external electric field and/or impurities in the system. Here we are interested in the effects of impurities and the corresponding spin-orbit induced interaction. Therefore, in fact we are dealing with following impurity term in Hamiltonian

$$H_{imp} = V_{imp} + \lambda(\nabla V_{imp} \times \overrightarrow{p}).\overrightarrow{\sigma} \tag{C.2}$$

where $\lambda = \frac{1}{4m_e c}$. In order to write this equation in tight binding form, we should calculate the expectation value of it in terms of the wavefunctions which are localized around each atom. To simplify the situation let us consider the local waves to be s-wave which has radial symmetry. Additionally let us consider that the impurity potential also depends only on radial coordinate r_i, which is interatomic distance from the impurity site i. Let us now find the expectation value for the above expression. Considering that $|\mathbf{n}\rangle$ presents the local basis of our system, we write

$$H_{imp} = V_{imp}+\lambda(\nabla V_{imp}\times \overrightarrow{p}).\overrightarrow{\sigma}\langle \mathbf{m}|(\nabla V_{imp}\times \overrightarrow{p}).\overrightarrow{\sigma}|\mathbf{n}\rangle = \sum_{\mathbf{m}'}(<\mathbf{m}|\nabla V_{imp})|\mathbf{m}'> \times <\mathbf{m}'|\overrightarrow{p}|\mathbf{n}>.\overrightarrow{\sigma} \tag{C.3}$$

Considering the following wavefunction

$$\langle \overrightarrow{r}|\mathbf{n}\rangle = \psi_{\mathbf{n}}(r), \tag{C.4}$$

which is a localized function around site $\mathbf{m}$, we can write

$$\langle \mathbf{m}|\overrightarrow{p}|\mathbf{m}'\rangle = \int dxdydz\psi^*_{\mathbf{m}}(r)\overrightarrow{p}\psi_{\mathbf{m}'}(r) = -i\hbar\int \frac{\overrightarrow{r}}{r}\psi^*_{\mathbf{m}}(r)\partial_r\psi_{\mathbf{m}'}(r)dxdydz \quad \text{(C.5)}$$

and

$$\langle \mathbf{m}|\nabla V_{imp})|\mathbf{m}'\rangle = \int dxdydz\psi^*_{\mathbf{m}}(r)\nabla V^{\mathbf{m}'}_{imp}\psi_{\mathbf{m}'}(r) = \int \frac{\overrightarrow{r}}{r}\psi^*_{\mathbf{m}}(r)(\partial_r V^{\mathbf{m}'}_{imp})\psi_{\mathbf{m}'}(r)dxdydz \quad \text{(C.6)}$$

For $\mathbf{m} = \mathbf{m}'$ we can see that both of integrands of these expressions are odd functions which give zero contribution. We note that this this is due to the fact that we have chosen local wavefunctions to be s-wave. In case we of other orbital wavefunctions one can check that we get $L.S$ terms for the SOI. For other elements of these expressions, considering enough localized wavefunctions and also localized impurity potential we can deduce that only first nearest neighbors have to be considered and other elements are negligible. In order to calculate nearest neighbor elements let us consider $\mathbf{m}' = 0$ and then choose the nearest neighbors to to be on $\widehat{x}$ axis "i.e." $\mathbf{m} = (\pm 1, 0, 0)$. Performing summation over these nearest neighbors, for above expressions we have

$$\sum_{\mathbf{m}}\langle \mathbf{m}|\overrightarrow{p}|\mathbf{0}\rangle = -i\hbar\int \frac{\overrightarrow{r}}{r}(\psi^*(|\overrightarrow{r} - a\widehat{x}|) + \psi^*(|\overrightarrow{r} + a\widehat{x}|)\partial_r\psi(r)dxdydz \quad \text{(C.7)}$$

and

$$\sum_{\mathbf{m}}\langle \mathbf{m}|\nabla V_{imp})|\mathbf{0}\rangle = \int \frac{\overrightarrow{r}}{r}(\psi^*(|\overrightarrow{r} - a\widehat{x}|) + \psi^*(|\overrightarrow{r} + a\widehat{x}|)\psi(r)\partial_r V_{imp}(r)dxdydz \quad \text{(C.8)}$$

We can easily see that both of the integrands are odd functions with respect to $\overrightarrow{r}$ which mean that result of the integrations is zero. Here again we note this is due to our choice of s-wave functions as our local functions. Therefore we can write

$$\langle \mathbf{m}|\overrightarrow{p}|\mathbf{m}'\rangle = it_x(\delta_{\mathbf{m},\mathbf{m}'+\widehat{i}} - \delta_{\mathbf{m},\mathbf{m}'-\widehat{i}})\widehat{x} + it_y(\delta_{\mathbf{m},\mathbf{m}'+\widehat{j}} - \delta_{\mathbf{m},\mathbf{m}'-\widehat{j}})\widehat{y} + it_z(\delta_{\mathbf{m},\mathbf{m}'+\widehat{k}} - \delta_{\mathbf{m},\mathbf{m}'-\widehat{k}})\widehat{z} \tag{C.9}$$

and

$$\begin{aligned}\langle \mathbf{m}|\nabla V_{imp}^{\mathbf{m}'})|\mathbf{m}'\rangle =& V_x^{\mathbf{m}'}(\delta_{\mathbf{m},\mathbf{m}'+\widehat{i}} - \delta_{\mathbf{m},\mathbf{m}'-\widehat{i}})\widehat{x} + V_y^{\mathbf{m}'}(\delta_{\mathbf{m},\mathbf{m}'+\widehat{j}} - \delta_{\mathbf{m},\mathbf{m}'-\widehat{j}})\widehat{y} \\ &+ V_z^{\mathbf{m}'}(\delta_{\mathbf{m},\mathbf{m}'+\widehat{k}} - \delta_{\mathbf{m},\mathbf{m}'-\widehat{k}})\widehat{z}\end{aligned} \tag{C.10}$$

where $\widehat{i} = (1,0,0), \widehat{j} = (0,1,0), \widehat{k} = (0,0,1)$ In this calculation we considered that impurity exists only on site $\mathbf{m}'$ and there's no impurity in neighboring sites. But what if we consider different impurity strenght for different sites? In this case one can readily get

$$\langle \mathbf{m}|\nabla V_{imp})|\mathbf{m}'\rangle = [(V_x^{\mathbf{m}'} - V_x^{\mathbf{m}})\delta_{\mathbf{m},\mathbf{m}'+\widehat{i}} - (V_x^{\mathbf{m}'} - V_x^{\mathbf{m}})\delta_{\mathbf{m},\mathbf{m}'-\widehat{i}}]\widehat{x} \tag{C.11}$$

$$+[(V_y^{\mathbf{m}'} - V_y^{\mathbf{m}})\delta_{\mathbf{m},\mathbf{m}'+\widehat{j}} - (V_y^{\mathbf{m}'} - V_y^{\mathbf{m}})\delta_{\mathbf{m},\mathbf{m}'-\widehat{j}}]\widehat{y} \tag{C.12}$$

$$+[(V_z^{\mathbf{m}'} - V_z^{\mathbf{m}})\delta_{\mathbf{m},\mathbf{m}'+\widehat{k}} - (V_z^{\mathbf{m}'} - V_z^{\mathbf{m}})\delta_{\mathbf{m},\mathbf{m}'-\widehat{k}}]\widehat{z} \tag{C.13}$$

In case of symmetric crystal where $a_x = a_y = a_z = a$ we can write

$$\langle \mathbf{m}|\nabla V_{imp})|\mathbf{m}'\rangle = (V^{\mathbf{m}'} - V^{\mathbf{m}})[(\delta_{\mathbf{m},\mathbf{m}'+\widehat{i}} - \delta_{\mathbf{m},\mathbf{m}'-\widehat{i}})\widehat{x} + (\delta_{\mathbf{m},\mathbf{m}'+\widehat{j}} - \delta_{\mathbf{m},\mathbf{m}'-\widehat{j}})\widehat{y} + (\delta_{\mathbf{m},\mathbf{m}'+\widehat{k}} - \delta_{\mathbf{m},\mathbf{m}'-\widehat{k}})\widehat{z}] \tag{C.14}$$

and

$$\langle \mathbf{m}|\overrightarrow{p}|\mathbf{m}'\rangle = it[(\delta_{\mathbf{m},\mathbf{m}'+\widehat{i}} - \delta_{\mathbf{m},\mathbf{m}'-\widehat{i}})\widehat{x} + (\delta_{\mathbf{m},\mathbf{m}'+\widehat{j}} - \delta_{\mathbf{m},\mathbf{m}'-\widehat{j}})\widehat{y} + (\delta_{\mathbf{m},\mathbf{m}'+\widehat{k}} - \delta_{\mathbf{m},\mathbf{m}'-\widehat{k}})\widehat{z}] \tag{C.15}$$

And finally for the elements of the SO Hamiltonian in tight binding model we get

$$(H_{SO})_{\mathbf{m},\mathbf{n}} = i\alpha \overrightarrow{L}_{\mathbf{m},\mathbf{n}}.\overrightarrow{\sigma} \tag{C.16}$$

where

$$(\overrightarrow{L}_{\mathbf{m},\mathbf{n}})_i = (V_{\mathbf{n}+\hat{k}}-V_{\mathbf{n}+\hat{j}})\delta_{\mathbf{m},\mathbf{n}+\hat{j}+\hat{k}}+(V_{\mathbf{n}-\hat{j}}-V_{\mathbf{n}+\hat{k}})\delta_{\mathbf{m},\mathbf{n}-\hat{j}+\hat{k}}+(V_{\mathbf{n}+\hat{j}}-V_{\mathbf{n}-\hat{k}})\delta_{\mathbf{m},\mathbf{n}+\hat{j}-\hat{k}}+(V_{\mathbf{n}-\hat{k}}-V_{\mathbf{n}-\hat{j}})\delta_{\mathbf{m},\mathbf{n}-\hat{j}} \tag{C.17}$$

and using cyclic property of coordinate one can get other components. One should note that we have included all unknown parameters of the system in parameter α, so $V_{\mathbf{m}}$ in above equation can effectively represent the strength of impurity at site $\mathbf{m}$.

Appendix D

LIST OF PUBLICATIONS

8. Farzad Mahfouzi and Branislav K. Nikolić, "Signatures of electron-magnon interaction in the current-voltage characteristics of magnetic tunnel junctions: A nonequilibrium many-body perturbation theory approach," *Phys. Rev. B* **90**, 045115 (2014).

7. Po-Hao Chang, Farzad Mahfouzi, Naoto Nagaosa, and Branislav K. Nikolić, "Spin-Seebeck effect due to thermally driven spin-polarized electronic transport on the surface of a three-dimensional topological insulator," *Phys. Rev. B* **89**, 195418 (2014).

6. Farzad Mahfouzi, Naoto Nagaosa, and Branislav K. Nikolić, "Spin-to-charge conversion in lateral and vertical topological-insulator/ferromagnet heterostructures with microwave-driven precessing magnetization," `http://arxiv.org/abs/1112.2314`.

5. Farzad Mahfouzi and Branislav K. Nikolić, "How to construct the proper gauge-invariant density matrix in steady-state nonequilibrium: Applications to spin-transfer and spin-orbit torques," *Spin*, **3**, 1330002, (2013).

4. Son-Hsien Chen, Chien-Liang Chen, Ching-Ray Chang, and Farzad Mahfouzi, "Spin-charge conversion in a multiterminal Aharonov-Casher ring coupled to precessing ferromagnets: A charge-conserving Floquet nonequilibrium Green function approach," *Phys. Rev. B* **87**, 045402 (2013).

3. Farzad Mahfouzi, Naoto Nagaosa, and Branislav K. Nikolić, "Spin-orbit coupling induced spin-transfer torque and current polarization in topological-insulator/ferromagnet vertical heterostructures," *Phys. Rev. Lett.* **109**, 166602 (2012).

2. Farzad Mahfouzi, Jaroslav Fabian, Naoto Nagaosa and Branislav K. Nikolić, "Charge pumping by magnetization dynamics in magnetic and semimagnetic tunnel junctions with interfacial Rashba or bulk extrinsic spin-orbit coupling," *Phys. Rev. B* **85**, 054406 (2012).

1. Farzad Mahfouzi, B. K. Nikolić, S.-H. Chen, and C.-R. Chang, "Microwave-driven ferromagnet-topological-insulator heterostructures: The prospect for giant spin battery effect and quantized charge pump devices," *Phys. Rev. B* **82**, 195440 (2010).